Innovative Microchannel-Structured Ceramic Beads for Intensifying Advanced Oxidation Processes

JIAOJIAO ZHENG

Doctor of Philosophy

Aston University

December 2024

Aston University

Innovative Microchannel-Structured Ceramic Beads for Intensifying Advanced Oxidation Processes

Jiaojiao Zheng

Doctor of Philosophy

2024

ABSTRACT

Diffusional mass transfer is vital in heterogeneous catalysis, influencing reactants reach catalytic active sites and product removal. The interplay between diffusion and reaction rates significantly impacts overall reaction performance, particularly in catalyst pellets, which are key in determining reactor pressure drops. Most academic research, laboratory experiments, simulations, and engineering innovations on diffusional mass transfer in catalyst pellets rely on porous structures of randomly packed fine particles, which possess fixed parameters (e.g., porosity and tortuosity), limiting advancements in enhancing internal diffusional mass transfer. This thesis introduces a novel approach to overcoming these limitations by creating a new microchannel structure within spherical beads, a geometry widely used in industrial catalytic processes. The research explores the modification and optimisation of this unique structure, material synergies and related topics such as reusability. The findings provide a comprehensive overview of this innovation by intensifying advanced oxidation processes (AOPs) and its potential benefits for other diffusion-limited reactions. Chapter 4 introduces alumina beads with oriented finger-like microstructures to revolutionise diffusional resistance within spherical beads. Two types of mesoporous materials (γ-Al_2O_3 in Chapter 5 and carbon xerogel in Chapter 6) were incorporated into these innovative alumina beads to further enhance their specific surface area, facilitating the uniform catalyst dispersion. Furthermore, alternative inorganic material, silica, was applied in Chapter 7 to prepare the microchannel-structured silica beads. Most importantly, all samples after being used and regenerated exhibited significantly higher catalytic performance than the fresh ones due to the enhanced accessibility of open pores on the bead surface during regeneration, highlighting the significance of intensifying the diffusional transfer process to benefit catalytic reactions. Such benefits are highly transferable to a broader spectrum of heterogeneous catalysis applications. Notably, the ceramic beads in this research are easily separable from the bulk solution, addressing scalability issues common with conventional nano- or micro-scale catalysts.

Key words: Diffusional mass transfer, process intensification (PI), microchannel-structured beads, catalytic reactions, AOPs, peroxymonosulfate (PMS), phase-inversion

DECLARATION

I hereby declare that this thesis and the work reported herein was composed by and originated entirely from me. All the sources of information derived from the published and unpublished work of others has been acknowledged in the text and the relevant references are included in this thesis. No part of the work in this thesis has been previously submitted for any degree or qualification at any other university.

Jiaojiao Zheng

December 2024

Acknowledgements

Pursuing a PhD overseas for me has not only been an academic endeavour but also a path of personal resilience. The ups and downs instilled in me an independent personality, a spirit of exploration, and a positive mindset towards conflict resolution. As I approach the culmination of this incredible journey, I would like to express my heartfelt gratitude to all those who have given me unwavering support throughout my PhD journey.

First and foremost, I would like to extend my greatest appreciation to my supervisors, Dr. Zhentao Wu and Prof. Anthony V. Bridgwater, whose mentorship, invaluable guidance, and constant support have been instrumental throughout this journey. I am grateful for the opportunities including participating in conferences, serving as a teaching assistant, and engaging in international collaborations, culminating in my international trip to Wuhan, China, which will forever be in my memory. I sincerely appreciate the exceptional hospitality and tremendous support offered by Prof. Haiping Yang, Prof. Yang Yang, Prof. Tingzhen Ming, Prof. Yongjia Wu, and their team members during my stay at Huazhong University of Science and Technology and Wuhan University of Technology.

My deepest thanks also go to the laboratory technician and managers, Dr. Jinesh Cherukkattu Manayil, Dr. Daniel Jozef Nowakowski, and Janine Bruce-Hughes. Whose consistent willingness to assist in equipment training, insightful discussions on experiment results, as well as health and safety issues were invaluable in conducting my experiments efficiently.

I am also thankful to my colleagues and friends, Dr. Michael R Rawlins, Dr. Mahesan Naidu Subramaniam, Mpho Thabang Rapoo, Memoona Khalid, Dr. Marta Masó Martínez, Dr. Zeinab Zandieh, Dr. Yating Hu, Salwan Cartwright-Shamoon, Dr. Huan Xiang, Dr. Qingwei Meng, Prof. Wenli Zhang, Dr. Chonghui Wang, Shuling Zhao, Hanyu Zhang, Yuanwei Yin, Dr. Teng Xiong, Yue Yang, Prof. Jiawei Wang, Prof. Patricia Thornley, Dr. Qingchun Yuan, Qiujia Du, Yining Yang, Junyao Hou, Juping Liu, Dr. Regina Siu, Dr. Iram Razaq, Josh Bond, Lewis Yandle, Muhammad Khan, Omar Mohammad, Marion Engole, Seyed Emad Hashemnezhad, and Dr. Sarah Brewster, for their assistance in the lab and for their emotional support, encouragement, and companionship. The sense of camaraderie and connection was a constant source of motivation that made this journey enjoyable.

My parents, Mr. Daoqing Zheng and Mrs. Xuexiang Zhu, deserve my deepest gratitude. Their unconditional support has always been my greatest source of strength. I know it must have been difficult for them to allow me to go so far away from home and to study overseas alone to pursue my dream. I am forever indebted to them both.

Finally, I would also like to acknowledge the School of Engineering and Applied Science and the Energy and Bioproducts Research Institute for granting me a full scholarship, which made this research possible. My experience of studying and working at Aston University has been incredibly rewarding. This opportunity has been life-changing, and I am deeply grateful for the support.

In closing, this journey has shaped me in more ways than I could have ever imagined. As I look to the future with excitement and enthusiasm, I know that the lessons I have learned and the people I have encountered along the way will continue to influence and inspire me for years to come. Thank you all for being a part of this remarkable chapter of my life.

Table of contents

Nomenclature

Abbreviation	Description
PI	Process intensification
CPSI	Cells per square inch
PPI	Pores per inch
PMS	Peroxymonosulfate
AOPs	Advanced oxidation processes
SMX	Sulfamethoxazole
GSA	Geometrical surface areas
CFD	Computational fluid dynamics
SMR	Steam methane reforming
CMR	Catalytic membrane reactor
BMR	Baffled membrane reactor
GHSV	Gas hourly space velocity
FTS	Fischer-Tropsch synthesis
DMSO	Dimethyl sulphoxide
NMP	N-methyl-2-pyyrolidone
PVA	Polyvinyl alcohol
SSA	Specific surface area
Arlacel P135	Ethyleneglycol 30-dipolydroxystearate
PMMA	Poly (methyl methacrylate)
PESf	Polyethersulfone
AIP	Aluminum isopropoxide
XRD	X-ray diffraction
BET	Brunauer–Emmett–Teller

BJH	Barrett, Joyner, and Halenda
MIP	Mercury intrusion porosimetry
XPS	X-ray photoelectron spectroscopy
SEM	Scanning electron microscopy
EDS	Energy-dispersive X-ray spectroscopy
TGA	Thermogravimetric Analysis
ICP-OES	Inductively coupled plasma-optical emission spectrometry
PPCP	Pharmaceutical and personal care products
p-HBA	4-hydroxybenzoic acid
YSZ	Yttria stabilized zirconia
p-BQ	p-benzoquinone
tBA	tert-butanol
IWI	Incipient wetness impregnation
BED-C	Backscattered electro detector-compositional
MeOH	methanol
FFA	furfuryl
MO	Methyl orange
TEMP	2,2,6,6-tetramethyl-4-piperidone
DMPO	5,5-dimethyl-1-pyrroline N-oxide

List of Figures

List of Tables

Chapter 1 Introduction

Chapter 1 provides a concise overview of the long-standing diffusional mass transfer limitations within porous catalyst pellets and how these limitations hinder reaction efficiency as well as the design and operation of packed bed reactors. Building on this foundation, the chapter introduces the overarching innovation of this thesis, outlines its aims and objectives, and provides an overview of the structure and content of each chapter.

1.1 Background

Catalysis plays a crucial role in chemical transformation, and straddles a wide range of disciplines, such as chemistry [1, 2], chemical engineering [3-5], material science [6], biology and biochemistry [7], environmental science [8], energy [9], and engineering [10], etc. Vast majority of industrial catalytic reaction processes involve heterogeneous catalysts, accounting for approximately 80% of the global market share [11]. However, the heterogeneous reaction systems are often limited by mass and/or heat transfer rather than by reaction kinetics [12]. In mass transfer-controlled reactions, the reaction rate is typically determined by how quickly reactants reach the reactive sites and how promptly products removed, often limited by slow diffusion at microscales or inadequate mixing in the bulk phase. Process intensification (PI) techniques have been investigated to address these limitations by, for example, configuring reactions within small channels, shortening diffusional distances, and thereby enhancing reactant diffusion efficiency [13, 14]. However, the small and narrow internal channel sizes (approximately 0.01-1 mm in diameter) of microreactors result in a high pressure drop as fluids pass through [15]. In traditional packed-bed reactors, the use of fine catalyst powders promotes diffusional transfer but result in high pressure drops. This necessitates the use of large particles or pellets (1-3 mm in diameter), which have less favourable diffusional transfer characteristics [16, 17]. The long-standing challenge of such trade-offs between intraparticle diffusion and pressure drop in catalytic reactors continues to limit advancements in catalysis and reaction engineering technology, necessitating new innovations.

One potential solution to this challenge involves catalyst substrate at millimetre-scale with certain pores to favourite diffusional mass transfer, a process-intensifying approach reported by Stankiewicz and Moulijn [18]. Examples of these substrates include monolithic substrates and ceramic foam supports [19-23]. Vega et al. reported novel 3D-printed Fe/SiC honeycomb monolithic reactors with various cell structures for phenol hydroxylation [20]. The results indicated that the catalytic performance of the monolithic reactor with triangular cells was superior to that of the slurry reactor and other intensified units (square and tronco-conical cells). Zhang et al. found that the production of monocyclic aromatic hydrocarbons increased from 39.15% with ZSM-5 powder catalysts to 78.96% when ZSM-5@ceramic foam catalysts were applied [19]. Additionally, it has been reported that the external mass transfer

coefficients for the conventional ceramic beads (1.5 mm and 3 mm in diameter), honeycombs (400 cells per square inch (CPSI)) and ceramic foams (20 pores per inch (PPI) and 45 PPI) followed a definite trend, with the ranking order of 1.5 mm beads >> 45 PPI foams > 20 PPI foams ≈ 3.3 mm beads > 400 CPSI honeycombs [24]. Meanwhile, the pressure drop was ranked in the following order: 1.5 mm beads > 3.3 mm beads ≈ 45 PPI foams ≈ 20 PPI foams > 400 CPSI honeycombs.

Technically, conventional ceramic bead with a uniform macroscopic catalyst distribution (homo-type, Figure 1-1) suffers from a significant mass transfer resistance, as reactants diffuse from external surface of the bead to reach the reactive catalytic sites within the inner cores, and vice versa for products leaving the catalyst bead. Differences in diffusion rate of reactants/products often leads to less controllable side reactions and poorer selectivity as a typical consequence. The degree of mass-transfer limitations in the catalytic system can be interpretated by the Thiele modulus, denoted as φ:

$$\varphi = \frac{V_P}{A_P}\sqrt{\frac{k_r}{D_e}} \qquad \textit{(Equation 1-1)}$$

where V_P is the volume of the catalyst support/beads, A_P is the external surface area of the catalyst support/beads, k_r is the first-order rate constant, and D_e is the effective diffusion coefficient [25]. When φ is greater than 0.3, the diffusion of the reactant through the pores is commonly considered as the rate determining step. As a result, a homogeneous distribution of the active phase in large catalyst supports is only beneficial for relatively slow catalytic processes that allow reactants to diffuse to the active sites. Otherwise, the catalytic reaction ends up being internally diffusion-limited when φ increases to 0.3 or higher.

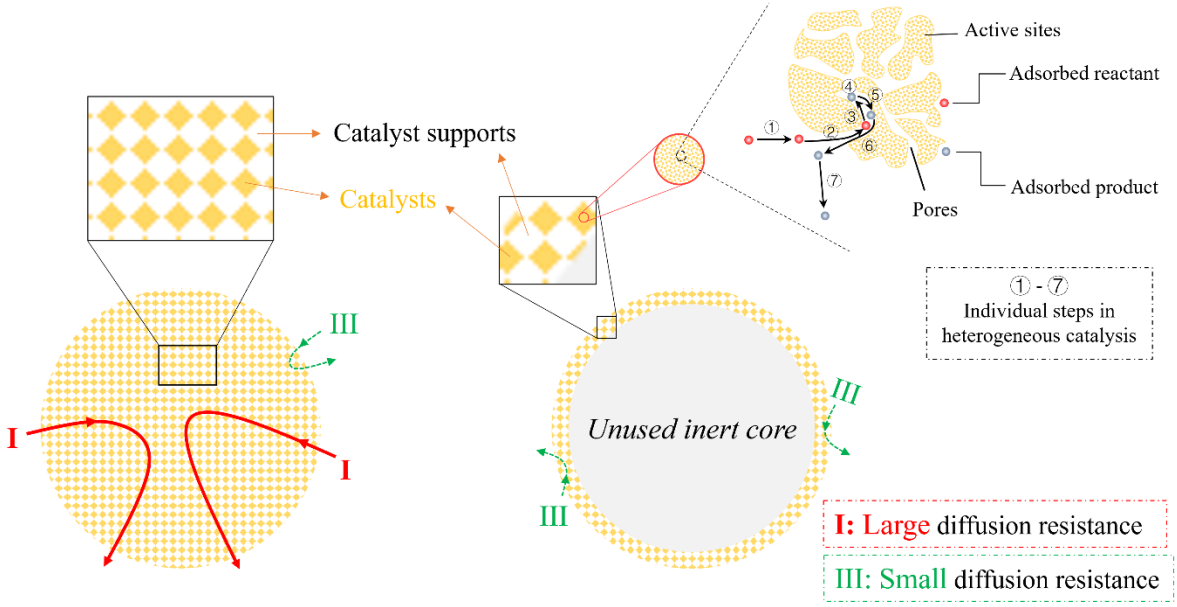

Figure 1-1 Schematic diagram of diffusional transfer inside commercial catalyst substrates.

To address this, a non-uniform macroscopic distribution of catalyst patterns, such as eggshell pellets (Figure 1-1), was introduced to circumvent the rules by replacing the pellet sizes with the thickness of the catalytic layer of several hundreds of micrometres [26, 27]. For instance, Fratalocchi et al. successfully prepared small eggshell Co/γ-Al_2O_3 catalysts by the multiple impregnation method, and the thin outer layer of cobalt, regarded as the active sites, greatly reduced the diffusion limitations, thus presenting high CO conversion, limited methane selectivity and high C_{5+} selectivity in the Fischer-Tropsch Synthesis [26]. Howeizi et al. synthetised a series of Pd/γ-Al_2O_3 catalysts and found that the sample with the egg-shell type of Pd dispersion exhibited the highest catalytic performance due to the higher accessibility of the reactants to Pd active sites in these strong diffusion-limited reactions [28]. However, although the trade-off between diffusional mass transfer and pressure drop could be solved by this type of catalyst support, there is a significant unused/inert volume of catalyst pellets. In other words, the core of the egg-shell pellets, which contains inert material, is not active and does not participate in the catalytic reaction. This inactivity reduces volumetric productivity and causes variations in reaction fronts, as well as thermal and mass fronts within the reactor.

In summary, over the past several decades, there has been limited progress in innovating porous structures to address the long-standing challenges of diffusional mass transfer limitations. Overcoming these limitations is crucial for advancing heterogeneous catalysis materials, processes, and the design and operation of related reactors, with implications across a wide range of applications and disciplines. Introducing new strategies to enhance diffusional mass transfer at the microscale has the potential to make a significant impact in these areas. This thesis aims to explore and initiate novel approaches from this perspective, by innovating microchannel structured ceramic beads. Based on the reported work related to the fabrication of microchannel-structured hollow fibre membranes [29, 30], the development of microchannel-structured ceramic beads appears to be relatively feasible.

1.2 Aims and objectives

The primary aim of this work is to design and validate innovative microchannel-structured ceramic beads and explore their potential application in diffusion-limited chemical reactions, such as peroxymonosulfate (PMS)-activated advanced oxidation processes (AOPs) reaction system. The four key objectives outlined below are aimed at achieving this:

(1) To develop and validate a methodology for fabricating finger-like microchannel-structured spherical ceramic beads to enhance diffusional mass transfer.

(2) To establish a material strategy for integrating a catalytically active phase with an auxiliary mesoporous material within the beads, enabling their application to general heterogeneous catalysis processes.

(3) To create synergies in material functionality to drive enhancements that go beyond innovations in pore structure design.

(4) To demonstrate the efficiency of these approaches through the PMS-activated AOPs system.

1.3 Thesis structure

This thesis consists of eight chapters in total. **Chapter 1** briefly introduces the research background of catalyst technology for process intensification, and outlines aims and objectives of this thesis. **Chapter 2** provides the fundamental knowledge of process intensification, conventional catalyst substrates for heterogeneous catalysis, and typical heterogeneous catalysis-AOPs, as well as key research gaps within the field of catalyst substrates and AOPs. **Chapter 3** presents the research methodology and characterisation techniques involved.

Chapter 4 focuses on the development and fabrication of innovative microchannel-structured alumina beads as the catalyst substrates to enhance diffusional mass transfer in heterogeneous catalysis, i.e., PMS-induced AOPs for catalytic degradation of sulfamethoxazole (SMX).

Chapter 5 explores a material strategy for integrating a catalytic active phase, i.e., 2 wt.% Co_3O_4, with an auxiliary mesoporous material (most commonly used γ-Al_2O_3) within the alumina beads, broadening their application to a wide range of heterogeneous catalysis processes. In this chapter, two different catalyst incorporation methods, i.e., two-step sequential impregnation method (2Co/AS*x*) and one-step co-impregnation method (2Co/AS*x* (co-imp.)), were examined to investigate the trade-offs of diffusional mass transfer and the specific surface area.

Chapter 6 investigates the integration of multifunctional carbon xerogels to drive enhancements that extend beyond pore structure innovations discussed in Chapter 4 and the auxiliary mesoporous materials examined in Chapter 5. The synergistic effects of mesoporous carbon xerogels facilitate the adsorption, catalyst dispersion, PMS activation, and pore confinement, building on the findings presented in the preceding chapters.

Chapter 7 introduces the design and fabrication of innovative microchannel-structured silica beads as catalyst substrates to advance diffusional mass transfer in heterogeneous catalysis. Different from Chapter 4, this chapter employs silica as an alternative inorganic material to demonstrate the versatility and applicability of these approaches across a broader range of materials. Additional interesting findings include the variation of diameters, porosity, and the specific surface area of the silica beads by differing the sintering temperatures. The effectiveness of these approaches from Chapter 4 to Chapter 7 were all demonstrated through the PMS-activated AOPs system. Additionally, transparent microchannel-

structured silica beads (SiO_2-1100C (6h)) were also successfully developed, offering significant potential for advancing large-scale photocatalysis, a distinct class of AOPs.

Finally, **Chapter 8** concludes the thesis by summarising the key findings and giving recommendations for the future work.

Chapter 2 Literature review

Chapter 2 provides a literature review on the process intensification (PI) at microscale that balances between the diffusional mass transfer and pressure drop. This includes the PI fundamentals and examples of PI methods, such as microreactors, membrane reactors, and millimetre-scale structured catalyst substrates, for heterogeneous catalysis. Based on this research background, the research gaps in structured catalyst substrates and AOPs – a typical model for heterogeneous catalytic reactions – have also been included for better understanding microscale process intensification.

2.1 Process intensification fundamentals

Process intensification, introduced by Ramshaw nearly five decades ago, is a strategy in chemical engineering aimed at making dramatical reductions in the size and complexity of chemical processes, while simultaneously achieving a substantially smaller, cleaner, safer and more energy efficient technology [31]. It entails the design of novel PI technology of increased volumetric productivity but reduced energy consumption, without compromising process safety and product quality. In such approaches, the rate of some process, e.g., reaction kinetics, may be increased due to the reduction of physical dimensions and transport limitations [32]. It is a fast-growing field that characterised by a vast majority of definition and interpretations, but there is no clear definition that all agree on so far. Van Gerven and Stankiewic [32] proposed four generic principles for PI design:

(1) *Maximize the effectiveness of intra- and intermolecular events* – this principle highlights a potentially critical yet underexplored aspect of PI, focus on improving process kinetics, the underlying factor for low conversion and selectivity.

(2) *Give each molecule the same processing experience* – this results in ideally uniform product distribution with minimum waste.

(3) *Optimise the driving forces at every scale and maximise the specific surface area to which these forces apply* – this principle emphasises optimising the transport rates across interfaces. Take, for example, microreactors that reduce channel diameters from millimetre to micrometre scales to enhance the mass and heat transfer [15].

(4) *Maximize the synergetic effects from partial processes* – this enables multitasking by integrating multiple processing tasks together, achieving higher efficiencies than standalone operations. Synergistic effects should be leveraged at all scales, often through macroscale multifunctionality.

The above principles outline explicit goals for process intensification. Principles (2) and (3) pertain to intensification of transport processes, whereas principles (1) and (4) refer to intensification in chemical and process design, respectively. As Van Gerven and Stankiewic stated [32], a completely intensified

process successfully implements all the above-stated principles, via the use of one or more fundamental PI approaches, which can be categorized into four domains, as illustrated in Figure 2-1:

(1) Spatial domain (structure) – introducing structure.

(2) Thermodynamic domain (energy) – introducing alternative energy forms or alternative ways of energy transfer.

(3) Functional domain (synergy) – introducing function integration.

(4) Temporal domain (time) – introducing dynamic operation.

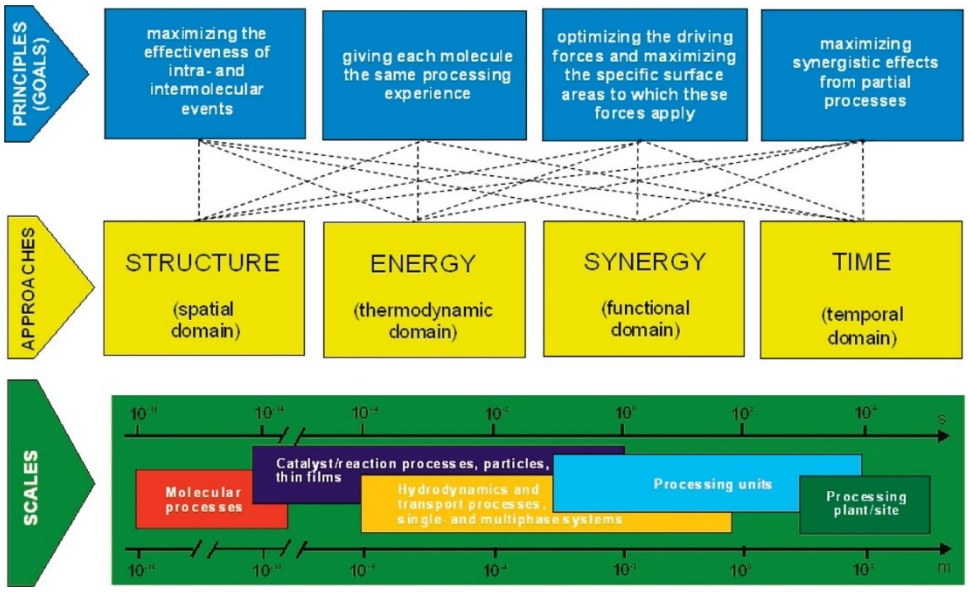

Figure 2-1 The concept of principles, approaches, and scales on process intensification, adapted from [32].

In process intensification, a well-defined geometry or structure, e.g., microchannels, honeycomb monoliths, is usually used to reduce spatial randomness, allowing for controlled movement toward the preset goal [32]. Spatial structuring in PI can be employed to implement any of the four PI principles, and it involves engineering at all scales, from nano- to macro-scale. At the molecular scale, the effectiveness of intra- and intermolecular events can be affected by structural measures [33]. The molecular reactor like zeolite catalyst is a powerful case in point, which position the small molecule within their pores for the reaction [34]. Similarly, the other three PI principles are achieved by introducing meso- and macroscale structures, such as structured catalytic packings to increase the geometrical surface areas (GSA) for the mass transfer and to allow synchronized chemical reactions [35, 36]. Examples include monolithic substrates [37, 38], foam structured catalyst supports [39, 40], nanofiber structured catalyst supports [41, 42], as well as milli- and micro-channel systems [43, 44].

These spatially structured units also enable multifunctional integration, achieving synergetic effects of the partial processes. It happens, for instance, in catalytic membrane reactors [45].

In terms of energy in PI, the fundamental theory is to optimise the way energy in its various forms (e.g. heat, pressure, and movement) is transmitted precisely and efficiently from source to recipient (ideally reactants only) [32]. Similar to spatial structuring (the first PI approach), the thermodynamic domain approach also applies to all four PI principles. At the molecular scale, it focuses on orienting molecules by magnetic fields [46, 47], strong electric fields [48, 49], or laser fields [50]. At the meso- and macroscale, alternative energy forms (e.g., electromagnetic radiation – microwaves and light [51, 52]) and alternative ways (e.g. rotating packed beds by creating artificial gravity fields [53, 54]) of transferring the energy have been revealed to boost mass and heat transport and to improve the contact of phases. Instead of relying on traditional energy transfer systems, the thermodynamic approach in PI encourages more direct energy transfer mechanism that effectively target localised areas in the process.

The functional domain is the third key approach in PI**,** focusing on combining multiple functions or processes together into a single unit or component (e.g. a molecule, a phase, or a reactor) to significantly improve overall catalytic efficiency, surpassing the effectiveness of performing separate function in sequence [32]. At the molecular scale, the catalytic function can be coupled with a secondary or tertiary function, such as multifunctional catalysts [55, 56] or adsorption [57, 58], and can also synergise with acoustic [59] or electromagnetic energy [60] inputs. Synergy at the macroscale can achieved by introducing multifunctional reactors, such as membrane reactors that integrates reaction and separation [45, 61], heat exchanger reactors that combines reactions with heat exchange [62, 63]. Synergy in PI is directly related to the fourth PI principle, as stated earlier. This PI approach seeks to foster synergy, with multifunctionality being essential for improving catalytic efficiency.

The last PI approach is the temporal domain, which basically involves either (i) manipulation of the time scales by, for instance, shortening the mixing times [64], or (2) the introduction of periodic dynamic operation (e.g., oscillating temperatures) [65] to intensify the process [32]. Intentionally introducing periodic operation can facilitate the implementation of all four PI principles. For example, purposeful cycling the liquid feed by pulse in trickled-bed reactors has demonstrated enhanced mass and heat transfer rates, fulfilling the third PI principle [66]. This approach complements the other PI domains by incorporating a time-based dimension into the process to enhance the catalytic activity, selectivity, or yield.

2.2 Classification of process intensification

According to Stankiewicz and Mouljin [18, 35], process intensification can be categorised into two major areas: process-intensifying equipment (hardware) and processing methods (software), as shown

in Figure 2-2. PI equipment refers to the innovation of structured devices with enhanced mass and heat transfer and/or intensive mixing, such as microreactors [14, 15], membrane reactors [67], and novel structured catalyst supports [40]. PI methods, however, provide innovative strategies to enhance the efficiency and effectiveness of chemical process. This technology involves the integration of reaction and other functions (e.g., multifunctional reactors), new hybrid separation (e.g., membrane adsorption), and alternative forms or ways of energy (e.g. microwave). There can be some overlaps between the two, as new methods may necessitate the development of innovative equipment and vice versa.

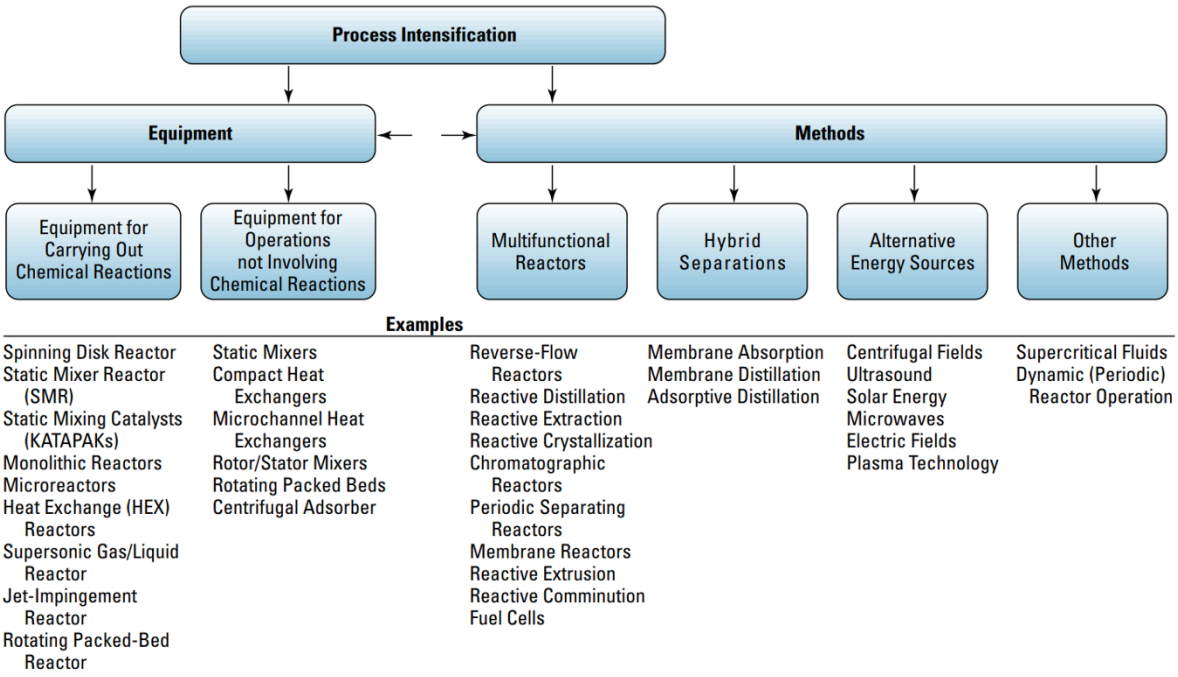

Figure 2-2 Classification of process intensification, adapted from [18].

2.2.1 Microreactors

As a promising PI equipment, microreactors have been widely applied in nanomaterial synthesis [68, 69], CO_2 capture [70, 71], Fischer-Tropsch Synthesis [72-74], methyl isobutyl ketone production [75, 76], wastewater treatment [77-79], biomedicine [80-82], and steam reforming [83]. On the one hand, one of the most significant advantages of microreactors is their microchannel structures with lateral dimensions ranging from 0.01 to 1 mm [84], providing shorter diffusion paths compared to conventional reactors. Technically, the reduced dimensions result in enhanced mass transfer efficiency and interfacial surface area. Take multi-channel microreactor for example, Gorges et al. immobilized TiO_2 catalysts onto the photocatalytic microreactor, which consists of 19 parallel channels with a channel cross-section of approximately 200 × 300 μm, for the degradation of 4-chlorophenol [85]. The mass transfer

coefficient estimated from Sherwood numbers demonstrated that there was no mass transfer limitation for this system. Additionally, the illuminated specific surface area of this microreactor surpassed that of traditional photocatalytic reactors by a factor of 4-400 times. Chen et al. anchored nanoscale zero-valent iron catalyst onto the reduced graphene oxide/polypyrrole nanocomposite microreactor, which could degrade 99% of p-nitrophenol within 50 s, outperformed the conventional batch reactors due to the strong convection and highly efficient mass transfer [86]. On the other hand, because of the small microchannel sizes and small fluid volumes involved, microreactors enable precise regulation of the reaction parameters, such as reactant concentrations, flow rates, mixing, reaction time control, mass and heat transfer rates [87]. This empowered the controlled nucleation and growth of nano- and micro-crystals with well-defined properties, which had been challenged in conventional bulk and batch procedures [69].

Despite of the noticeable mass transfer efficiency and precise process control over the reaction parameters of microreactors, their drawbacks and challenges should be acknowledged. On the one hand, due to the small microchannel dimensions, incorporating catalysts of this size range (micrometre scale) typically cause a high pressure drop [88]. This is why the industry tends to employ relatively large particles (1-3 mm) to enable less pressure drops inside packed bed reactors [16, 17]. That, in turn, results in more significant mass transfer resistance, especially when catalyst and/or catalyst support sizes surpass 300 μm.

On the other hand, the low throughput of microreactors pose a significant challenge for industrialisation, although it has been reported that microreactors offered potential for straightforward scaling up. There are two primary scale-up strategies: numbering-up and size-up, as shown in Figure 2-3 [89]. Parallel numbering up focuses on the increase of multiple microreactors/microchannels in parallel, which seeks to retain the hydrodynamic properties, exceptional mass transfer coefficients, and catalytic performance of the microreactors [69].

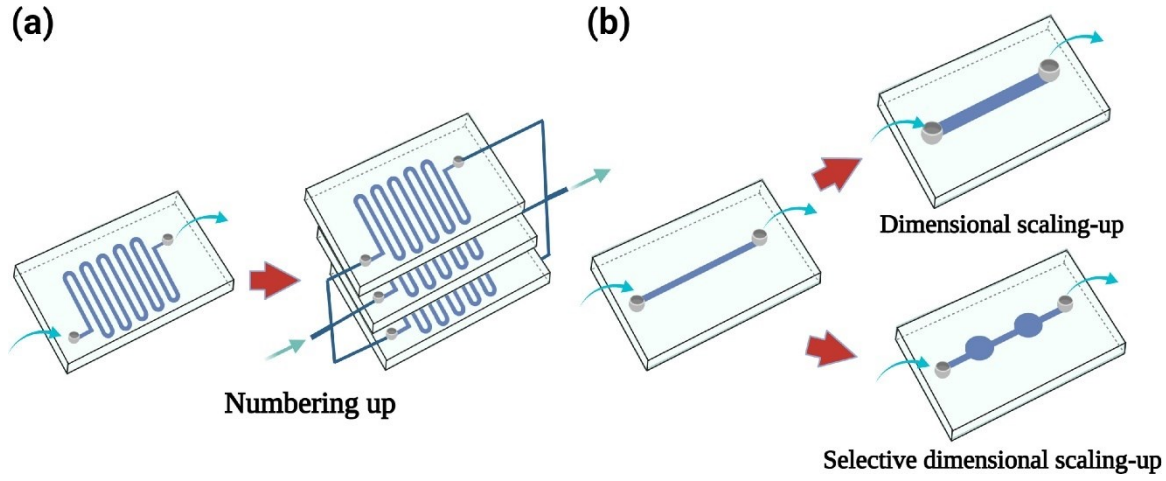

Figure 2-3 Two primary scale-up strategies for microreactors: (a) numbering-up and (b) dimensional scaling-up, adapted from [77].

Nevertheless, managing multiple identical microreactors/microchannels require sophisticated monitoring and regulation system to ensure consistent operation across units [90]. At the same time, operating multiple units in parallel also significantly increases the overall energy demand for both monitoring and process control, as well as equipment and maintenance costs [91]. Dimensional scaling-up, however, scaling up the internal volume of a single microreactor, enables the physical dimensions of the reactor increase from micrometre to millimetre scales or beyond [77]. However, as the microchannel sizes increase, the microreactor fluid flow pattern progressively shifts from surface-force driven to gravity-driven, compromising inherently process efficiency of microreactors by poor dissipation and less effective mass transfer [77, 89].

Yang et al. investigated the scale-up effect of mini-fluidized bed reactor for the photocatalytic degradation of methylene blue by increasing the quartz tube inner diameter from 1 mm to 3 mm [92]. The results demonstrated that the photocatalytic performance of 1 mm tube was 4.5 times higher than that of 3 mm tube, which could be attributed by the changes of radiation flux density, specific surface area, mass transfer resistance, and light penetration depth. Krummradt et al. found that the yields of organic product remained relatively stable (> 90%) at scales below 1 mm but might sharply decline with size [93]. Elvira et al. reported that for a wide range of residence times (0-250 s), the flow dynamics in reactor channels with diameter ranging from 100 μm to 1 mm were comparable, but starkly different in a 5 mm diameter channel [94]. It is noteworthy that continuing scaling up the dimension of microreactors to millimetre-scale leads to a reaction pattern resembling that of packed-bed reactors, which suffers from a longstanding challenge of balancing pressure drop with mass and heat transfer. Therefore, innovation is highly demanded for both the scaling up of microreactors and the catalyst substrates employed in pack-bed reactors.

2.2.2 Membrane reactors

Membrane reactors are a particular example of multifunctional reactors as the permeable membrane combines the chemical reaction with a separation process in a single unit. The permeable membrane here is a system consists of a barrier that permits certain substances (e.g., hydrogen, oxygen) to travel through while blocking unwanted ones [95]. This system significantly simplified the downstream purification, thereby reducing the capital cost and enhancing energy efficiency [96]. Interesting applications including hydrogen production [97, 98], CO_2 hydrogenation [99, 100], wastewater treatment [101-103], fuel cells [104, 105], photocatalysis [106, 107], etc..

For instance, Biao et al. showed that the Ag-TiO_2 catalysts immobilised on Al_2O_3-based photocatalytic membrane reactor could achieve up to 99.9% rejection rates and 23.3% removal for both simulated and real polyester microplastic fibres from laundry processes [108]. Despite this, membrane reactors are

susceptible to biological fouling, membrane clogging, or the development of a cake layer over time, as shown in Figure 2-4, which significantly reduces their efficiency [109]. Alardhi et al. reported that both the permeate flux and the rejection coefficient decreased as feed concentrations and flow rates increased when polyvinyl chloride hollow fibre ultrafiltration membrane was applied for methyl green removal, particularly at higher feed concentrations (40 mg/L, 50 mg/L) and flow rates (150 ml/min, 200 ml/min) [96]. The decline was caused by membrane pore blockage, adsorption within the pores, concentration polarization, and the formation of a gel layer. The most common approach to mitigate this issue is to construct fouling-resistant membrane surfaces, typically hydrophilic or super-hydrophilic, by chemical pre-treatment, such as surface coating, surface grafting, surface bioadhesion, physical blending and surface segregation [110].

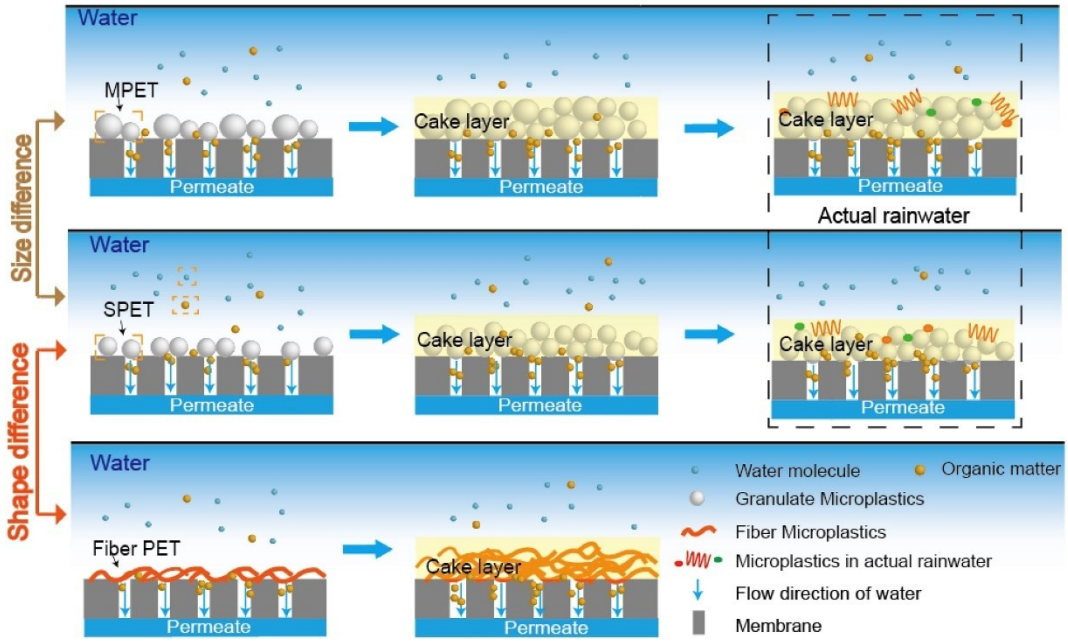

Figure 2-4 The primary membrane fouling behaviour during microplastics-containing wastewater treatment, adapted from [109].

As noted, membrane reactors allow for selective in-situ separation of reactants and products, leading to a favourable thermodynamic equilibrium shift and thereby promoting higher conversion rates and yields [18, 111]. Gallucci et al. claimed that zeolite membrane reactor displayed the highest catalytic hydrogenation of CO_2 at the same reaction conditions (temperature, pressure, H_2/CO_2 ratio, and space velocity) with regard to traditional reactor and the lithiated Nafion membrane reactor [99]. The CO_2 yield derived from zeolite membrane reactor (8.7%) was higher than that of traditional reactor (2.4-2.8%) and lithiated Nafion membrane reactor (2.5%). Moreover, the ability for membrane reactors to

continuously remove products could avoid side reactions, which enhances the overall catalytic efficiency (e.g., conversion, selectivity, and yields) in equilibrium-limited reactions [112].

It is important to note that these benefits are only achievable with the appropriate membrane properties and operation conditions. When engineering a membrane reactor, the key point is to ensure that the permeable membrane is suitable for the operating conditions, such as high temperatures, pressures, and potential interactions between the membrane and catalysts [111]. For example, inorganic membranes (e.g., carbon, ceramics, or metals) basically are more suitable for hydrogen processes, because these membrane materials function at high reaction temperatures from 300-800˚C, with some capable of enduring temperatures as high as 1000˚C [111]. Zeolite membranes ideally permeate only small molecules like H_2O and H_2 [113]. Porosity of the membrane materials also plays a key role as membranes with small porosity exhibit a higher mass transfer resistance, leading to lower flux and higher aeration energy demands [114].

To the end, in terms of the second drawback of membrane reactors, it should be the scalability issues in large-scale industrial applications. Similar to microreactors in Section 2.2.2, membrane reactors can also be scaled up by either increasing the size of the membrane tubes or increasing the number of the membrane tubes [115]. Scaling up a membrane reactor by enlarging its size makes it difficult to maintain the identical catalytic efficiency, as the proportional surface area available for reactions should match the pre-scale-up configuration [116]. This results in reduced membrane strength at larger sizes, limiting the feasibility of membrane reactor under high pressure and temperature conditions [115].

Instead, numbering-up the membrane area is more promising, as it allows for optimal design through assorted potential arrangements of multiple parallel tubes. Chompupun et al. scaled up the membrane reactor to a square honeycomb monolith pattern, which was composed of a square reactor with four adjacent quadrant reactors [116]. Ma et al. designed 7-tube cylindrical modules and 19-tube cylindrical modules using computational fluid dynamics (CFD) simulations for hydrogen separation [117]. Choi et al. simulated the steam methane reforming (SMR) reaction kinetic model and permeation model using CFD simulations under catalytic membrane reactor (CMR) and baffled membrane reactor (BMR) [115]. They found that the BMR experienced more complex flow patterns compared to CBR, resulting in higher driving force for H_2 permeation, and thereby higher SMR reaction efficiency. However, the CH_4 conversion and permeate H_2 yield for both membrane reactors decreased rapidly with the increase of gas hourly space velocity (GHSV) and number of membrane tubes. Moreover, membrane reactors with different geometries after scaling up does not generally preserve sufficient similarity compared to original single membrane unit [118]. This potentially undermine the credibility and practicality of the scale-up process by causing issues like temperature deviations, resulting instability in long-term operation [115, 119].

2.2.3 Structured catalyst substrates

Although microreactors and membrane reactors provide several benefits from their miniaturisation of the equipment, their challenges in scaling up, limited throughput, and complex design and operations restrict their use in large-scale industrial applications. Besides the miniaturisation of reactors, constructing specialised geometrical structures for catalyst substrates is a favourable option. These structured catalyst substrates provide a structural framework or surface on which the catalytic active phases can be well deposited or embedded. One the one hand, they share the common characteristics of conventional less structured and irregular catalyst supports (e.g., spherical, cylindrical, or extruded pellets with homogeneous catalyst distribution), such as enhancing the surface area of catalysts by dispersing active species, maintaining the mechanical strength of catalysts during the reaction, stabilising the active metals against agglomeration and oxidation, and improving mass and heat transfer [120-122]. On the other hand, these specific structures are capable of balancing pressure drop with mass and heat transfer to a certain extent, particularly at high gas hourly space velocity.

Up to now, structured catalyst substrates including catalyst supports featuring monolithic structures [123-126], foam structures [39, 127, 128], and nanofibers [129-131], by which intensive mixing, or enhanced mass and heat transfer is achieved [18]. Figure 2-5 shows three commonly used structured catalyst substrates: honeycomb monoliths, foams, and pellets. In contrast to microreactors and membrane reactors illustrated in Section 2.2.1 and Section 2.2.2, these catalyst substrates offer both reduced pressure drop and enhanced mass and heat transfer, as previously mentioned [37]. Also, they present fewer design and operational challenges, which can be directly assembled in the packed-bed reactors, along with simpler scaling-up processes.

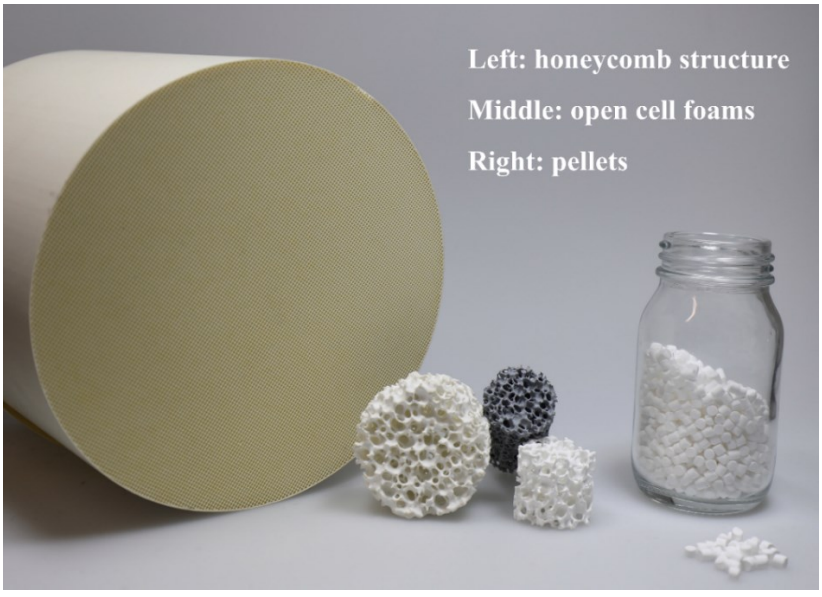

Figure 2-5 Commonly used catalyst support structures, adapted from [132].

2.2.3.1 Monolithic substrates

A case in point, structured honeycomb monolithic substrates feature numerous straight, thin-walled narrow parallel cells/channels to improve the mass transfer effectiveness [18, 133]. In general, monolithic substrates with larger GSA per reactor volume tend to come with more small parallel channels, which leads to higher values of CPSI. The catalytic active phase can be incorporated to these structures by various techniques, with washcoating being the most commonly employed method [134]. The catalyst applied to the surface of washcoat layers made of porous material experiences lower mass transfer resistance, resulting in enhanced reaction activity. Meanwhile, pressure drop can also be lowered to one to two orders of magnitude than that of conventional randomly packed pellets or beads in packed bed systems [133].

Jacquot et al. systematically studied the effect of two model packing configurations: 3D printed catalyst alumina monoliths (800 μm in diameter, porosity of 61%) and packed-bed conventional commercial alumina spheres from Sasol (800 μm in diameter, porosity of 44%, type I as shown in Figure 1-1) on the pressure drop and velocity profiles over selective oxidation of benzyl alcohol to benzaldehyde [135]. It was found that the pressure drop in the packed-bed spheres (Simulation: 400 kPa/m at 5 m/s; Experiment: 150 kPa/m at 5 m/s) was noticeably higher than that in the monoliths (Simulation: 20 kPa/m at 5 m/s; Experiment: 20 kPa/m at 5 m/s). This could be attributed to the fact that the monolith follows a creeping flow pattern while the flow around spheres is more turbulent, resulting in superior inertia loss and, consequently, a higher pressure drop. Moreover, following 24 hours of continuous reaction, the conversion rate for monoliths (~ 63%) exceeded that of their crushed packed-bed counterparts (~ 32%) and packed-bed spheres (~ 24%).

However, a further increase of CPSI, such as reaching 900 for conventional monolithic catalytic converter, to ensure sufficient active catalytic surface led to a sharp rise in pressure drop, therefore only monolithic substrates of 400 CPSI and 600 CPSI have been more commonly applied in automotive industry [136, 137]. Mahyon et al. reported a novel hollow fibre substrate with radial microchannels (900 CPSI), which could reduce the diffusional resistance inside catalytic layers but maintain a low pressure drop [22]. After wash-coating a thin layer of gamma-Al_2O_3, serving as the support for the active species (0.7 wt.% Pd), on the inner walls of these microchannels, the wash-coated samples could further lower the light-off temperatures of CO oxidation at low pressure drops.

2.2.3.2 Foam substrates

Another promising type of structured catalyst substrate, foams with three-dimensional frameworks full of solid struts, have spurred extensive research across various fields due to their high foam porosity, tortuous transport paths through the matrix, high temperature resistance, large surface-to-volume ratios,

and mechanical strength [127, 138, 139]. Interesting applications include Fischer-Tropsch synthesis (FTS) [140, 141], steam methane reforming [142, 143], photocatalysis [144, 145], catalytic combustion [146, 147], and nitrogen oxide removal [148], etc.

As illustrated in Figure 2-6, foams can be categorised into two types based on their pore structures: open-cell and closed-cell [146]. Closed-cell ceramic foams contain isolated and closed-off pores that possess superior mechanical strength and low thermal conductivity, rendering them more commonly applied to thermal insulation, such as sintering furnace liners [149]. In contrast, open-cell ceramic foams characterised by solid edges and open faces, allowing fluids or gases to pass through interconnected pores, usually used for filtration, catalytic reactions, or as catalyst supports and sound-absorbing materials [127].

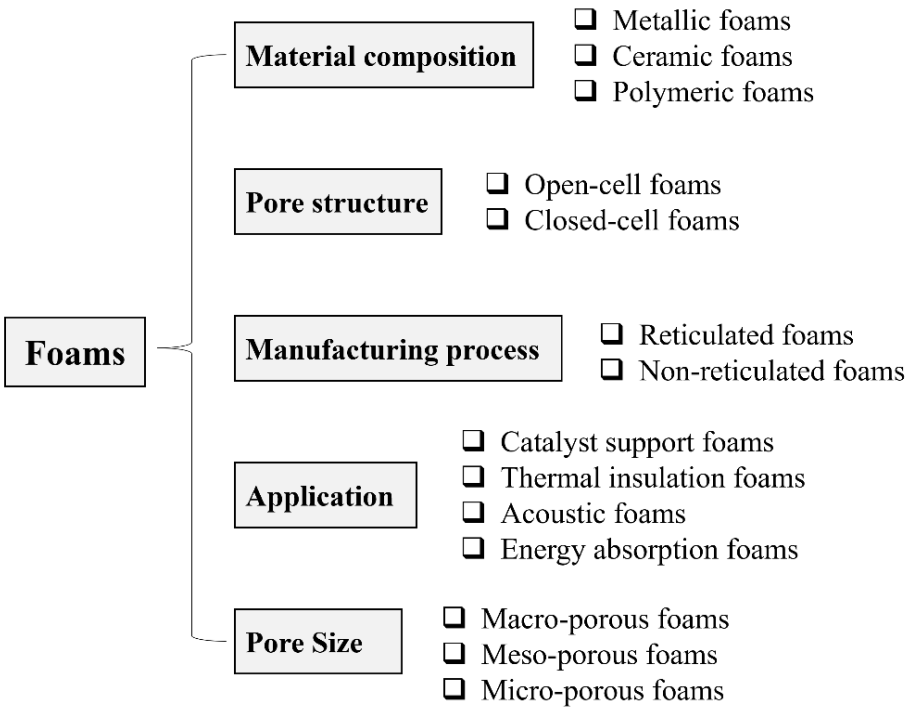

Figure 2-6 Category of foams based on different criteria.

Figure 2-7 showcases the pore structures of open-cell ceramic foams, which are composed of three components: cells, windows, and struts [149]. The struts construct the solid framework of the ceramic form, providing structural integrity, rigidity, and the mechanical strength. The composition of the struts determines the mechanical properties of the foam, including its compressive strength and resistance to wear. Cells are spherical or elliptical voids enclosed by struts, while windows are openings that connect these cells to one another. In general, ceramic foams have pore density of 10-100 PPI, implying an

interconnecting porosity of 75-90% or even higher [146]. Few studies have been reported in the ceramic foams with a porosity higher than 90%, because the imperfect pore structure stemming from the openings significantly reduces the mechanical properties of ceramic foams, severely restricting their practical applications [150].

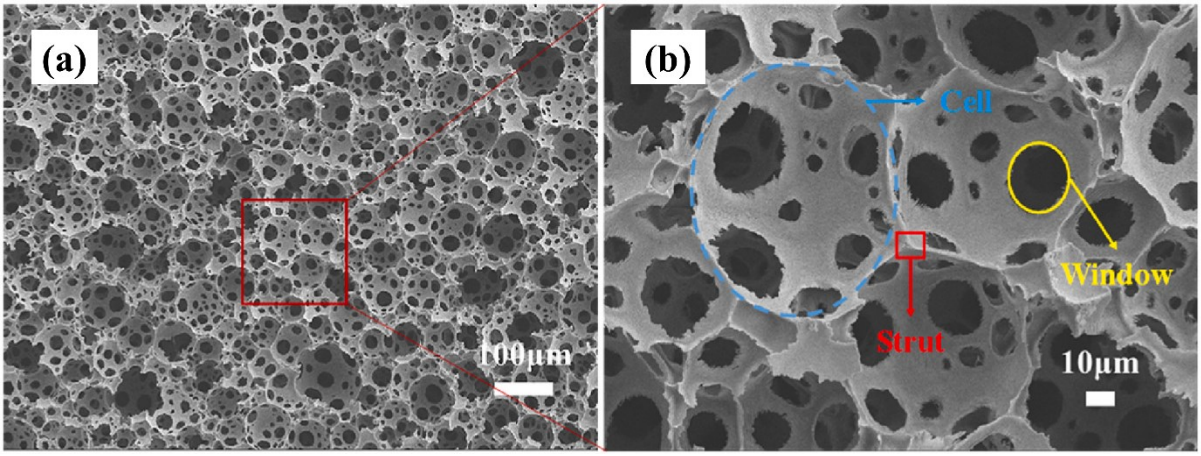

Figure 2-7 SEM images of open-cell ceramic foams with varied magnification, adapted from [149].

These ceramic foams can be fabricated by various raw materials, e.g., alumina [139, 149, 151], silicon carbide [152, 153], and aluminium silicates [154]. There are also precedential studies on the preparation of foamed ceramics using industrial solid waste, such as vitrification slag (industrial byproduct of metallurgical processes) [155], fly ash (a fine powder waste from thermal power plants rich in silica, alumina, and other oxides) [156], and red mud (harmful solid waste from aluminium and steel industries) [157, 158]. Chen et al. combined 40-50 wt.% red mud, 26.25-40 wt.% fly ash, 15-20 wt.% sodium borate (fluxing agent), and 5 wt.% sodium silicate (foaming agent) to prepare foam ceramics with porosity of 64.14-74.15%, compressive strength of 4.04-10.63 MPa, and bulk density of 0.51-0.64 g/cm^3 [159].

To the end, sufficient contact between the gas/bulk phase and surface reactions is attained in both monoliths and foams. In a packed bed reactor containing ceramic monolithic substrates or ceramic foam substrates rather than random packing, the high bed porosity endows them with a lower pressure drop and improved mass and heat transfer, and vice versa [143]. Thompson et al. compared the total pressure drop of honeycomb monolith (20 CPSI, bed porosity of 52%), foam (7 PPI, bed porosity of 80%), and random particle at different gas flow velocities for the catalytic combustion of lean methane–air mixtures [160]. They found that the pressure drops for three catalyst loading patterns at 1.5 m/s are ranked as follows: random particle (55 KPa) >> foam (10 KPa) > honeycomb monolith (5 KPa). Eggenschwiler et al. revealed that the pressure drop in honeycomb monoliths follows a linear

relationship, whereas the pressure drop across ceramic foam substrates varies as a quadratic function of the flow velocity [161]. Also, at mean flow velocity of 25 m/s, the pressure drops were approximately 10 KPa/m, 70 KPa/m, 72 KPa/m, and 128 KPa/m for honeycomb monolith (400 CPSI), ceramic foam (8 PPI), ceramic foam (10 PPI), and ceramic foam (15 PPI), respectively. This sequence of pressure drop echoes the work by Thompson et al [160].

More importantly, Patcas et al. additionally included the conventional ceramic beads in the comparison of volumetric rate constants (K_v) and pressure drop ($\Delta P/L$) as functions of the superficial gas velocity [24]. They selected five ceramic substrates: foams (20 PPI, bed porosity of 73.7%), foams (45 PPI, bed porosity of 75.2%), honeycomb (400 CPSI, bed porosity of 70.9%), conventional beads (3.3 mm, bed porosity of 44.0%), and conventional beads (1.5 mm, bed porosity of 41.1%) for the analysis. The selection criterion for foams and honeycombs was based on their comparable pore/channel count (20 PPI ≈ 400 CPSI) or surface area (45 PPI ≈ 400 CPSI), whereas the ceramic beads possessed geometric surfaces similar to those of foams (20 PPI ≈ 3.3 mm, 45 PPI ≈ 1.5 mm). As shown in Figure 2-8, Patcas et al. found that the external mass transfer coefficients for conventional uniform ceramic beads (type 1 as shown in Figure 1-1), honeycombs and ceramic foams followed a definite trend, with the ranking order of: 1.5 mm beads >> 45 PPI foams > 20 PPI foams ≈ 3.3 mm beads > 400 CPSI honeycombs (Figure 2-8 (a)). Meanwhile, the pressure drop was ranked in the following order: 1.5 mm beads > 3.3 mm beads ≈ 45 PPI foams ≈ 20 PPI foams > 400 CPSI honeycombs (Figure 2-8 (b)), as highlighted in Section 1.1.

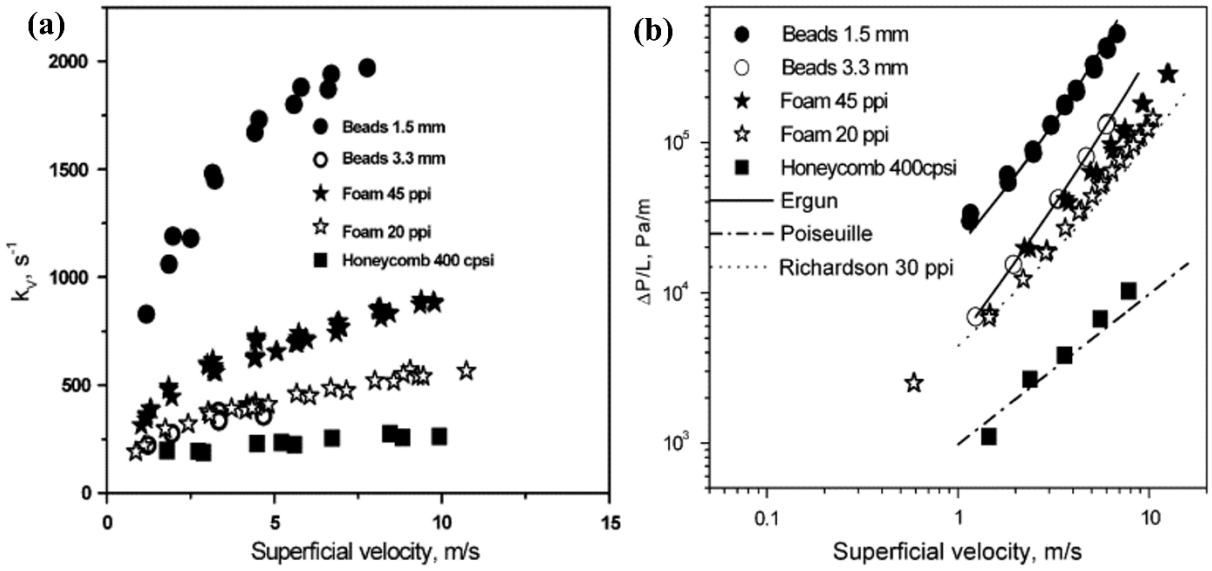

Figure 2-8 (a) Volumetric rate constants (K_v, s^{-1}) as a function of the superficial gas velocity (m/s) over different ceramic substrates in the mass transfer controlled kinetic regime, and (b) the pressure drop as a function of the superficial gas velocity, adapted from [24].

2.2.3.3 Research gap 1 - Lack of studies on the innovative microchannel-structured beads

In the development of process intensification, particularly structured catalyst substrates, there is a noticeable lack of innovations aimed at intensifying PI at the microscale or within the pellets. Spherical catalyst substrates featuring innovative special structures, such as shape-selective designs, optimised pore radii distributions and connectivity, might be a turning point to facilitate the reaction process [35]. According to the CO oxidation reaction results derived from Figure 2-8, one can conclude that the volumetric rate coefficients (proportional to the mass transfer coefficients [24]) and pressure drop for packings with comparable geometric surface areas (1.5 mm beads ≈ 45 PPI foams ≈ 400 CPSI honeycomb) decreased in the order: beads > foams > honeycomb. The mass transfer coefficients of 1.5 mm ceramic beads were drastically higher than others, holding significant promise for further enhancement with the design and development of innovative microstructures for the beads. In addition, even though the 1.5 mm beads had a relatively high pressure drop due to their small size, it has been confirmed to decline as low as foams when the bead size was increased to 3 mm (Figure 2-8 (b)). Therefore, 3 mm ceramic beads with distinctive microstructures are anticipated to exhibit the highest mass transfer coefficient compared to ceramic foams and monoliths, while still preserving a low pressure drop.

Currently, commercial catalyst supports are available in various shapes, including spheres, cylinders, rings, and extrudates, with spheres being the most widely used shape. Spheres normally ensure uniform packing and provide better resistance to attrition than other shapes, achieving a relative lower pressure drop. However, as noted in Section 1.1, the commercial catalyst supports in packed-bed reactors are typically either porous beads with isotropic structures (Figure 1-1 , type 1) [162, 163] or eggshell pellets with a thin catalyst layer on the surface (Figure 1-1 , type 2) [28]. This is due to the long-standing challenges of balancing pressure drop (1-3 mm) and intraparticle diffusion resistance (< 300 μm), as previously described for microreactors in Section 2.2.1.

To fill this research gap, an innovative microchannel-structured ceramic beads (Figure 2-9) with radial straight finger-like microchannels inside was developed in Chapter 4 to decouple structural limitations of current catalyst design, i.e., trade-off between diffusional mass transfer and pressure drop of packed bed units [164]. This unique bead can maintain a low pressure drop (3 mm in diameter) within a reactor while simultaneously provide high geometrical surface areas (finger-like microchannels). For any sphere beads, the simplest textual model for the effective diffusion coefficient ($D_{e,i}$) derived from the molecular diffusion coefficient (D_i), the average porosity (ε_p) and tortuosity (τ_p) of the material [165]:

$$D_{e,i} = \frac{\varepsilon_p}{\tau_p} D_i \qquad \textit{(Equation 2-1)}$$

At a fixed particle porosity, the effective diffusion coefficient is inversely proportional to tortuosity. Therefore, the tradeoff between tortuosity and geometrical surface area in conventional uniform beads

makes it difficult to sustain a high value of $D_{e,i}$. This also mirrors the lower mass transfer coefficients of 3.3 mm beads compared to 1.5 mm beads in Figure 2-8 (a).

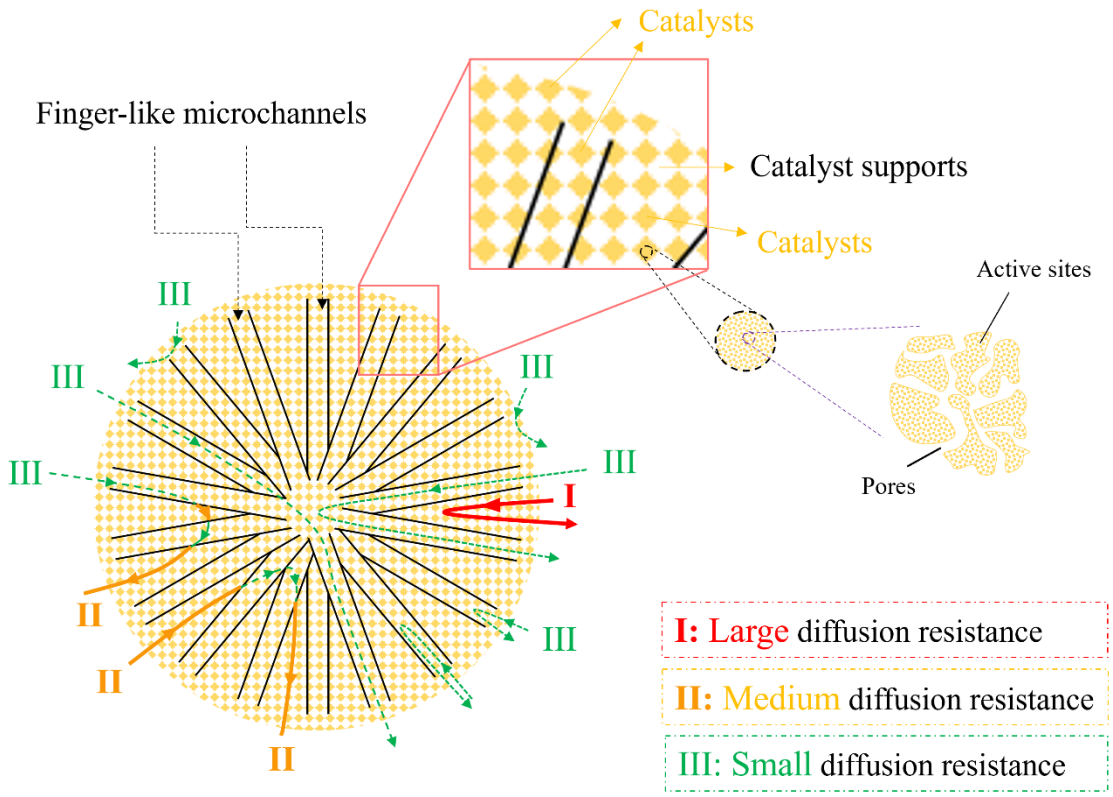

Figure 2-9 Schematic diagram of diffusional transfer inside novel microchannel-structured ceramic beads.

In contrast, microchannel-structured ceramic beads (MSCBs) possess shorter transport distances and lower tortuosity due to the presence of finger-like microstructures, leading to a diffusion process that more closely mimics bulk diffusion and thereby resulting in a significantly higher $D_{e,i}$ compared to the conventional homogeneous-type beads. Unlike traditional beads as shown in Figure 1-1 , which consist of macro-pores formed by the random packing of micro- or meso-porous particles and have complex diffusion routes inside, these micro-structured ceramic beads (Figure 2-9) dramatically boost the effective diffusivity.

It is worth noting that these beads were engineered for industrial use, with consideration given to the mechanical strength of materials, so α-Al_2O_3 was chosen in Chapter 4 other than γ-Al_2O_3 despite its relatively higher specific surface area. Generally, the weak mechanical strength of γ-Al_2O_3 can lead to

rapid crumbling under intense loading. This produces dust and fragments that obstruct the spaces between pellets, resulting in a premature increase in bed pressure drop [166]. However, due to the inherent small specific surface area of α-Al_2O_3, modifications are required to enhance its catalytic performance. Hence, Chapter 5 and Chapter 6 introduced γ-Al_2O_3 and carbon xerogels as washcoating layers onto the surface of the microchannels within the alumina beads to boost the specific surface area. The catalytic performance of these materials was carried out for the degradation of organic pollutants in a PMS-activated AOPs system under mild reaction conditions, a representative chemical reaction for wastewater treatment, despite the generic benefits are transferrable to wider reaction systems.

2.3 Microchannel-structured catalyst substrates

In order to prepare microchannel-structured ceramic beads, the fabrication process applied for micro-structured ceramic membrane exemplified by Li`s group are unquestionably highly feasible [167-171]. As shown in Figure 2-10 (a-b), Wu et al. prepared a unique micro-structured inorganic hollow fibre membrane, which was comprised of finger-like voids in the cross section and a thin sponge-like layer on the outer surface [167]. Finger-like voids were formed during the non-solvent induced phase-inversion process, in which the solvent in the polymer suspension and nonsolvent (miscible with the solvent) in the coagulant bath, commonly water, underwent exchange at the interface between two contact phases [172]. The consolidation of the shaped hollow fibre membrane precursor also took place during this process.

Later, Lee et al. developed microchannel-structured membranes with five different solvents – dimethyl sulphoxide (DMSO), N-methyl-2-pyyrolidone (NMP), dimethylacetamide, dimethylformamide and triethyl phosphate – resulting in microchannels with different shapes, either cylindrical or sponge-like or pear-shaped conical structures [173]. Figure 2-10 (c) presents the SEM images of the cross-sectional and surface views of a ceramic membrane fabricated using DMSO as the solvent, [173]. It can be observed that the diameters and lengths of the microchannels in Membrane-DMSO specimen differ from the top layer to the bottom layer. The top region of the membrane was the interface initially in contact with the non-solvent during the microchannel growth process. The long, straight, and cylindrical microchannels were categorised by their propagation depth for a more intuitive observation, with the deepest channels being the longest and widest, and each successive layer towards the upper region having shorter and narrower channels. In fact, the gradual increase in channel size and the reduction in density towards the bottom layer are key features of membranes produced through the phase-inversion process [168, 174]. As stated, when the polymer suspension is subjected to the non-solvent, a steep concentration gradient results in rapid solvent/non-solvent exchange and quick solidification at the top layer [172]. This rapid phase inversion process leads to the formation of small microchannels on the upper layer. In contrast, the bottom layer of the membrane, being farther away from the instant contact

with the non-solvent, undergoes a slower solvent/non-solvent exchange, taking more time for the generation of finger-like microchannels and thus a wider channel size distribution [173].

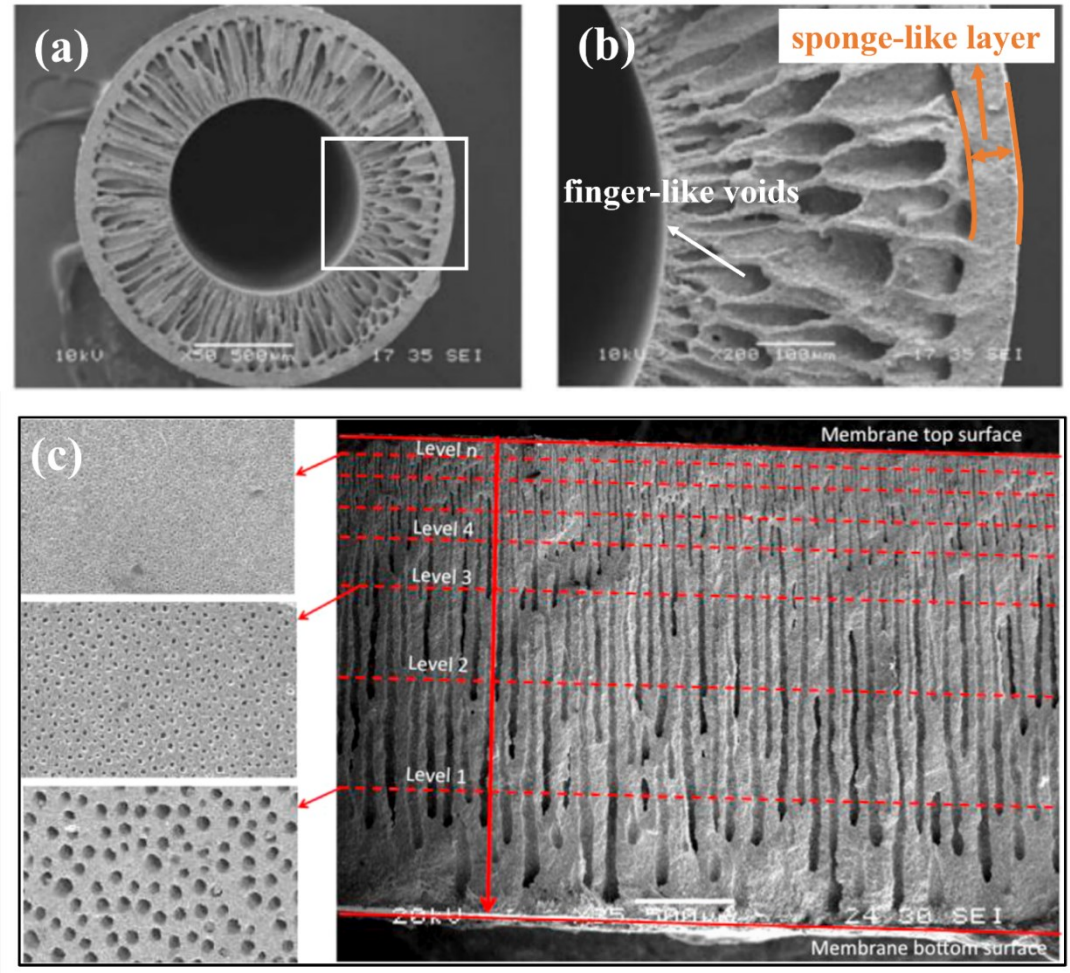

Figure 2-10 SEM images of the asymmetric alumina hollow fibre membrane sintered at 1450 ˚C for 4 h: (a) whole view, (b) cross section, adapted from [167]; (c) SEM images of the cross-sectional views of ceramic membrane-DMSO with the labelled hierarchical levels, adapted from [173].

In theory, this method can be a viable strategy for the fabrication of microchannel-structured ceramic beads with both finger-like structures within the beads and sponge-like structures on the surface layer, provided that the shaped spherical ceramic beads can be produced. Figure 2-11 illustrates two main methods for the formation of spherical beads, i.e., colloidal vibration moulding and needle system [175-179]. The former approach (Figure 2-11 (a)) tended to shape the green B_4C beads by rotating the commercial boron carbide powders with polyvinyl alcohol (PVA) in a planetary ball mill [175]. The size and sphericity of the B_4C beads were determined by the rotation time and the concentration of PVA solution. In contrast, the latter technique (Figure 2-11 (b)) provided a laboratory scale bead-forming apparatus, with ceramic suspension continuously being extruded out of the nozzle and then dropped

into the dropping column [176]. Simultaneously, ethanol was dripped from the intravenous tubing into the reaction column, which was added to lower the surface tension and preserve sufficient gelling solution during the shaping process [176]. Notwithstanding the production of spherical ceramic beads by these two methods, finger-like microstructures have not been developed, as the compositions of the ceramic suspension and coagulant bath (non-solvent) are decisive. Therefore, the needle system will be applied in this research, and the physical/chemical parameters of the bead-forming process will be systematically examined as well, as detailed in Chapter 4.

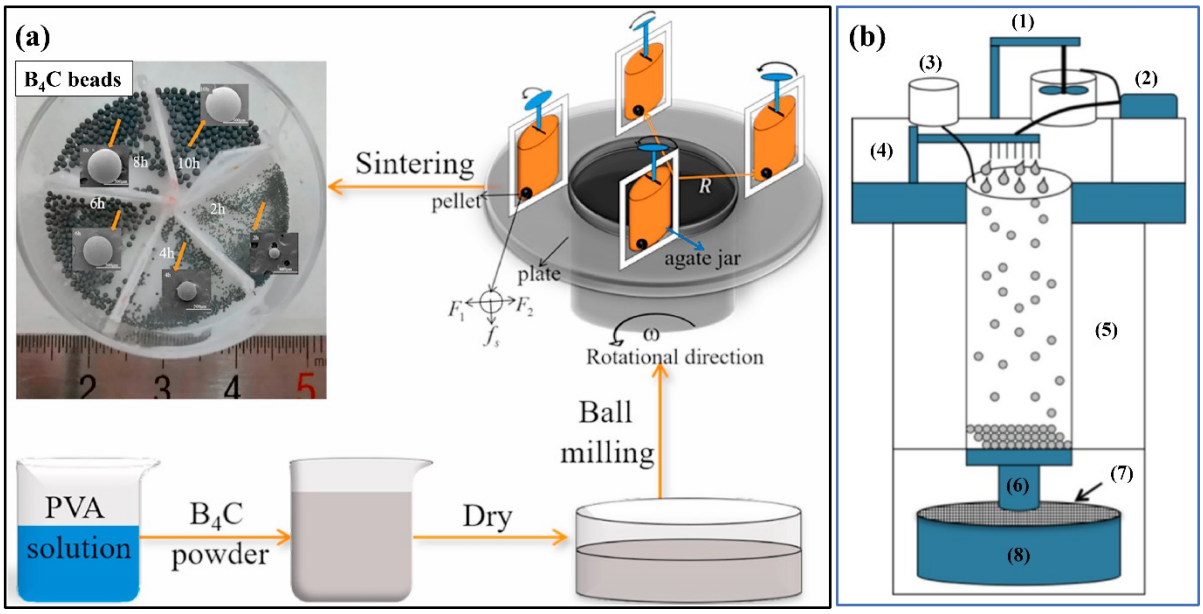

Figure 2-11 Schematic of two bead-forming methods: (a) planet-type rotation method, adapted from [175]; (b) needle system with (1) slurry stirrer, (2) slurry transportation pump, (3) intravenous tubing for ethanol, (4) nozzle and nozzle position controller, (5) dropping column, (6) manual valve, (7) metallic filter net, and (8) collection container, adapted from [176].

2.4 Mesoporous washcoating materials

Once the base innovative catalyst substrates are developed, it is necessary to integrate mesoporous materials with strong adherence and high surface-to-volume ratio to achieve their full potential, as α-Al_2O_3 exhibits extremely high mechanical strength, chemical and thermal resistance, but has a low specific surface area, as noted in Section 2.2.3.3. The adhesive strength of the washcoats on the base catalyst supports is vital as it determines the durability and reusability of the constructed catalyst supports, particularly under harsh reaction conditions [180]. High specific surface area (SSA) values of the washcoat layer deposited on the catalyst supports typically provides numerous active sites and ensures a sufficient surface to disperse and anchor catalysts, which is beneficial in catalytic reactions [181]. Additionally, mesoporous, and well adherent coatings would reduce the diffusional resistance,

therefore higher chemical reaction kinetics and activity [182]. Given these distinct advantages, the washcoating layer has been widely introduced onto various catalyst supports, including microreactors, honeycomb monoliths, ceramic form substrates, and ceramic membranes [22, 183]. It is worth noting that washcoating layers in AOPs predominantly comprise the catalyst itself, with minimal research available on this subject and no reported cases of washcoating layers being used to increase the specific surface area of the catalyst support. Table 2-1 summarised various mesoporous materials used for washcoating structured catalyst substrates, including a few AOPs reactions where the catalyst itself serves as the washcoating layer, with γ-Al_2O_3 being the most commonly used material.

Table 2-1 An overview of various washcoatings introduced onto the catalyst supports.

NO.	Catalyst supports	Washcoating layer	Catalyst	Application	Ref.
1	Cordierite honeycomb	Al/Zr pillared bentonite clay (Al/Zr-PILCs)	13-39 wt.% Al/Zr-PILCs (3:1)	Catalytic wet air oxidation	[184]
2	Porous alumina ceramic	$La(Co_{0.2}Al_{0.2}Fe_{0.2}Mn_{0.2}Cu_{0.2})O_3$ catalyst	$La(Co_{0.2}Al_{0.2}Fe_{0.2}Mn_{0.2}Cu_{0.2})O_3$	AOPs	[185]
3	Capillary microreactor (fused silica)	γ-Al_2O_3	0.02 wt.% Pd	Hydrogenation of 3-methyl-1-pentyn-3-ol	[186]
4	Chip-based microreactors	Zeolite (ZSM-5), silicate	0.1% Pd, 2% Pd	Production of methyl-iso-butyl-ketone, hydrogenation of 3-methyl-1-pentyn-3-ol	[75]
5	Stainless steel microreactors (porous disks)	Zeolite (mordenite, zeolite Y, ETS-10)	/	/	[187]
6	Ceramic monoliths (cordierite, 400 CPSI)	N-doped carbon nanotubes (CNTs)	CNT-BM-M	Catalytic wet oxidation	[188]
7	Stainless steel meshes	TiO_2 and Ti_1-xSn_xO_2 catalyst	TiO_2 and Ti_1-xSn_xO_2	Photocatalysis	[189]
8	Al_2O_3 foam	Mesoporous CoSi catalysts	Mesoporous CoSi	Catalytic Fenton-like oxidation	[190]
9	Monolithic supports	γ-Al_2O_3	Ir	/	[191]
10	Capillary microreactor (fused silica)	TiO_2	Au, Pt–Sn	Citral hydrogenation	[192]
11	Microreactor	Mesoporous silica, TiO_2, mesoporous titania	Pt	Nitrobenzene hydrogenation	[193]

12	Microreactor	polydopamine	Pd	Nitrobenzene hydrogenation	[194]
13	Microchannel reactor	Silica	Au-Pd	Synthesis of hydrogen peroxide	[195]
14	Stainless steel tubular microreactors	MCM-41	/	/	[196]
15	Cu foam supports	γ-Al_2O_3	CuZnZr	/	[197]
16	Honeycomb monolith	ZSM-5	1% Pd	Ethylene removal	[198]
17	Micro-channel reactor	γ-Al_2O_3	Pt	Methane catalytic combustion	[199]
18	Monolithic supports	Carbon nanofiber	Ni	Methane decomposition	[200]
19	Ceramic foams	γ-Al_2O_3	/	Properties and pressure drop analysis	[201]
20	Stainless steel foams	TiO_2 (Degussa P25) catalyst	TiO_2 (Degussa P25)	Photocatalysis	[202]
21	Hollow fiber membrane	γ-Al_2O_3	0-10wt.% Pd	CO oxidation	[22]
22	FeCrAlloy microreactors	γ-Al_2O_3	20wt.% Pt	methane combustion	[183]

In some cases, particularly for structured catalyst supports with low specific surface area, applying a thin γ-Al_2O_3 washcoating layer enhances porosity, facilitating uniform catalyst dispersion and thus improving catalytic performance. For example, Singh et al. investigated different NiMo/γ-Al_2O_3 washcoatings (12.0 wt.% MoO_3/2.0 wt.% NiO, 18.6 wt.% MoO_3/3.2 wt.% NiO, 24.3 wt.% MoO_3/4.0 wt.% NiO) and different catalyst sizes (0.275 mm and 1.5 mm) on 400 CPSI cordierite monolith for hydrodesulfurization of dibenzothiophene in a packed-bed rector [203]. It was observed that as metal loadings increased, the specific surface area of NiMo/γ-Al_2O_3 decreased from 164.0 m^2/g to 109.1 m^2/g, resulting in reduced metal dispersion and, consequently, lower conversion efficiency. Additionally, the rate constants of all 1.5 mm catalysts were lower than that of 0.275 mm due to the enhanced diffusional mass transfer resistance, either at 548 K or 593 K. Ballarini et al washcoated a thin γ-Al_2O_3 layer (15 μm) to 2 mm α-Al_2O_3 spheres to uniformly disperse Pt, PtSn and PtGe catalysts for n-butane dehydrogenation [204]. The specific surface area of α-Al_2O_3 spheres dramatically elevated from 4.7 m^2/g to 175 m^2/g after the introduction of γ-Al_2O_3, and the bimetallic catalysts (PtSn and PtGe) exhibited superior catalytic performance compared to the monometallic catalyst (Pt).

To the best of our knowledge, another washcoating material used in this thesis, i.e., carbon xerogel, has not been employed to function as the washcoating layer yet. However, some studies have explored other carbonaceous materials, such as carbon nanotubes (CNTs) [188, 205] and carbon nanofibers (CNFs)

[206], for similar applications. For instance, Soghrati et al. found that the catalytic performance of methane decomposition for CoMo catalyst deposited on the CNT-washcoated monoliths (98%) was higher than that on the conventional γ-Al_2O_3 support (91%) or on acid-treated monoliths (88%) [205]. This can be ascribed to the higher BET surface area of CNTs, the well-adhered CNTs washcoating layer for catalyst dispersion, and the greater ease of sulfidation of MoO_2 catalyst compared to MoO_3 catalyst (the primary active molybdenum phase in other CoMo-based samples).

2.5 Advanced Oxidation Processes

2.5.1 Overview

AOPs were first proposed by William H. Glaze in the 1980s for drinking-water treatment with ozone, a powerful disinfectant and oxidant [207, 208]. The AOP concept was evolved from the oxidation processes involving highly reactive chemical species, particularly hydroxyl radicals (·OH), to other reactive species, such as sulphate radicals ($SO_4^{\cdot-}$), for efficient water/wastewater purification [209, 210]. Different from common radicals like chloride (1.27 V vs. NHE) and ozone (2.07 V vs. NHE), the radicals involved in AOPs like hydroxyl radicals (1.8-2.7 V vs. NHE) and sulphate radicals (2.5-3.1 V vs. NHE) have considerably higher oxidation potentials, facilitating the oxidation of a wider range of organic pollutants [211-213]. Taking advantages of higher oxidation potentials and non-selectivity, AOPs have diverse applications in industrial effluents treatment, such as distillery [214], hazardous effluent [215], pharmaceutical waste [126, 216], metal-plating wastes [217], and persistent dyes [218]. Table 2-2 exhibits seven main types of AOPs based on the published research [164, 219-222].

Table 2-2 Classification of advanced oxidation processes and key features

AOPs	Radicals	Energy source	Key features	Ref.
Ozone oxidation	·OH	the oxidizing potential of ozone	Powerful oxidiser; inhibits both bacteria and fungus; high concentration dosage required; expensive; complex process, etc.	[219, 220]
Electrochemical oxidation	·OH, $\cdot O_2^-$, h^+	electrical energy	Removes highly toxic compounds; no hazardous by-product; energy source needed; electrode's maintenance, etc.	[220]
Fenton oxidation	·OH	the chemical reaction between H_2O_2 and Fe^{2+}	No need for external energy; cost-effective and simple operation; narrow pH range (2.5-3.5); generation of iron sludge, etc.	[223]
Photocatalysis	·OH, $\cdot O_2^-$, h^+	light energy (UV/visible light)	Uses natural energy source; low catalyst used; no need for additional chemicals;	[221]

			complex reactor design; difficulty in large-scale application, etc.	
Radiolysis	H·, $\cdot O_2^-$, ·OH	high-energy ionizing radiation (e.g., γ-rays or electron beams)	high penetration power of radiation; highly efficient generation of reactive species; high capital cost; secondary pollution; safety concerns, etc.	[224]
Sonolysis	H·, $HO_2\cdot$, ·OH	ultrasonic sound waves	highly efficient generation of reactive species; no need for additional chemicals; effective in turbid or highly contaminated water; high energy consumption; machines undergo tear and wears; noise pollution, etc.	[222]
Sulphate-radical based AOPs (SR-AOPs)	$SO_4\cdot^-$, ·OH, $\cdot O_2^-$, $^1O_2$	Heat/UV/transition metal catalysts (e.g., Co^{2+}) /electrical activation/sonolysis	high oxidation potentials; longer half-life time of $SO_4\cdot^-$; wide pH range (2.0-8.0); limited large-scale applications, etc.	[164, 223]

Recently, SR-AOPs stand out as a preferred emerging technology to degrade organic contaminants into non-toxic or low-toxic small molecules in water bodies [164]. This can be attributed to the generation of highly reactive species, such as sulphate radicals and other reactive oxygen species (ROS), which can be generated by peroxymonosulfate (PMS, HSO_5^-) or persulfate (PS, $S_2O_8^{2-}$) under heat, ultrasounds, transition metal ions/oxides or UV light [225, 226]. One of the main advantages of the SR-AOPs is that it can be effectively functioned over a wide pH range of 2.0-12.0, with optimal catalytic performance normally observed between 3.0 and 8.0, owing to the stability of $SO_4\cdot^-$ and PMS/PS [227-229]. In addition, as shown in Table 2-2, the oxidation potential of $SO_4\cdot^-$ (2.5-3.1 V vs. NHE) is higher than that of ·OH (1.8-2.7 V vs. NHE), a typical radical involved in Fenton reactions [230]. Furthermore, $SO_4\cdot^-$ has longer half-life time ($t_{1/2}$ = 30 μs) than ·OH ($t_{1/2}$ = 20 ns) [212, 213]. As a result, SR-AOPs is a promising AOPs technology in water and wastewater treatment.

In SR-AOPs, PMS (also known as Oxone®) displays a more efficient catalytic performance for the degradation of organic pollutants than PS [231]. It has received more attention because of its high reactivity, resulting from an asymmetric structure (HO-O-SO_3^-) and favourable large length of the O-O bond (1.326 Å) that needs less energy to break [229, 232]. This characteristic facilitates the activation processes to generate ROS, such as $SO_4\cdot^-$ and ·OH. PMS is a strong oxidising agent, with the redox potential of 1.82 V [231]. However, it is hard to be decomposed naturally, resulting in low reaction activity, and thus appropriate activation method is required to accelerate the generation of $SO_4\cdot^-$. A viable and economically feasible technique within SR-AOPs is the activation of PMS by transition metal-mediated heterogeneous catalysts, such as Co^{2+}, Mn^{2+}, Fe^{2+}, and Ru^{3+}, etc., to generate $SO_4\cdot^-$ and other ROS for the powerful wastewater treatment [233].

For example, Wu et al encapsulated confined Co_3O_4 within carbon shells and integrated them onto Mn_2O_3 nanorods for efficient PMS activation and bisphenol A degradation [234]. These carbon shells

function as electronic conductors, facilitating electronic interactions between Co_3O_4 and Mn_2O_3, while also serving as protective layers to mitigate oxidation during AOPs reactions. Zhu et al employed microbial-treated Fe^{2+}/PMS and Co^{2+}/PMS AOPs systems to degrade high concentrations of aniline (1000 mg/L), achieving a residual concentration of 1.08 mg/L after 96 hours under reaction conditions of pH 7 and 30 ˚C [235]. Anipsitakis and Dionysiou also reported nine transition metals for the activation of three oxidising agent, including PMS [236]. They found that the PMS activation by transition metals for the degradation of 2,4- Dichlorophenol followed this order: $Ni^{2+} < Fe^{3+} < Mn^{2+} < V^{3+} < Ce^{3+} < Fe^{2+} < Ru^{3+} < Co^{2+}$, with Co^{2+} and Ru^{3+} being the best metal catalysts. Compared to Co^{2+}, the high cost and limited natural abundance of Ru impede its widespread application in industrial settings, as is the case with AOPs.

2.5.2 Research gap 2 - Lack of studies on the innovative catalyst substrates for AOPs

In PMS activation, cobalt-based catalyst, particularly cobalt oxide (Co_3O_4), is one of the most active transition metal-based catalysts in AOPs reaction system for water treatment and purification [237-239]. A key drawback of cobalt-based catalysts is the potential leaching of cobalt ions, as the released cobalt ions are both toxic and challenging to recycle [213]. Catalyst immobilisation on catalyst supports has been demonstrated an appropriate strategy to address this problem. For example, Zou et al anchored Co_3O_4 on chitosan-derived biochar for the degradation of 10 mg/L phenacetin, and the results indicated that the rate constant was 6 times higher than Co_3O_4 alone [213]. Furthermore, cobalt ions leaching for the first run is 0.3 mg/L, lower than the cobalt emission standard of 1 mg/L and other research work under similar reaction conditions, such as yolk-shell Co_3O_4 spheres (9.5 mg/L) [240], RGO/Fe_3O_4-Co_3O_4 yolk-shell nanostructures (1.5 mg/L) [241], and 3C-Co_9S_8 (3.4 mg/L) [242]. Additionally, non-immobilised Co_3O_4 catalysts usually suffer from uneven dispersion and agglomeration in water, which in turn limit the electron transfer rate and the overall catalytic activity [243]. As a result, exposing more active sites on the stable substrates is a promising strategy to improve the cobalt dispersion and stability, other than its separation from the treated water.

Various materials, such as carbon-based materials, metal oxide, and zeolites have been employed as the substrates and have shown encouraging results [244-248]. Macias-Quiroga et al. reported that carbon-based catalysts (68.5%) constitute the primary catalysts and/or catalytic supports used in AOPs, followed by TiO_2 (20.4%), SiO_2 (5.2%), Pillared Interlayered Clays (3.1%), Al_2O_3 (1.6%) and zeolites (1.2%) [249]. Al_2O_3 accounted for a small proportion although it is one of the most common and robust substrates with an extremely high mechanical strength, thermal and chemical stability under rigorous conditions [250]. Furthermore, researchers often focus on loading catalysts onto Al_2O_3 powder for AOPs reactions, particularly γ-Al_2O_3. This is because it has a large specific surface area, although it is less stable compared to α-Al_2O_3 [250-252]. Nevertheless, it remains a difficulty to separate the used

catalyst powders from the treated water, leading to the potential release of nanoparticles into the environment and resulting in secondary pollution.

The use of powdered catalysts also presents challenges for the upscaling of AOPs and other catalytic reaction processes in industrial applications, particularly within packed-bed reactors. While the use of fine powders ensures good access to catalyst active sites and reduces diffusional mass-transfer resistance, industry more commonly employs catalyst pellets of millimetre size. This approach helps mitigate the pressure drop issues associated with fine powders inside packed bed reactors. However, these relatively large spheres suffer from diffusion limitation issues, making the distribution of active sites critical.

As noted, SR-AOPs is a promising wastewater treatment technology, but the conflicts between pressure drop and mass transfer resistance in catalyst substrates prevent the AOPs from large-scale practical applications. As far as we know, the study on the influence of diffusion resistance on organic pollutant purification by PMS-based AOPs is limited. Moral-Rodriguez et al. investigated the intraparticle diffusion of ronidazole and SMX during adsorption onto granular activated carbon (1.016 mm) from an aqueous solution. Their findings indicated that the overall adsorption rates of both antibiotics were primarily controlled by intra-particle diffusion [253]. This also necessitates the exploration of novel catalyst substrates to resolve persistent challenges associated with intraparticle diffusion at large particle sizes. As mentioned in Section 2.2.3.3, innovative microchannel-structured ceramic beads with a diameter of 3 millimetres hold terrific potentials in this respect.

Chapter 3 Methodology

Chapter 3 presents the research methodology of the whole PhD project, from the preparation of catalyst substrates to the catalytic reactions, and characterisation techniques involved for the intuitive observation and analysis of the microstructured ceramic beads.

The design and preparation of innovative microchannel-structured ceramic beads are the most significant parts of this research. As mentioned in Section 2.2.3.3, conflicts between diffusional resistance and pressure drop in conventional catalyst technology necessity the novelty of the catalyst supports. This chapter details the research methodology including (i) the preparation of novel catalyst supports, (ii) material characterisation techniques, and (iii) catalytic activity analysis. The flow chart of the thesis methodology is depicted in Figure 3-1.

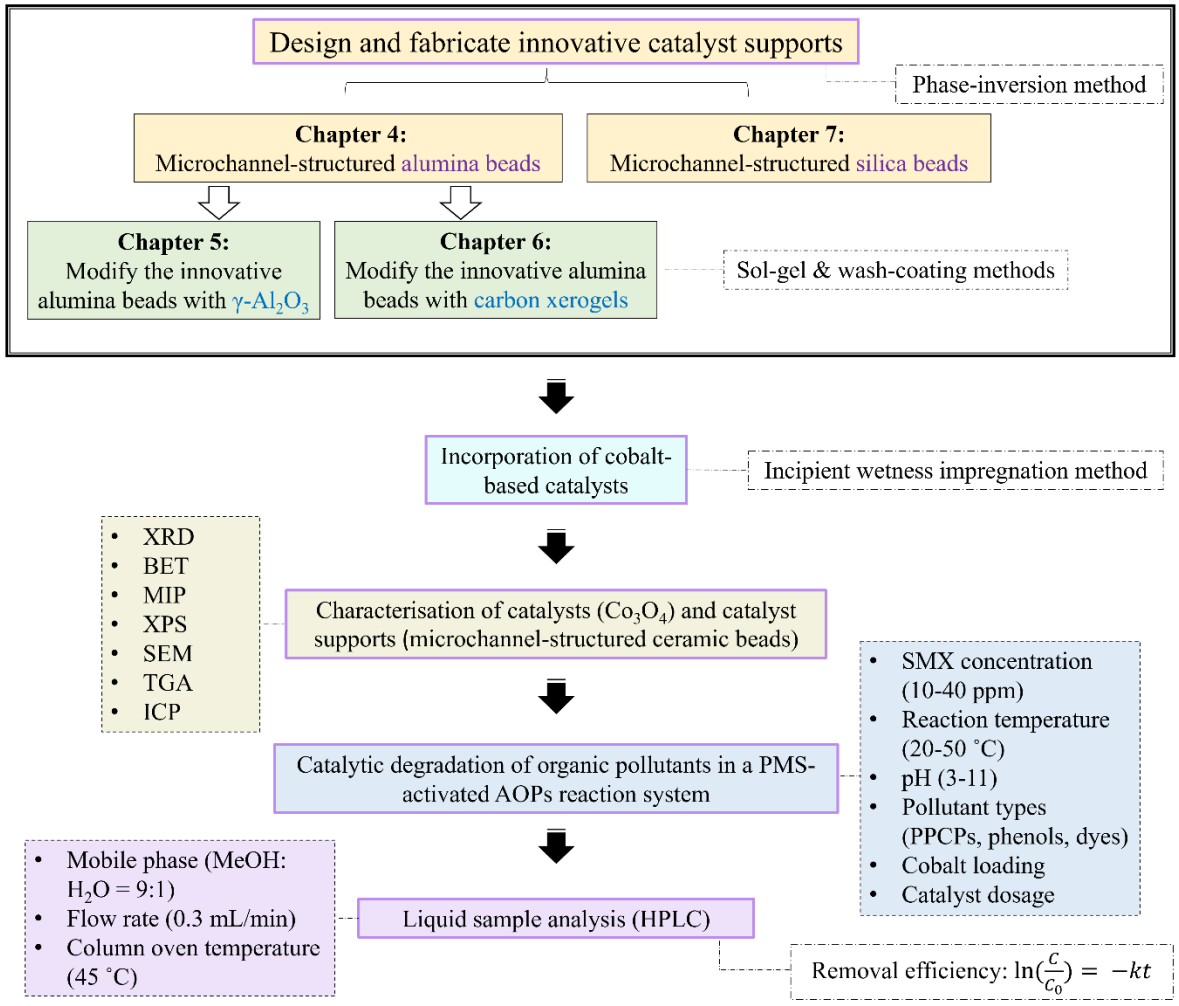

Figure 3-1 Flow chart of the thesis methodology.

3.1 Preparation method

In this thesis, four main methods, i.e., phase inversion, sol-gel, dip-coating, and wetness incipient impregnation methods, were included for the preparation of ceramic beads, washcoating layers (γ-Al_2O_3 and carbon xerogel), modified ceramic beads, and cobalt-based ceramic beads. The phase-inversion method is a well-known technique for the preparation of micro-structured inorganic membranes, which is widely used in a plurality of fields, such as steam methane reforming [171, 254], hydrogen purification [255, 256], oxidative coupling of methane [257, 258], gas separation [29], and solid oxide fuel cells [170, 259, 260]. It involves solvent/non-solvent exchange at the interface between ceramic suspension and non-solvent, resulting in the formation of finger-like microstructures, as mentioned in Section 2.3. Figure 3-2 shows the flowchart of three stages involved in the preparation of micro-structured ceramic beads in this research. Inspired by Li`s group [167-171], the homogeneous ceramic suspension is a mixture of dispersant – ethyleneglycol 30-dipolyhydroxystearate (Arlacel P135), solvents – NMP or DMSO, and polymer binders – Poly (methyl methacrylate) (PMMA) or poly-polyethersulfone (PESf). Afterwards, the degassed ceramic suspension is transferred into a 100 mL stainless steel syringe and dripped into a water bath prior to the phase inversion process. Finally, the ceramic green body is sintered in a furnace to burn off the polymer binder and densify the ceramic materials.

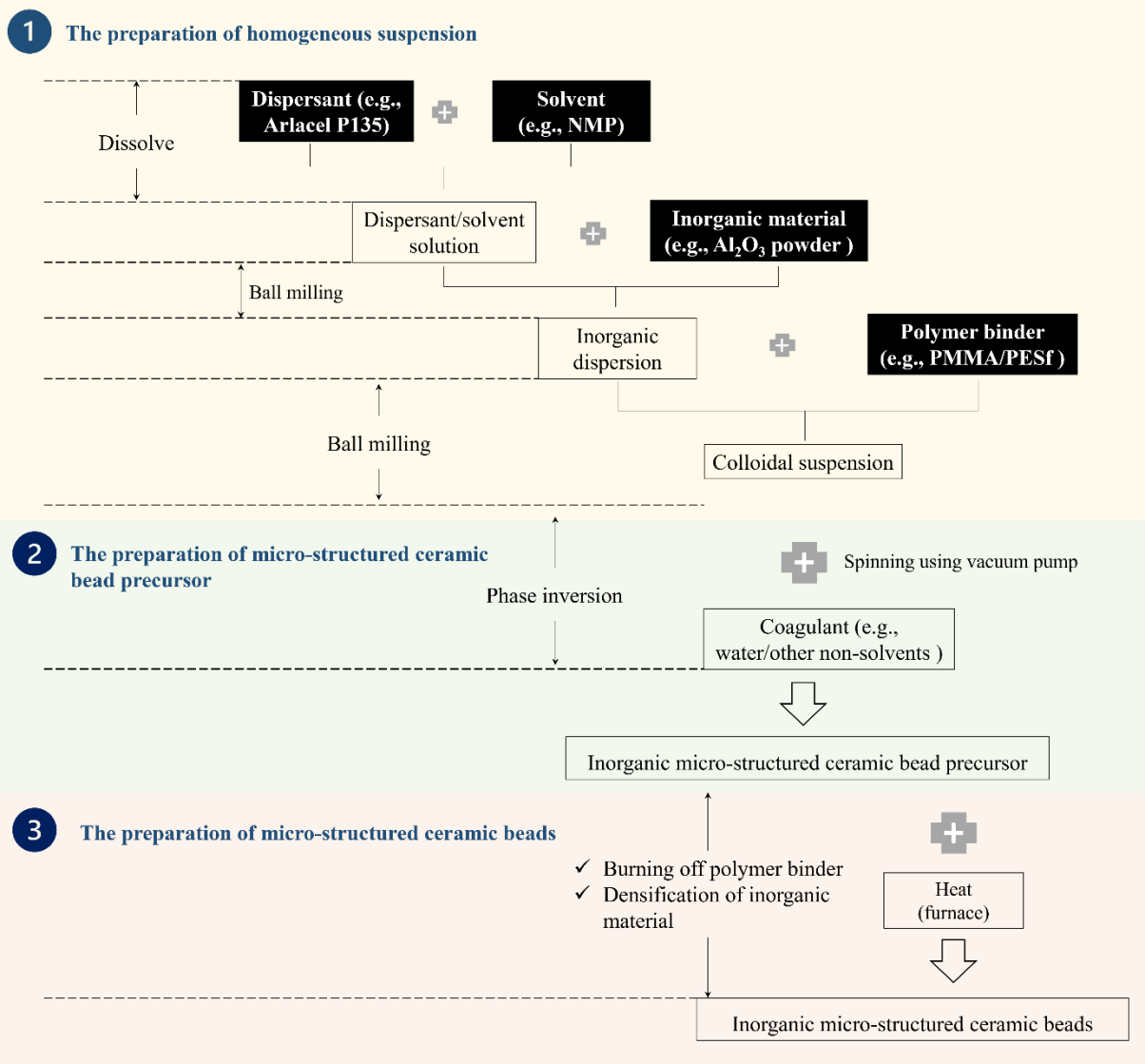

Figure 3-2 A flowchart outlining the fabrication process for micro-structured ceramic beads.

In terms of the sol-gel method, Figure 3-3 exhibits two schematic diagrams of the preparation of γ-Al_2O_3 sols (for Chapter 5) and carbon xerogel sols (for Chapter 6). As shown in Figure 3-3 (a), a cooling reflux apparatus is setup to prepare γ-Al_2O_3 sols, with a mixture of aluminium isopropoxide (AIP) and DI water in their molar ratio of 1:100 being refluxed and stirred vigorously at 90 ˚C for several hours until the suspension is converted into a clear sol, which was built upon the literature [261-263]. In contrast, carbon xerogel can be synthesised by mixing certain amounts of resorcinol, formaldehyde, sodium carbonate, and DI water [264, 265].

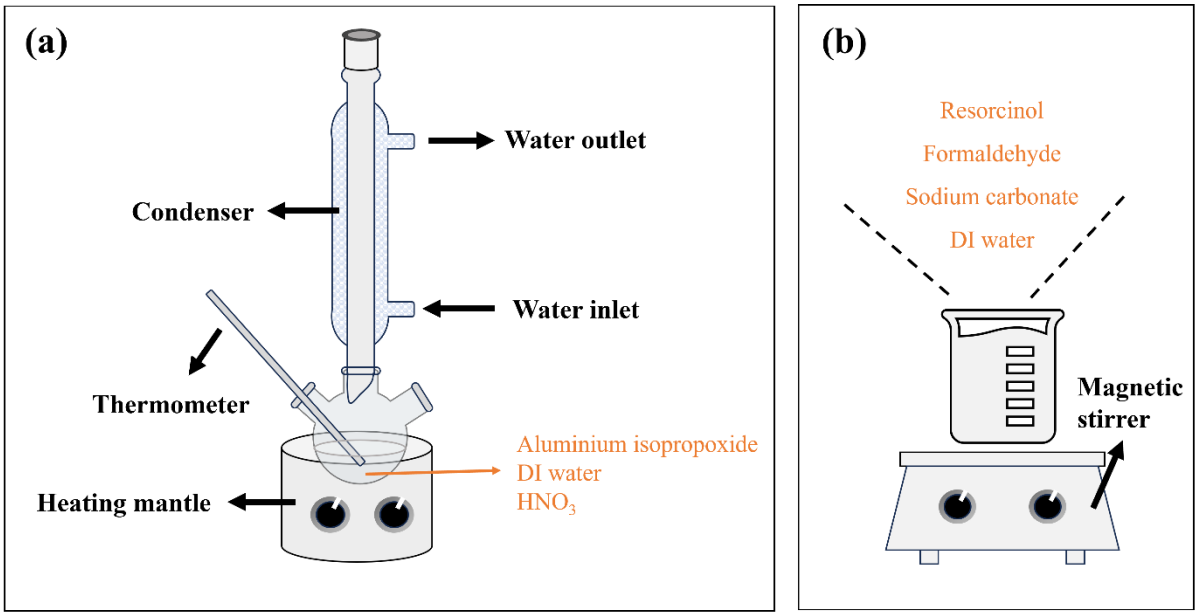

Figure 3-3 Schematic illustration of the preparation of washcoatings by the sol-gel method: (a) γ-Al_2O_3 sol and (b) carbon xerogel sol.

3.2 Characterisation

This research focuses on designing and preparing innovative catalyst substrates, with a strong reliance on various characterisation techniques to analyse and understand the physicochemical properties of the prepared materials. Table 3-1 lists a summary of the characterisation techniques, the corresponding instrument models, and the specific purpose of each technique used in this thesis. The analysis is summarised in detail as outlined below.

Powder X-ray diffraction (XRD) spectra were recorded on an advanced X-ray diffractometer (Bruker D8, Germany) with Cu Kα radiation (λ=1.5418Å) in the range of 2θ = 5-80˚ at room temperature, operated at 40 kV and 40 mA. The specific surface area of samples was obtained at -196˚C with liquid nitrogen on a Nova 4000 porosimeter, using the Brunauer–Emmett–Teller (BET) method and the Barrett, Joyner, and Halenda (BJH) method. Prior to the measurement, samples were gently ramped to 130˚C and degassed under vacuum for 5-6 h. Mercury intrusion porosimetry (MIP, Autopore IV 9500, Micromeritics) was used to investigate the pore structure of ceramic beads before and after removing the outer skin layer. The mercury intrusion data were collected under absolute pressure ranging from 0.10 to 60000.00 psia with an equilibration time of 10 s. The chemical composition analyses were investigated on an X-ray photoelectron spectroscopy (XPS, Thermo Scientific K-Alpha Photoelectron spectrometer, USA) system equipped with an Al Kα source. All binding energies were calibrated using the contaminant carbon (C 1s = 284.8 eV) as a reference. The morphology and composition of ceramic beads were analysed by a scanning electron microscopy (SEM, JEOL JSM-IT200, operating at 5 kV and working distance of 10 mm) and energy-dispersive X-ray spectroscopy (EDS), respectively.

Thermogravimetric analysis (TGA) was carried out on the TGA-DSC 2 STAR system (Mettler Toledo) with a heating rate of 10˚C/min in either air or nitrogen atmosphere for different sample analysis. The cobalt content was analysed by an inductively coupled plasma-optical emission spectrometry (ICP-OES) apparatus (iCAP 7000 Series).

Table 3-1 Characterisation techniques and prototype

No.	Characterization	Instrument	Purpose
1	X-ray diffraction (XRD)	Bruker D8, Germany	To study the crystallographic structure, chemical composition, and physical properties of the prepared ceramic beads before and after catalyst incorporation
2	Brunauer–Emmett–Teller (BET)	Nova 4000 porosimeter	To investigate the BET surface area, total porosity or total pore volume, median pore diameter, and pore size distribution of the innovative ceramic beads
3	Mercury intrusion porosimetry (MIP)	Autopore IV 9500, Micromeritics	To further understand the porosity and pore size distribution of macro-sized ceramic beads, particularly beads before and after removing the thin skin layer on the beads` surface
4	X-ray photoelectron spectroscopy (XPS)	Thermo Scientific K-Alpha Photoelectron spectrometer, USA	To analyze the elemental composition and chemical state of elements in the cobalt-based ceramic beads, particularly the chemical state of element Co
5	Scanning electron microscopy (SEM)	JEOL JSM-IT200	To intuitively observe the high-resolution images of the surface of ceramic beads, including surface topography, morphology, and composition
6	energy-dispersive X-ray spectroscopy (EDS)	JEOL JSM-IT200	To analyze the elemental composition and distribution of ceramic beads
7	Thermogravimetric analysis (TGA)	TGA-DSC 2 STAR system (Mettler Toledo)	To measure changes in the mass of a material as a function of temperature or time, so as to analyze the decomposition of materials
7	Inductively plasma optical emission spectroscopy (ICP-OES)	iCAP 7000 Series	To analyze the cobalt concentrations in both solid catalyst samples and aqueous pollutant solutions after reaction

3.3 Evaluation of catalytic performance

Environmental pollution arising from pharmaceutical and personal care products (PPCPs) that include but are not limited to antibiotics, antimicrobial agents, cosmetics, etc. has been attracting a great deal of attention in recent years [266, 267]. Many antibiotics, such as SMX, paracetamol, and naproxen, have been ubiquitously detected in surface and ground waters in concentrations ranging from nanograms to micrograms per litre, posing risks to public health and the ecosystem and becoming contaminants of emerging concerns [226, 268, 269]. SMX is a typical sulphonamide antibiotic drug widely used against human and veterinary infections but recalcitrant to conventional water and wastewater treatment plants due to its strong hydrophilicity, high stability, and antibacterial nature [228, 267]. Although it was detected in low concentration (0.01-2.0 μg/L) in surface water, continuous exposure or the accumulation of SMX concentration in the long term owing to continuous discharge could pose an adverse threat to human health, such as chronic diseases and genetic mutation [216, 270, 271].

In contrast, the second type of organic pollutants, phenols (e.g., p-HBA, phenol), are major toxic and recalcitrant organic compounds that commonly exist in effluents from various industries, such as pesticide, pharmaceutical, and petrochemical sectors [272, 273]. Phenol and phenolic compounds comprise of a hydroxyl group (-OH) bonded directly to an aromatic hydrocarbon ring, typically a benzene ring. Their concentration in the discharged effluents can reach thousands of parts per million, which poses severe risks to both aquatic ecosystems and human health [274]. But, the WHO has recommended a threshold of 1.0 μg/L (or 1.0 parts per billion) for the phenol concentration in drinking water to prevent any adverse effects of organoleptic properties [275]. Likewise, dye wastewater also causes serious environmental concern due to its complex composition (a mixture of dyes, surfactants, salts, heavy metals, and other chemicals) and high pollution potential, such as affecting aquatic organisms by decreasing light penetration, lowering dissolved oxygen levels, and impeding photosynthesis [276].

In this thesis, the catalytic performance of cobalt-based catalysts supported on the innovative microchannel-structured ceramic beads was evaluated for the degradation of three types of organic pollutants (PPCPs, phenols, and dyes) in a PMS activated system. The experiments were carried out in a batch reactor in a water bath and connected with a mechanical overhead stirrer. Initially, a certain amount of catalyst was placed in 100 mL of SMX solution with vigorously stirring at 150 rpm for 30 min to achieve the adsorption-desorption equilibrium. Afterwards, the catalytic reactions were initiated by adding PMS (0.31 mM) and continued for another 120 min. When the reaction was in process, 1 mL of aqueous solution was withdrawn by a syringe at fixed time intervals and filtered by a 0.2 μm PTFE syringe filter, and then immediately injected into a HPLC vial which was already injected with 0.5 mL methanol as a quenching agent. This is because that methanol has a high reactivity with both ·OH and $SO_4^{\cdot-}$ ($k_{\cdot OH} = 9.7 \times 10^8\ M^{-1}s^{-1}$, $k_{SO4^{\cdot-}} = 3.2 \times 10^6\ M^{-1}s^{-1}$) [277, 278]. The concentrations of organic pollutant

solutions were analysed on an ultra-high performance liquid chromatography (UHPLC, Shimadzu Prominence, Japan) using a UV detector set at different wavelengths (270 nm for SMX, p-HBA, and phenol, 464 nm for MO) [229, 279, 280]. A C-18 column (Restek Rapter, 2.7 μm, 100 × 2.1 mm, France) was used to differentiate the organics and the column oven temperature was set to 45 ˚C. Methanol and ultrapure water (pH 3.5 adjusted by acetic acid) with a volume ratio of 90:10 was used as the mobile phase at a flowrate of 0.3 mL/min. The catalytic degradation kinetics of SMX followed the pseudo-first-order kinetic model and can be estimated using the following equation:

$$ln\left(\frac{C}{C_0}\right) = -kt \qquad \textit{(Equation 3-1)}$$

where k is the apparent reaction rate constant (min^{-1}), and C_0 and C are the initial SMX concentration (mg/L), and the SMX concentration at specific time intervals (mg/L), respectively. All experiments were carried out in triplicate to ensure reliability, leading to minimal variations and therefore extremely small error bars, except for Figure A7, where the effect of PMS concentrations on SMX degradation was evaluated.

3.4 Key abbreviations and definitions

To ensure clarity and ease of understanding in describing the samples prepared and used in this research, we have introduced additional abbreviations specific to the catalysts used in the four experimental chapters (Chapters 4-7), in addition to the universal nomenclature presented on pages 10-11, as summarised in Table 3-2.

Table 3-2 Key abbreviations and their definitions of samples used in this thesis

No.	Abbreviations	Chapter	Short definition
1	MSCB	4	Microchannel-structured ceramic beads
2	MSCB0	4	Microchannel-structured ceramic beads type I: beads with a common isotropic structure without radial microchannels
3	MSCB1	4	Microchannel-structured ceramic beads type II: beads with radial finger-like microchannels and a denser outer skin-layer on the bead surface
4	MSCB2	4	Microchannel-structured ceramic beads type III: beads with radial finger-like microchannels and no skin-layer on the bead surface
5	2Co/MSCB0	4	2 wt.% of Co_3O_4 to the microchannel-structured ceramic beads type I
6	2Co/MSCB1	4	2 wt.% of Co_3O_4 to the microchannel-structured ceramic beads type II

7	*x*Co/MSCB2	4	*x* wt.% of Co_3O_4 to the microchannel-structured ceramic beads type III (*x* = 0.5, 1, 2, and 5)
8	AS*x*	5	Microchannel-structured alumina beads type III (labelled as "MSCB2" in Chapter 4) with γ-Al_2O_3 sols after drying at 35 ˚C for different time (*x* = 0, 1, 2, 3, and 4); Detailed in Section 5.2.2
9	2Co/AS*x*	5	2 wt.% of Co_3O_4 to the microchannel-structured ceramic beads type III after washcoating with γ-Al_2O_3 sols via two-step sequential impregnation method
10	2Co/AS*x* (co-imp.)	5	2 wt.% of Co_3O_4 to the microchannel-structured ceramic beads type III after washcoating with γ-Al_2O_3 sols via one-step co-impregnation method
11	CX*x*	6	Carbon xerogel sols with different concentrations (*x* = 0, 1, 2, 3, and 4); Detailed in Section 6.2.2
12	ACX*x*	6	Microchannel-structured alumina beads type III (labelled as "MSCB2" in Chapter 4 and "AS0" in Chapter 5) modified with carbon xerogel sols of different concentrations
13	2Co/ACX*x*	6	2 wt.% of Co_3O_4 to the microchannel-structured ceramic beads type III after washcoating with carbon xerogel sols
14	SiO_2-*x*C	7	Microchannel-structured silica beads after being sintered at different temperatures (*x* = 1000, 1020, 1100, and 1200 for the main text); Detailed in Section 7.2.2
15	2Co/SiO_2-*x*C	7	2 wt.% of Co_3O_4 to the microchannel-structured silica beads after being sintered at different temperatures

Chapter 4 Innovative microchannel-structured alumina beads to address diffusional transfer resistance

Chapter 4 presents the preparation and characterization of innovative alumina beads for the degradation of SMX solutions in a PMS-activated system. To study the efficacy in reducing diffusional transfer resistance—a process intensification approach at microscales—beads without microchannels and with an outer skin layer were also prepared for comparison of reaction performance under various conditions.

A part of this chapter is presented in this paper:

Zheng, J, Wu, Z, et al. Catalytic micro-structured ceramic beads and efficacy evaluation through SMX degradation in PMS-activated systems [J]. Separation and purification Technology, 354 (2025): 129060.

4.1 Introduction

As mentioned in Chapter 2, there is a long-standing challenge of balancing pressure drop of packed bed reactor and diffusional resistance in catalyst supports with millimetre-scale diameters. A homogenous distribution of the active phase in large catalyst particles or pellets is only beneficial for relatively slow catalytic processes that allow reactants to diffuse to all the active sites. While for faster reactions, current catalyst technology has employed the non-uniform macroscopic distribution patterns, such as eggshell pellets with a thin catalyst layer on the surface of inert core, to bypass the issues of diffusional mass transfer. However, a significant volume of unused inert inner core exists, which reduces the volumetric productivities and leads to varying reaction fronts, as well as thermal and mass fronts within the reactor.

In this chapter, the innovative microchannel-structured ceramic beads (MSCBs) with a significantly different diffusion pathways were prepared for the degradation of SMX, a representative reaction for addressing emerging organic pollutants in water. Unlike traditional beads, which consist of macro-pores formed by the random packing of micro- or meso-porous particles and have complex and long diffusion routes inside, these microchannel-structured ceramic beads can dramatically boost the effective diffusivity. This enhancement is achieved by reducing diffusion restrictions from the random pore network through the creation of radial micro-channels, leading to a diffusion process that more closely mimics bulk diffusion. This advancement will facilitate the potential upscaling of AOPs by better meeting with the industrial requirements for the catalytic materials.

Herein, a transition metal catalyst, Co_3O_4, was impregnated in the MSCBs for the degradation of SMX in the PMS-activated AOPs reaction system under different reaction conditions (e.g., catalyst concentration, reaction temperature, and SMX concentration). The morphologies of the cross-sectional and surface of these ceramic beads were examined by SEM and EDS analysis, and other

physicochemical properties were systematically characterised. Furthermore, the stability and reusability of the as prepared 2Co/MSCBs were investigated. Finally, the active species involved in the 2Co/MSCB2|PMS reaction system were analysed through quenching experiment, and the catalytic mechanism of this reaction system was further proposed.

4.2 Experimental

4.2.1 Chemicals and materials

Alpha-alumina powder and Yttria Stabilized Zirconia (YSZ) grinding media were purchased from Inframat Advanced Materials (USA). PMMA, Oxone® (PMS, $KHSO_5 \cdot 0.5KHSO_4 \cdot 0.5K_2SO_4$), SMX, p-benzoquinone (p-BQ, ≥ 98%), tert-butanol (tBA, ≥ 99.5%), sodium azide (NaN_3, ≥ 99.5%), and acetic acid (ReagentPlus®, ≥ 99%) were all provided by Sigma-Aldrich. Cobalt nitrate hexahydrate ($Co(NO_3)_2 \cdot 6H_2O$, 99% pure)/methanol (HPLC grade, ≥ 99.8%), PESf (Radel A-300), NMP (99+%, ACS reagent) and Arlacel P135 were provided by Fisher Scientific, Ameco Performance (USA), ACROS Organics and Uniqema (UK), respectively. All chemicals were used as received without any further purification. Milli-Q water (18.3 MΩ cm) was used during the whole experimental process.

4.2.2 Preparation of micro-structured ceramic beads (MSCBs)

Microchannel-structured Al_2O_3-based beads of 2-3 mm in diameter were fabricated for the first time by a phase-inversion and sintering method, as shown in Figure 4-1, inspired by the work in Li's group [169, 172]. Specifically, prior to the addition of α-alumina powders (150 g), Arlacel P135 (1.05 g) was dissolved in NMP solvent (122.41 g), and the mixture was milled with 20 mm agate milling balls with an approximate alumina/agate weight ratio of 2 for 48 h. After the addition of PMMA, the suspension was continued for milling for another 48 h. The suspension was then transferred to a gas-tight vacuum degassing chamber (DP 27, Applied Vacuum Engineering) and degassed under vacuum for 3 h until no bubbles were visible at the surface, and then the suspension was transferred to a 100 mL stainless steel syringe fitted with polytetrafluoethylene O-rings and extruded at 0.1 mL/min into a water bath (a non-solvent for the polymer). The actual flow rate of the extrusion was controlled by a Chemyx Fusion 6000-X syringe pump, ensuring the uniformity of the prepared precursor ceramic beads. These precursor ceramic beads were kept in the water bath for 24 h to allow the completion of phase inversion. Finally, the dried ceramic beads were sintered in stagnant air (furnace BRF 16/5, Elite) at 600 ˚C for 2 h and then 1450 ˚C for 4 h with a heating and cooling rate of 5 ˚C/min. The sintered microchannel-structured ceramic beads were named as MSCB1. Afterwards, the thin skin layer on the surface of MSCB1 was removed by blending them with coarse silica carbide (46 grit) in a volume ratio of 1:2 and

place them in the Jarmill. The continuous rotation of SiC and MSCB1 in the Jarmill ensures the removal of skin layer due to wear and abrasion caused by the higher Moh's hardness of SiC (13) than α-Al_2O_3 (9). The resulting sample was denoted as MSCB2. For comparison, ceramic beads without radial microchannels (MSCB0) were prepared by the same method, wherein PMMA was substituted with PESf, and the quantity of NMP was augmented from 122.41 to 133.95 g.

It is worth noting that the formation of spherical ceramic beads is dependent on various operating parameters, e.g., suspension compositions, extrusion rates, nozzle dimensions, air gap and even the depth of the water bath. Detailed experiments and discussions are summarised in Text A1 in the supplementary information.

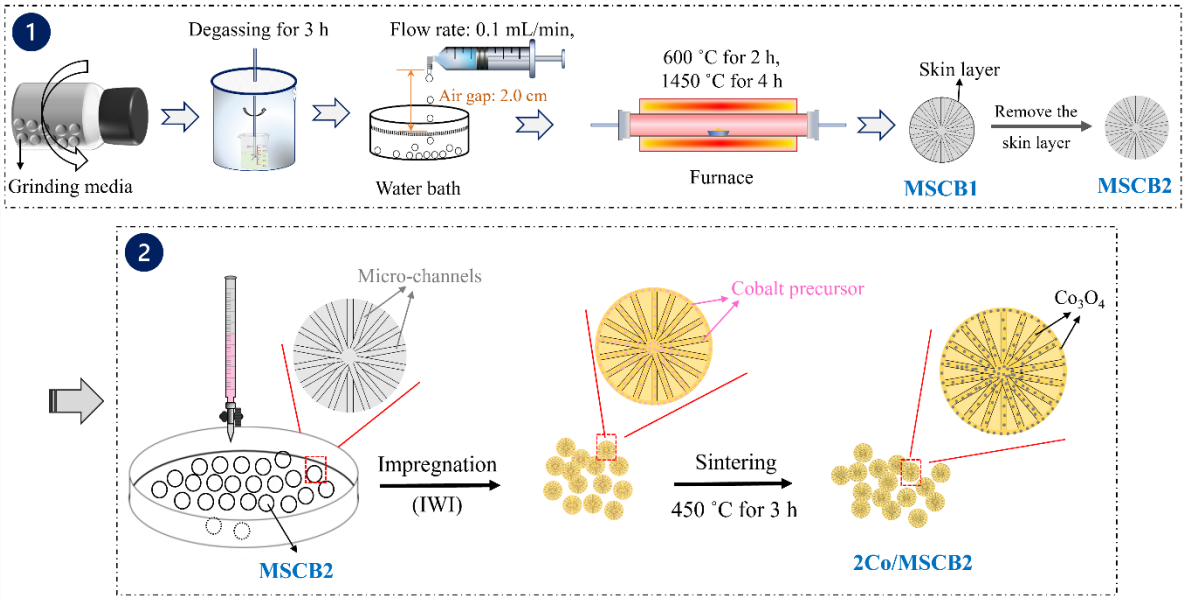

Figure 4-1 Schematic illustration of the preparation of the micro-structured ceramic beads and the cobalt incorporation process, via phase inversion and incipient wetness impregnation method, respectively.

4.2.3 Preparation of Co-based catalytic ceramic beads (Co/MSCBs)

Cobalt oxide was loaded on the ceramic beads by the traditional incipient wetness impregnation (IWI) method, where a pre-determined volume of cobalt nitrate hexahydrate aqueous solution was added to the ceramic beads [281, 282]. Then, the catalyst precursor was dried at 35˚C overnight before being calcined at 450˚C in stagnant air for 3 h at heating and cooling rates of 5˚C /min, as shown in Figure 4-1. The as-prepared samples were denoted as *x*Co/MSCB*y*, where "*x*" refers to the weight percentage of Co_3O_4 to the ceramic beads, and "*y*" implies the specific ceramic beads (e.g., MSCB2 for the micro-structured ceramic beads without the skin layer).

4.2.4 Characterisation and catalytic performance test

The characteristics of the microchannel-structured alumina beads before and after cobalt loading were analysed by a series of characterisation techniques, including XRD, XPS, SEM, EDS, BET, MIP, and ICP. Further details can be found in Section 3.2. The catalytic performance of three types of catalytic ceramic beads – 2Co/MSCB0 (beads with a common isotropic pore structure), 2Co/MSCB1 (beads with radial finger-like microstructures and a denser outer skin-layer), and 2Co/MSCB2 (beads with finger-like microstructures and no outer skin layer) – was evaluated for the degradation of SMX solutions in a PMS-activated system. The experiments were carried out in a batch reactor in a water bath at 20 ˚C and connected with a mechanical overhead stirrer. Other detailed information can be found in Section 3.3.

4.3 Results and discussion

4.3.1 Characterisations of ceramic beads and Co-based MSCBs

The crystallographic structures of ceramic beads before and after cobalt impregnation were analysed by XRD. As shown in Figure 4-2 (a), all diffraction peaks were well matched with the rhombohedral phase of Al_2O_3 referenced in JCPD file no. 88-0826 [283]. However, the characteristic peaks of Co_3O_4 were barely visible in the three cobalt-based samples, which can be attributed to the low concentration and high dispersion of cobalt oxide [284]. This is supported by the XRD patterns of ceramic beads MSCB2 with a higher Co_3O_4 loading (Figure 4-2 (b)), high-resolution XPS spectra of Co in the sample 2Co/MSCB2 (Figure 4-3 (d)), the EDS mapping images (Figure 4-6), alterations in colour of the cobalt oxide concentration from 0.5 wt.% to 5 wt.% (Figure 4-10 (a)), and the ICP results (Figure 4-10 (c)). It can be seen from Figure 4-2 (b) that the main characteristic peak at 36.9˚, indexed to the (311) plane of Co_3O_4 (JCPDS # 42-1467), appeared when the Co_3O_4 loading increased to above 5 wt.% (5Co/MSCB2) [285, 286]. In fact, a small characteristic peak for (311) plane of Co_3O_4 could be found when zooming in the *x*-axis in the coordinate, as shown in the inset of Figure 4-2 (a), further confirmed the existence of Co_3O_4.

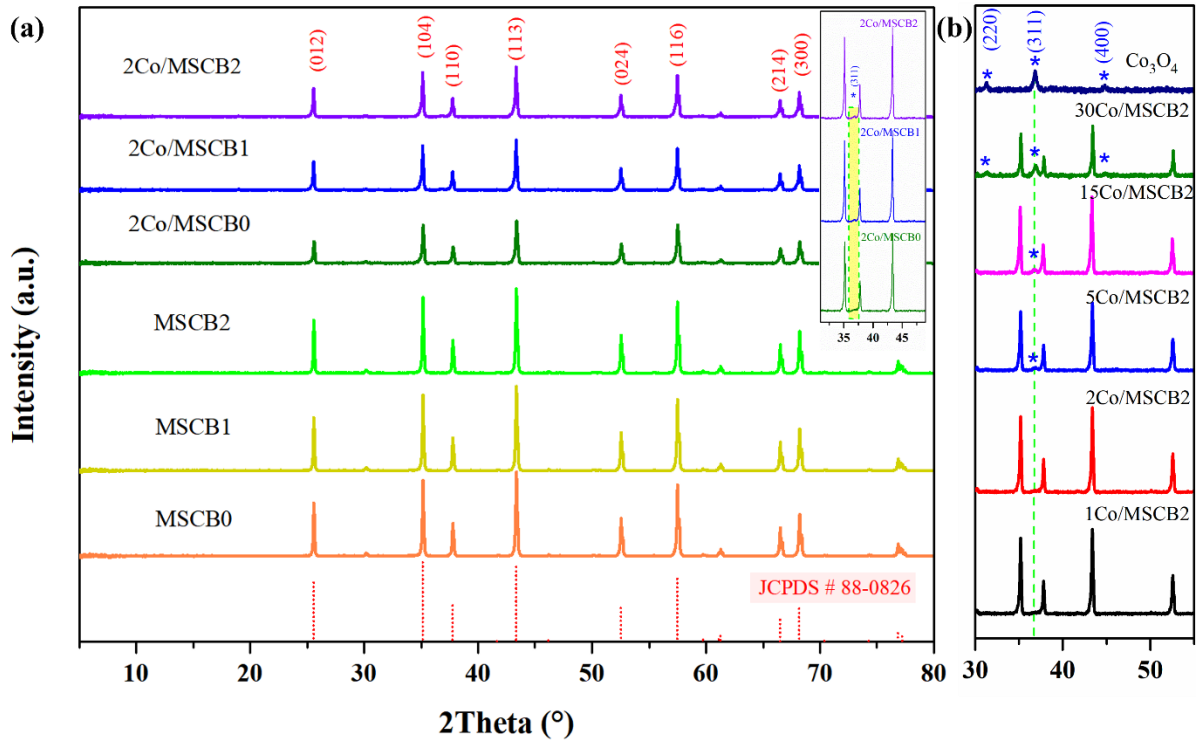

Figure 4-2 XRD patterns of (a) three types of ceramic beads (MSCB0, MSCB1, MSCB2) before and after Co_3O_4 impregnation, and (b) ceramic beads MSCB2 with different Co_3O_4 loading.

Additionally, chemical compositions of the sample 2Co/MSCB2 were further investigated by XPS analysis, as shown in Figure 4-3 (a-d). Figure 4-3 (a) exhibited elemental compositions of 2Co/MSCB2 in the XPS survey spectra, which confirmed the presence of elements Al, O, C and Co. The C 1s spectrum belongs to the adventitious carbon originated from the carbon grid during the sampling process. In Figure 4-3 (b), the main peak at 73.8 eV could be attributed to Al^{3+}, while the extremely weak peak at 75.3 eV resulted from the formation of small amounts of aluminium suboxide during the cobalt impregnation process [287, 288]. The O 1s spectrum in Figure 4-3 (c) could be divided into two components: the signal at 530.5 eV is characteristic peak of lattice oxygen species in Al-O bond of Al_2O_3, and 531.3 eV was related to the Al-O-H, suggesting that hydroxyl groups were attached on the surface of Al_2O_3 [289, 290]. The existence of hydroxyl groups could be either attributed to residue water precursors during the process, or to the exposure of the catalysts to humid atmospheres prior to the XPS measurement [291]. As for the Co 2p spectra (Figure 4-3 (d)), two peaks at 780.0 eV and 795.0 eV corresponded to Co $2p_{3/2}$ and Co $2p_{1/2}$ of Co^{3+}, respectively, while two subpeaks at 781.6 eV and 797.1 eV were associated with Co $2p_{3/2}$ and Co $2p_{1/2}$ of Co^{2+}, respectively [292, 293]. A spin energy interval of 15 eV refers to the mixed valence of Co_3O_4 [294]. Furthermore, two prominent shake-up satellite peaks (denoted as "Sat.") for Co^{2+} could also be observed at binding energy of 786.4 eV and 804.5 eV [240]. These findings further testified the successful incorporation of Co_3O_4, aligning with the XRD results.

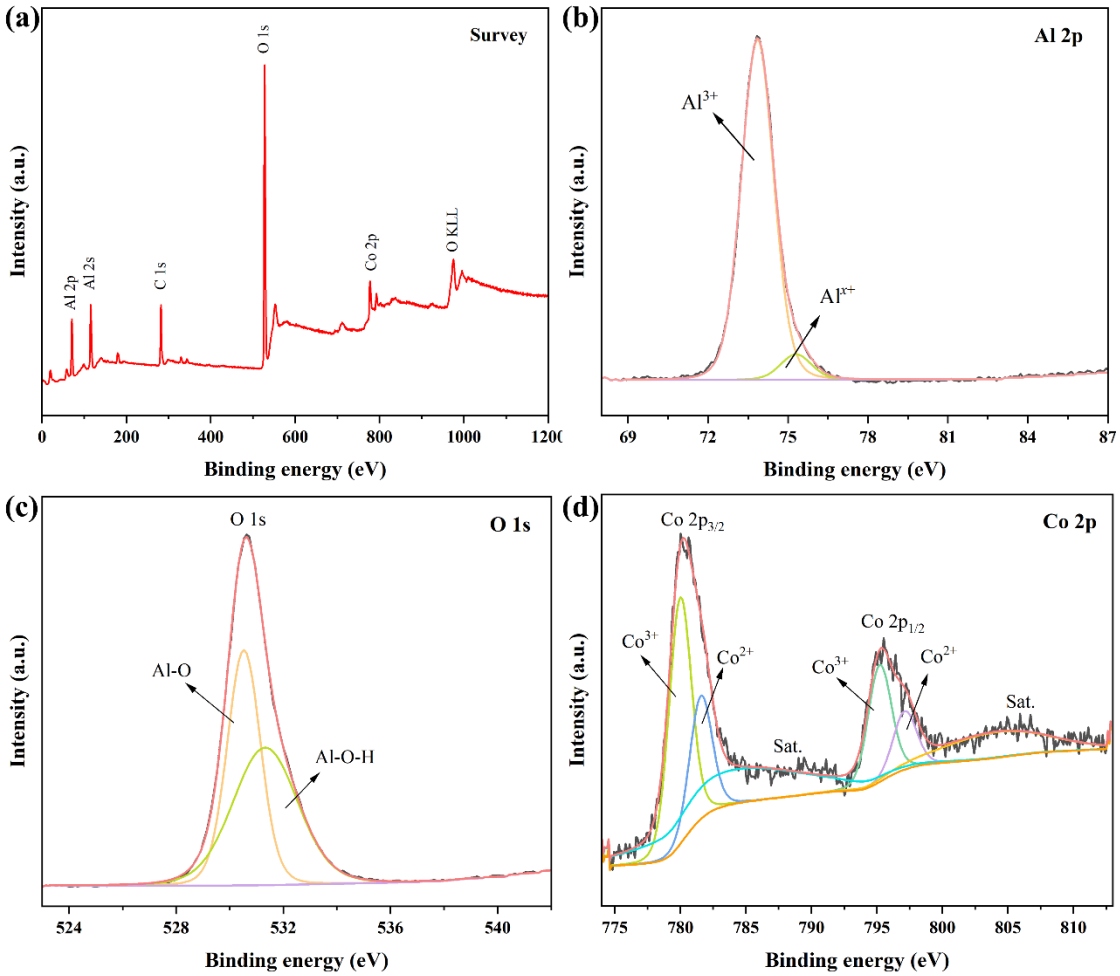

Figure 4-3 (a) XPS survey spectra and high-resolution XPS spectra of (b) Al (c) O, and (d) Co for the sample 2Co/MSCB2.

Prior to conducting SEM analysis, ceramic beads were halved using a knife to expose their cross-sections, and the corresponding SEM images of both the cross-sectional and surface views can be observed in Figure 4-4. Figure 4-4 (a) and Figure 4-4 (b) depict the sponge-like structure in both the cross-section and surface of MSCB0, while Figure 4-4 (c) reveals a finger-like structure of MSCB1 in the cross-section with exposed microchannel sizes ranging from 150 to 1200 µm in length and 50 to 100 µm in width, depending on the cutting patterns. It is worth noting that the actual dimensions of microchannels are relatively uniform, as these structures developed in all directions inside the beads. Apparently, a dense sponge-like skin layer with a thickness of 70 µm on the cross-sectional edge of MSCB1 could be noticed, as corroborated by the surface view of MSCB1 depicted in Figure 4-4 (d), which exhibits a similar sponge-like structure to that of MSCB0. However, it can be seen from Figure 4-4 (e-h) that the dense skin layer disappeared in MSCB2, and some small open channels with diameters ranging from 1.97 to 15.54 µm (Figure 4-4 (f) and Figure 4-4 (i)) could be observed on the surface layer of the beads. This confirmed that the skin layer has been successfully removed, facilitating the transportation of reactants and products in catalytic reactions.

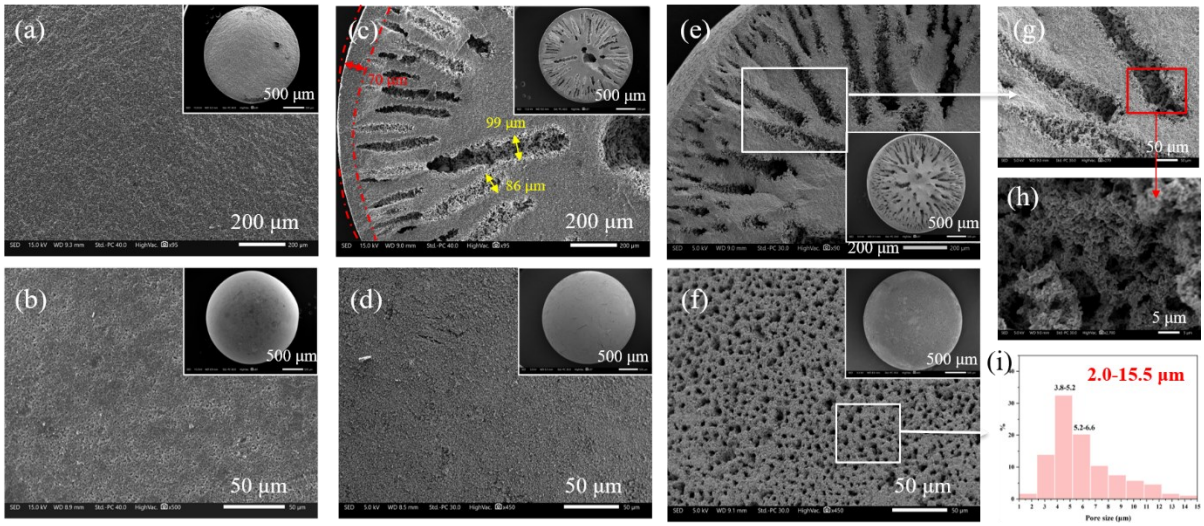

Figure 4-4 SEM images of (a) the cross-sectional view and (b) the surface view of MSCB0, (c) the cross-sectional view and (d) the surface view of MSCB1, (e, g, h) the cross-sectional views and (f) the surface view of MSCB2 with different magnification levels, along with their corresponding whole views (inset), and (i) the size distribution of open channels on the surface of MSCB2.

After incorporating with 2 wt.% Co_3O_4, these samples were further analysed by SEM analysis and EDS mapping to investigate the formation and dispersion of cobalt oxide. Figure 4-5 confirms that the introduction of Co_3O_4 did not change the pristine morphologies of ceramic beads. The EDS mapping of Al, O and Co elements on both the cross-sectional view (Figure 4-6 (a)) and surface view (Figure 4-6 (b)) of MSCB2 demonstrated the high stability of these MSCBs and the high dispersion of Co_3O_4. Noting that the difficulty in identifying Co_3O_4 within the micro-channels of the cross-sectional view in Figure 4-6 (a) arises from the fact that the depth of pores falls below the detectable limit of the equipment. Furthermore, the EDS mapping of MSCB0 (Figure A5 (a)) and MSCB1 (Figure A5 (b-c)) demonstrated comparable extensive cobalt dispersion.

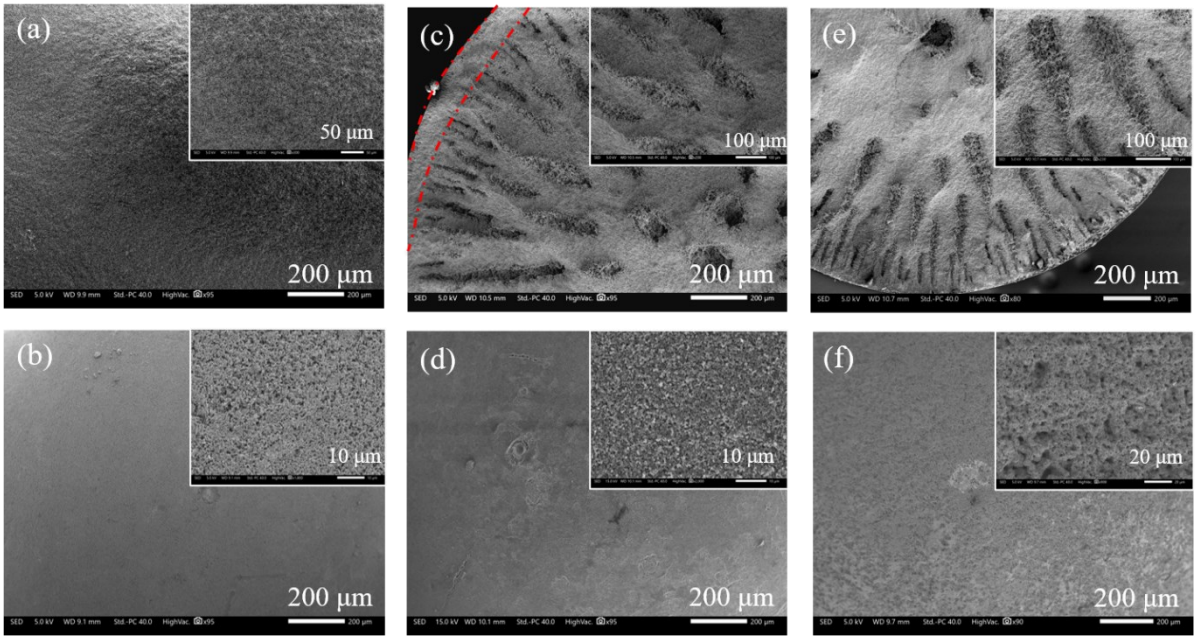

Figure 4-5 SEM images of (a) the cross-sectional view and (b) the surface view of 2Co/MSCB0, (c) the cross-sectional view and (d) the surface view of 2Co/MSCB1, (e) the cross-sectional view and (f) the surface view of 2Co/MSCB2, along with their corresponding whole views (inset).

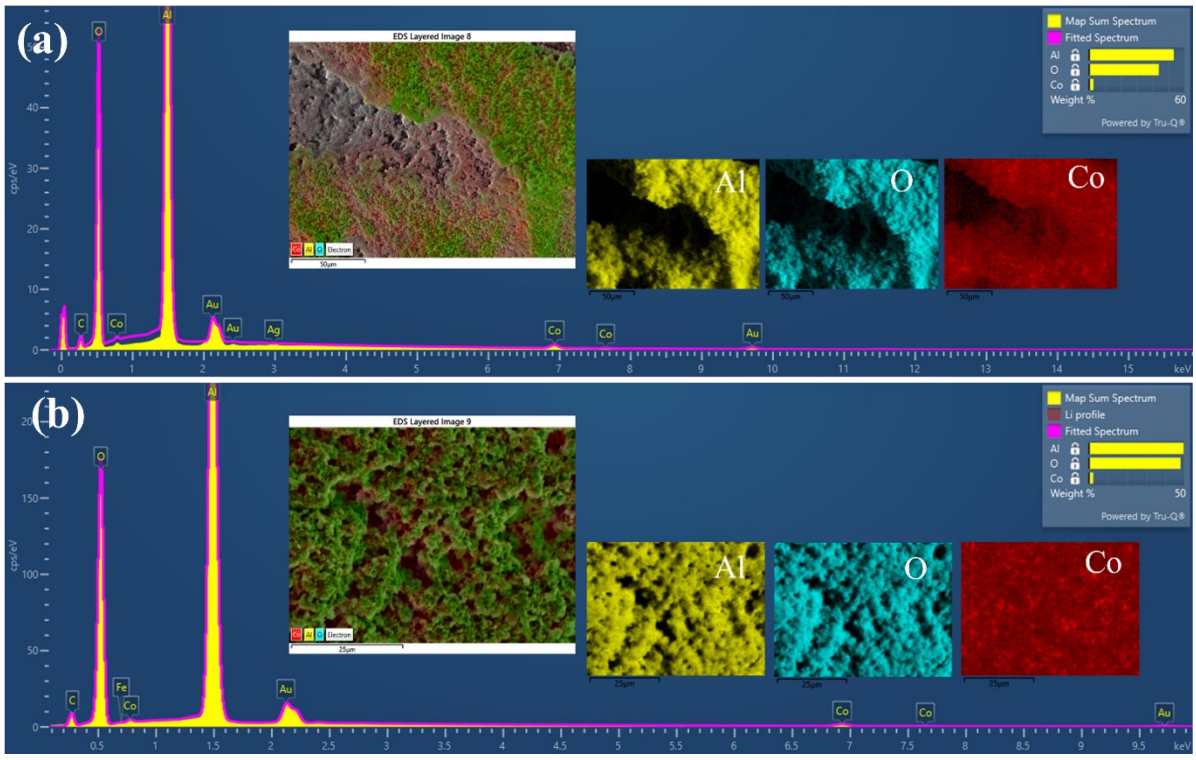

Figure 4-6 EDS mapping results of Al, O and Co elements for the cross-section of (a) 2Co/MSCB1 and (b) 2Co/MSCB2.

The textural characteristics of three types of ceramic beads before and after cobalt impregnation were depicted by the nitrogen physisorption experiments, as shown in Table A1. It could be found that all samples have small surface area owing to the intrinsic properties of α-Al_2O_3 and there were no significant differences among them in terms of surface area, total pore volume and pore diameters.

The limitations of the BET method in assessing anisotropic pore structures necessitated the use of mercury intrusion porosimetry. As depicted in Figure 4-7, the pore size distribution curve for these ceramic beads reveals differing pore structures. MSCB1 has smaller pores with an average diameter (D_p) of 387.5 nm, while MSCB2 has significantly larger pores with a broader size distribution (D_p ranging from 5,000 to 300,000 nm). The MIP measurement mechanism, which requires a higher pressure for mercury to infiltrate smaller pores, suggests that 387.5 nm represents the average pore size of the skin layer on MSCB1's outer surface (refer to Figure A6 (c) and the inset (1) in Figure 4-7). The peak area of the distribution curve thus represents the pore volume of both the sponge-like structure and the radial micro-channels. Upon removal of the skin layer, mercury can directly access the micro-channels at a substantially lower pressure. This results in the detection of larger pores in MSCB2 (the insect (2) in Figure 4-7). Increasing the pressure further allows mercury to infiltrate the remaining sponge-like pores within the beads. These observations are consistent with the SEM results presented in Figure 4-4. For additional details on MIP measurements for other MSCBs samples with different specifics, refer to Figure A6. Additionally, the porosity and pore volume data of MSCB1 and MSCB2 exhibit minimal changes. This can be attributed to the thin skin layer, which constitutes less than 5% of the bead radius.

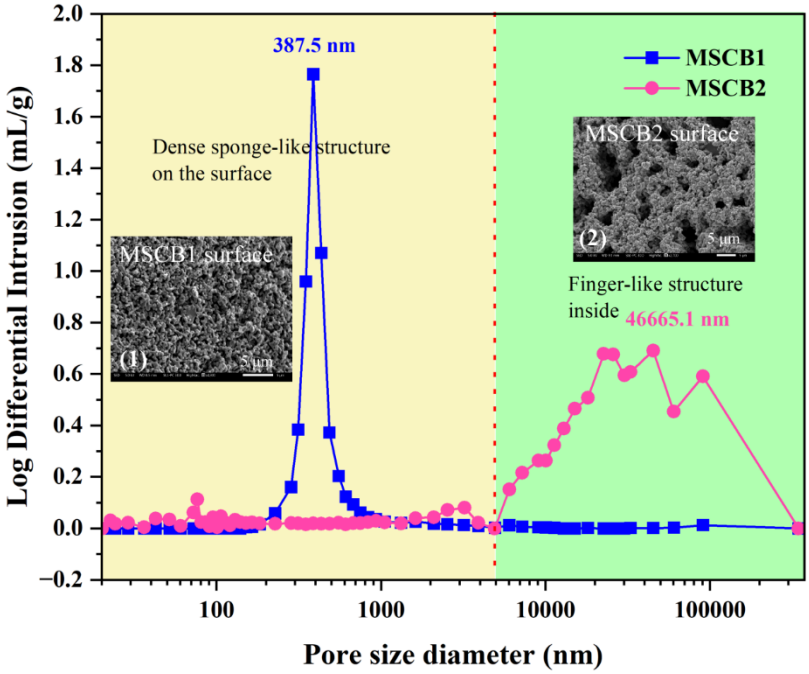

Figure 4-7 Pore size distribution of micro-structured ceramic beads with dense sponge-like structures (MSCB1) and exposed open channels (MSCB2) on the surface layer.

4.3.2 Catalytic degradation of SMX

In the liquid-solid reaction system, intraparticle diffusion becomes more significant, especially for catalyst particles with a diameter larger than 0.20-0.25 mm [295]. However, the creation of micro-channels within catalyst substrates can address this issue by enabling the radial micro-channels to serve as a "highway", thereby facilitating the transport of both reactants and products. Herein, the influence of the microstructures of catalyst substrates was investigated by the degradation of SMX under different reaction conditions, such as the reaction temperatures and SMX concentrations, as shown in Figure 4-8 and Figure 4-9. Before finalising the PMS dosage for three types of samples, the effect of PMS concentrations has been investigated (Figure A7), with 0.1 g/L exhibiting the most suitable catalytic performance (28.1%). This is comparable to the research with a similar PMS dosage [185, 296]. Figure 4-8 (a) displays the degradation of 20 mg/L SMX at 20 ˚C using the three ceramic beads. It is evident that the self-degradation of SMX and its purification using 2Co/MSCB2 only were negligible (0.1%), and there was limited difference among these samples under this reaction condition, with 2Co/MSCB2 (70.5%) slightly surpassing others. This is consistent with the results of the corresponding reaction kinetics (Figure 4-8 (b)) and rate constants (Figure 4-8 (c)). It is worth noting that at the beginning stage (5 min), the reaction rate constant k_{app} for 2Co/MSCB0 (0.04572 min^{-1}) is the lowest compared to 2Co/MSCB1 (0.05279 min^{-1}) and 2Co/MSCB2 (0.05285 min^{-1}). This is mainly attributed to the greater intra-particle diffusion resistance caused by the isotropic structure of 2Co/MSCB0. As the reaction continued, this disparity gradually diminished because the concentration gradient of the contaminants between external and internal surfaces of the catalyst support decreased. Additionally, the diffusion coefficient in liquid phase (10^{-10}-10^{-9} m^2/s) is very slow and is almost always overshadowed by convection.

Nevertheless, as the SMX concentration increased to 40 mg/L (Figure 4-8 (d)), the degradation efficiency saw an enhancement from 49.6% with 2Co/MSCB0 to 59.1% with 2Co/MSCB2, indicating that the specific microchannels within the ceramic beads promotes the transportation of reactants and products. Moreover, the exposed open channels on the surface layer of MSCB2 contributed to a reduction in diffusion resistance compared to the one with a thin dense skin on the surface layer, i.e., 2Co/MSCB1 (54.9%). Likewise, Figure 4-8 (f) indicates that the rate constants of 2Co/MSCB2 throughout the entire process were higher than those of 2Co/MSCB0, with the k_{app} value of 2Co/MSCB2 being 1.32 times that of 2Co/MSCB0. Further increasing the SMX concentration to 50 mg/L displayed a comparable scenario, as shown in Fig. A8 (a-b).

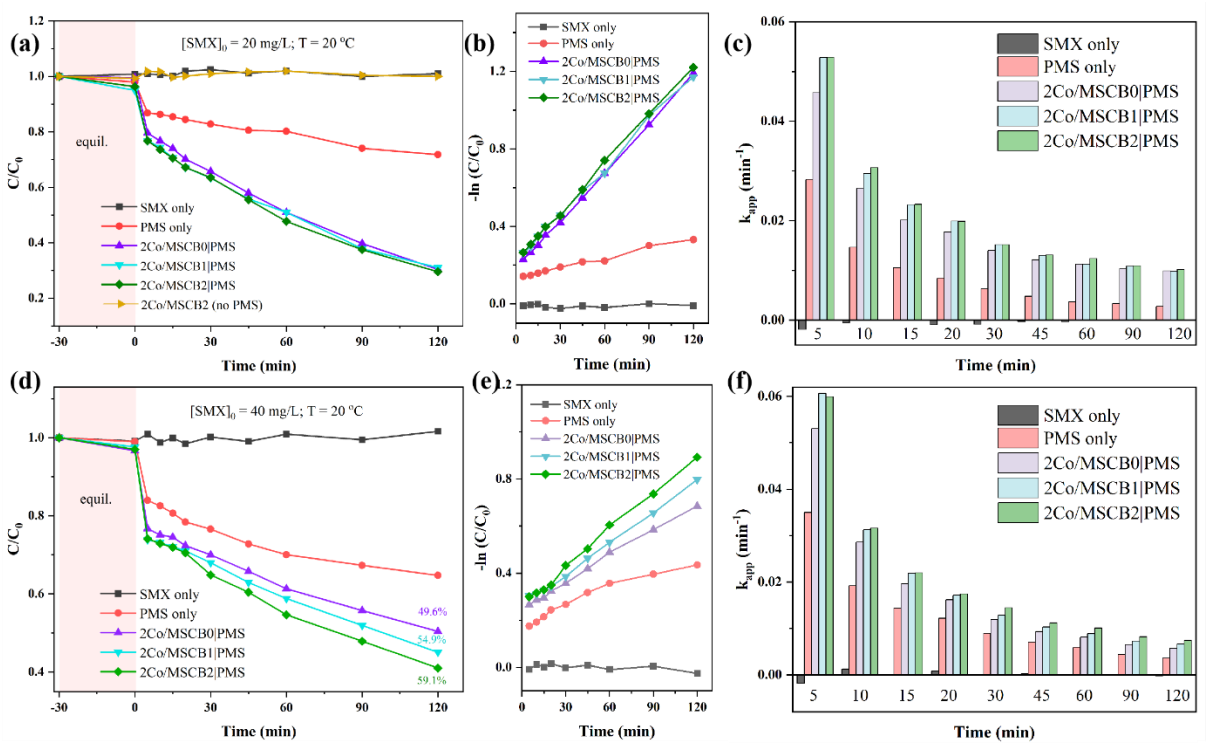

Figure 4-8 Degradation of different SMX concentrations at 20 °C, their reaction kinetics, and the corresponding rate constants (insert): (a, b) $[SMX]_0$ = 20 mg/L; (c, d) $[SMX]_0$ = 40 mg/L. Reaction Conditions: $[PMS]_0$ = 0.1 g/L, T = 20 °C, $[catalyst]_0$ = 0.2 g/L.

As known, reaction temperature is another key parameter for affecting the intra-particle diffusion as a higher temperature usually results in a faster movement of molecules. Apparently, Figure 4-9 (a) revealed that 2Co/MSCB2 (96.0%) performed the best catalytic performance within 60 min, in comparison to 2Co/MSCB0 (86.4%) and 2Co/MSCB1 (87.6%) when the reaction temperature increased from 20˚C to 50˚C for the degradation of SMX under the same reaction conditions. All catalysts showed increased catalytic activity as the activation energy for diffusion is lower at a higher temperature, according to Arrhenius equation [297].

$$D = D_0 exp\left(\frac{-E_A}{RT}\right) \qquad \textit{(Equation 4-1)}$$

where D denotes the diffusion coefficient (in m^2/s); D_0 is the prefactor of diffusion coefficient (in m^2/s); E_A is the activation energy for diffusion (in J/mol); R ≈ 8.31446 J/(mol·K) is the universal gas constant and T is the thermodynamic temperature (in K). The degradation efficiency of 2Co/MSCB0 and 2Co/MSCB1 is similar, which can be attributed to the thin skin layer (~70 μm) on the surface of the beads. Under this reaction condition, the rate constant of 2Co/MSCB2 is 1.62 times and 1.54 times of those of 2Co/MSCB0 and 2Co/MSCB1, respectively (Figure 4-9 (c)). Similarly, the degradation patterns of 2Co/MSCB2 followed a similar trend with the elevation of SMX concentrations to 40 mg/L (Figure 4-9 (d, e, f) and 50 mg/L (Figure A8 (c, d) at 50 ˚C. Overall, the experimental advantages of

this novel micro-structured catalyst substrate were investigated and verified by the PMS-activated AOPs reaction system.

Arrhenius law was applied to investigate the activation energy of 2Co/MSCB2 in the reaction system at three SMX concentrations.

$$k = Ae^{-\frac{E_A}{RT}} \qquad \textit{(Equation 4-2)}$$

Where A denotes the pre-exponential factors. The reaction activation energies (E_A) were calculated via linear fitting of ln*k* versus 1/T and were determined to be 38.52 kJ/mol, 21.09 kJ/mol, and 14.20 kJ/mol for SMX concentrations of 20 mg/L, 40 mg/L, and 50 mg/L, respectively. These results demonstrate that the reaction between SMX solutions and 2Co/MSCB2 occurs more easily as SMX concentration rises. Given that the E_A values for SMX were higher than that of diffusion-controlled reactions (10-13 kJ/mol) [298], it can be concluded that the degradation process is dominated by the chemical reaction rate at the solid-liquid interface. However, E_A for 50 mg/L SMX mineralization was nearly that of a diffusion-controlled reaction. This implies that increasing the SMX concentration further would lead to a diffusion-limited reaction, thereby enabling the structural advantages of this catalyst substrate more apparent. This will be explored in our future work.

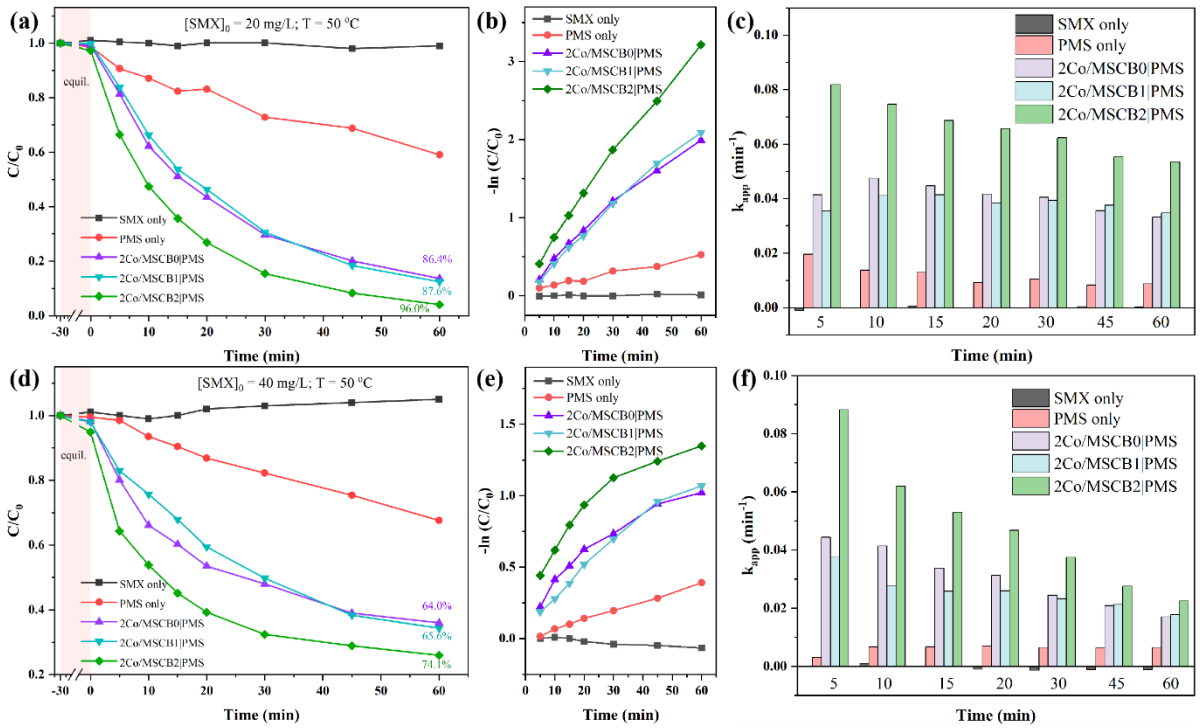

Figure 4-9 Degradation of different SMX concentrations at 50 °C, their reaction kinetics, and the corresponding rate constants (insert): (a, b) $[SMX]_0$ = 20 mg/L; (c, d) $[SMX]_0$ = 40 mg/L. Reaction Conditions: $[PMS]_0$ = 0.1 g/L,, T = 50 °C, $[catalyst]_0$ = 0.2 g/L.

In addition, the effect of Co_3O_4 loading and catalyst concentrations on SMX removal in Co/MSCBs|PMS system was further explored. As shown in Figure 4-10 (a), the SMX removal rate rose as the Co_3O_4 loading increased from 0.5 wt.% to 2 wt.%, which could be attributed to the increased of Co_3O_4 addition, resulting in more active sites for PMS activation. This, in turn, generated more accessible reactive radicals ($SO_4^{\cdot-}$, $^1O_2$, and $\cdot OH$) for the reaction. However, further increasing it to 5 wt.% led to a decline in SMX degradation efficiency, which could be attributed to the agglomeration of cobalt oxide, as supported by the SEM results in Figure A4 (h-i) and EDS mapping result of Co in the insert of Figure 4-10 (a). Herein, the brighter colour highlighted in the insert of Figure 4-10 (a) mirror the backscattered electron detector-compositional (BED-C) images depicted in Figure A4 (h-i), although conducting EDS mapping for micro-channels in the cross-section at high magnifications proved to be challenging due to the depth of these finger-like structures. It is worth noting that the colour of these beads changed from grey to dark as more cobalt oxide was loaded on them. The real Co_3O_4 content of all samples was investigated by ICP and is presented in Figure 4-10 (c). The disparity between the expected weight and the real weight is minimal. Besides, Figure 4-10 (b) shows that the SMX removal increased from 28.7% to 65.6% within 30 min with the catalyst dosage increase from 0.04 g/L to 1 g/L, thanks to more active sites. The leaching of cobalt ions in this reaction system was acceptable, as all catalytic systems showed cobalt leaching levels below 0.40 mg/L, which aligns with the published work [299].

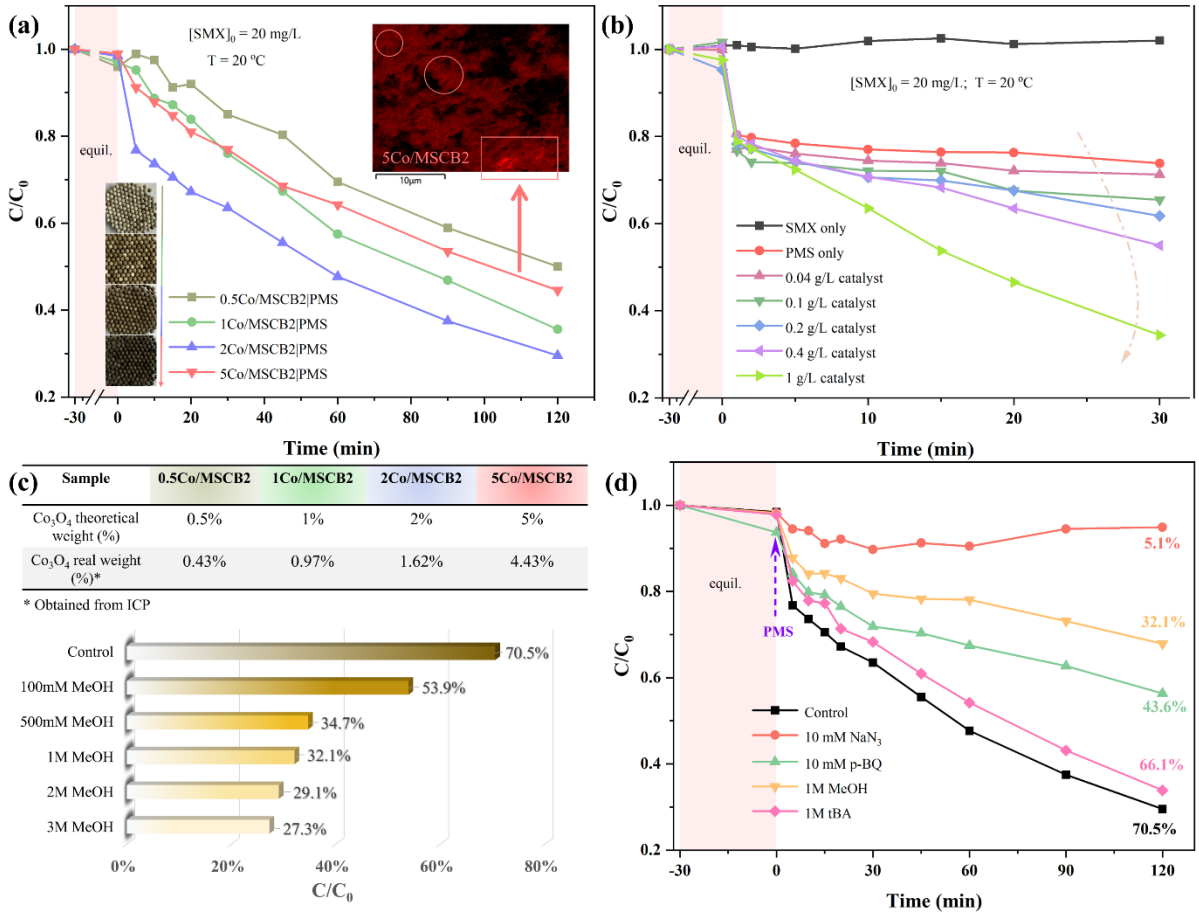

Figure 4-10 Degradation profiles of SMX with different (a) Co_3O_4 loading ([catalyst]$_0$ = 0.2 g/L) and (b) catalyst concentration (catalyst: 2Co/MSCB2). (c) Co_3O_4 theoretical content and real content obtained by ICP method, and quenching effect on SMX degradation efficiency under different MeOH addition. (d) Effect of quenching agents on SMX degradation (catalyst: 2Co/MSCB2). Reaction Conditions: [PMS]$_0$ = 0.1 g/L, [SMX]$_0$ = 20 mg/L, T = 20 ℃.

4.3 Possible catalytic reaction pathways and mechanism

In order to determine the main reactive species and their contributions to the 2Co/MSCB2|PMS system for SMX degradation, radical quenching experiments were carried out. Herein, certain amounts of NaN_3, p-BQ, methanol (MeOH) and tBA were introduced into the 2Co/MSCB2|PMS system for the degradation of SMX, as shown in Figure 4-10 (d). As known, NaN_3, p-BQ, and tBA could be acted as the scavenger for $^1O_2$, $\cdot O_2^-$, and ·OH, respectively, while MeOH is commonly used as a quencher of $SO_4^{\cdot-}$ and ·OH [300, 301]. When NaN_3 was introduced in the system, the SMX removal efficiency was significantly suppressed from 70.5% to 5.1%. Recent research by Wang`s group revealed that NaN_3 could directly interact with PMS and affect the removal efficiency of target contaminants [302]. It is also reported that another popular $^1O_2$ quencher, furfuryl (FFA), could react with $^1O_2$ and ·OH, and might also consume $SO_4^{\cdot-}$ during quenching tests [284]. Therefore, the depressed SMX degradation efficiency shown in Figure 4-10 (d) may not directly indicate that $^1O_2$ plays a dominant role in the

reaction system. Subsequent research will further examine the contribution of $^1O_2$ in the 2Co/MSCB2|PMS system. In contrast, the introduction of p-BQ and tBA caused a suppression of 26.9% and 4.4% for the degradation of SMX, demonstrating the partial contribution of $\cdot O_2^-$ and the negligible effect of ·OH, respectively. However, when MeOH was added, the degradation efficiency declined to 32.1%, leading to a 38.4% suppression of $SO_4^{\cdot-}$ and ·OH, ultimately resulting in a 34.0% reduction in $SO_4^{\cdot-}$ alone. Furthermore, as the methanol concentration rose from 100 mM to 500 mM, the inhibitory effect gradually intensified (Figure 4-10 (c)). Continuing to increase it to 1M, 2M and 3M led to limited alteration, with 27.3% degradation still occurring during the reaction. This indicated that the 2Co/MSCB2|PMS reaction system may follow radical and non-radical pathways.

In summary, due to the co-existence of radical pathway ($SO_4^{\cdot-}$, $\cdot O_2^-$, and ·OH) and non-radical pathway ($^1O_2$) in the 2Co/MSCB2|PMS system, a possible catalytic mechanism for the efficient degradation of SMX in the 2Co/MSCB2|PMS system was proposed in Figure 4-11. On the one hand, Co^{2+} on the surface of 2Co/MSCB2 could successfully be activated to generate $SO_4^{\cdot-}$, accompanying the formation of Co^{3+} (Equation 4-3). Simultaneously, the generated Co^{3+} can convert to Co^{2+} by reacting with $HSO_5^{\cdot-}$, resulting in the redox cycle of Co^{2+}/ Co^{3+} and the formation of $SO_5^{\cdot-}$ (Equation 4-4). As reaction proceeded, the generated $SO_4^{\cdot-}$ was partially transferred to ·OH (Equation 4-5), but it played a negligible role (4.4%) in this reaction system. At the same time, the produced $SO_5^{\cdot-}$ could be transformed to $SO_4^{\cdot-}$ (Equation 4-6). Moreover, some PMS reacted with ·OH to form $HO_2\cdot$, and $HO_2\cdot$ further self-decomposed to $\cdot O_2^-$ (Equations 4-7, 4-8). In the non-radical pathway, $^1O_2$ can be produced by the consumption of $\cdot O_2^-$ and ·OH (Equation 4-9). As per the synergistic interaction between radicals and non-radicals, the rapid regeneration of Co (II) was achieved, greatly enhanced the catalytic performance for PMS activation and SMX decomposition (Equation 4-10).

$$Co\ (II) + HSO_5^{\cdot-} \rightarrow Co\ (III) + SO_4^{\cdot-} + OH^- \quad \textit{(Equation 4-3)}$$

$$Co\ (III) + HSO_5^{\cdot-} \rightarrow Co\ (II) + SO_5^{\cdot-} + H^+ \quad \textit{(Equation 4-4)}$$

$$SO_4^{\cdot-} + OH^- \rightarrow \cdot OH + SO_4^{2-} \quad \textit{(Equation 4-5)}$$

$$SO_5^{\cdot-} + 2H_2O \rightarrow SO_4^{\cdot-} + \cdot OH \quad \textit{(Equation 4-6)}$$

$$HSO_5^{\cdot-} + \cdot OH \rightarrow HO_2\cdot \quad \textit{(Equation 4-7)}$$

$$HO_2\cdot \rightarrow H^+ + \cdot O_2^- \quad \textit{(Equation 4-8)}$$

$$\cdot O_2^- + \cdot OH \rightarrow {}^1O_2 + OH^- \quad \textit{(Equation 4-9)}$$

$$^1O_2/SO_4^{\cdot-}/\cdot O_2^-/\cdot OH/PMS + SMX \rightarrow intermediates + CO_2 + H_2O \quad \textit{(Equation 4-10)}$$

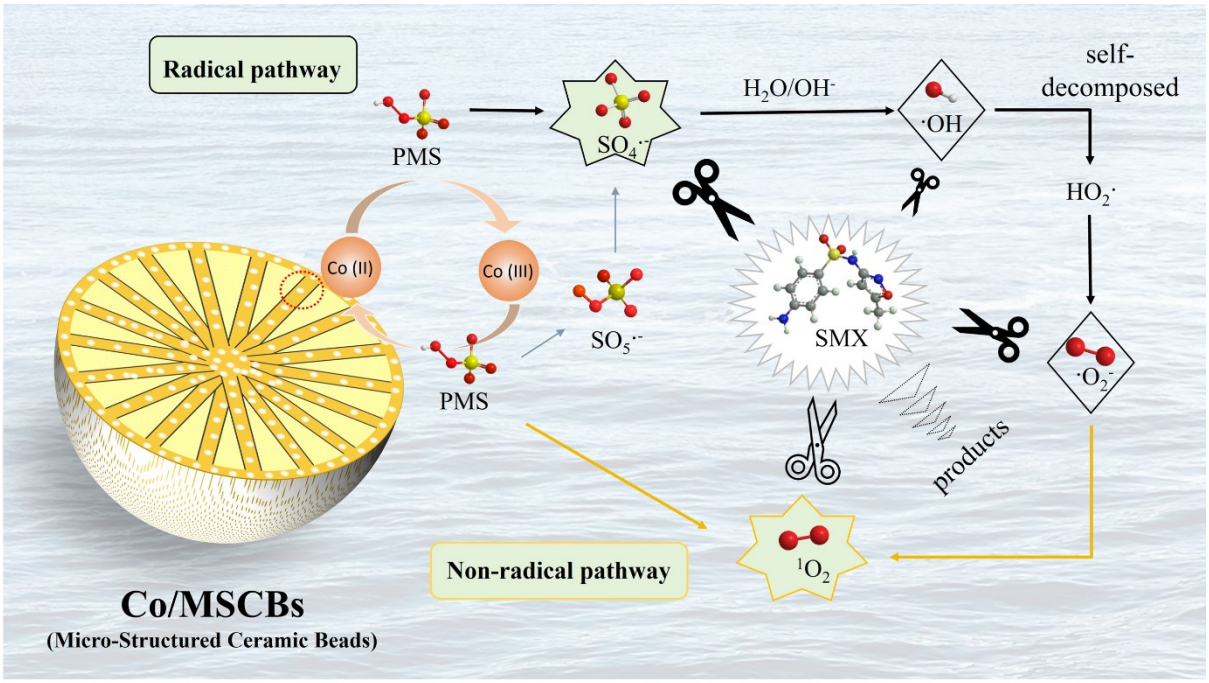

Figure 4-11 A proposed mechanism for catalytic oxidation of SMX by 2Co/MSCB2|PMS system.

4.4 Reusability and stability of 2Co/MSCB2

Reusability is crucial for commercial and practical applications of catalysts. Figure 4-12 shows the cyclic experimental results of the 2Co/MSCB2 for the SMX degradation with different regeneration methods under the same reaction conditions. As shown in Figure 4-12 (a), when the catalysts were separated from the liquid phase and washed with DI water only, the SMX degradation decreased from 70.5% to 63.5%, 53.3%, 46.7% and 40.5% within 120 min in the 2nd, 3rd, 4th, 5th run, respectively. This might be attributed to the adsorption of organic pollutants on the surface of catalysts, which reduced the amounts of exposed active sites, preventing the degradation of target organic pollutants, as evidenced by the SEM images (Figure 4-13 (g)). Most importantly, the SMX removal efficiency recovered instantly after regenerating the catalysts by post-sintering at 450 ˚C for 1 h (6th cycle). More than that, 94.7% of SMX was removed within 120 min in this cycle, surpassing the fresh one (70.5%) by a considerable margin. The regenerated catalysts were capable to achieve a similar removal efficiency (69.8%) with a reaction time of 45 minutes. However, the SMX removal efficiency fell back to its original level (59%) when the catalysts were continuously used for the subsequent cycle (7th). Likewise, this phenomenon recurred during the second (12th, 98.7% SMX removal in 120 min, 68.5% SMX removal in 30 min) and third regenerations (16th, 100% SMX removal in 120 min, 70.9% SMX removal in 20 min), underscoring its scientific rather than sporadic nature. To the best of our knowledge, this is the first time that used AOPs catalysts could demonstrate a much higher catalytic performance than the fresh one. Zhu et al. reported a novel MOF-derived CuO-Fe_3O_4@C catalyst for bisphenol A mineralization, and the reusability results exhibited a similar trend to this work before and after

regeneration [303]. Initially, the BPA removal efficiency was 100%, but it dropped to 41.5% after three consecutive cycles. When the catalyst was regenerated by washing and post-sintering, its performance immediately returned to 94.3% for the third cycle. This aligns with most previous research, where the reactivity and stability of catalysts technically exhibited a downward trend in the mineralization of antibiotic pollutants, although some studies demonstrated that catalysts retained high efficiencies comparable to the initial test over a few cycles [226, 266, 304]. These findings are still insufficient to verify their high cycling potential because of the continuous depletion of exposed active sites and the intrinsic properties of the catalyst powders. However, in this work, the unique catalyst substrate could facilitate the sustained exposure of accessible cobalt sites and reduce the intraparticle diffusion resistance over the long term. The major reason responsible for this was likely related to the larger and increased number of exposed open channels on the surface of the beads after post-sintering, as shown in Figure 4-13 (e). The interesting findings provide a new insight into the preparation of catalysts and/or catalyst substrates in the academic and industrial applications.

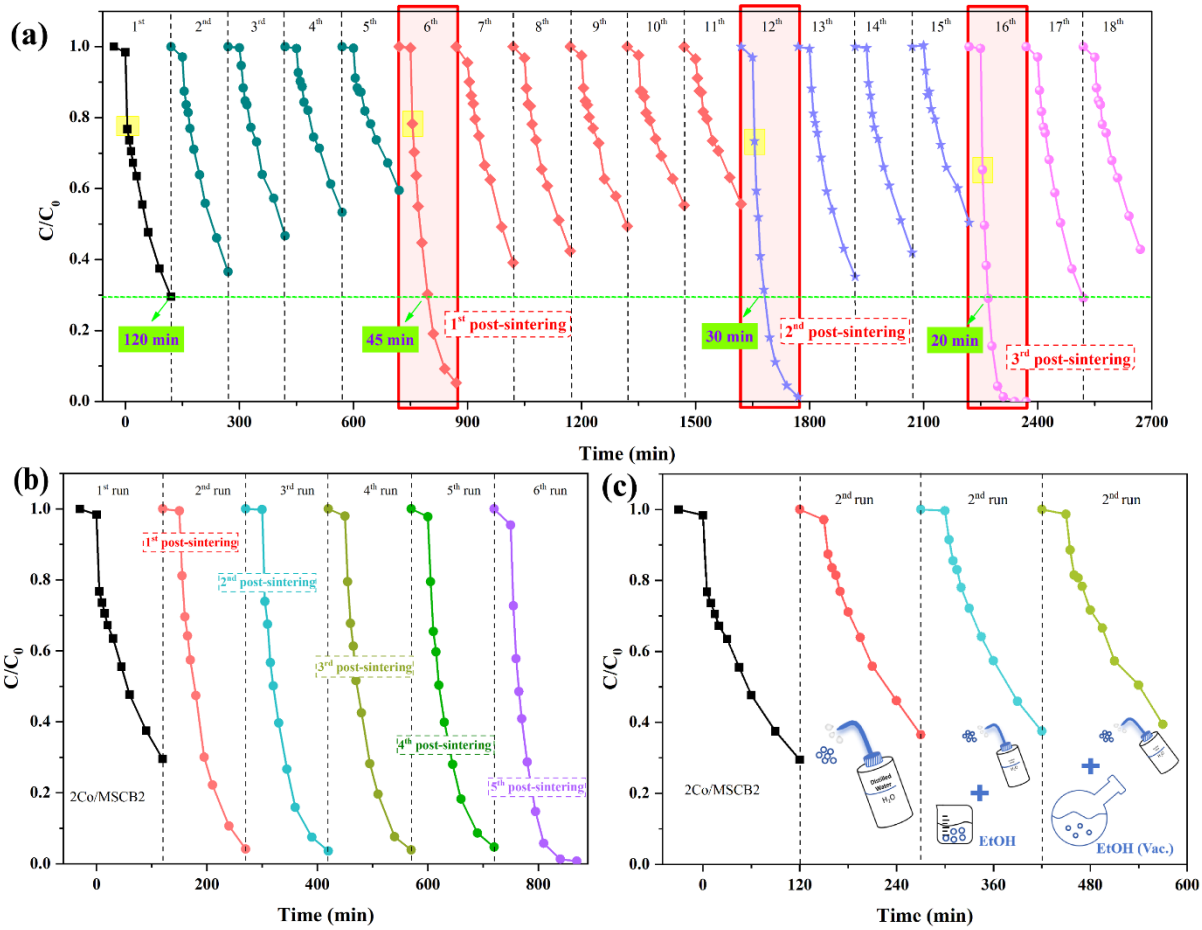

Figure 4-12 Recycling and reuse of the 2Co/MSCB2 for (a) 18 successive cycles with cleaning by DI water only (1st, 2nd, 3rd, 4th, 5th, 7th, 8th, 9th, 10th, 11th, 13th, 14th, 15th, 17th, 18th) or regenerating by sintering at 450 ˚C for 1h (6th, 12th, 16th), (b) 6 successive cycles with regenerating by post-sintering at 450 ˚C for 1h, and (c) two cycles with cleaning by different approaches. Reaction Conditions: $[PMS]_0$ = 0.1 g/L, $[catalyst]_0$ = 0.2 g/L, $[SMX]_0$ = 20 mg/L, T = 20 ˚C.

In order to verify the impact of this regeneration method, another set of catalysts was employed for the cyclic experiments. The used catalysts were subjected to post-sintering at 450 ˚C for 1 hour after each reaction, as illustrated in Figure 4-12 (b). Obviously, the SMX degradation efficiency enhanced gradually as the increased number of cycles, with SMX removal of 70.4%, 95.8%, 96.4%, 96.1%, 99.0%, and 99.3% for the 1st, 2nd, 3rd, 4th, 5th, and 6th cycle. This implies that post-sintering is a practical and efficient strategy for regenerating the used catalysts, thereby sustaining a notably improved degradation efficiency during continuous utilisations. Finally, Figure 4-12 (c) demonstrated that apart from regenerating catalysts through post-sintering, there was minimal distinction among alternative approaches (i.e., cleaning with DI water three times, rinsing with DI water three times and ethanol three times, washing with DI water three times followed by washing with ethanol under vacuum in the round-bottom flask three times).

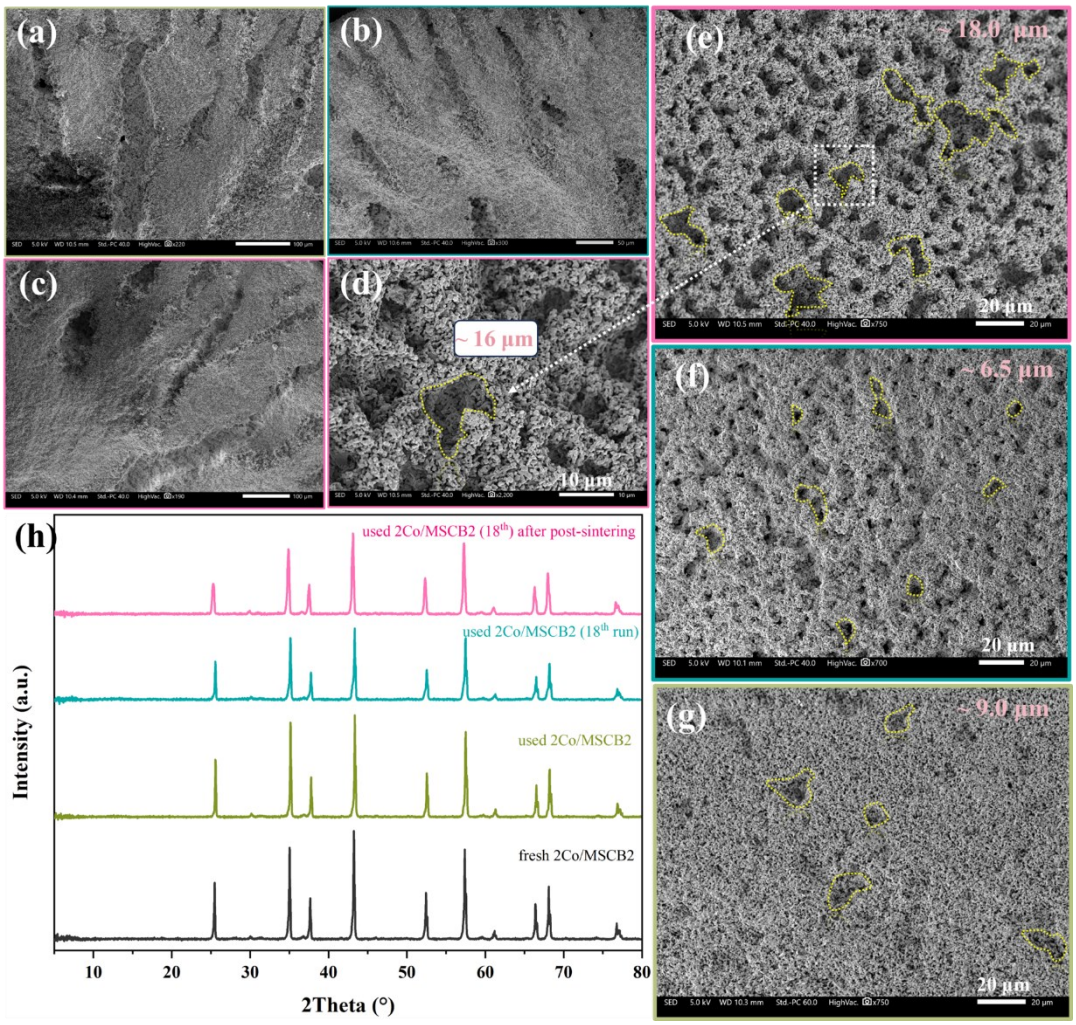

Figure 4-13 SEM images of cross-sectional view of 2Co/MSCB2 after recycled for (a) twice (used 2Co/MSCB2), (b) 18th (used 2Co/MSCB2 (18th run)), and (c) post sintering treatment after 18th cycles (used 2Co/MSCB2 (18th after post sintering)); SEM images of surface views of 2Co/MSCB2 after recycled for (g) twice, (f) 18th, and (d, e) post sintering treatment after 18th cycles; (h) XRD patterns of 2Co/MSCB2 before and after use.

Figure 4-13 depicts the XRD patterns and SEM images of fresh and used 2Co/MSCB2 samples. As shown in Figure 4-13 (h), no obvious changes of XRD diffraction patterns could be observed among samples before and after use for once, 18 times, and 18 times after being regenerated by post-sintering. This revealed that the catalyst and catalyst substrate had excellent stability, which is accord with the cyclic experimental results in Figure 4-12 (a). Additionally, with regard to the SEM morphologies among three samples after used, it is clear that although the cross-sectional view of these beads (Figure 4-13 (a-c)) did not undergo significant alterations, the sizes and number of open channels on the surface layer of beads (Figure 4-13 (e-g) boosted as the cyclic experiments increased. The increased openness of the surface could potentially be attributed to the removal of loosely packed alumina powders during thermal cycles. These powders were formed on the bead surface during the grinding processes and partially blocked some surface pores. Moreover, the post-sintering process facilitated the clearage of adsorbed reactants and products, which are difficult to be cleaned by DI water and/or methanol. This is in keeping with the previous findings in Figure 4-12 (c). As indicated in Figure 4-13 (g), most of the exposed open channels on the surface layer of used 2Co/MSCB2 have been adsorbed and blocked by the reactants and products, with only a small number of pores (approximately 9 μm in diameter) could be detected. However, when the catalyst was used for 18 times, more detectable pores with smaller sizes (~6.5 μm) could be identified in Figure 4-13 (f). This might be related to the exposure of inner layer of the bead surface after the active sites on the outer layer have been consumed during the reaction. Technically, when the phase inversion happens, the micro-channels commence near the surface region of the ceramic beads and progressively expand as they propagate, resulting in relative wider channels inside than that of the surface region [173]. Therefore, we can reasonably anticipate that with an increased number of cyclic experiments in this reaction system, there will be a further enhancement in catalytic performance owing to the more and larger exposed open channels. This aligns well with the efficacy of the MSCBs in reducing diffusional transfer resistance inside porous catalyst pellets. Furthermore, in contrast to the used 2Co/MSCB2 (18^{th} run) with partial blockage of the open channels, further post-sintering treatment contributed to the complete clearance of adsorbed organic pollutants and products. This explains the larger pores, i.e., approximately 18 μm, in Figure 4-13 (e) and Figure 4-13 (d) and boosted catalytic performance in Figure 4-12 (a). These findings represent a considerable breakthrough in the way of design catalyst substrates in catalytic reactions.

In contrast to conventional strategies, which focus on increasing the effective surface area of the nano catalysts or enhancing PMS activation through surface engineering of heterogeneous catalysts to expose more active sites and accessible surfaces, this work provided a new insight into improving the reactivity and stability of catalysts in PMS-activated cobalt-based AOPs systems. The large particle size of the 2Co/MSCB2 (3 mm in diameter), featuring distinctive radial micro-channels, can effectively address the long-standing challenge of balancing pressure drop and intra-particle diffusion in packed-bed reactors while also facilitating easy separation and recycling from the bulk fluid. Consequently, this

study highlights significant advancements in catalyst technology research and demonstrates considerable potential for both academic and industrial applications.

4.5 Conclusion

In summary, this chapter investigated the 2Co/MSCB*x*|AOPs reaction system for the degradation of different SMX solutions under mild reaction conditions, with key findings summarised below:

(1) Novel microchannel-structured alumina beads were successfully prepared for the first time by a simple phase-inversion and sintering-assisted method. Three different configurations of ceramic beads were analysed through various physiochemical techniques and employed for the catalytic oxidation of SMX in the PMS activated AOPs system. As expected, 2Co/MSCB2 exhibited the best degradation efficiency towards PMS activation as compared to 2Co/MSCB0 and 2Co/MSCB1, particularly when operating at higher SMX concentrations and higher reaction temperatures. The improved SMX removal efficiency could be attributed to the reduced diffusion resistance and abundant available active sites on the micro-channels inside the beads, which aligns with initial hypotheses, directly addressing the first research aim in Section 1.2.

(2) Reaction parameters including catalyst dosage, SMX concentration, reaction temperatures validate the advantage of this specific catalyst substrate configuration.

(3) More importantly, 2Co/MSCB2 after used and regenerated exhibited a significantly higher catalytic performance (16^{th} run, 70.83% in 20 min) than the fresh one (70.47% removal in 120 min), and this recurred when regenerating the catalysts by post-sintering at 450 ˚C for 1 h. This could be ascribed to the more and larger exposed open channels on the surface layer of micro-structured ceramic beads, which further reduced the intraparticle diffusion resistance in the AOPs reactions.

(4) Finally, the radical quenching experiment was conducted, and the catalytic mechanism of the radical and non-radical pathways associated with SMX degradation were explored.

These findings pave a foundation for further study on exploring material integration with auxiliary multifunction (Chapters 5 and 6) and the preparation of other microchannel-structured ceramic beads (Chapter 7).

Chapter 5 Innovative microchannel-structured alumina beads with enhanced specific surface area for intensifying SMX abatement inside microchannels

Building on Chapter 4, Chapter 5 introduces gamma-alumina mesoporous coating throughout the microchannel-structured beads using two impregnation methods. This aims to enhance the specific surface area, improve the distribution of the catalytic active phase, and intensify catalytic reactions within the microchannels.

A part of this chapter is presented in this paper:

Zheng, J, Wu, Z. Innovative microchannel-structured beads for microscale process intensification: A case study on water treatment for sulfamethoxazole abatement [J]. Chemical Engineering Journal, 504 (2025): 158527.

5.1 Introduction

Chapter 4 introduces novel microchannel-structured alumina beads (3 mm in diameter) with radial straight finger-like microchannels (20-100 μm in width) inside to decouple structural limitations of current catalyst design, i.e., trade-off between diffusional mass transfer and pressure drop of packed bed units. These unique beads can maintain a low pressure drop within a packed-bed reactor while simultaneously provide high geometrical surface areas. However, because these beads were engineered for industrial use, with consideration given to the mechanical strength of materials, so α-Al_2O_3 was chosen other than γ-Al_2O_3 despite its higher specific surface area. As noted, the weak mechanical strength of γ-Al_2O_3 can lead to rapid crumbling under intense loading. This produces dust and fragments that obstruct the spaces between pellets, resulting in a premature increase in bed pressure drop [166]. Due to the inherent small specific surface area of α-Al_2O_3, modifications are required to enhance its catalytic performance, i.e. increasing specific surface area for better distribution of catalytic phase of smaller size, and intensifying interactions with reactants.

In this chapter, γ-Al_2O_3 sol was prepared by a simple sol-gel method and washcoated onto the microchannels of microchannel-structured alumina beads (labelled as "MSCB2" in Chapter 4 but "AS0" in this chapter for simplicity) for the first time. The increased specific surface area of AS*x* samples will offer more accessible active sites for any diffusion-limited catalytic reactions. Two different catalyst impregnation methods, i.e., two-step (2Co/AS*x*) and one-step (2Co/AS*x* (co-imp.)) approaches, were investigated and the prepared samples were systematically characterised by a series of characterisation techniques, such as BET, SEM, XPS, etc. The structural advantages of these samples were validated in a PMS-activated AOPs reaction system for the degradation of SMX under mild reaction conditions.

Furthermore, the stability and reusability of samples were discussed to better meet with the industrial requirements. Finally, the active species involved in the 2Co/AS4|PMS reaction system were analysed through quenching experiment, and the catalytic mechanism of this reaction system was further proposed.

5.2 Materials and methods

5.2.1 Chemicals and materials

In this chapter, cobalt nitrate hexahydrate (Co $(NO_3)_2 \cdot 6H_2O$, 99%), methanol (HPLC grade, ≥ 99.8), and nitric acid (HNO_3, analytical reagent grade, 70%) were purchased from Fisher Scientific. Aluminium isopropoxide (AIP), Oxone® (PMS, $KHSO_5 \cdot 0.5KHSO_4 \cdot 0.5K_2SO_4$), SMX, p-benzoquinone (p-BQ, ≥ 98%), tert-butanol (tBA, ≥ 99.5%), sodium azide (NaN_3, ≥ 99.5%), and acetic acid (ReagentPlus®, ≥ 99%) were all obtained from Sigma-Aldrich. All chemicals were used as received without any further purification. Milli-Q water (18.3 MΩ cm at 25˚C) was used during the whole experimental process.

5.2.2 Preparation of γ-Al_2O_3-washcoated ceramic beads (ASx)

Microchannel-structured alumina beads of 3 mm in diameter were prepared by a phase-inversion and sintering-assisted method, as reported in our previous work (Chapter 4) [164]. After that, a sol-gel method [261] was used to prepare γ-Al_2O_3-washcoated alumina beads. Initially, 11.34 g of AIP was dissolved in 100 g of DI water to give a 1 M aqueous solution, and then a small amount of HNO_3 was added to the solution to maintain the pH of the suspension ~3.5. The suspension was refluxed and stirred vigorously at 85˚C for several hours until it transformed into a clear sol. The sol was then allowed to cool down to room temperature in preparation for wash-coating, where four different γ-Al_2O_3 sols were obtained by drying the cooled sol in an oven at 35˚C for 0 h, 8 h, 23 h, and 31 h, designated as sol 1, sol 2, sol 3, and sol 4, respectively, as per the aging time. The as-prepared sol was subsequently incorporated into the alumina beads (AS0) by immersing the beads into the sol under vacuum for 20 minutes. This degassing process would facilitate the infiltration of the sol into the micro-channels. Finally, the sol-gel γ-Al_2O_3 coated specimens were sintered at 500˚C in a muffle furnace for 1 hour. For simplicity, the specimens were denoted as AS1, AS2, AS3 and AS4, respectively. The increased mass of γ-Al_2O_3 sol coatings for each sample and surface area increment were summarised in Table 5-1.

Table 5-1 Weight increase and specific surface area increment of γ-Al_2O_3 wash-coated samples.

Sample	γ-Al_2O_3 sol aging time (h)	Mass before wash-coating (g)	Mass after wash-coating (g)	Wash-coated γ-Al_2O_3 (g)	γ-Al_2O_3 mass fraction (%)	Surface area increment fraction (%)
AS1	0	5.0107	5.1054	0.0947	1.90	72.5
AS2	8.5	5.0075	5.1712	0.1637	3.27	159.7
AS3	23	5.0089	5.2536	0.2447	4.89	363.7
AS4	31.5	5.0080	5.5049	0.4969	9.92	587.1

5.2.3 Preparation of Co-based catalysts (Co/ASx)

Cobalt oxide was incorporated throughout the beads by the incipient wetness impregnation method. Firstly, 0.74 g of cobalt nitrate hexahydrate was dissolved in 4.5 mL of DI water, and then added to 10 g of AS*x* beads, resulting in a Co_3O_4 to alumina bead weight ratio of 2 wt.%. Then, the catalyst precursor was dried and sintered at 450˚C for 3 h at heating and cooling rates of 5˚C /min, as shown in Figure 5-1. These catalysts were denoted as 2Co/AS*x*, where "*x*" refers to the γ-Al_2O_3 sol, as previously illustrated. In comparison, one-step co-impregnation method was applied to prepare samples 2Co/AS*x* (co-imp.). Specifically, after the preparation of γ-Al_2O_3 sol, 0.74 g of cobalt nitrate hexahydrate was mixed in 4 mL of γ-Al_2O_3 sols, and then 10 g of alumina beads (AS0) was added into the sols, being degassed under the vacuum for 20 minutes. Finally, the dried 2Co/AS*x* (co-imp.) was sintered at 450˚C for 3 hours. Rather than washcoating alumina beads in the prepared γ-Al_2O_3 sol, sintering, and then incorporating with cobalt precursors, this method could incorporate the entire catalyst onto the microchannel walls in one step.

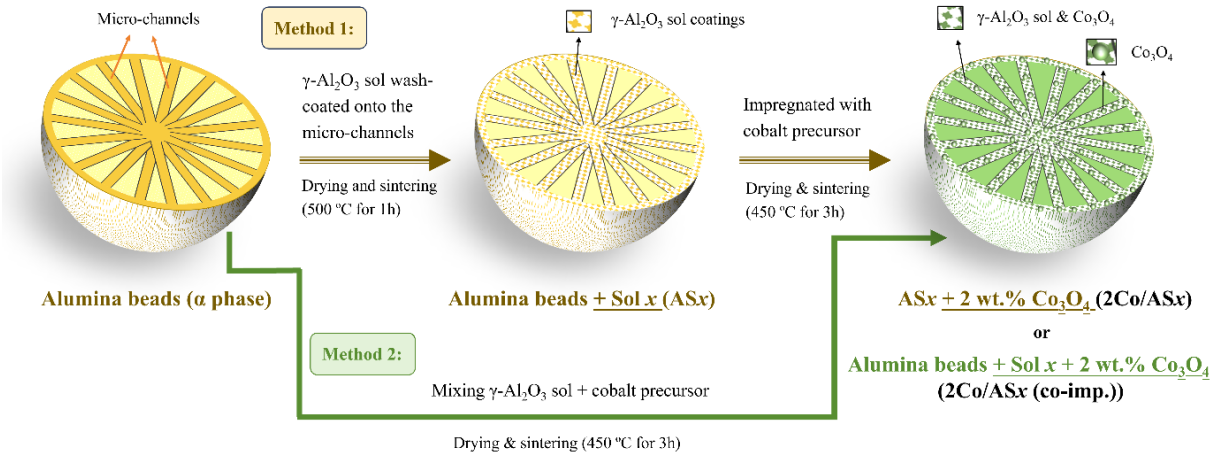

Figure 5-1 Diagrammatic representation of the γ-Al_2O_3 wash-coating process and catalyst integration

5.2.4 Characterisation and catalytic performance test

The physiochemical properties of AS*x*, 2Co/AS*x*, 2Co/AS*x* (co-imp.) samples were examined by a series of characterisations, including XRD, BET, XPS, SEM, and ICP. Details can be found in Section 3.2. Additionally, the catalytic performance of 2Co/AS*x* and 2Co/ASx (co-imp.) was evaluated for the degradation of SMX solutions in a PMS activated system. The experiments were carried out in a batch reactor in a water bath and connected with a mechanical overhead stirrer. Other detailed information can be found in Section 3.3.

5.3 Results and discussion

5.3.1 Phase compositions of ASx and 2Co/ASx

Four different γ-Al_2O_3 sol coatings were incorporated into the microchannel-structured alumina beads, and their XRD patterns in Figure 5-1 demonstrated that all diffraction peaks of samples before and after cobalt impregnation were well matched with the rhombohedral phase of α-Al_2O_3 referenced in JCPD file no. 88-0826 [283]. There are no characteristic peaks of γ-Al_2O_3 observed due to the low intensity of γ-Al_2O_3 phase compared to α-Al_2O_3. A slight shift of three main characteristic peak positions (Figure 5-1 (b) and (c)) for AS*x* samples might be linked to the presence of γ-Al_2O_3 [305]. No characteristic peaks of Co_3O_4 were detected in either 2Co/AS*x* or 2Co/AS*x* (co-imp.) samples, which can be ascribed to the low concentration and high dispersion of cobalt oxide. This aligns with our previous research [164] and will be further examined by the XPS result (Figure 5-3 (b)), ICP results (1.77 wt.% of Co for 2Co/AS4 and 1.74 wt.% of Co for 2Co/AS4 (co-imp.)), and BET results (Table 5-2).

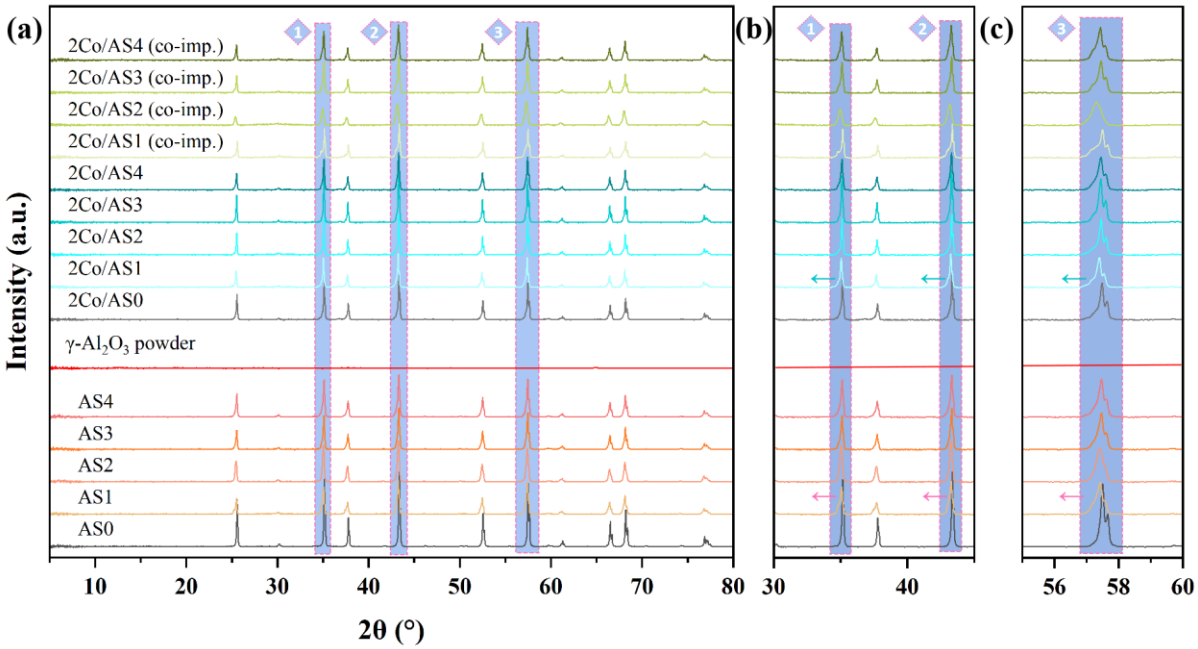

Figure 5-2 XRD patterns of ASx (innovative alumina beads before and after washcoating γ-Al_2O_3 sols), 2Co/ASx (ASx beads after cobalt impregnation via two-step sequential impregnation method), and 2Co/ASx (co-imp.) (ASx beads after cobalt impregnation via one-step co-impregnation method) samples.

Table 5-2 summarises the textual properties of γ-Al_2O_3 sol gel-washcoated alumina beads before and after cobalt impregnation using N_2 adsorption. By adding different γ-Al_2O_3 sols into the microchannel-structured alumina beads AS0, the surface areas of AS*x* samples gradually enhanced as the aging time for γ-Al_2O_3 sol increased, facilitating the dispersion and deposition of active components [306]. More γ-Al_2O_3 washcoatings for AS4 resulted in a much higher BET surface area (36.03 m^2/g), nearly 10 folds of the one without washcoating layers (AS0, 3.65 m^2/g). Meanwhile, the average pore diameter dropped slightly, accordingly, indicating the successful incorporation of γ-Al_2O_3. BET analysis of γ-Al_2O_3 powder synthesised by the sol gel method was also include for comparison, which possessed similar S_{BET} and D_p to the literature [307].

Table 5-2 Textural properties of γ-Al_2O_3 sol-washcoated alumina beads (ASx) before and after cobalt impregnation.

Sample	S_{BET} (m^2/g)	V_T (cc/g)	D_p (nm)
AS0	3.65	0.01	14.82
AS1	7.49	0.02	9.45
AS2	9.40	0.02	9.97
AS3	13.98	0.03	7.55
AS4	36.03	0.05	5.78

γ-Al_2O_3 (sol-gel)	202.00	0.21	4.24
2Co/AS1	6.31	0.02	13.52
2Co/AS2	7.65	0.02	11.93
2Co/AS3	12.45	0.04	13.19
2Co/AS4	21.05	0.05	9.29
2Co/AS1 (co-imp.)	10.69	0.03	10.14
2Co/AS2 (co-imp.)	9.16	0.02	9.23
2Co/AS3 (co-imp.)	10.43	0.02	8.76
2Co/AS4 (co-imp.)	14.47	0.04	9.81

S_{BET}: surface area; V_T: Total pore volume; D_P: Average pore diameter.

After cobalt deposition, four samples prepared using the two-step method (2Co/AS*x*) experienced a slight reduction in surface area, whereas the four samples prepared by the one-step method (2Co/AS*x* (co-imp.)) displayed a similar surface area (~10 m^2/g) for samples 2Co/AS1-3 (co-imp.). As for the highest surface areas for each method, 2Co/AS4 (co-imp.) (14.47 m^2/g) showed a lower value than 2Co/AS4 (21.05 m^2/g). This might be attributed to two reasons. On the one hand, the different thermal treatment methods for 2Co/AS*x* and 2Co/AS*x* (co-imp.) might result in different material properties. In this work, 2Co/AS*x* underwent two calcination processes (500˚C and 450˚C for the formation of γ-Al_2O_3 and Co_3O_4, respectively), whilst 2Co/AS*x* (co-imp.) experienced merely one (450˚C). Researchers have reported that the calcination processes would lead to different specific surface area of the γ-Al_2O_3 washcoat [183, 262]. However, 450˚C was normally used as the calcination temperature to transform Co $(NO_3)_2 \cdot 6H_2O$ into Co_3O_4 [281, 307, 308]. Further increasing the sintering temperature might result in the formation of $CoAl_2O_4$ due to the strong interaction between Co_3O_4 and γ-Al_2O_3 [307, 309, 310], as confirmed by the XRD results and colour change of Co/γ-Al_2O_3 pellets sintered at different temperatures (Figure A9). On the other hand, when the catalytically active component, i.e. cobalt-based precursor, was mixed with the prepared γ-Al_2O_3 sol prior to the washcoating procedure, the rheological properties of the washcoated layer might be greatly influenced [183, 311], affecting the specific surface areas accordingly.

XPS spectra of 2Co/AS0 and 2Co/AS4 were measured to verify the presence of Co element and the chemical state of 2Co/AS*x* samples. As shown in Figure 5-3 (a), the XPS survey spectra confirmed the presence of elements Al, O, C and Co in both samples. The C 1s spectra for both samples centred at 284.8 eV belong to adventitious carbon, which originated from the carbon grid during sample preparation process [312]. The Co 2p spectra revealed that cobalt existed in two chemical states (Co^{3+}, Co^{2+}) in both 2Co/AS0 and 2Co/AS4, corresponding to the compositions of Co_3O_4. Additionally, the shift of binding energy from 2Co/AS0 (780.0 eV) to 2Co/AS4 (780.3 eV), lower intensity of Co 2p

spectrum but relatively higher intensity of cobalt satellite peaks (786.6 eV and 803.8 eV) in 2Co/AS4 could be attributed to the presence of γ-Al_2O_3, which is consistent with the BET results (Table 5-2) [292, 293]. Likewise, the existence of γ-Al_2O_3 sol coatings in 2Co/AS4 resulted in higher intensities of the O 1s spectrum (Figure 5-3 (d)), and Al 2p spectrum (Figure 5-3 (c)) as well as the disappearance of extremely weak peak centred at 75.3 eV in 2Co/AS0, which was associated with the formation of small amounts of aluminium suboxide during the cobalt impregnation process [164, 287, 288].

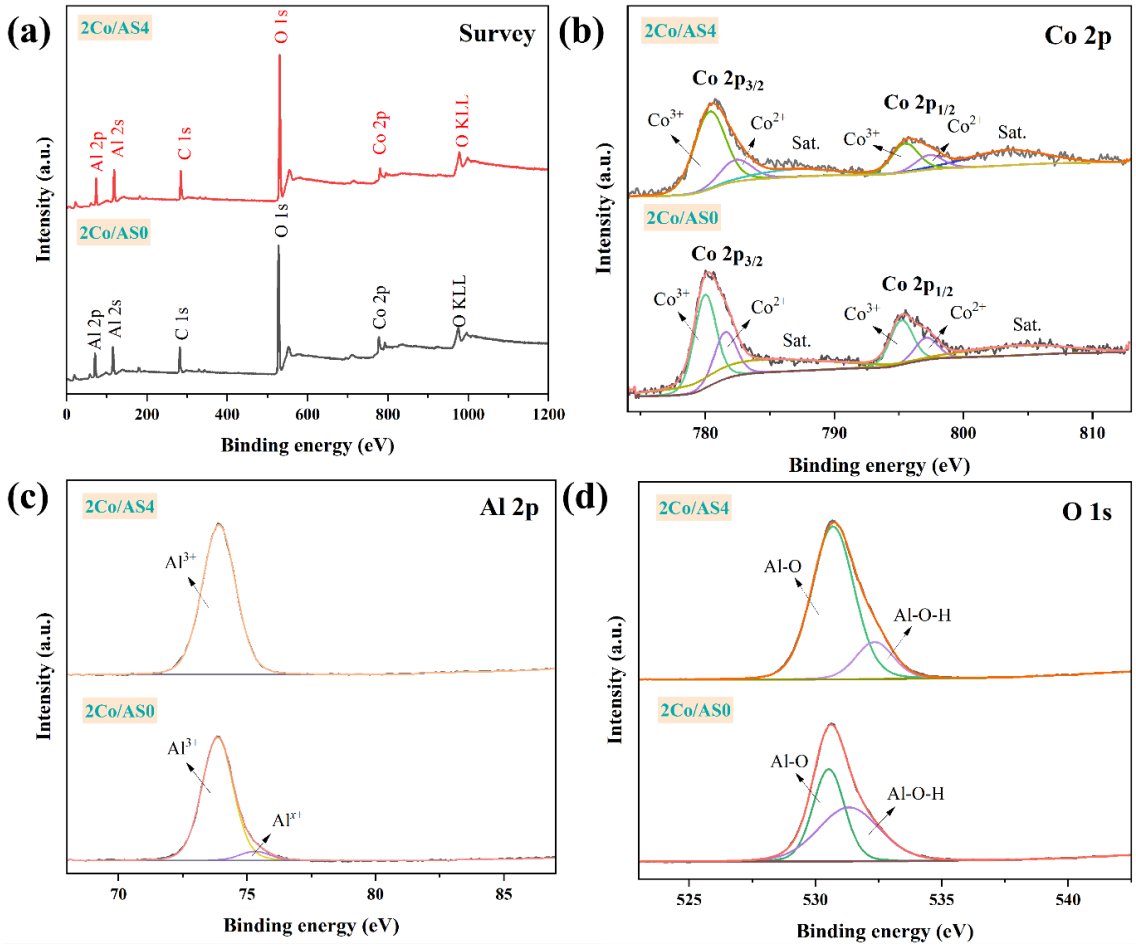

Figure 5-3 (a) XPS survey spectra and high-resolution XPS spectra of (b) Co 2p, (c) Al 2p and (d) O 1s of cobalt-impregnated microchannel-structured alumina beads before (2Co/AS0) and after γ-Al_2O_3 washcoatings (2Co/AS4).

5.3.2 Morphology of AS*x* samples before and after cobalt incorporation

SEM images of both the cross-sectional and surface views of microchannel-structured alumina beads without (AS0) and with γ-Al_2O_3 sol washcoatings (AS*x*) are depicted in Figure 5-4. Before conducting SEM analysis, these beads were halved by a knife to expose their cross-sections. Figure 5-4 (a-e) and Figure 5-4 (a_2-e_2) presented the cross-section of AS*x* samples with radial microchannels, which consist of irregularly packed granules sized at approximately 400 nm. As the amount of γ-Al_2O_3 coatings

increased, the average width of radial microchannels decreased accordingly, with 85.59 μm, 81.92 μm, 74.62 μm, 56.98 μm, and 54.03 μm measured for AS0, AS1, AS2, AS3 and AS4, respectively. All measurements were performed from the half radii of the beads, i.e., the 1/4 region of the beads' diameter, to ensure consistency. Different from the loosely packed granular structures of α-Al_2O_3 at the inner surface of microchannels in AS0 (Figure 5-4 (a_2)), γ-Al_2O_3 with a smooth and flat surface, marked by yellow dashed frames, could be observed in the enlarged SEM images of AS1-4 samples (Figure 5-4 (b_2-e_2)). With further increased the loadings of γ-Al_2O_3 sol, the number of this thin coating layer gradually grew with the increase of γ-Al_2O_3 sol aging time. This aligns with the BET results aforementioned in Table 5-2 and SEM images of γ-Al_2O_3 powder in Figure 5-4 (f, f_2). Furthermore, gamma-Al_2O_3 inside the microchannels did not cover and block the opening ends of oriented microchannels, and even the sample with the highest γ-Al_2O_3 sol loadings (AS4) remained unblocked. As shown in Figure 5-4 (a_3, a_4), before washcoating with γ-Al_2O_3 sol, the surface of the sample AS0 exhibited numerous small open channels, with an average pore size of 6.02 μm. The introduction of γ-Al_2O_3 did not change the pristine morphologies of alumina beads, but some open channels were partially blocked by γ-Al_2O_3 coatings. This might potentially increase the mass transport resistance when over-loaded with the γ-Al_2O_3 washcoatings. It is worth noting that there were no significant changes on the overall average pore sizes of open channels for AS*x* samples, although large amounts of γ-Al_2O_3 coatings could be observed on the surface layer of AS4. In certain areas, γ-Al_2O_3 nanoparticles partially obstructed the open channels, similar to samples AS1-3, with the average pore size in these regions being 4.42 μm (Figure 5-4 (e_4)). In contrast, γ-Al_2O_3 washcoatings accumulated into large submicron flakes in some areas, yet substantial cracks (Figure 5-4 (e_3)) and exposed pores (Figure 5-4 (f_3, f_3)) with an average size of 4.35 μm pertained.

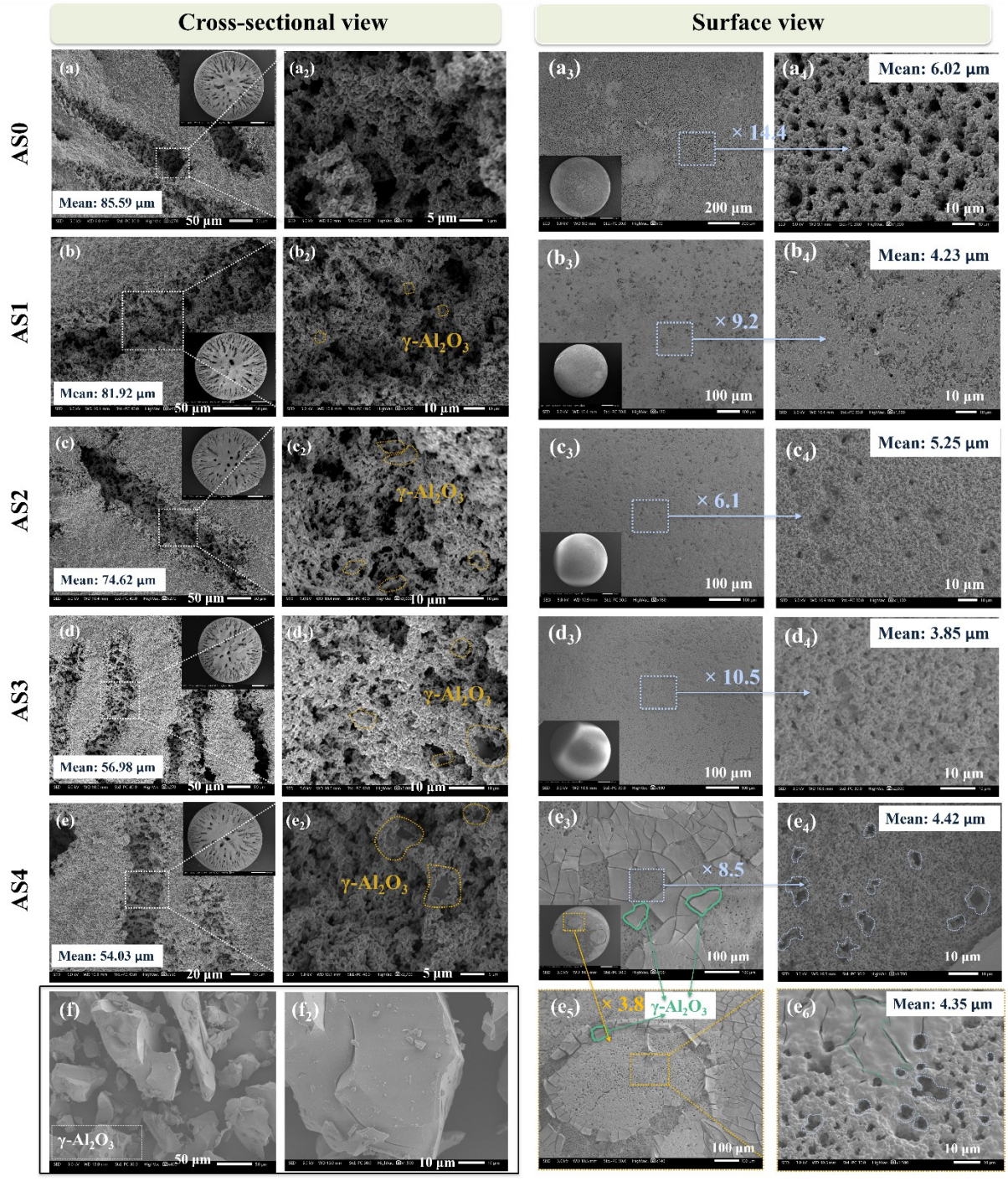

Figure 5-4 SEM images of the cross-sectional views of (a, a_2) microchannel-structured alumina beads (AS0), microchannel-structured alumina beads modified with (b, b_2) γ-Al_2O_3 sol 1(AS1), (c, c_2) γ-Al_2O_3 sol 2 (AS2), (d, d_2) γ-Al_2O_3 sol 3 (AS3), and (e, e_2) γ-Al_2O_3 sol 4 (AS4); the surface views of (a_3, a_4) AS0, (b_3, b_4) AS1, (c_3, c_4) AS2, (d_3, d_4) AS3, and (e_3, e_4, e_5, e_6) AS4; (f, f_2) SEM images of γ-Al_2O_3 powder.

Figure 5-5 displayed the SEM images of AS4 samples after incorporating 2 wt.% Co_3O_4 by two-step sequential impregnation method (2Co/AS4) and one-step co-impregnation method (2Co/AS4 (co-imp.)). Apparently, the introduction of Co_3O_4 did not alter the pristine morphologies of both alumina beads. Figure 5-5 (b, b_2) and Figure 5-5 (d, d_2) demonstrated that all finger-like microchannels for these

two samples remained and no catalyst agglomerations could be found in the cross-section. The surface views of 2Co/AS4 in Figure 5-5 (a, a_2, a_3) displayed a relative coarse texture, with an average exposed open channel size of 8.16 µm. In contrast, Figure 5-5 (c, c_2, c_3) illustrated that the surface of 2Co/AS4 (co-imp.) was coated with small γ-Al_2O_3 submicron flakes, of which the sizes of flakes and exposed open channels were 20 µm and 8.01 µm, respectively. Details regarding other 2Co/AS*x* and 2Co/AS*x* (co-imp.) samples are provided in the supplementary information (Text A2-2, Fig. A10).

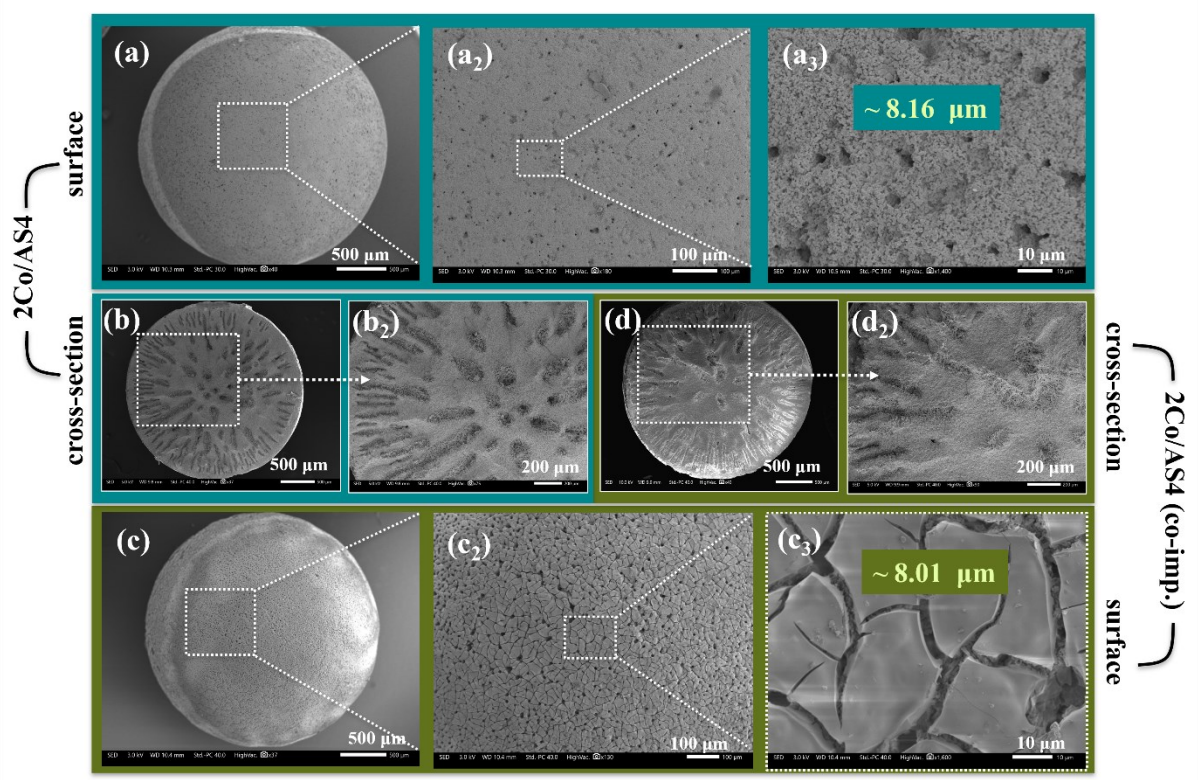

Figure 5-5 SEM images of (a, a_2, a_3) the surface views of 2Co/AS4, (b, b_2) cross-sectional views of 2Co/AS4, (c, c_2, c_3) the surface views of 2Co-AS4 (co-imp.), and (d, d_2) the cross-sectional views of 2Co-AS4 (co-imp.).

5.3.3 Evaluation of the catalytic performance

Based on the above characterisation results, innovative microchannel-structured alumina beads with enhanced specific surface area have been successfully prepared and cobalt-based catalysts have been deposited on the beads. If their catalytic performance proves remarkable, it would be critically important and advantageous for microscale process intensification. The catalytic efficiency of two types of cobalt-based AS*x* samples was investigated by degrading SMX solutions (10 mg/L, 20 mg/L, 40 mg/L) at different reaction temperatures (20˚C, 40˚C) in a PMS-activated AOPs system, as shown in Figure 5-6, Figure 5-7, and Figure A12.

Figure 5-6 displays the degradation of different SMX concentrations at 20˚C, comparing the sample before washcoating with γ-Al_2O_3 sol (2Co/AS0) to six samples that were washcoated by two different methods (2Co/AS*x* and 2Co/AS*x* (co-imp.)). The self-degradation of SMX for all reaction conditions (SMX concentrations, reaction temperatures) in this work was all negligible (< 0.1 %). As shown in Figure 5-6 (a), when the initial SMX concentration was 10 mg/L, PMS alone could degrade 32.58% of SMX, which is comparable to the research with a similar PMS dosage [313]. While the SMX removal efficiency was greatly improved using 2Co/AS0 (90.56%). Additionally, all samples with enhanced surface area could completely remove SMX in 120 minutes, and 2Co/AS4 (co-imp.) could degrade 100% SMX within 45 minutes. The removal efficiency for SMX in 2Co/AS*x* system witnessed a gradually increased performance as the increase of γ-Al_2O_3 sol loadings, i.e., increased specific surface area, with 2Co/AS1 (78.53%) < 2Co/AS2 (87.01%) < 2Co/AS3 (98.37%) < 2Co/AS4 (100%) within 60 min, respectively. In contrast, the catalytic activity of two 2Co/AS*x* (co-imp.) samples was also investigated, following the trend 2Co/AS2 (co-imp.) (95.01%) < 2Co/AS4 (co-imp.) (100%) within 60 min. Under this reaction condition, 2Co/AS*x* (co-imp.) samples exhibited higher catalytic performance than those in 2Co/AS*x*, probably due to the high dispersion of cobalt-based catalysts and larger open channel sizes on the surface, as shown in Figure A10. Likewise, the reaction kinetics (Figure A12 (a)) and the corresponding rate constants (Figure 5-6 (b), Figure A12 (b)) were consistent with the degradation performance. Therefore, the enhanced catalytic performance and improved utilization efficiency of volumetric productivity of 2Co/AS*x* and 2Co/AS*x* (co-imp.) samples validate the potential of these materials for the process intensification at microscale.

Moreover, when the SMX concentration increased to 20 mg/L, the degradation efficiency displayed a comparable scenario, as shown in Figure 5-6 (c-d) and Figure A12 (c-d). Nevertheless, as the SMX concentrations increased to 40 mg/L (Figure 5-6 (e)), the reaction rate for 2Co/AS4 (co-imp.) was lower than 2Co/AS*x* samples before 120 min, which could be ascribed to the partial blockage of some regions in 2Co/AS*x* (co-imp.) by γ-Al_2O_3 submicron flakes (Figure 5-5 (c_2)). These flakes resulted in less effective interactions between SMX molecules and active sites, thereby impeding the rapid diffusion of reactants and products, particularly at higher concentrations of organic pollutants [22]. As shown in Figure A9 (d-f), the surfaces of samples prepared by method 2 were more easily obstructed, with the blocked regions increasing progressively from 2Co/AS1 (co-imp.) to 2Co/AS4 (co-imp.). Additionally, the disparity for SMX removal efficiency between the sample before (2Co/AS0) and after washcoating (2Co/AS*x*) decreased, with 59.02%, 64.75%, 70.14%, 74.84%, 74.86%, and 75.00% for 2Co/AS0, 2Co/AS1, 2Co/AS2, 2Co/AS3, 2Co/AS4, and 2Co/AS4 (co-imp.), respectively. This indicated that there is a balance between the BET surface area and the intraparticle diffusion (e.g., open channels sizes on the bead surface) at high concentrations of organic pollutants. At higher SMX concentrations, more reactants from the bulk solution are required to diffuse into the alumina beads for the catalytic reaction, but the γ-Al_2O_3 washcoating films on the surface impaired their ability for intraparticle diffusion.

Consequently, the rate constants for 2Co/AS4 and 2Co/AS4 (co-imp.) decreased from being 2.58 times and 3.72 times higher than 2Co/AS0 at 20 mg/L SMX to 1.55 times and 1.57 times higher at 40 mg/L SMX, respectively, as shown in Figure 5-6 (d) and Figure 5-6 (f). This is consistent with the previously published catalytic performance results, where thicker wash-coating layers led to an increase in light-off temperature, despite the large BET areas [22].

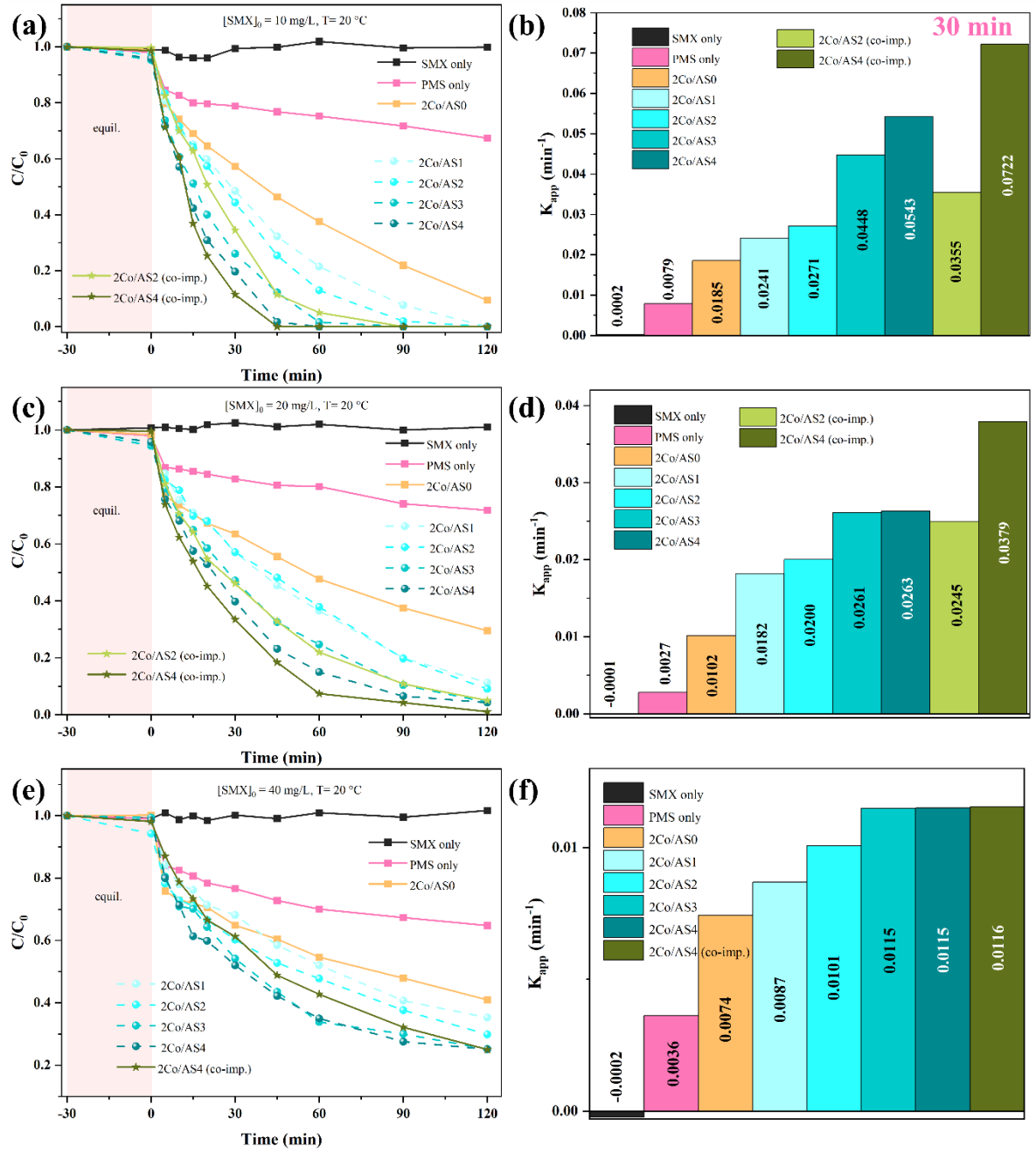

Figure 5-6 Degradation of different SMX concentrations at 20 ˚C and the corresponding rate constants: (a, b) $[SMX]_0$ = 10 mg/L; (c, d) $[SMX]_0$ = 20 mg/L; (e, f) $[SMX]_0$ = 40 mg/L. Reaction Conditions: $[PMS]_0$ = 0.1 g/L, T = 20 ˚C, $[catalyst]_0$ = 0.2 g/L, r = 150 rpm.

Reaction temperature is a key parameter influencing the intra-particle diffusion, as a higher temperature usually results in a faster movement of molecules. Figure 5-7 revealed that at 40 ˚C, SMX degraded more easily under 2Co/AS*x* and 2Co/AS4 (co-imp.) systems, in comparison to 2Co/AS0. At the beginning stage, such as 5 min, the SMX degradation efficiency (Figure 5-7 (a)) reached 24.47%, 44.69%, 53.24%, 58.03%, 67.54%, and 70.65% for 2Co/AS0, 2Co/AS1, 2Co/AS2, 2Co/AS3, 2Co/AS4, and 2Co/AS4 (co-imp.), respectively. Similarly, Figure 5-7 (c) depicted that the rate constants of 2Co/AS4 and 2Co/AS4 (co-imp.) at 5 min were 4.01 times and 4.37 times than that of 2Co/AS0. Apparently, at high reaction temperatures, the diffusion coefficient escalated, implying that the diffusion resistance for γ-Al_2O_3-loaded samples was less significant than at low temperatures; On the contrary, the surface area and dispersion of cobalt oxides had a greater impact on the catalytic performance. As the reaction continued, such as the rate constants of 120 min in Figure 5-7 (d), this disparity gradually diminished because the concentration gradient of the contaminants between external and internal surfaces of the catalyst support decreased.

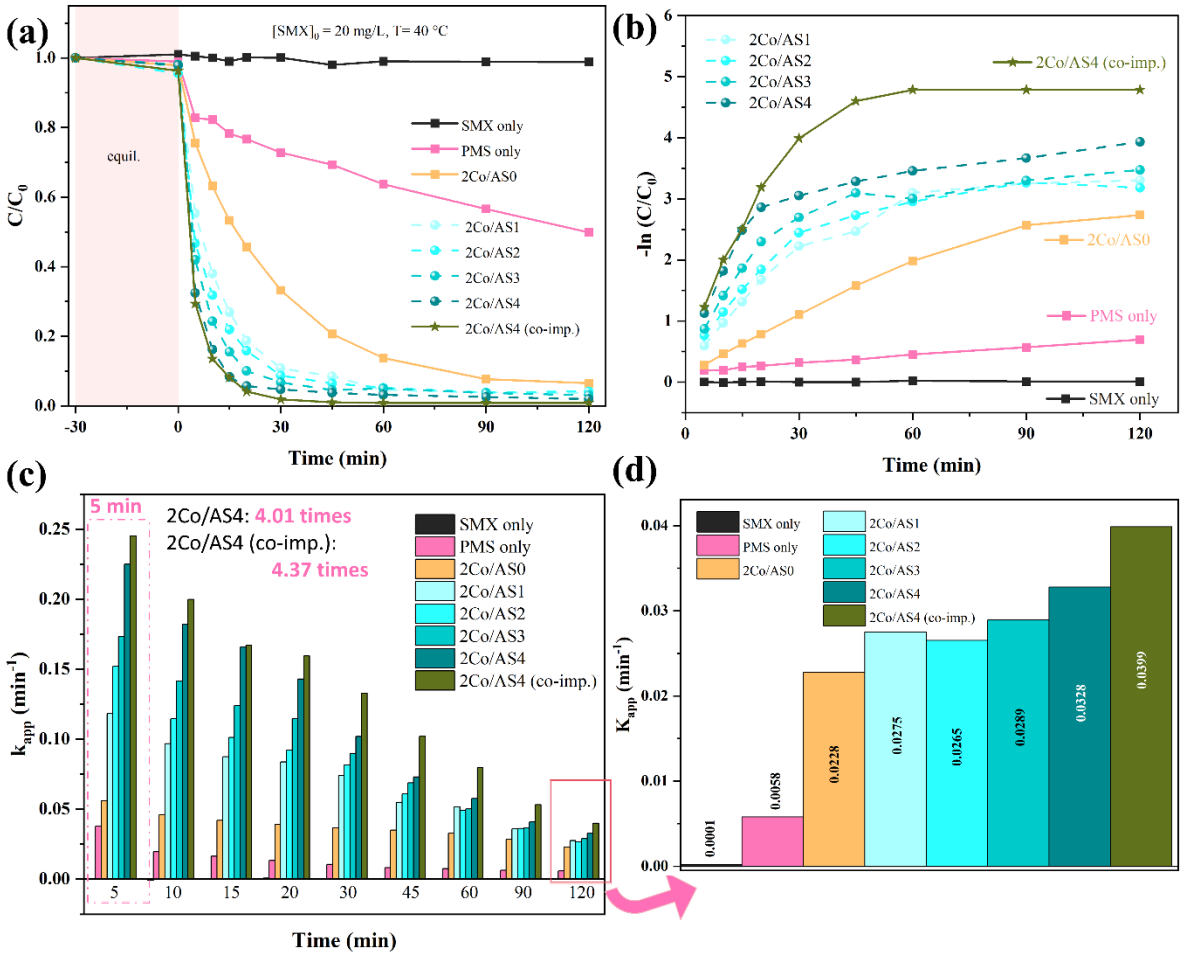

Figure 5-7 (a) Degradation of 20 mg/L SMX at 40 ˚C, (b) their reaction kinetics, and (c, d) the corresponding rate constants. Reaction Conditions: $[PMS]_0$ = 0.1 g/L, T = 20 ˚C, $[catalyst]_0$ = 0.2 g/L, r = 150 rpm.

In short, all innovative microchannel-structured alumina beads after modification, whether synthesised using two-step sequential impregnation method or one-step co-impregnation method, demonstrated significantly enhanced catalytic performance for SMX abatement. As noted, this result is vital for advancing the PI technology. Although some research has explored PI at the process unit level, such as employing ceramic foam structures [19, 138] and honeycomb monoliths [20, 21] as catalyst supports to potentially balance mass transfer and pressure drop, it has also been reported that the external mass transfer coefficients for conventional uniform beads (1.5 mm, 3 mm), honeycombs (400 CPSI) and ceramic foams (20 PPI), 45 PPI) are ranked in the following order: 1.5 mm beads >> 45 PPI foams > 20 PPI foams ≈ 3.3 mm beads > 400 CPSI honeycombs [24]. Therefore, on the one hand, this work addressed the long-standing challenge of balancing mass transfer and pressure drop by creating innovative finger-like microchannels in beads with millimetre-scale diameter. The external mass transfer coefficient of this novel 3 mm beads (AS0) would be significantly higher than that of 3 mm conventional uniform bead, and even more so when compared to ceramic foams. On the other hand, AS*x* samples, with their increased specific surface area of the base substrates, could better disperse and deposit active components, leading to more efficient catalytic reaction simultaneously in microscale process intensification.

5.3.4 Possible catalytic reaction pathways and mechanism

To understand the contributions of possibly generated reactive species to the 2Co/AS4 reaction system for SMX degradation, entrapping experiments were carried out. Herein, NaN_3 (5 mM), p-benzoquinone (p-BQ, 5 mM), methanol (MeOH, 1M) and tert-butanol (tBA, 1M) were introduced into the system to capture $^1O_2$, $\cdot O_2^-$, $SO_4^{\cdot-}$/·OH, and ·OH, respectively [300, 314]. As shown in Figure 5-8, when NaN_3 was introduced to the system, the SMX removal efficiency was significantly suppressed from 95.75% to 8.45%. Recent research revealed that two most common quenches, NaN_3 and furfuryl, could both consume either PMS or $^1O_2$/·OH, affecting the removal efficiency of target contaminants [315]. Therefore, the depressed SMX degradation efficiency by adding NaN_3 may not directly reflect the dominant role of $^1O_2$ in the reaction system. Subsequent research will be conducted to explore the contribution of $^1O_2$. In contrast, the addition of p-BQ and tBA provoked the partial inhibition of 35.85% and 1.37% for the degradation of SMX, demonstrating a relatively minor role of $\cdot O_2^-$ and the negligible effect of ·OH, respectively. However, when MeOH was added, the degradation efficiency fell into decline rapidly (31.17%), leading to a 64.58% suppression of $SO_4^{\cdot-}$ and ·OH, ultimately resulting in a 63.21% reduction in $SO_4^{\cdot-}$ alone, suggesting that $SO_4^{\cdot-}$ played a key role in the process.

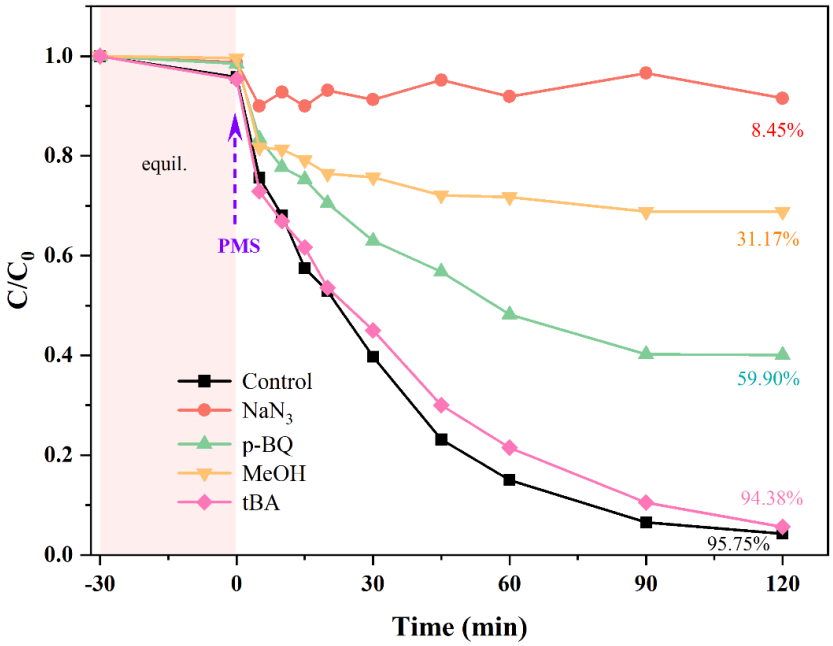

Figure 5-8 Effect of quenching agents on SMX degradation (catalyst: 2Co/AS4). Reaction Conditions: $[PMS]_0$ = 0.1 g/L, $[SMX]_0$ = 20 mg/L, T = 20 ˚C, $[catalyst]_0$ = 0.2 g/L, r = 150 rpm.

Based on the above analysis and experimental results, a possible activation mechanism of AOPs over 2Co/AS4 for the efficient degradation of SMX was speculated in Figure 5-9. In the metal oxide/PMS system, the breakdown of O-O bond in PMS (HSO_5^-) by receiving electrons from M^{n+} typically triggers the generation of $SO_4^{\cdot-}$ and ·OH, where M represents metals such as Co, Fe, Cu, etc., and n indicates different valence states [316]. When PMS was introduced, Co^{2+} on the surface of 2Co/AS4 initially activated PMS directly to generate $SO_4^{\cdot-}$ and Co^{3+} (Equation 4-3). Simultaneously, the produced Co^{3+} could react with PMS to convert back to Co^{2+}, thereby establishing a redox cycle between Co^{2+} and Co^{3+}, along with the formation of SO_5^- (Equation 4-4). This process may be accompanied by the generation of non-radical $^1O_2$ (Equation 4-9). As reaction proceed, some of the $SO_4^{\cdot-}$ radicals transformed to ·OH (Equation 4-5) and then $\cdot O_2^-$ (Equations 4-7, 4-8), while some $SO_4^{\cdot-}$ reacted with PMS to further be transformed to $SO_5^{\cdot-}$ (Equation 5-1), which continues to react with H_2O to form $^1O_2$ (Equation 5-2). Consequently, the primary ROS ($SO_4^{\cdot-}$) and secondary ROS ($\cdot O_2^-$, $^1O_2$) contributed to the catalytic SMX abasement by breaking it down into smaller molecules, eventually fully mineralising it into CO_2 and H_2O (Equation 4-10).

$$SO_4^{\cdot-} + HSO_5^{\cdot-} \rightarrow SO_5^{\cdot-} + HSO_4^- \quad \textit{(Equation 5-1)}$$

$$2SO_5^{\cdot-} + H_2O \rightarrow 1.5\ {}^1O_2 + 2HSO_4^- \quad \textit{(Equation 5-2)}$$

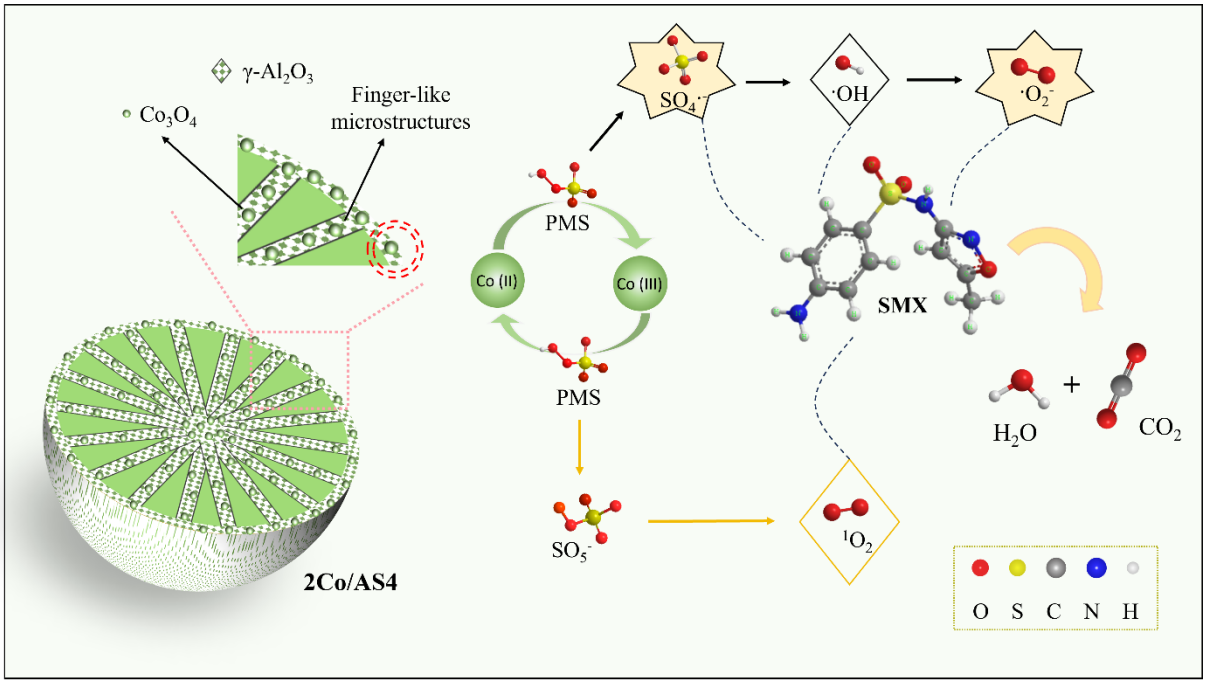

Figure 5-9 A proposed mechanism for catalytic oxidation of SMX by 2Co/AS4|PMS system.

5.3.5 Reusability and stability of 2Co/AS4

The practical application of catalysts, particularly the microchannel-structured ceramic beads designed for industrial use in this study, also depends heavily on their reusability and stability. Herein, 2Co/AS4 was typically selected to degrade SMX for successive 16 runs. After each run, the beads were collected by simplying pouring out the aqueous solution and then rinsed with deionised water. Before 5th, 9th, and 13th run, the beads were further regenerated by sintering at 450˚C for 1 hour to remove the residue reactants and products adsorbed. As shown in Figure 5-10, the sample exhibited superior reusability, with SMX removal efficiency maintained at 95.75%, 88.86%, 86.07%, and 85.17% within 120 min for the 1st, 2nd, 3rd, and 4th run, respectively, when the sample was only reinsed with DI water. The minor reduction could be ascribed to the coverage of surface active sites by reactants and products during the degradation process, as evidenced by the SEM images in Figure 5-12 (a_2, a_3). Most importantly, the regenerated sample, after sintering, demonstrated a significantly enhanced SMX removal efficiency (100%), even exceeding that of the fresh sample (95.75%). This enhancement also reflected in being able to achieve a comparble removal efficiency (96.28%) within a reaction time of just 30 min. Likewise, this phenomenon recurred during the second (9th, 100%) and third (13th, 100%) regenerations, whereas almost all studies have reported a downward trend due to the continueous depletion of exposed active sites and intrinsic nature of catalyst powders [300, 317]. As far as we know, aside from our recent publication [164], this is the another instance where catalytic efficiency not only remained stable for reusability test but actually further improved as the cycling experiments progressed. In addition, the

XRD patterns of the used samples (Figure 5-11 (c)), whether used for once or 16 times, showed similar patterns without significant variation before and after reaction. This indicates the exceptional stability of the catalysts and catalyst supports throught the catalytic process.

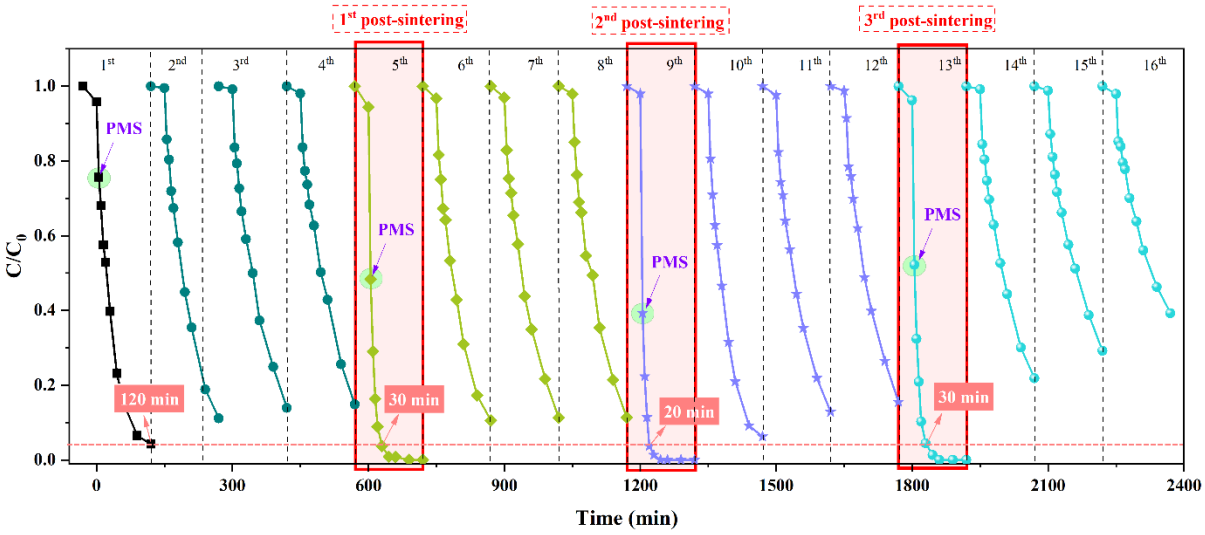

Figure 5-10 Reusability of the sample 2Co/AS4 on the degradation of SMX for 16 successive cycles with being cleaned by DI water only (1st, 2nd, 3rd, 4th, 6th, 7th, 8th, 10th, 11th, 12th, 14th, 15th 16th) or being regenerated by post-sintering at 450 ˚C for 1h (5th, 9th, 13th). Reaction Conditions: [PMS]$_0$ = 0.1 g/L, [SMX]$_0$ = 20 mg/L, T = 20 ˚C, [catalyst]$_0$ = 0.2 g/L, r = 150 rpm.

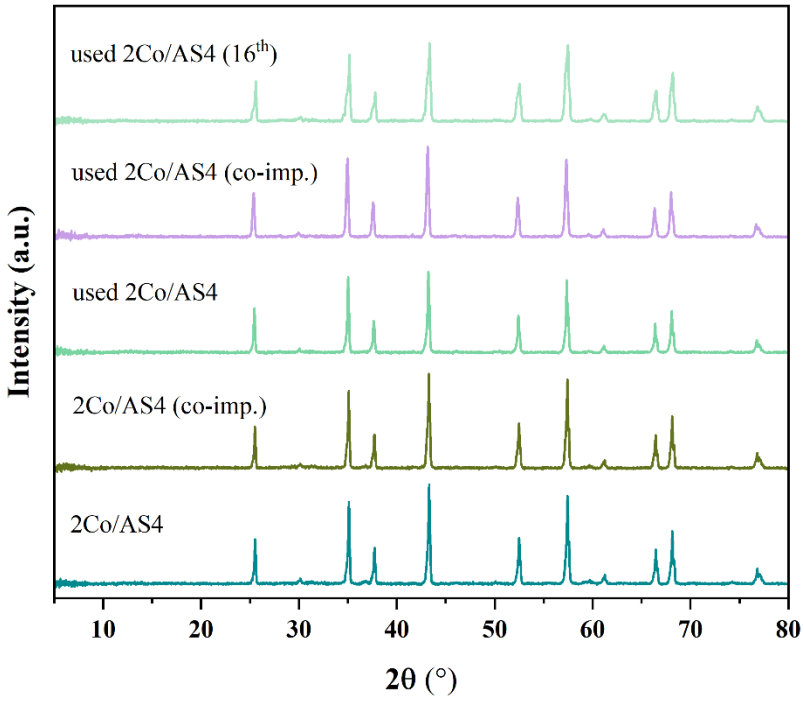

Figure 5-11 XRD patterns of 2Co/AS4 before and after reaction.

In order to explore the reasons behind the improved SMX removal efficiency, Figure 5-12 depicts the morphologies of the used samples at different magnifications. As illustrated in Figure 5-12 (a, a_2, a_3), the surface of the used 2Co/AS4 for once was partially blocked by adsorbed reactants and products after reaction, and for other unblocked open channels, the average size was approximately 7.14 μm. The shapes of the microchannels inside in Figure 5-12 (a_4, a_5) showed no obvious changes, except for a brighter colour, which might be due to the adsorbed pollutants. This is consistent with the slight decrease of catalytic SMX removal efficiency. Similarly, used 2Co/AS4 after 16th run in Figure 5-12 (b, b_2, b_3) had a similar obstructed phenomenon and relatively smaller open channels sizes (6.99 μm). However, when the used sample 2Co/AS4 after 16th run was regenerated by post-sintering (Figure 5-12 ((c, c_2, c_3)), more detectable exposed open channels could be observed, with a mean pore size of 6.77 μm. The post-sintering process facilitated the clearage of adsorbed reactants and products, which are challenging to cleaned with DI water. Meanwhile, the size of these open channels increased compared to the ones before (Figure 5-4 (e_4, e_6), ~ 4.4 μm) and after cobalt loading (Figure 5-5 (a_3), ~ 5.82 μm). This might be linked to the removal of loosely packed alumina powders from the bead surface during the post-sintering treatment, which aligns with the reusability test result for 2Co/AS0 reported in previous studies [164]. Interestingly, the size of the exposed open channels in this work after the post-sintering procedure (~ 6.77 μm) is smaller than that of 2Co/AS0 reported in the literature (~ 18 μm) [164]. This indicates that modifying AS0 with γ-Al_2O_3 sol may also enhance the stability of the catalyst supports during the catalytic reaction process, leading to reduced loss of loosely packed alumina powders. Overall, the synergistic effects of having more and larger exposed open channels in this work contributed to intraparticle diffusion, significantly enhancing the catalytic performance of SMX degradation.

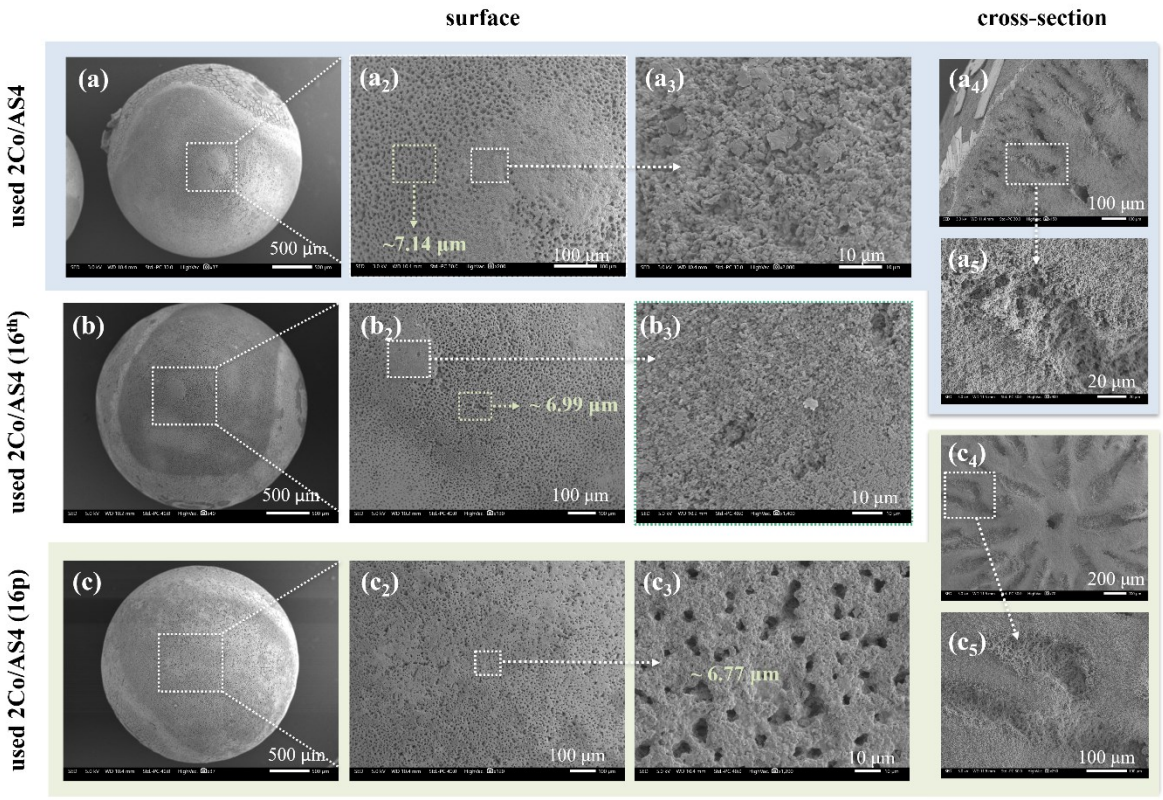

Figure 5-12 SEM images of (a, a_2, a_3) the surface views and (a_4, a_5) cross-sectional views of the used 2Co/AS4; (b, b_2, b_3) the surface views of the used 2Co/AS4 for 16 times; (c, c_2, c_3) the surface views and (c_4, c_5) cross-sectional views of the used 2Co/AS4 for 16 times after regeneration.

5.4 Conclusion

In this chapter, novel microchannel-structured alumina beads (AS0) with enhanced specific surface area (AS*x*) were prepared by phase-inversion and sol-gel methods and were investigated for intensifying diffusional mass transfer via the reaction the catalytic degradation of SMX in the PMS-activated system, with key findings summarised below:

(1) The improved surface area was achieved by washcoating a thin layer of γ-Al_2O_3 sol onto the inner surface of the microchannels within the alumina beads. SEM images revealed a well-defined finger-like microstructures within the alumina beads and confirmed the presence of γ-Al_2O_3 on both the surface of the alumina beads and the inner surfaces of the microchannels inside.

(2) Cobalt oxide was successfully incorporated onto the beads by two approaches: two-step sequential impregnation method (2Co/AS*x*) and one-step co-impregnation method (2Co/AS*x* (co-imp.)). As expected, the degradation efficiency of samples prepared by these two methods improved with the rise in surface area due to the increased accessible active sites. However, 2Co/AS*x* (co-imp.) exhibited higher catalytic activity than 2Co/AS*x*. This might be attributed

to the high dispersion of cobalt oxide and the larger exposed open channels on the bead surface, which facilitated intraparticle diffusion. It is noteworthy that samples 2Co/AS*x* (co-imp.) were more easily blocked by γ-Al_2O_3 granules at high γ-Al_2O_3 sol loadings, such as sol 4 in this study, and exhibited similar open channel sizes compared to 2Co/AS4. This might be the main reason behind the lower catalytic activity at high SMX concentrations (40 mg/L) than 2Co/AS4. The enhancement of the catalytic performance of 2Co/AS*x* and 2Co/AS*x* (co-imp.) samples well align with the second research aim in Section 1.2.

(3) It is unusual that after being used and regenerated, 2Co/AS4 demonstrated substantially higher catalytic performance (96.32% in 20 min) than the fresh catalyst (95.75% in 120 min). This enhancement was consistently observed when the catalysts were regenerated by post-sintering at 450 ˚C for 1 h, which could be attributed to the relatively increased number and size of exposed open channels on the surface of 2Co/AS4, which further reduced the intraparticle diffusion resistance in the AOP reactions.

We believe that the transferable advantages demonstrated in this work can advance the development of a broad spectrum of heterogeneous catalysis for efficient and durable catalytic reactions, including process intensification at the microscale level, benefiting both academia and industry.

Chapter 6 Innovative Microchannel-Structured Alumina Beads Modified by Functionalised Carbon Xerogel for the Degradation of Organic Pollutants

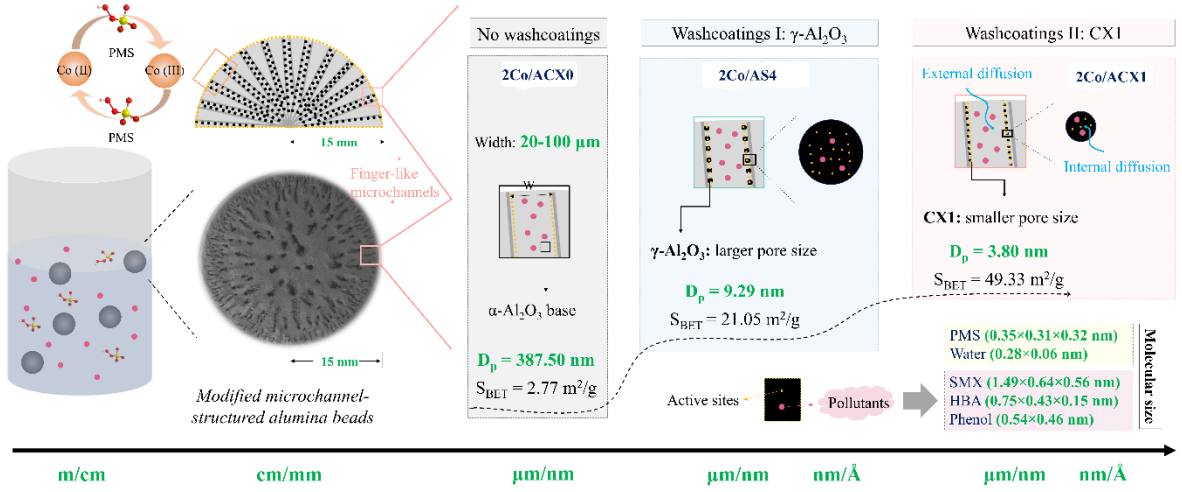

Building on Chapters 4 and 5, Chapter 6 incorporates carbon xerogels as a more advanced mesoporous coating material into the microchannel-structured beads. To elevate the material research beyond the previous chapters, the carbon-based mesoporous material is expected to further intensify the reaction by reducing the dimensions of the Co-based catalyst, promoting better catalyst distribution, and enhancing adsorption. This should lead to greater SMX abatement performance compared to the previous chapters, further highlighting the potential of the microchannel-structured beads in intensifying diffusional mass transfer and integrating with different functional materials.

A part of this chapter is presented in this paper:

J. Zheng, F. García-García, Y. Yang, K. Li, T. Bridgwater, H. Yang, Z. Wu*. Carbon xerogel-enhanced microchannel-structured beads for organic pollutants degradation: A novel catalyst for synergistic microscale process intensification [J]. Applied Catalysis B: Environment and Energy, 366 (2025): 125069.

6.1 Introduction

Chapter 4 demonstrated innovative alumina beads featuring both large pores (micrometre-sized microchannels) and small pores (nanometre-sized clusters of alumina granules), with large pores reducing the mass transfer resistance by prompt transportation of large molecules, and small pores contributing to dispersing catalytic active phase. Given the limitations of its relatively small specific surface area due to the intrinsic nature of alpha-phase alumina, **Chapter 5** introduces gamma-phase alumina as wahcoatings to enhance the SSA of these beads and confirmed its feasibility. This provides

a solid foundation for exploring alternative mesoporous materials, such as carbon materials, which offer significantly higher SSA and additional functionalities compared to γ-Al_2O_3, to fulfil their potential for diverse applications in the future. As noted in **Chapter 5**, AS*x* samples experienced blockage on the surface layer of alumina beads when excessive γ-Al_2O_3 sols were applied, which hindered the growth of gamma-Al_2O_3 sol and thereby limited any additional increase in surface area.

Carbonaceous materials with high specific surface area, such as activated carbons [318, 319], graphene [320], carbon nanotubes [321], and carbon xerogels (CXs) [318, 322], have been widely used as functional catalyst supports for adsorption, hydrogenation, oxidation, ammonia decomposition, etc.. Cheap and porous carbon xerogels are a new type of nanocarbons, which offer large SSA, high purity, and tuneable textual and structural properties [264, 318]. Furthermore, carbon xerogels can be produced using the conventional sol-gel method [318, 323], which facilitates the incorporation of a thin CX washcoat layer into the ceramic beads. Therefore, carbon xerogels were applied as the functional washcoating material within the microchannel-structured ceramic beads in this chapter.

The decontamination of organic pollutants in PMS-activated AOPs was used as the model reaction system, validating the transferable material and microstructural advantages of this design. In AOPs, carbon materials also exhibited remarkable adsorption capacity [322, 324] and carbon materials with oxygen-containing functional groups, particularly C═O, were favourable to PMS activation [325-327], potentially contributing to a synergistic effect towards AOPs reactions. This would streamline multiple operational units/equipment and process tasks into a single multifunctional alumina bead, fulfilling another crucial principle of the PI technology [18, 328], thereby achieving synergistic process intensification at microscale process unit.

As a result, PMS-activated AOPs will be applied as the model reaction system in this chapter to validate the micro-structural advantages of novel modified microchannel-structured alumina beads (ACX*x*). For comparison, base microchannel-structured alumina beads (ACX0, equal to MSCB2 in Chapter 4 and AS0 in Chapter 5) and modified microchannel-structured alumina beads with the most commonly used washcoat, γ-Al_2O_3, namely AS4 in Chapter 5, were also applied. After incorporating with cobalt-based catalyst (2Co/ACX*x*), we will systematically investigate the influences of the specific surface area, washcoating properties (carbon xerogels and γ-Al_2O_3), sulfamethoxazole concentrations (10 mg/L, 20 mg/L, 40 mg/L), reaction temperatures (20˚C, 30˚C, 40˚C), catalyst dosage, and organic pollutant types - type I: PPCPs (sulfamethoxazole); type II: phenols (4-hydroxybenzoic acid and phenol); type III: dyes (methyl orange) - on the catalytic performance. Furthermore, we will examine the catalytic mechanism of 2Co/ACX*x*|PMS system, as well as its stability and reusability.

6.2 Experimental

6.2.1 Chemicals and materials

Resorcinol (ACS reagent, ≥ 99%), formaldehyde (ACS reagent, 37 wt.% sol.), sodium carbonate (BioXtra, ≥ 99%), Oxone® (PMS, $KHSO_5 \cdot 0.5KHSO_4 \cdot 0.5K_2SO_4$), SMX, 4-hydroxybenzoic acid (p-HBA), phenol, p-benzoquinone (p-BQ, ≥ 98%), tert-butanol (tBA, ≥ 99.5%), sodium azide (NaN_3, ≥ 99.5%), methyl orange (MO, ACS reagent), and acetic acid (ReagentPlus®, ≥ 99%) were all obtained from Sigma-Aldrich. Cobalt nitrate hexahydrate ($Co(NO_3)_2 \cdot 6H_2O$, 99 % pure), methanol (HPLC grade, ≥ 99.8%), and nitric acid (HNO_3, analytical reagent grade, 70%) were purchased from Fisher Scientific. All chemicals were used as received without any further purification. Milli-Q water (18.3 MΩ cm at 25˚C) was used during the whole experimental process.

6.2.2 Preparation of carbon xerogel-based alumina beads (ACX*x*)

Microchannel-structured alumina beads (ACX0) of 3 mm in diameter were synthesised by a phase-inversion and sintering-assisted method, as reported in our previous work [279]. Prior to the dip coating process, carbon xerogels, labelled as CX, were prepared by a conventional sol-gel method [318]. Specifically, a precursor solution of resorcinol (R), formaldehyde (F) and sodium carbonate (C) with molar ratios of R/C = 200 and R/F = 0.5 were stirred for 30 min. The starting solution was named as CX1, and then it was mixed with DI water to produce the rest of CX*x* sols and *x* hereafter refers to the CX solution concentrations. The volume ratios of starting solution (CX1) to the top up DI water for CX2, CX3 and CX4 were set as 4:1, 4:2, and 4:3, respectively.

Afterwards, the microchannel-structured alumina beads were immersed in the four CX*x* sol solutions for 10 min, then dried at 65˚C for 20 min in a rotavapor (Buchi), and gelated at 100˚C in an oven overnight. The dried samples were then sintered at 800˚C for 1 h in a nitrogen atmosphere with a heating rate of 5˚C/min to carbonize the carbon xerogel gels in the beads. The prepared CX*x*-based alumina beads were labelled as ACX*x* (*x* = 0, 1, 2, 3, 4). The schematic diagram of the synthesis of ACXx samples was presented in Fig. 6-1. For comparison, CX powder was prepared using the same approach without the addition of alumina beads; Another sample AS4 prepared by the sol-gel method [261] with surface area between ACX0 and ACX*x* samples (same as the one used in Chapter 5), was also included for reference.

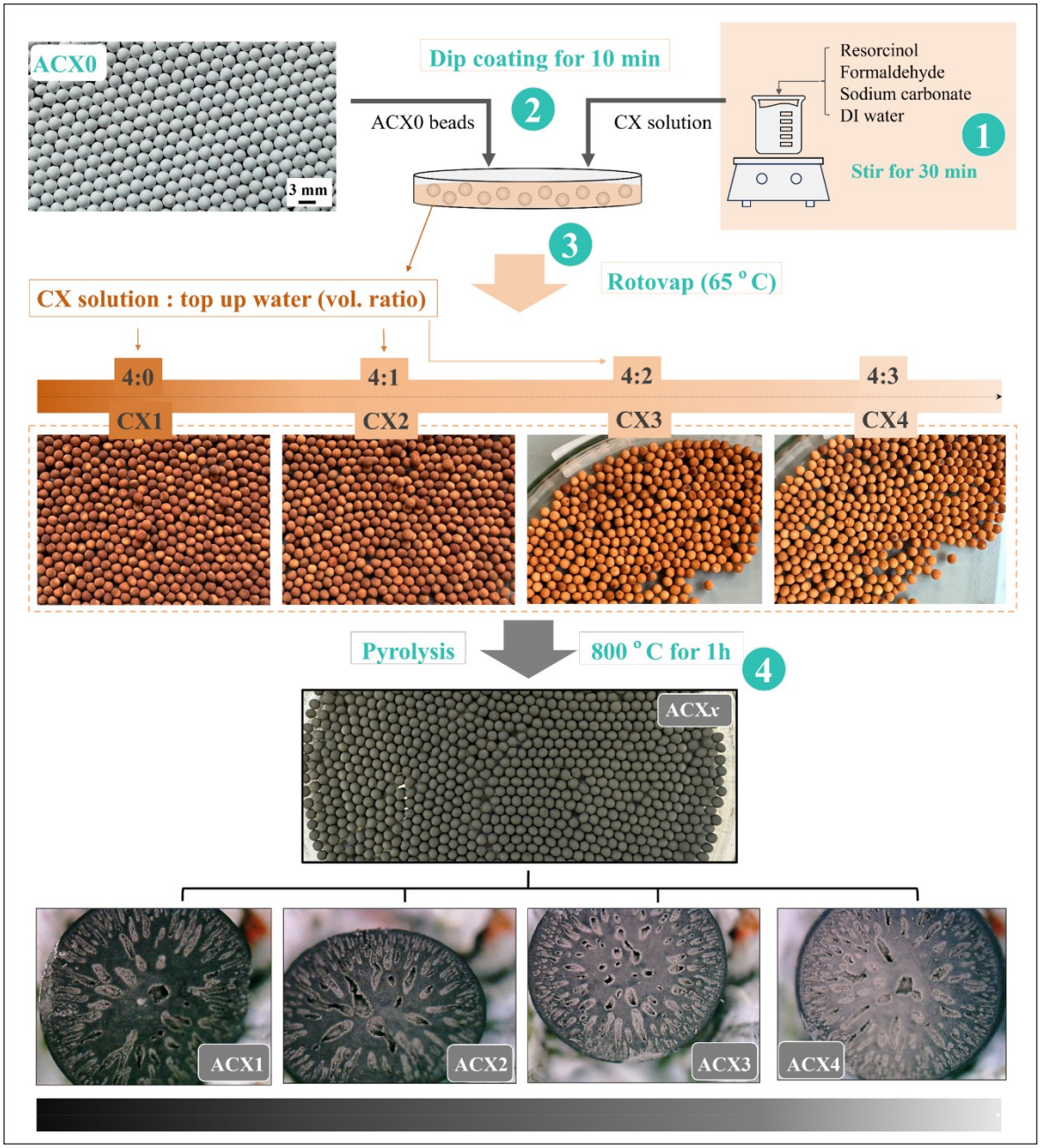

Figure 6-1 Schematic diagram of the synthesis of ACXx samples.

6.2.3 Preparation of Co-based catalysts (2Co/ACX*x*)

2 wt.% of cobalt oxide was incorporated on the ACX*x* beads, including ACX0 without carbon xerogel loadings, by the traditional incipient wetness impregnation method [279]. Firstly, 0.74 g of cobalt nitrate hexahydrate was dissolved in 4.5 mL of DI water, and then slowly added to 10 g of ACX*x* beads, resulting in a Co_3O_4 to ACX weight ratio of 2 wt.%. Then, the dried samples were sintered at 450˚C for 3 h in a flow of N_2 atmosphere (100 mL/min) at a heating rate of 5˚C /min. These catalysts were denoted as 2Co/ACX*x*, where "*x*" refers to the CX*x* sol concentration, as previously illustrated. 2Co/AS4 was

synthesised using the same impregnation method with an identical cobalt loading, as noted in Section 5.2.3.

6.2.4 characterisation and catalytic performance test

The physicochemical properties of ACX*x* and 2Co/ACX*x* samples were characterised by XRD, BET, TGA, SEM, XPS and ICP, with additional detailed information available in Section 3.2. Furthermore, the catalytic performance of 2Co/ACX*x* was evaluated for the degradation of three types of organic pollutants (PPCPs – SMX, phenols – p-HBA and phenol, dyes – MO) in a PMS activated system. The experiments were carried out in a batch reactor in a water bath and connected with a mechanical overhead stirrer. Further detailed information, e.g., mobile phase and stirring speed, can be found in Section 3.3.

6.3 Results and discussion

6.3.1 XRD, BET, and TGA analysis of ACX*x* and 2Co/ACX*x* samples

Figure 6-2 shows the XRD patterns of the samples before and after CX and cobalt loadings. All ACX*x* samples in Figure 6-2 (a) demonstrated diffraction peaks corresponding to the α-Al_2O_3 (JCPD file no. 88-0826) [279], and no diffraction signals of carbon xerogels could be observed. This might be attributed to the weak diffraction peaks for the pure CX powder owing to their intrinsic nature [329], as shown in Figure 6-2 (a-b). However, the presence of carbon xerogel in ACX*x* samples was evident due to the noticeable colour change after CX loadings, as shown in Figure 6-1. Additional evidence will be provided in the following characterisation results, including significant S_{BET} increasement (Table 6-1), TGA results (Figure 6-4), SEM images (Figure 6-6) and XPS spectra (Figure 6-8 (d)). Likewise, no significant differences were observed in the XRD patterns for 2Co/ACX*x* samples after cobalt incorporation (Figure 6-2 (c)) compared to ACX*x* samples, which could be ascribed to the low Co content of 2 wt.% and uniform distribution of Co on the alumina beads [221, 279]. Furthermore, the detection of 1.72 wt.% Co in 2Co/ACX1 sample through ICP measurement could validate the existence of cobalt alternatively.

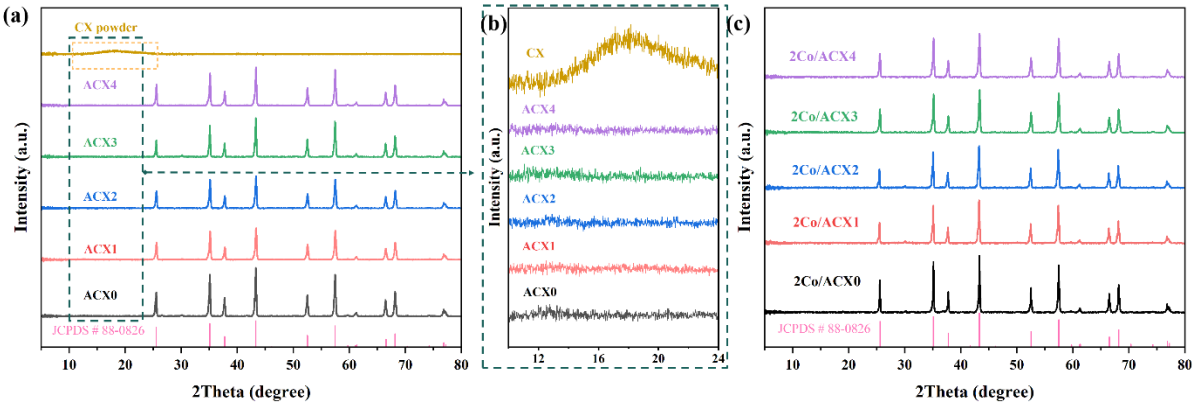

Figure 6-2 XRD patterns of (a) samples before and after RF-derived CX loadings, (b) the magnified x-axis for ACXx samples, and (c) ACXx samples after cobalt incorporation.

Table 6-1 summarised the structural characteristics of three types of microchannel-structured alumina beads: (1) ACX0 (without any washcoatings), (2) AS4 (with γ-Al_2O_3 washcoatings), and (3) ACX*x* (with carbon xerogel washcoatings) samples before and after cobalt impregnation. Apparently, the base ACX0 beads without any washcoatings had the lowest BET surface area (S_{BET} = 3.65 m^2/g). As dip coating with γ-Al_2O_3 sols, the specific surface area significantly increased to 36.03 m^2/g, which is 9.9 times higher than that of ACX0. When changed the coatings to carbon xerogel sols, the S_{BET} further increased, with 66.98 m^2/g, 59.92 m^2/g, 56.62 m^2/g, and 37.20 m^2/g for ACX1, ACX2, ACX3 and ACX4, respectively. Herein, ACX1 sample with lowest water content possessed the highest surface area, which is 18.6 times and 1.9 times than those of ACX0 and AS4 samples. For comparison, the surface areas for pure γ-Al_2O_3 and carbon xerogel powders were 202.00 m^2/g and 691.41 m^2/g, respectively.

Additionally, the average pore diameter of ACX0 dropped from 387.50 nm (mercury intrusion results as reported in our recently published work [279]) to 5.78 nm, 3.15 nm, 2.39 nm, 2.59 nm, and 2.58 nm after modified with γ-Al_2O_3, ACX1, ACX2, ACX3, and ACX4, respectively. This indicates the successful incorporation of high-surface-area materials, which might contribute to more accessible active sites for the high dispersion of cobalt-based catalysts on the alumina beads, thereby higher catalytic efficiency in the chemical reaction process. Simultaneously, the nanoconfined space may enrich pollutant molecules in the pores [330]. After cobalt incorporation, all samples exhibited a similar slight decrease trend in BET surface area and increase in average pore diameter. Studies related to doping with metallic oxides reveals a similar pattern, typically attributed to the reduction in micropores that were partially obstructed by the metallic oxide particles [331, 332]. In this sense, the reduction in S_{BET} for 2Co/ACX_x samples was probably associated with the introduction of cobalt oxide, particularly the partial blockage of microporosity by the Co_3O_4. That, in turn, revealed the successful incorporation of cobalt-based catalysts.

Table 6-1 Textural properties of AS4 and ACXx samples before and after cobalt impregnation.

Sample	S_{BET} (m^2/g)	V_T (cc/g)	D_p (nm)
ACX0	3.65	0.01	/
AS4	36.03	0.05	5.78
ACX1	66.98	0.05	3.15
ACX2	59.92	0.04	2.39
ACX3	56.62	0.04	2.59
ACX4	37.20	0.02	2.58
γ-Al_2O_3 powder	202.00	0.21	4.24
CX powder (before pyrolysis)	345.18	0.35	4.05
CX powder (800 ºC)	691.41	0.44	2.55
2Co/ACX0	2.77	1.16	/
2Co/AS4	21.05	0.05	9.29
2Co/ACX1	49.33	0.05	3.80
2Co/ACX2	44.87	0.05	4.12
2Co/ACX3	37.05	0.03	3.37
2Co/ACX4	35.52	0.03	3.35

S_{BET}: Specific surface area; V_T: Total pore volume; D_P: Average pore diameter.

The N_2 adsorption-desorption isotherms in Figure 6-3 were consistent with the S_{BET} results, with all ACX*x* samples displaying a low but increasing adsorption capacity as carbon xerogel sol concentration rose, which follows a type IV isotherm according to the IUPAC classification [279]. In contrast, carbon xerogel powder exhibited a high adsorption capacity, corresponding to a type IV isotherm, which is typical for mesoporous materials [323]. It is noteworthy that the carbon xerogel powder before pyrolysis (Figure A13) presented a lower adsorption capacity, confirming that the pyrolysis treatment preferably generated more nanopores in the CX-modified samples [333]. Consequently, all ACX*x* samples in this work were sintered at 800˚C for 1 h under a flow of nitrogen. In general, the specific surface area of carbon xerogels is highly dependent on the chemical compositions, drying temperatures, and sintering profile. For example, Moreno et al. found that increasing the pyrolysis temperature from 700˚C to 950˚C resulted in a reduction in the specific surface area of large carbon xerogel particles (>212 μm), decreasing from 585 m^2/g to 471 m^2/g [334]. Peikolainen et al. reported that Na_2CO_3 is critical to deprotonate resorcinol during the synthesis of resorcinol-formaldehyde gel, thereby facilitating its reaction with formaldehyde [335]. Furthermore, the concentration of Na_2CO_3 has a significant impact on cluster formation and growth, with higher Na_2CO_3 concentrations leading to the formation of smaller

clusters and smaller pores between them, ultimately producing materials with an increased specific surface area.

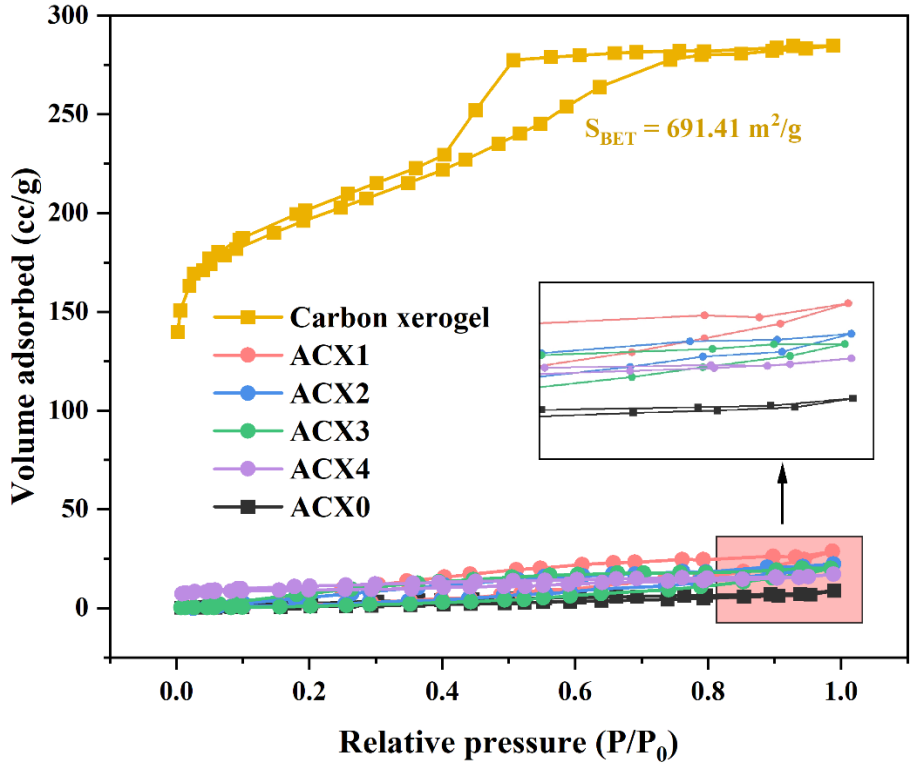

Figure 6-3 N_2 adsorption-desorption isotherms of ACXx samples.

The thermal behaviour of ACX*x* and 2Co/ACX*x* samples shown in Figure 6-4 was examined by TGA analysis throughout the 40-800˚C temperature range under a flow of air. This was conducted to determine the actual content of carbon xerogels, as carbon xerogels can be completely decomposed into CO_2 and H_2O in the presence of oxygen. For ACX0 beads composed of α-Al_2O_3, there was negligible weight loss, indicating the superior thermal stability of the base alumina beads. In contrast, samples after carbon xerogel modification experienced a weight loss when the temperature reached at approximately 600˚C. It can be seen from the inset that the residual weights of ACX1, ACX2, ACX3, and ACX4 at 800˚C were 95.49%, 95.99%, 96.85%, and 97.32%, respectively, corresponding to a total weight loss of 4.51%, 4.01%, 3.15%, and 2.68%. These results could confirm the weight percentage of carbon xerogels in each sample due to the consumption of carbon matrix in the air atmosphere. The weight loss results exhibited a downward trend as the CX sol concentration decreased, which are also in concordance with the experimental findings on carbon xerogel mass fraction during the sample preparation process, as shown in Table A2. Compared to the TGA results for ACX*x* samples prior to cobalt loading, 2Co/ACX*x* samples experienced two weight loss stages, occurring between 40-290˚C

and 290-325˚C. The initial stage, showing only a 1.1% weight loss, could be ascribed to the minimal consumption of Co_3O_4, as documented in the literature [336], while the subsequent stage was related to the decomposition of carbon xerogels in an air atmosphere, similar to what was observed in ACX*x* samples. It is important to emphasize that the transformation of Co_3O_4 from cobalt precursor under nitrogen flow was verified by the TGA profile of cobalt nitrate hexahydrate (Figure A14 (a)) and XRD pattern (Figure A14 (b)). A detailed discussion was provided in the appendix (Text A3-1). Likewise, a similar decline trend in carbon xerogel contents for 2Co/ACX*x* samples was observed, but the decomposition temperature reduced to 320˚C. This can be linked to the interactions between cobalt oxide and carbonaceous materials. Gao et al. observed a similar phenomenon of which the initial decomposition temperature decreased from 522˚C to 255˚C-270˚C as the Co_3O_4 content increased [337].

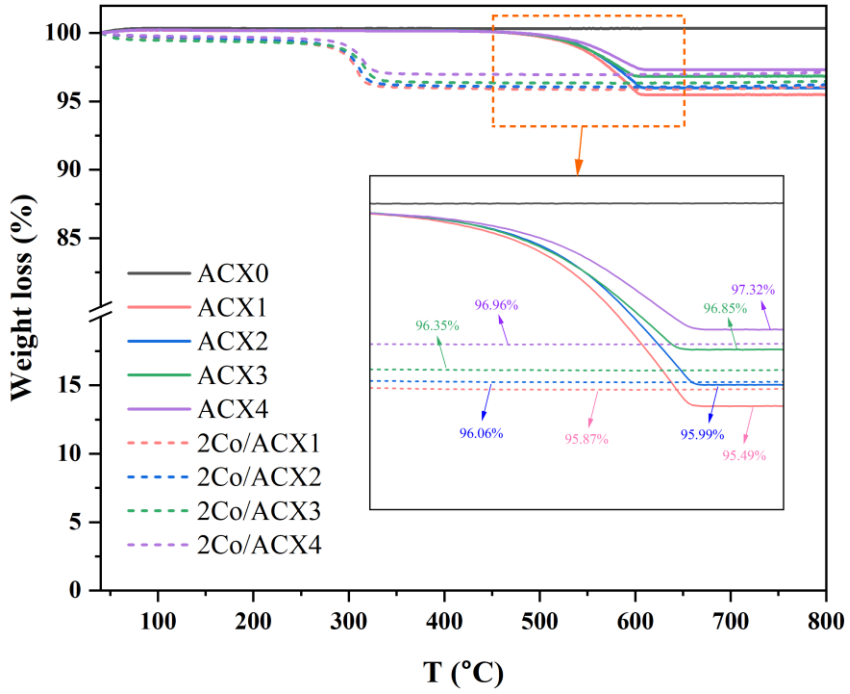

Figure 6-4 TGA profiles of ACXx and 2Co/ACXx in air atmosphere with a heating rate of 5 ˚C/min.

6.3.2 Morphological analysis

Figure 6-5 depicts the SEM images of samples before (ACX0) and after carbon xerogel modifications (ACX1-4) at different magnification levels. The cross-sectional views in Figure 6-5 (a-e) revealed that all samples possessed radial finger-like microchannels, with no significant differences observed among them. This is due to the fact that carbon xerogels consisted of microclusters assembled by microspheres at the nanometre scale, as highlighted by the higher magnification morphologies of ACX1 shown in Figure 6-6 (a-c). This result aligns with the SEM images of RF-derived carbon xerogel reported in the

literature [338]. Regarding the surface views, ACX0 (Figure 6-5 (a_2, a_3)) exhibited numerous exposed open channels, but as the sol concentrations increased, these channels were partially obstructed by carbon xerogels, particularly ACX1 with the highest concentration of carbon xerogel. Moreover, as illustrated in Figure 6-6 (d-f), numerous carbon xerogels were detectable on the surface of ACX1 at high magnifications, further confirming the successful incorporation of carbon xerogel washcoatings.

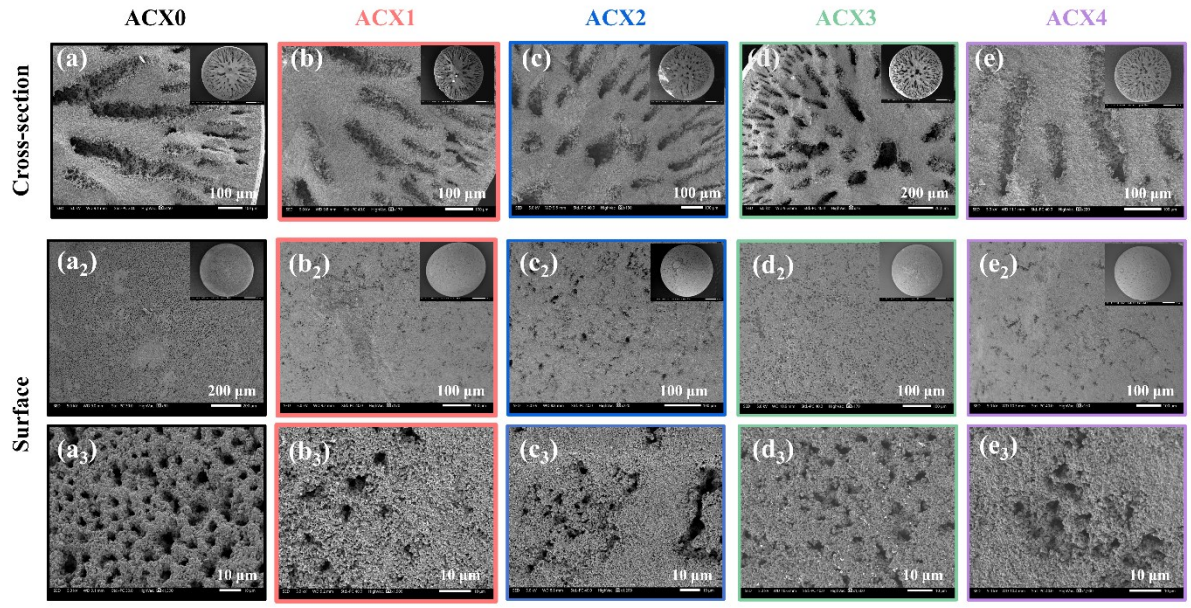

Figure 6-5 SEM images of the cross-sectional views of (a) microchannel-structured alumina beads (ACX0), microchannel-structured alumina beads modified with different carbon xerogel concentrations: (b) ACX1, (c) ACX2, (d) ACX3, and (e) ACX4; and the surface views of (a_2, a_3) ACX0, (b_2, b_3) ACX1, (c_2, c_3) ACX2, (d_2, d_3) ACX3, and (e_2, e_3) ACX4.

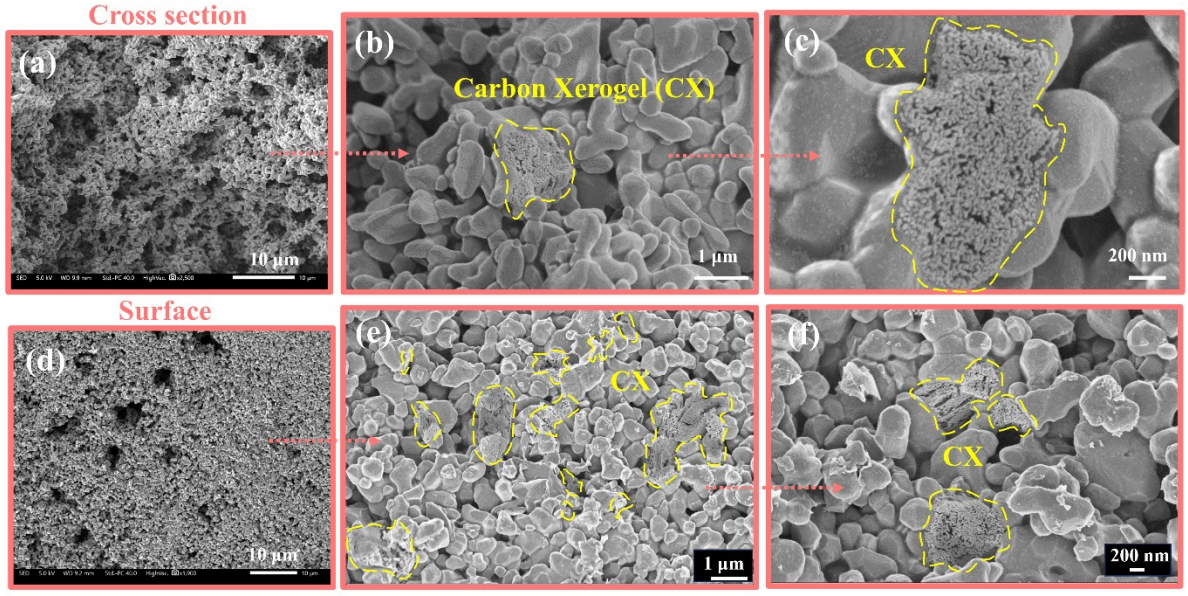

Figure 6-6 High magnification SEM images of (a-c) finger-like microstructures in the cross-section and (c-e) surface of ACX1.

Figure 6-7 displayed the SEM images of two representative samples, i.e., ACX1 and ACX3, after incorporating 2 wt.% Co_3O_4 by a simple impregnation method. The introduction of Co_3O_4 did not alter the original morphologies, such as finger-like microchannels in the cross-section and exposed open channels on the surface, of both alumina beads. It can be seen from Figure 6-7 (a_2, a_3) and Figure 6-7 (b_2, b_3) that 2Co/ACX3 exhibited more noticeable exposed open channels due to the lower carbon xerogel loadings and sol concentrations, leading to the less partially blocked pores by carbon xerogels, which is in accordance with the SEM images of ACX1 (Figure 6-5 (b_2)) and ACX3 (Figure 6-5 (d_2)) before cobalt incorporation.

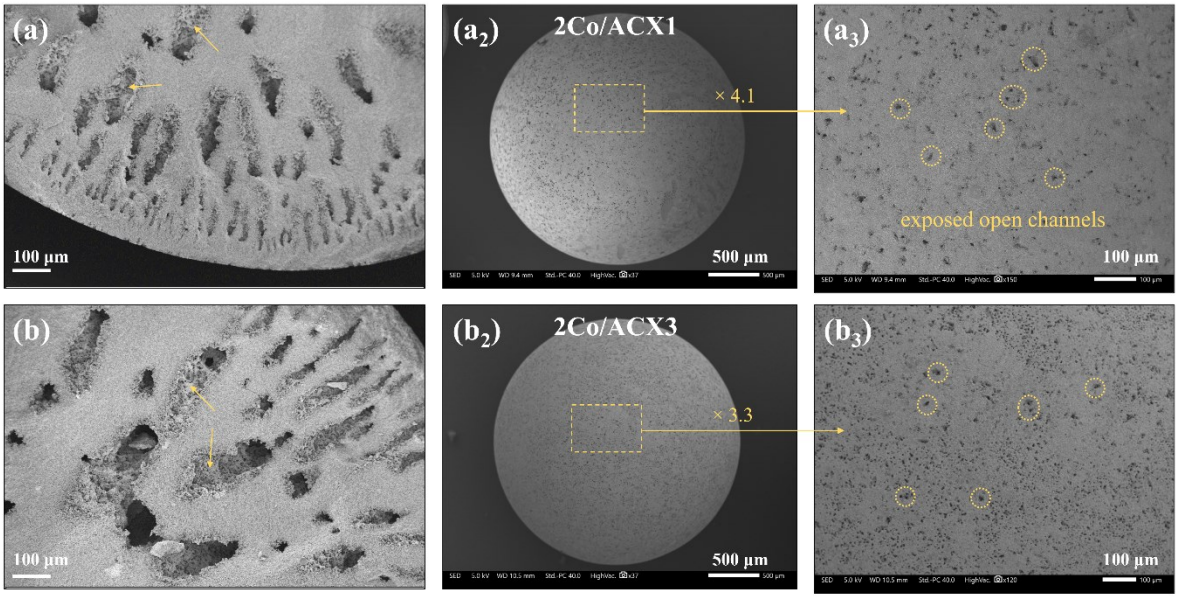

Figure 6-7 SEM images of (a) the cross-sectional view and (a_2, a_3) the surface views of 2Co/ACX1, (b) the cross-sectional view and (b_2, b_3) the surface views of 2Co-ACX3.

6.3.3 XPS analysis

To verify the presence of Co element and probe the chemical valence state of 2Co/ACX*x* samples, XPS spectra of 2Co/ACX0 and 2Co/ACX1 were analysed. As shown in Figure 6-8 (a), the XPS survey spectra confirmed the presence of elements Al, O, C and Co in both samples. The corresponding high resolution XPS spectra of Al 2p (Figure 6-8 (b)), O 1s (Figure 6-8 (c)), and Co 2p (Figure 6-8 (e)) revealed that the existence of carbon xerogel sol coatings in 2Co/ACX1 resulted in lower intensities of the Al 2p, O 1s, and Co 2p spectra. Simultaneously, an extremely weak peak centred at 75.3 eV in 2Co/ACX0, associated with the formation of trace amounts of aluminium suboxide during the cobalt impregnation process [279, 287, 288], was no longer observed in the 2Co/ACX1 sample. This finding could be attributed to the presence of carbon xerogels, which is further supported by the BET results

(Table 6-1) [292, 293], and in accordance with the XPS results as shown in Section 5.3.1 (Figure 5-3) [279]. As noted, cobalt oxide was not detected in the XRD patterns, but the Co 2p spectra revealed that cobalt was present in two chemical states (Co^{3+}, Co^{2+}) in both 2Co/ACX0 and 2Co/ACX1, corresponding to the compositions of Co_3O_4.

In contrast, the C 1s spectra in Figure 6-8 (d) displayed a higher intensity for 2Co/ACX1 compared to 2Co/ACX0. This increased intensity was directly linked to the additional carbon source from the carbon xerogel in 2Co/ACX1. As observed, the deconvolution of the XPS spectra for the C 1s regions revealed two peaks for 2Co/ACX0 and three peaks for 2Co/ACX1. The adventitious carbon centred at 284.8 eV in both samples was originated from the carbon grid during sample preparation process [312]. Both peaks centred at 286.4 eV and 285.9 eV were assigned to C═O bond, as reported by Kim et al. [339]. They indicated that peaks within the 285.9-286.4 eV range are associated with C═O bond in phenol, alcohol, and ether, etc. In addition, the third peak existed in 2Co/ACX1 at 288.8 eV was attributed to carbon in carboxylic groups [230, 323]. Consequently, the XPS spectra verified the presence of Co element in two chemical valence states, as well as the successful incorporation of CXs.

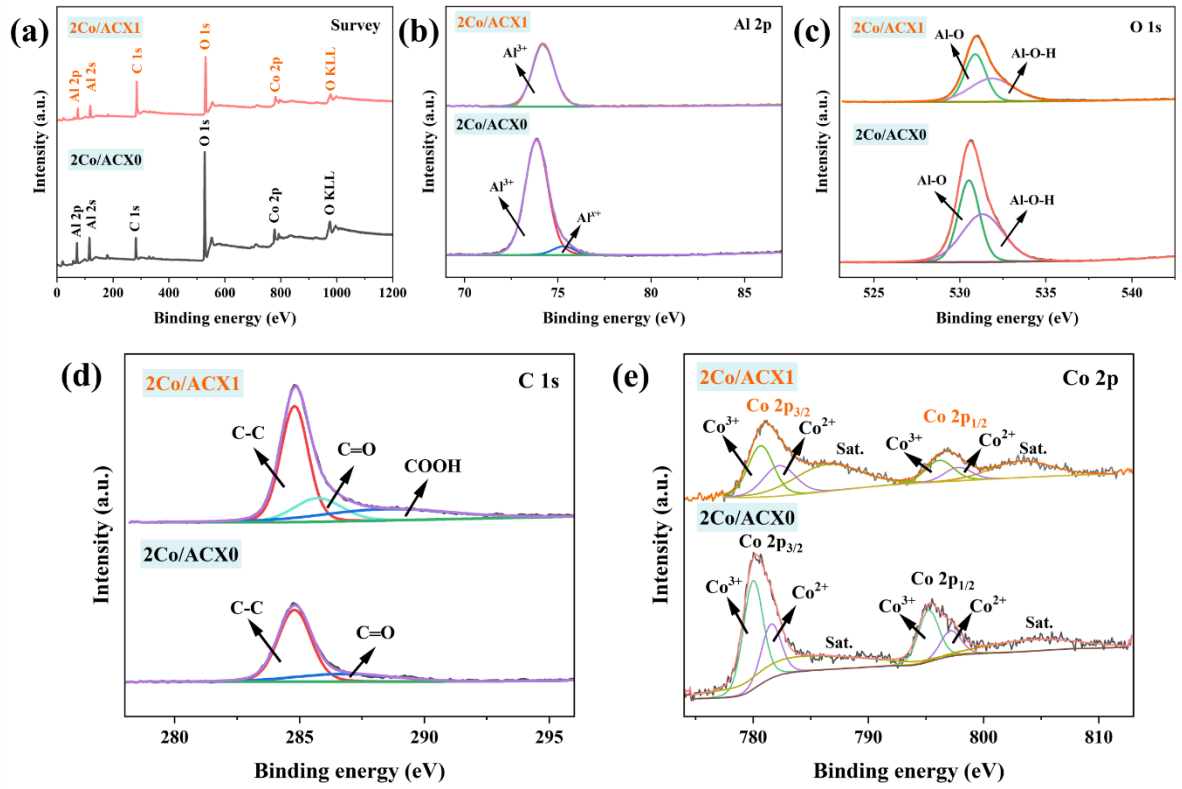

Figure 6-8 (a) XPS survey spectra, and high-resolution XPS spectra of (b) Al 2p, (c) O 1s, (d) C 1s, and (e) Co 2p of cobalt-impregnated microchannel-structured alumina beads before (2Co/ACX0) and after CX loadings (2Co/ACX1).

6.3.4 Evaluation of the catalytic activity

6.3.4.1 Effect of SMX concentrations and reaction temperature

The introduction of CXs improved the dispersion of the catalytic active phase, leading to more accessible active sites participating in the catalytic reaction, which is expected to result in enhanced catalytic activity. In this work, the catalytic performance of novel 2Co/ACX*x* samples was investigated by the degradation of organic pollutants in a PMS-activated AOPs reaction system. The influences of SMX concentrations (10 mg/L, 20 mg/L, and 40 mg/L), reaction temperatures (T = 20˚C, 30˚C, and 40˚C), organic pollutant types (SMX, p-HBA, phenol, and MO), the contribution of the BET surface area, and washcoating properties (γ-Al_2O_3 sol washcoatings as reference, carbon xerogel sol washcoatings as primary) were all included, as shown in Figure A15, Figure 6-9, Figure 6-10, Figure 6-12, Figure A16, and Figure A17. For all SMX degradation reactions, the blank experiments, which involved the 2Co/ACX1 catalyst alone without the addition of PMS, demonstrated negligible catalytic performance (< 0.1%).

Figure 6-9 (a) depicts the degradation of 20 mg/L SMX at 20˚C. The results demonstrated that the removal efficiency for PMS only, 2Co/ACX0, 2Co/AS4, 2Co/ACX1, and 2Co/ACX3 was 26.4%, 34.9%, 52.2%, 99.2%, and 97.0%, respectively. Meanwhile, the reaction kinetics in Fig. 8 (b) and the corresponding rate constants in Fig. 8 (c) were consistent with the catalytic performance. It is obvious that 2Co/ACX1 with the highest BET surface areas possessed the highest catalytic activity, and the rate constant of 2Co/ACX1 was 15.3 times, 10.9 times, and 6.3 times higher than those of PMS alone, 2Co/ACX0, and 2Co/AS4, respectively. This was further validated during the degradation of 10 mg/L SMX, as illustrated in Figure A15 and Text A3-2 in the supplementary information. The remarkably boosted catalytic performance may be related to the enhanced S_{BET}, and this will be further explored in the subsequent reactions.

Figure 6-9 (b) demonstrated that this pattern persisted when the SMX concentration was raised to 40 mg/L, though the differences between 2Co/ACX1 and 2Co/ACX3 became slightly less pronounced. The diminishing difference is probably owing to more exposed open channels of 2Co/ACX3 on the bead surfaces, as corroborated by the SEM images in Figure 6-5 (a_3, b_3), which contributed to reducing the mass transfer resistance at higher pollutant concentrations. It is widely recognized that high pollutant concentrations typically increase the demand for accessible active sites, and a greater number of open channels on the surface certainly aids in transporting more pollutants into the microchannels to interact with the active sites. This is comparable to our recent published work at high SMX concentrations [279, 340]. However, this restricted mass transfer could be improved by increasing the reaction temperature to 30˚C, because the diffusion coefficient increases with rising reaction temperature, according to Arrhenius equation [297]. As a result, the degradation efficiency of 2Co/ACX1 and 2Co/ACX3

followed the trend of 40˚C > 30˚C > 20˚C, a pattern also observed in the reaction kinetics (Figure 6-9 (e)) and the corresponding rate constants (Figure 6-9(f)).

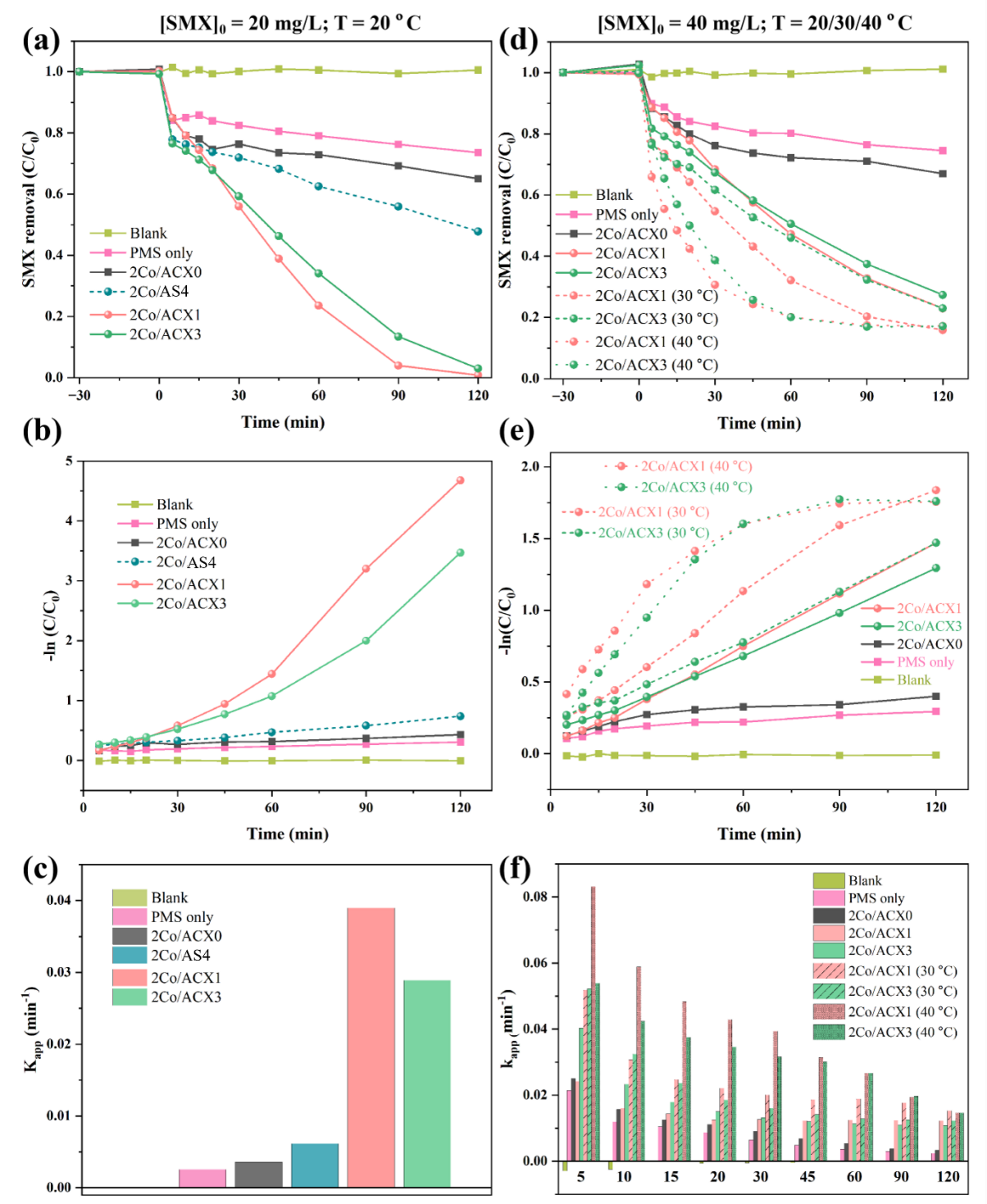

Figure 6-9 (a) Degradation of 20 mg/L SMX using three types of catalysts at 20 ˚C, (b) their reaction kinetics, and (c) the corresponding rate constants; (d) Degradation of 40 mg/L SMX using three types of catalysts at three reaction temperatures, (e) their reaction kinetics, and (f) the corresponding rate constants during the whole reaction process. Reaction Conditions: $[PMS]_0$ = 0.1 g/L, $[catalyst]_0$ = 0.02 g/L, r = 150 rpm.

6.3.4.2 Effect of catalyst dosage and pH

Besides the effects of SMX concentrations and reaction temperatures, the degradation of SMX was also studied under varying catalyst dosages and pH levels, as depicted in Figure 6-10. As expected, the SMX removal progressively grew from 21.3% to 92.2% within 30 min with the catalyst dosage increase from 0.002 g/L to 0.2 g/L, thanks to more accessible active sites for PMS activation. This, in turn, generated more reactive radicals, such as $SO_4^{\cdot-}$ and $\cdot O_2^-$, for the efficient degradation of organic pollutants. In this work, a catalyst dosage of 0.02 g/L was selected as the target for SMX elimination, expect for Figure A16, where 0.2 g/L of catalyst was used in all reactions to assess the catalytic activity at higher catalyst dosages.

Figure 6-10 (b) shows the SMX removal efficiency at an initial pH range of 3-11. At pH levels of 5-10, the degradation efficiency remained robust, consistently nearly 100%. However, the degradation rate decreased under strong acid and base conditions, with 86.9% of SMX breaking down at pH 3 and only 16.2% at pH 11, even though the efficiency remained satisfactory at pH 3. This is due to the fact that, on the one hand, in strong acid solutions, excess H^+ consumes HSO_5^-, preventing the redox cycle of Co (II)/Co (III), and consequently poor SMX degradation [341]; On the other hand, in strong base solutions, the main reactive species, $SO_4^{\cdot-}$ (E° =2.5-3.1 V, $t_{1/2}$ = 30 μs), transformed to $\cdot OH$ with lower redox potential (E° =1.8-2.7 V) and a shorter half-life time ($t_{1/2}$ = 20 ns) [212, 213].

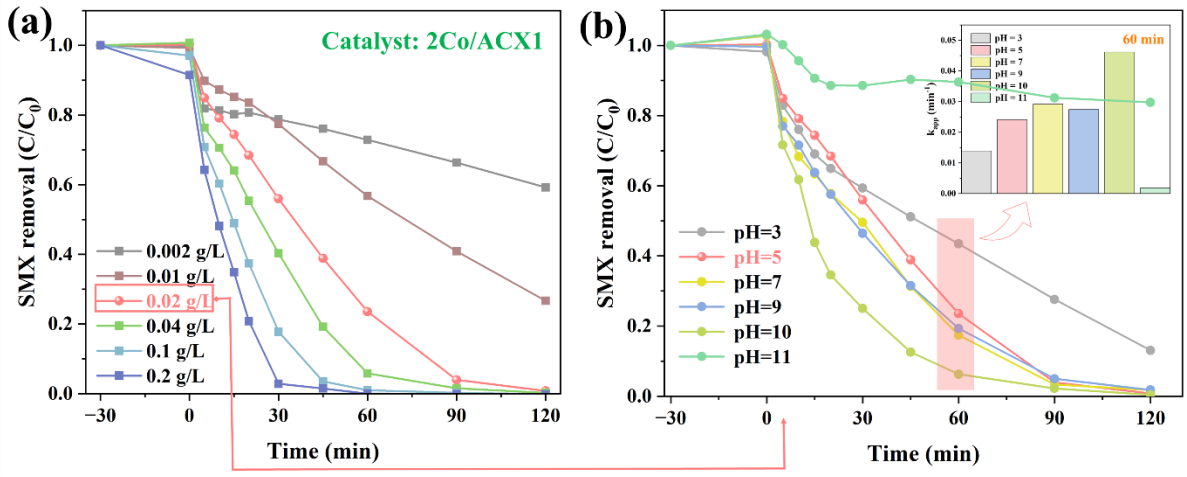

Figure 6-10 (a) Effect of catalyst dosage and (b) initial solution pH on the degradation of 20 mg/L SMX using 2Co/ACX1. Reaction Conditions: $[PMS]_0$ = 0.1 g/L, T = 20 ℃, r = 150 rpm.

6.3.4.3 Preliminary analysis of PMS activation by carbon xerogels

Carbon materials containing oxygen-functional groups, such as -COOH and C═O, have been reported to activate PMS [342], thereby facilitating the catalytic activity. To the best of our knowledge, reported work on carbon xerogels for AOPs are scarce, including Co and Fe in carbon xerogels [343] and N-doped carbon xerogels [344]. However, in order to explore the role of carbon xerogels in PMS activation, we conducted a preliminary analysis of catalytic reactions using a spectrophotometer (UV-Vis Evolution 220, Thermo Scientific), as illustrated in Figure 6-11 and Figure A18. Figure 6-11 displays the UV-Vis spectra of SMX concentrations over time during reactions with different catalysts. The results indicated that ACX1, i.e., 2Co/ACX1 before cobalt loading, showed minimal degradation of SMX in the absence of PMS (Figure 6-11 (a)). However, when PMS was added, ACX1 could degrade 25.1% of SMX within 4 hours (Figure 6-11 (b)), accompanied by a wavelength shift from 267 nm to 270 nm. This red shift in the absorption edge is consistent with the 2Co/ACX1 result in Figure A18 (c), implies that PMS was activated by ACX1 even without a cobalt catalyst [345]. Additionally, ACX1 powder (obtained by grinding ACX1) exhibited enhanced SMX degradation (56.9% in 4h) and a more pronounced red shift in absorption (Figure 6-11 (d)). On the one hand, this highlighted the significance of mass transfer in catalytic reactions, as catalyst powder typically diffuses faster than large beads; on the other hand, we can conclude that PMS could be activated by carbon xerogel-based materials. For comparison, Figure A18 (a, b, d) shows the absorption spectra of 2Co/ACX1, 2Co/ACX1 powder, and CX powder in the absence of PMS, where SMX degradation occurred without a shift in the absorption edge. This indicates that this degradation process was attributed to the adsorption capacity of the carbon xerogel, as supported by Figure A19.

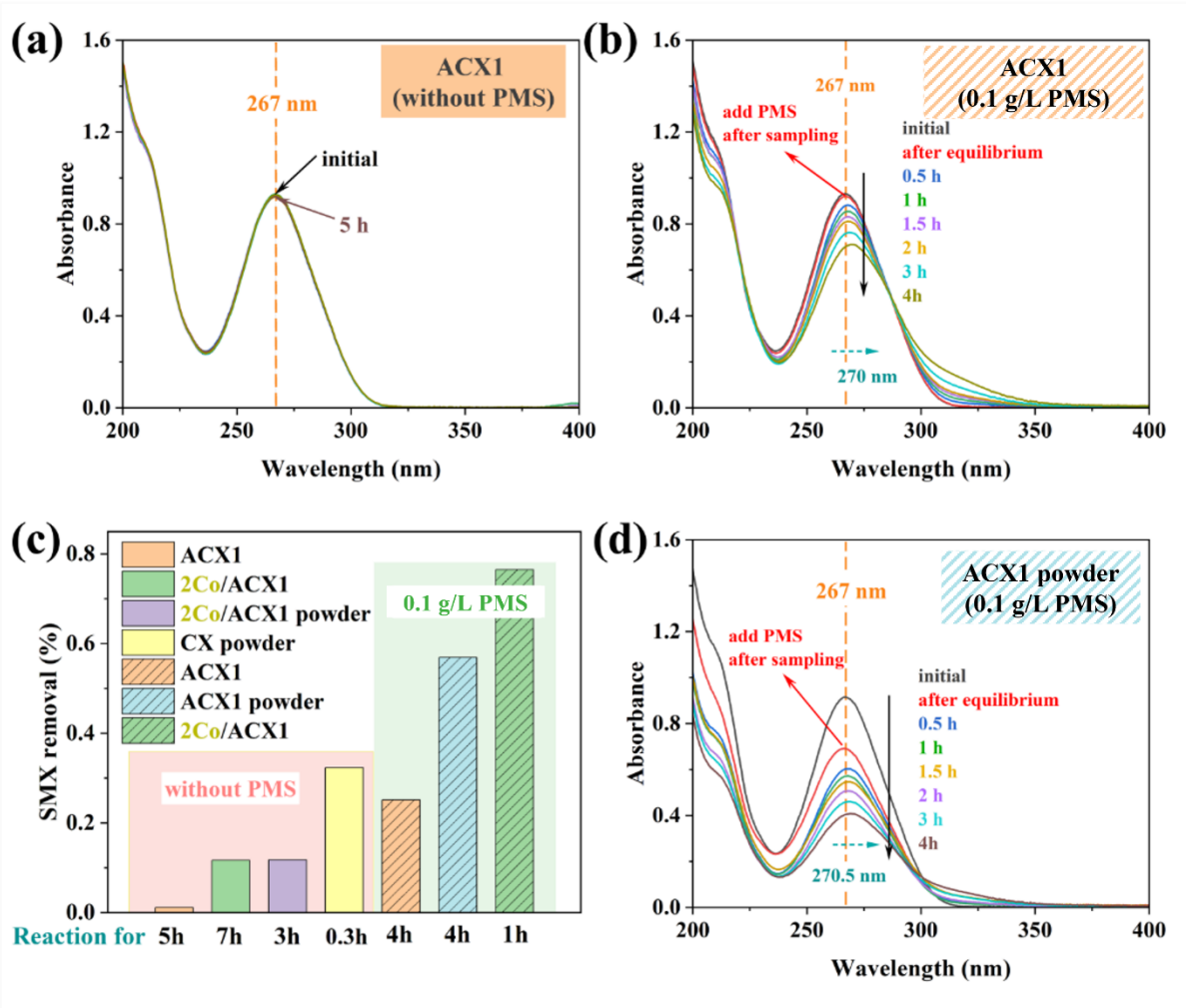

Figure 6-11 UV-Vis spectra of (a) ACX1 without PMS, (b) ACX1 with 0.1 g/L PMS, and (d) ACX1 powder with 0.1 g/L PMS for the degradation of SMX; (c) SMX degradation with different catalysts in the presence and absence of PMS. Reaction conditions: [SMX] = 20 mg/L, [catalyst]$_0$ = 0.2 g/L, T = 20 ˚C, r = 150 rpm.

6.3.4.4 Effect of organic pollutants

For practical applications, the catalytic ability of materials for different types of organic pollutants was pivotal. To further study the capability of the 2Co/ACX*x*|PMS system, degradation of phenols (p-HBA and phenol) and dyes (MO) was also assessed, as shown in Figure 6-12 and Figure A17. Figure 6-12 provided compelling evidence for the efficacy of p-HBA and phenol elimination using the 2Co/ACX*x* samples, drastically surpassing the performance of 2Co/ACX0 and 2Co/AS4, aligning with the SMX removal in Figure 6-9 and Figure A15-16. In the case of blank experiments for the degradation of these two pollutants, 2Co/ACX1 sample alone oxidized 13.2% of p-HBA and 14.4% of phenol without the addition of PMS. This can be ascribed to the adsorption capacity of carbon xerogels. Comparable results for p-HBA and phenol adsorption on various carbon materials have been documented in the literature [280, 299, 346]. It is crucial to point out that the considerably high adsorption capacity of CX powder, beyond than of γ-Al_2O_3 – both the commercial ones and sol-gel type used in this study – has been proven

in Figure A19. Furthermore, a similarly substantial enhancement in MO elimination using 2Co/ACX1 is also discovered in Figure A17.

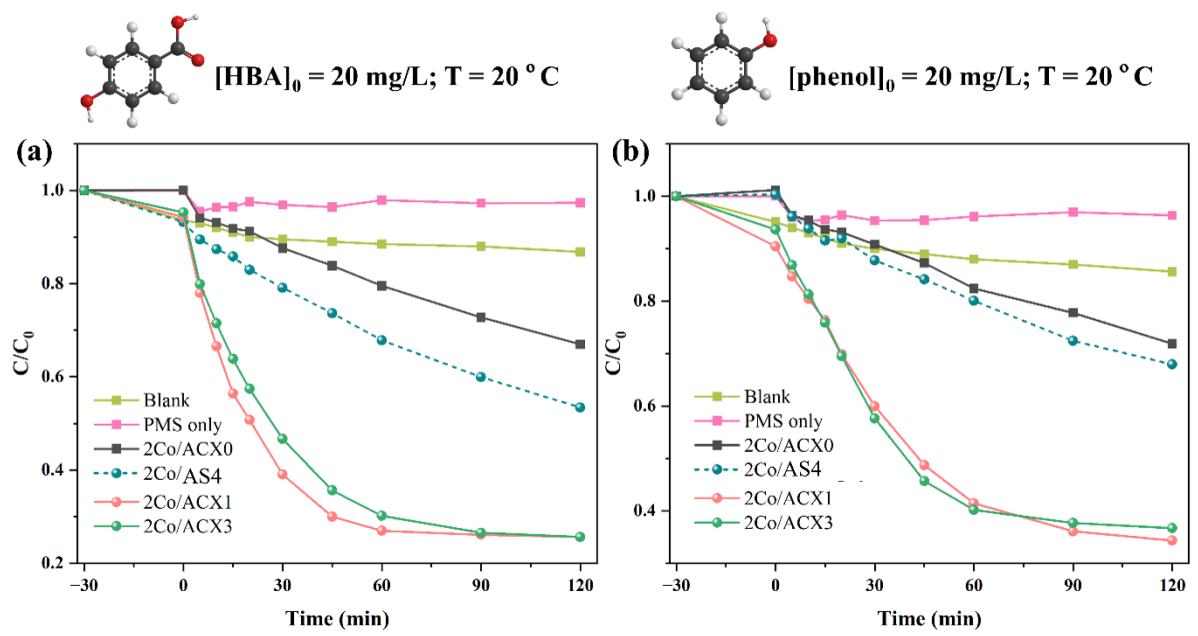

Figure 6-12 Degradation of (a) 20 mg/L p-HBA and (b) 20 mg/L phenol using three types of catalysts. Reaction Conditions: $[PMS]_0$ = 0.1 g/L, $[catalyst]_0$ = 0.1 g/L, T = 20 ˚C, r = 150 rpm.

Based on the above catalytic results, the exceptional catalytic performance of 2Co/ACX*x* samples in all reactions has been validated. This can be attributed to a synergistic effect of the following factors: (a) The enhanced BET surface area of 2Co/ACX1 unquestionably contributed to improving the dispersion of the catalytic active phase, i.e., cobalt oxide, thereby facilitating the generation of more reactive radicals for the reaction; (b) In comparison to both the base alumina beads (2Co/ACX0) and γ-Al_2O_3-modified alumina beads (2Co/AS4), carbon xerogel in CX-modified alumina beads (2Co/ACX*x*) also contributed to the catalytic reaction by boosting the adsorption capacity for the degradation of organic pollutants; (c) The doped carbonaceous materials could catalyse the self-decomposition of PMS to generate reactive oxygen species [320, 321, 347, 348], so partial PMS activation by carbon xerogels might be advantageous in the 2Co/ACX*x*|PMS as well; (d) The nanoconfined pore effect on PMS activation within the nanoparticles of 2Co/ACX*x* samples (D_p = 3.80-4.12 nm) could play a role in accelerating chemical reactions, as interactions between the nanoconfinement and either reactants (organic pollutants including SMX, p-HBA, phenol, and MO), oxidizing agent (PMS), the transition state, the product, or the catalysts (2Co/ACX*x*) in a nanoconfined space may alter the reaction energy diagram [330, 349].

As exemplified in Figure 6-13, the bare microchannel-structured alumina beads have catalysts directly loaded onto the substrates with a large pore size of 387.50 nm, based on the mercury intrusion data

from our recently published paper (Chapter 4, Figure 4-7) [279]. After applying a washcoat of γ-Al_2O_3 or carbon xerogels, however, the catalysts could be deposited on the washcoating layers, where the pore diameters were lowered to 9.29 nm for γ-Al_2O_3 and 3.80 nm for CX. Taking into account the molecular sizes of PMS (0.315 × 0.305 × 0.350 nm), SMX (1.49 × 0.64 × 0.56 nm), p-HBA (0.75 × 0.43 × 0.15 nm), phenol (0.54 × 0.46 nm), and water molecules (0.28 × 0.06 nm) [350-353], the smaller pore diameter in 2Co/ACX*x* samples could allow up to twelve layers of PMS molecules to diffuse into the nanopores and interact with the catalytic active phase, resulting in a confinement effect that improved the utilisation of short-lived reactive oxygen species; (e) The tremendous diffusional mass transfer in the three-millimetre diameter alumina beads with finger-like microstructures promoted the transport of reactants and products, which, in turn, improved the catalytic reactions across all three types of alumina beads. In short, the synergistic process intensification at the microscale process unit, i.e., microchannel-structured alumina beads paired with functional carbon xerogels, endued the system with the exceptional catalytic performance for the decontamination of various organic pollutants.

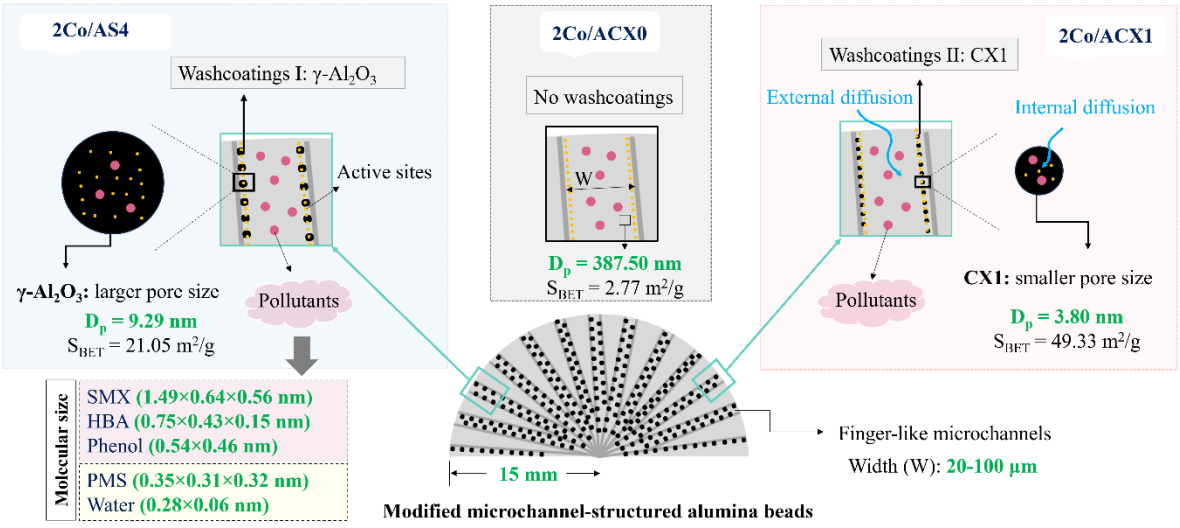

Figure 6-13 A schematic diagram illustrating three types of catalysts with (2Co/A(γ-Al_2O_3) and 2Co/ACXx) and without (2Co/ACX0) washcoatings.

6.3.4.5 Possible catalytic reaction pathways and mechanism

A series of selective radical quenching agents (10 mM NaN_3, 10 mM p-BQ, 1 M MeOH, 1 M tBA) were introduced to the 2Co/ACX1|PMS reaction system to assess the contribution of each reactive species, as shown in Figure 6-14. When NaN_3 and p-BQ were was added, the SMX removal efficiency was drastically surpressed from 99.19% to 7.30%, and 54.82%, respectively. This might be related to the crucial role of $^1O_2$ [279] and $\cdot O_2^-$ [221]. However, it has been recently reported that NaN_3 and p-BQ may also quench $SO_4^{\cdot -}$ and ·OH [354-356], so additional evidence – electron paramagnetic resonance

(EPR) – were conducted to further verify their contributions in AOPs. As illustrated in Fig. 10 (c), when 2,2,6,6-tetramethyl-4-piperidone (TEMP) was added into 2Co/ACX1|PMS reaction system, distinct three-line signals with peak strength of 1:1:1 for TEMP-$^1O_2$ were detected, and the intensity increased as the reaction time progressed from 10 min to 20 min. In contrast, the addition of 5,5-dimethyl-1-pyrroline N-oxide (DMPO) (Fig. 10 (d)) resulted in the formation of $\cdot O_2^-$ signals. This served as direct evidence for the formation of $^1O_2$ and $\cdot O_2^-$ [221, 357].

Additionally, tBA performed a minimal inhibitory effect, less than 4.7%, on SMX removal in the range of 100 mM to 1000 mM (Figure A20 (a)), revealing the negligible contribution of ·OH [358], although dintinct four-line signals with peak strength of 1:2:2:1 for DMPO-·OH were detected in Fig. 10 (e) [355]. Furthermore, as MeOH can react with both ·OH ($k = 9.7 \times 10^8$ M s^{-1}) and $SO_4^{\cdot-}$ ($k = 2.5 \times 10^7$ M s^{-1}) [353], the massive supression of SMX removal by MeOH suggested that $SO_4^{\cdot-}$ was the primary ROS in the system. Similarly, 1000 mM MeOH efficiently quenched ·OH and $SO_4^{\cdot-}$, as evidenced by Figure A20 (a), where various amounts of MeOH were added and stabilised at 1000 mM. The generation of $SO_4^{\cdot-}$ can be evidenced by the detection of six-line signals corresponding to DMPO-$SO_4^{\cdot-}$ adducts in Fig. 10 (e) [357]. It is also important to note that the weak signals for DMPO-·OH and DMPO-$SO_4^{\cdot-}$ observed with PMS alone in Fig. 10 (e) align with the self-degradation of contaminants when catalysts were absent in Fig. 6, Fig. S5, Fig. S6, Fig.9, and Fig. S7.

Moreover, the reaction rate constants (k) are consistent with the quenching experiment, as shown in Figure A20 (b). It is also worth noting that the quenching experiments across the three systems (Figure A21 (a)) revealed only slight variation in the contributions of active species, with a ranking order of $SO_4^{\cdot-}$ > $\cdot O_2^-$ > ·OH and a difference range of 6-11%. Notwithstanding the deficiency of definitive evidence for the involvement of $^1O_2$ and $\cdot O_2^-$ for all systems, observations from the quenching results revealed a gradual increase in its role. This trend might be attributed to more frequent redox cycles driven by more accessible active sites, as $^1O_2$ can be obtained by the transformation of $\cdot O_2^-$, the decomposition of PMS, and the reactions of $SO_5^{\cdot-}$ (Figure A21 (b)) [359].

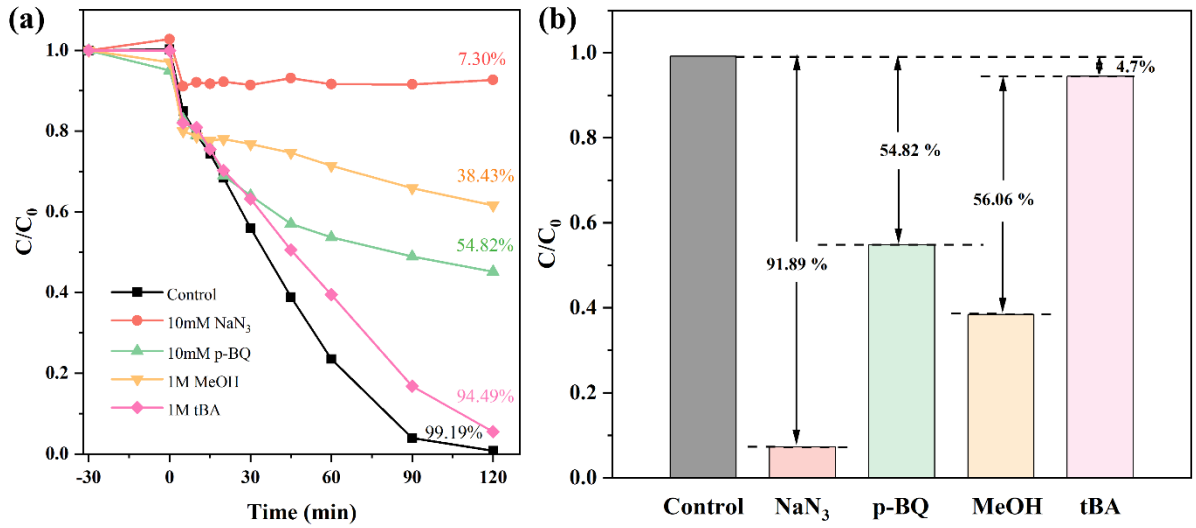

Figure 6-14 (a) Effect of quenching agents on degrading SMX and (b) contribution of each scavenger (catalyst: 2Co/ACX1).

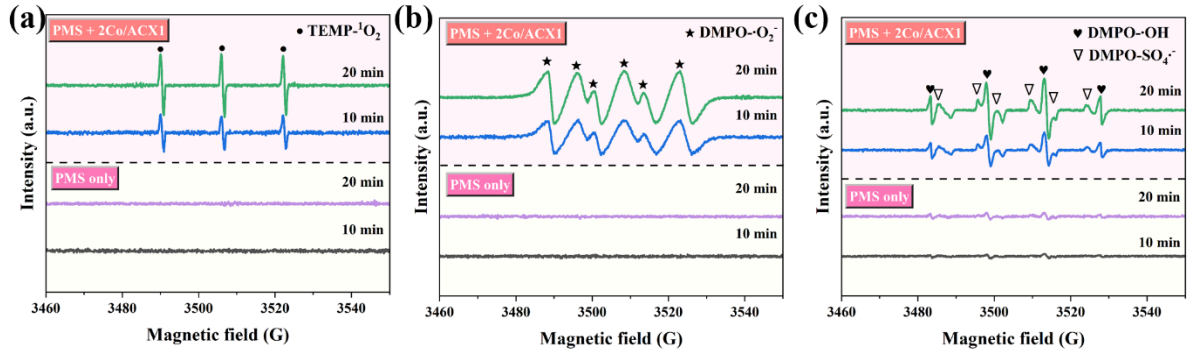

Figure 6-15 EPR signals detected in 2Co/ACX1|PMS system for (a) TEMP-$^1O_2$ adducts, (b) DMPO-$\cdot O_2^-$, and (c) both DMPO-·OH and DMPO-$SO_4^{\cdot -}$.

Based on the quenching experiments, a possible catalytic mechanism for the degradation of SMX by 2Co/ACX1 was proposed and illustrated in Figure 6-16. When PMS was added to the reaction system, it quickly diffused into the finger-like microchannels (20 -100 μm in width) of the ceramic beads (3 mm in diameter). Subsequently, up to twelve layers of PMS molecules (0.315 × 0.305 × 0.350 nm) further diffused into the pores of carbon xerogel washcoating layers (D_p = 3.8 nm), and then interacted with catalytic cobalt active phase (Co^{2+}) to trigger the reaction, generating large amounts of $SO_4^{\cdot -}$ and Co^{3+}. Meanwhile, HSO_5^- was then oxidised by Co^{3+} to yield $SO_5^{\cdot -}$, with Co^{3+} being reduced back to Co^{2+}. Therefore, the redox cycle of Co^{2+}/Co^{3+} was established, facilitating the robust and long-term catalytic degradation of contaminants. As the reaction progressed, $SO_4^{\cdot -}$ radicals were partially converted into ·OH radicals, which had a minimal role in this system but contributed to the formation of the predominant $\cdot O_2^-$ radicals. As noted, $^1O_2$ was produced by the conversion of $O_2^{\cdot -}$, the reactions of

$SO_5^{\cdot-}$ with water or PMS, and the self-dissociation of the generated $SO_5^{\cdot-}$ (Figure A21 (b)). In the end, the generated radicals ($SO_4^{\cdot-}$ and $\cdot O_2^-$) and non-radical species ($^1O_2$) reacted with the target contaminants, driving the decontamination process.

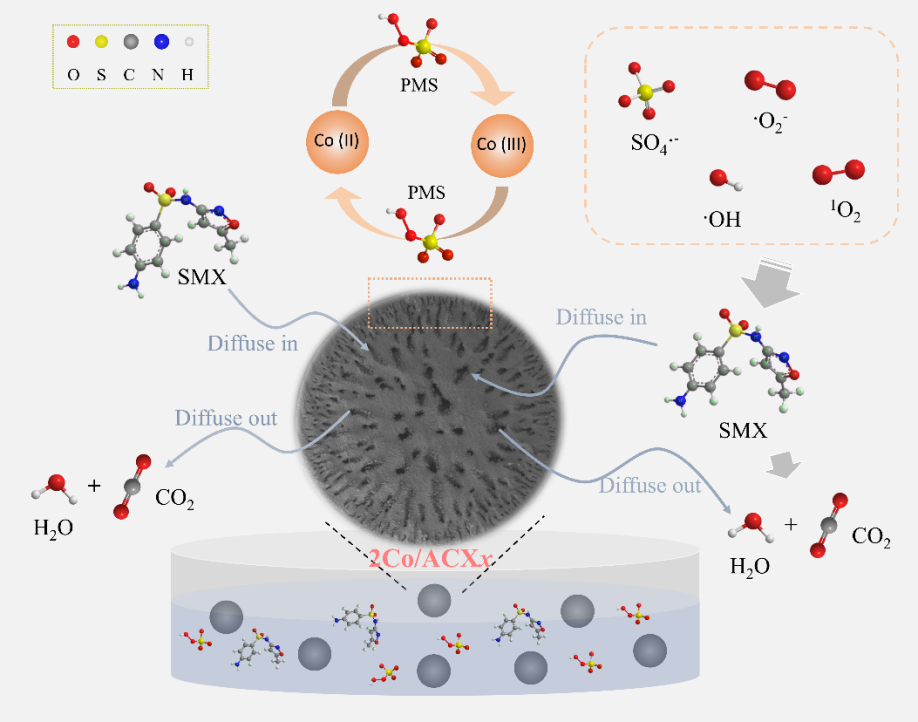

Figure 6-16 A proposed mechanism for catalytic oxidation of SMX by 2Co/ACX1.

6.3.4.6 Reusability and stability

Cycling experiments were carried out using 2Co/ACX1 to decompose SMX over five consecutive runs, in order to evaluate its reusability and stability for practical applications. As shown in Figure 6-17 (a), the catalytic performance remained highly efficient after five recycle runs, implying the superior stability and reusability of 2Co/ACX1 catalyst. In addition, unlike powdered catalysts, these bead samples are straightforward to separate from the bulk solution without energy consumption. Separation can be achieved with minimum effort through simply pouring out the aqueous solution and rinsing with deionised water. Chemical seperation is estimated to account for about 10-15% of global total energy consumption [360]. This work, however, eliminated the requirement of thermal-energy-intensive separation procedure, bringing down operational cost while preserving marvellous catalytic efficiency. Furthermore, the XRD patterns of the fresh and used samples shown in Figure 6-17 (b) highlighted their extraordinary stability. It is noteworthy that the metal ions leaching for 2Co/ACX0, 2Co/AS4, and 2Co/ACX1 samples during the reusability tests have been investigated, as shown in Appendix 3 (Text A3-3 and Figure A22). In addition, the XPS analysis of 2Co/ACX1 after the 5th cycle (Figure A23)

further confirmed its stability, as no significant changes were observed in the valence states of the elements. Only a slight reduction in the intensity of Co 2p (Figure A23 (b)) and C 1s (Figure A23 (c)) was detected, potentially due to the consumption of the Co_3O_4 catalyst and minor leaching of metal ions, as evidenced by Figure A22.

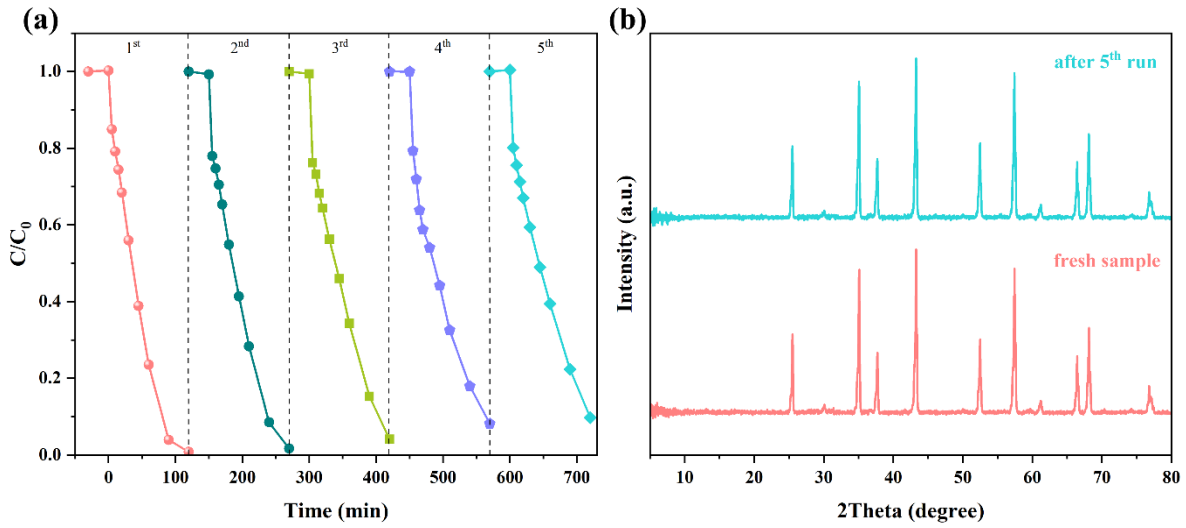

Figure 6-17 (a) Recycling test of the sample 2Co/ACX1 for SMX degradation (cleaned by DI water only), and (b) the XRD patterns of the 2Co/ACX1 before and after 5th run. Reaction Conditions: $[PMS]_0$ = 0.1 g/L, $[SMX]_0$ = 20 mg/L, T = 20 ˚C, $[catalyst]_0$ = 0.02 g/L, r = 150 rpm.

6.4 Conclusion

Overall, this chapter investigated the 2Co/ACX*x*|AOPs reaction system for the degradation of different organic pollutants under mild reaction conditions, with key findings summarised as below:

(1) Innovative microchannel-structured alumina beads with enhanced specific surface area have been successfully prepared by the phase-inversion and sol-gel methods. Two types of washcoatings (γ-Al_2O_3 in Chapter 5 and carbon xerogels) were introduced into the beads` microchannels.

(2) The influences of the BET surface area, washcoating properties, organic pollutant types, SMX concentrations, and reaction temperatures on the catalytic performance were systematically investigated. Experimental results demonstrated that the alumina beads with increased S_{BET} by incorporating CX washcoatings (2Co/ACX1) exhibited the highest catalytic activity than the base one (2Co/ACX0, labelled as "2Co/MSCB2" in Chapter 4) and γ-Al_2O_3 washcoatings (2Co/AS4 in Chapter 5). Under identical reaction conditions, the reaction rate of 2Co/ACX1 is 10.83 times higher than that of 2Co/ACX0 and 6.39 times higher than that of 2Co/AS4. This could be attributed to a synergistic effect resulting from a better dispersion of cobalt catalytic

phase, remarkable adsorption capacity of carbon xerogels, the coexistence of two PMS activation species, nanoconfined pore effect, and reduced mass transfer resistance, within the AOPs system. Therefore, the multifunctional carbon xerogel-modified alumina beads successfully addressed the third and fourth research objectives in Section 1.2.

(3) The synergistic process intensification at the microscale process unit in this research demonstrated exceptional catalytic activity, reusability, and stability. It also effectively balanced mass transfer resistance and pressure drop, potentially fully harnessing the profits of integrating nanoporous carbon materials with microchannel-structured ceramic beads for large-scale diffusion-limited chemical reactions.

Chapter 7 Preparation of innovative microchannel-structured SiO_2 beads and their application in the AOPs

Chapter 7 presents a new material perspective compared to previous chapters. Instead of using alpha alumina for bead preparation followed by modifications with mesoporous coatings, this chapter uses mesoporous SiO_2 as the starting material for bead preparation. This approach aims to eliminate the extra modification step and simplify the bead fabrication process. Although not detailed in this thesis, we have identified new and impactful research on SiO_2 beads in photocatalysis, further extending the scope and impact of this research.

7.1 Introduction

As noted in Section 4.1, innovative microchannel-structured Al_2O_3 beads possessed the enhanced intraparticle diffusion for the catalytic degradation of SMX in a PMS-activated system. Further enhancing the specific surface area of these structured alumina beads by introducing gamma-alumina (**Chapter 5**) and carbon xerogel (**Chapter 6**) sols has been evidenced to further improve their catalytic performance, owing to the enhanced available active sites and other functional characteristics (e.g., synergistic effects). This chapter investigates the fabrication and characterisation of microchannel-structured SiO_2 beads of various diameters (2-3 mm) through a combined phase-inversion and sintering-assisted approach at sintering temperatures ranging from 1000˚C to 1200˚C. Likewise, finger-like microstructures were also generated within these silica beads, but the width was way below alumina beads, approximately 10-20 μm.

Different from α-Al_2O_3 powder used for the preparation of alumina beads in **Chapter 4**, **Chapter 5**, and **Chapter 6**, amorphous SiO_2 powder has a high specific surface area (175-225 m^2/g), low density (2.2 g/cm^3), and non-crystalline forms, which contributed to the formation of beads with intrinsic high BET surface area. Interestingly, the sintering temperature plays a crucial role in the porosity, crystallinity, mechanical strength, and even the transparency of the silica beads, depending on additives and processing conditions. The transformation of amorphous SiO_2 to combined cristobalite and quartz structures (crystalline forms) occurred at a sintering temperature of 1200˚C in this chapter. It was also found that the diameter of the silica beads varied at different sintering temperatures, and this process gave rise to the densification and the reduction the specific surface area, and thereafter the decline in the catalytic performance. In addition, the influence of the reaction temperature (20˚C, 30˚C, 40˚C, 50˚C) and pH of the initial aqueous SMX solutions (3, 5, 7, 8, 9, 10) were systematically investigated in this chapter. The stability and reusability of 2Co/SiO_2-1000C, and a plausible catalytic mechanism of 2Co/SiO_2-1000C|PMS system were also explored. It is worth noting that transparent microchannel-

structured silica beads have also been prepared in this chapter, which would be advantages to large-scale photocatalysis, and a comprehensive investigation were provided in the appendix for reference.

7.2 Experimental

7.2.1 Chemicals and materials

Silicon oxide (amorphous fumed, S.A. 175-225 m^2/g), cobalt nitrate hexahydrate ($Co(NO_3)_2 \cdot 6H_2O$, 99% pure), methanol (HPLC grade, ≥ 99.8%), and nitric acid (HNO_3, analytical reagent grade, 70%) were purchased from Fisher Scientific. YSZ grinding media and NMP (99+%, ACS reagent) were purchased from Inframat Advanced Materials (USA) and ACROS Organics and Uniqema (UK), respectively. PMMA, Oxone® (PMS, $KHSO_5 \cdot 0.5KHSO_4 \cdot 0.5K_2SO_4$), SMX, p-benzoquinone (p-BQ, ≥ 98%), tert-butanol (tBA, ≥ 99.5%), sodium azide (NaN_3, ≥ 99.5%), and acetic acid (ReagentPlus®, ≥ 99%) were all obtained from Sigma-Aldrich. All chemicals were used as received without any further purification. Milli-Q water (18.3 MΩ cm at 25˚C) was used during the whole experimental process.

7.2.2 Preparation of microchannel-structured SiO_2 beads (SiO_2-*x*C)

Microchannel-structured silica beads of 2-3 mm in diameter were synthesised for the first time by a combined phase-inversion and sintering-assisted method. Detailed procedures are outlined as below: Initially, 15 g of amorphous SiO_2 powder and 107.73 g of NMP solvent was milled with agate grinding media (20 mm balls) for 48 h to achieve a homogeneous suspension. Then, 13.64 g of PMMA was added and the suspension was continued for milling for another 48 h. The final transparent suspension was transferred to a gas-tight vacuum degassing chamber (DP 27, Applied Vacuum Engineering) and degassed under vacuum for 3 h, eliminating any trapped air within the suspension. Afterwards, the degassed suspension was transferred into a 100 mL stainless steel syringe and extruded at 0.2 mL/min into a water bath. The actual flow rate of the extrusion was controlled by a Chemyx Fusion 6000-X syringe pump, ensuring the uniformity of the prepared precursor silica beads. Throughout the entire extrusion process, the air gap between the water surface and the flat-tipped tube (1/4 inch) that connected to the syringe pump was set as 4.0 cm. Finally, after the completion of the phase inversion process by leaving the precursor silica beads in the water bath for 24 h, all beads were dried and then sintered in stagnant air (furnace BRF 16/5, Elite) at different temperatures (1000˚C, 1020˚C, 1050˚C, 1100˚C, 1200˚C) for 3 h with a heating rate of 5˚C/min. According to the sintering temperature, the sintered microchannel-structured SiO_2 beads were named as SiO_2-*x*C, and *x* hereafter refers to the specific sintering temperatures (*x* = 1000, 1020, 1050, 1100, and 1200). For comparison, other annealing temperatures including 1040˚C, 1060˚C, 1080˚C, 1120˚C, 1180˚C, 1250˚C, 1300˚C, and 1350˚C were

also included in this work to investigate the decrease in BET surface area, changes in shrinkage percentage, and the phase transformation of SiO_2 from amorphous to cristobalite as temperature increased, as shown in Figure A24 and Figure A25. The selection of five sintering temperatures (i.e., 1000˚C, 1020˚C, 1050˚C, 1100˚C, and 1200˚C) in the main text was primary based on BET surface area, while other sintering temperatures (i.e., 1040˚C, 1060˚C, 1080˚C, 1120˚C, 1180˚C, 1250˚C, 1300˚C, 1350˚C) were explored to gain a deeper understanding their relationship with various material properties, including the shrinkage percentage, porosity, phase transitions, and bead transparency.

7.2.3 Preparation of cobalt-based catalysts (2Co/SiO_2-*x*C)

Cobalt oxide was incorporated into the silica beads by the conventional incipient wetness impregnation method. Firstly, 0.74 g of cobalt nitrate hexahydrate was dissolved in a certain amount of DI water, and then slowly added to 10 g of microchannel-structured SiO_2 beads, resulting in a Co_3O_4 to SiO_2 beads weight ratio of 2 wt.%. The amount of DI water added was just enough to immerse the SiO_2 beads, and it varied because of the differing porosity and hygroscopicity of beads sintered at different temperatures, with 24.3 g, 15.4 g, 8.1 g, 7.6 g, and 6.0 g for SiO_2-1000C, SiO_2-1020C, SiO_2-1050C, SiO_2-1100C, and SiO_2-1200C, respectively. Capillary motion could draw the cobalt precursor solution into the pores of silica beads [361]. Then, the catalyst precursor was dried and sintered at 450˚C for 3 h at a heating rate of 5˚C /min. These catalysts were denoted as 2Co/SiO_2-*x*C, where "*x*" refers to the sintering temperatures, as previously illustrated.

7.2.4 Characterisation and catalytic performance test

The physicochemical properties of SiO_2-*x*C and 2Co/SiO_2-*x*C samples were characterised by XRD, BET, MIP, SEM, XPS and ICP, with additional detailed information available in Section 3.2. Furthermore, the catalytic performance of 2Co/SiO_2-*x*C was evaluated for the degradation of SMX solutions in a PMS activated system. The experiments were carried out in a batch reactor in a water bath at 20 ˚C and connected with a mechanical overhead stirrer. Initially, 0.02 g of catalyst was placed in 100 mL of pollutant solutions with vigorously stirring at 150 rpm for 30 min to achieve the adsorption-desorption equilibrium. Afterwards, the catalytic reactions were triggered by adding PMS (0.1 g/L) and continued for another 120 min. Other detailed information, e.g., mobile phase and stirring speed, can be found in Section 3.3.

7.3 Results and discussion

7.3.1 Phase compositions

Figure 7-1 (a) presents the XRD patterns of SiO_2 beads sintered at temperatures ranging from 1000˚C to 1200˚C. At sintering temperatures of 1000˚C, 1020˚C, 1050˚C, and 1100˚C, the SiO_2 beads remained in an amorphous state, exhibiting a broad and weak diffraction peak cantered at 22.01˚ [362, 363]. Increasing the sintering temperature further to 1200 ˚C resulted in the formation of combined cristobalite and quartz structures. In this sample, main characteristic peaks at 21.98˚, 28.44˚, 31.46˚, 36.08˚, 42.66˚, 44.84˚, 47.06˚, 48.61˚, 54.16˚, 57.08˚, 60.30˚, 62.02˚, and 65.10˚ correspond to (101), (111), (102), (200), (211), (202), (113), (212), (203), (301), (311), (302), (312) planes of cristobalite SiO_2 (JCPDS PDF no. 39-1425) [364]. Partial weak peaks related to quartz SiO_2 (JCPDS PDF no. 46-1045) were also detected, notably 20.86˚ and 26.64˚ [363].

After cobalt oxide was incorporated, the samples sintered at temperatures of 1000˚C, 1050˚C, and 1050˚C exhibited no notable changes, except for the appearance of characteristic Co_3O_4 peaks (JCPDS PDF no. 42-1467) [285], confirming the successful loading of Co_3O_4. However, 2Co/SiO_2-1100C showed a similar pattern to 2Co/SiO_2-1200C, commencing the crystallisation process in the same way as SiO_2-1200C did prior to cobalt loading. This phenomenon is consistent with previous results, in which the crystal transformation pathways of silica were altered in the presence of metallic oxide [363]. It has also been reported that the presences of metals prominently lowered the phase transformation temperature of silica [364, 365]. It is worth nothing that there were some 2Co/SiO_2-1100C beads remained amorphous and untransformed, similar to SiO_2-1100C before cobalt loading, as shown in the XRD patterns in Figure A26. Note that no distinct Co_3O_4 peaks could be observed in these two samples, probably due to their dense structures (Figure 7-2, Figure 7-5 (e)) and low specific surface area (Table A3), which inhibited the incorporation of excess cobalt precursor.

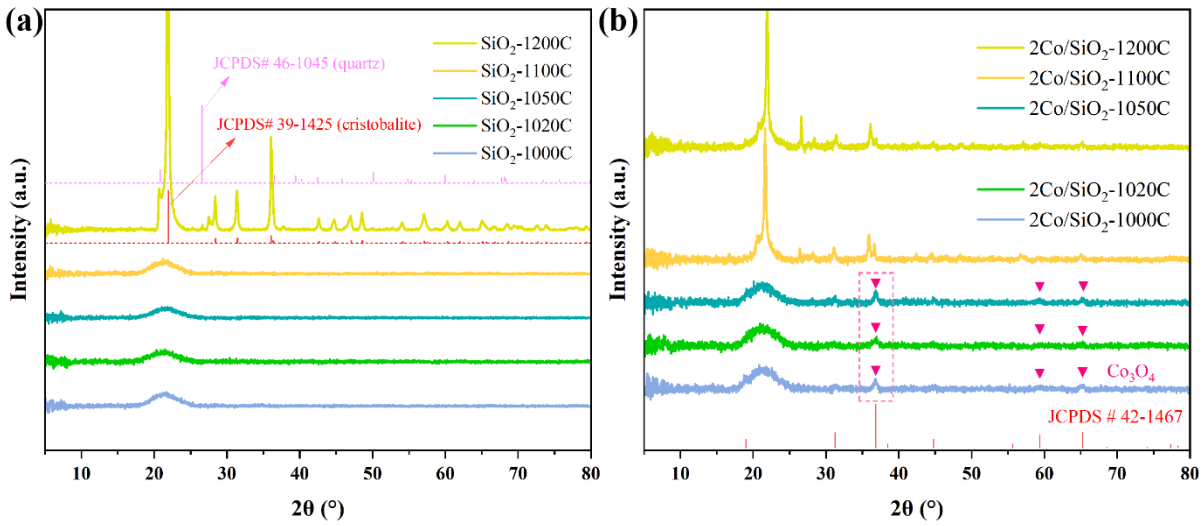

Figure 7-1 XRD patterns of (a) SiO_2 beads sintered at temperatures ranging from 1000 ˚C to 1200 ˚C, and (b) sintered SiO_2 beads after the incorporation of cobalt oxide.

Table 7-1 summarises the textural properties, diameters, and shrinkage percentage of SiO_2 beads before and after sintering at temperatures ranging from 1000˚C to 1200˚C. As can be seen from Table 7-1 and Table A3, SiO_2-1000C possessed the highest BET surface area (112.10 m^2/g) and the largest diameter (3.06 nm), which is beneficial for cobalt impregnation and adsorption of pollutant during AOPs reactions. The increase in sintering temperature caused a reduction both in the S_{BET} and diameter accordingly, representing greater densification at higher temperatures [255]. As the calcination temperature rose to 1100˚C, SiO_2-1100C showed an extremely limited S_{BET} (8.06 m^2/g), indicating that virtually all porous silica structures had vanished, and dense structures were formed instead. An overview of the photographic images and shrinkage percentage of silica beads before and after sintering (1000-1350˚C) can refer to Figure A25.

Table 7-1 Textural properties of SiO_2 beads sintered at temperatures ranging from 1000˚C to 1200˚C.

Sample	S_{BET} (m^2/g)	V_T (cc/g)	D_p (nm)	Diameter (mm)	Shrinkage percentage (%)
SiO_2 (before sintering)	81.14	0.62	30.52	3.52	/
SiO_2-1000C	112.10	0.84	29.97	3.06	13.07
SiO_2-1020C	94.18	0.66	27.99	2.77	21.31
SiO_2-1050C	26.66	0.16	23.37	2.21	37.22
SiO_2-1100C	8.06	0.02	12.20	2.00	43.18
SiO_2-1200C	0.26	0.01	/	1.90	46.02

S_{BET}: Specific surface area; V_T: Total pore volume; D_P: Average pore diameter.

To further assess the impact of such densification, the pore structure of SiO_2 beads after sintering at 1000˚C, 1050˚C, 1100˚C and 1200˚C was analysed using MIP. As shown in Figure 7-2 (a), the peak between 10 nm and 100 nm, which represents the pore size of the microchannels entrances (Figure 7-3 (a_2)), was significantly affected by the sintering temperatures [255]. In addition, the peak intensity was obviously declined as the sintering temperature increased from 1000˚C to 1200˚C, which aligns with the BET results (Table 7-1), detailed MIP results (Table 7-2) and the SEM images (Figure 7-2 (b)), confirming densification at high sintering temperatures (1100 ˚C and 1200 ˚C). It can also be inferred that SiO_2-1000C, SiO_2-1020C and SiO_2-1050C beads remained porous, although the porosity decreased progressively from 75.88% to 57.70%. In contrast, SiO_2-1100C (15.32%) and SiO_2-1200C (3.70%) became dense, which might have an adverse impact on the catalyst deposition.

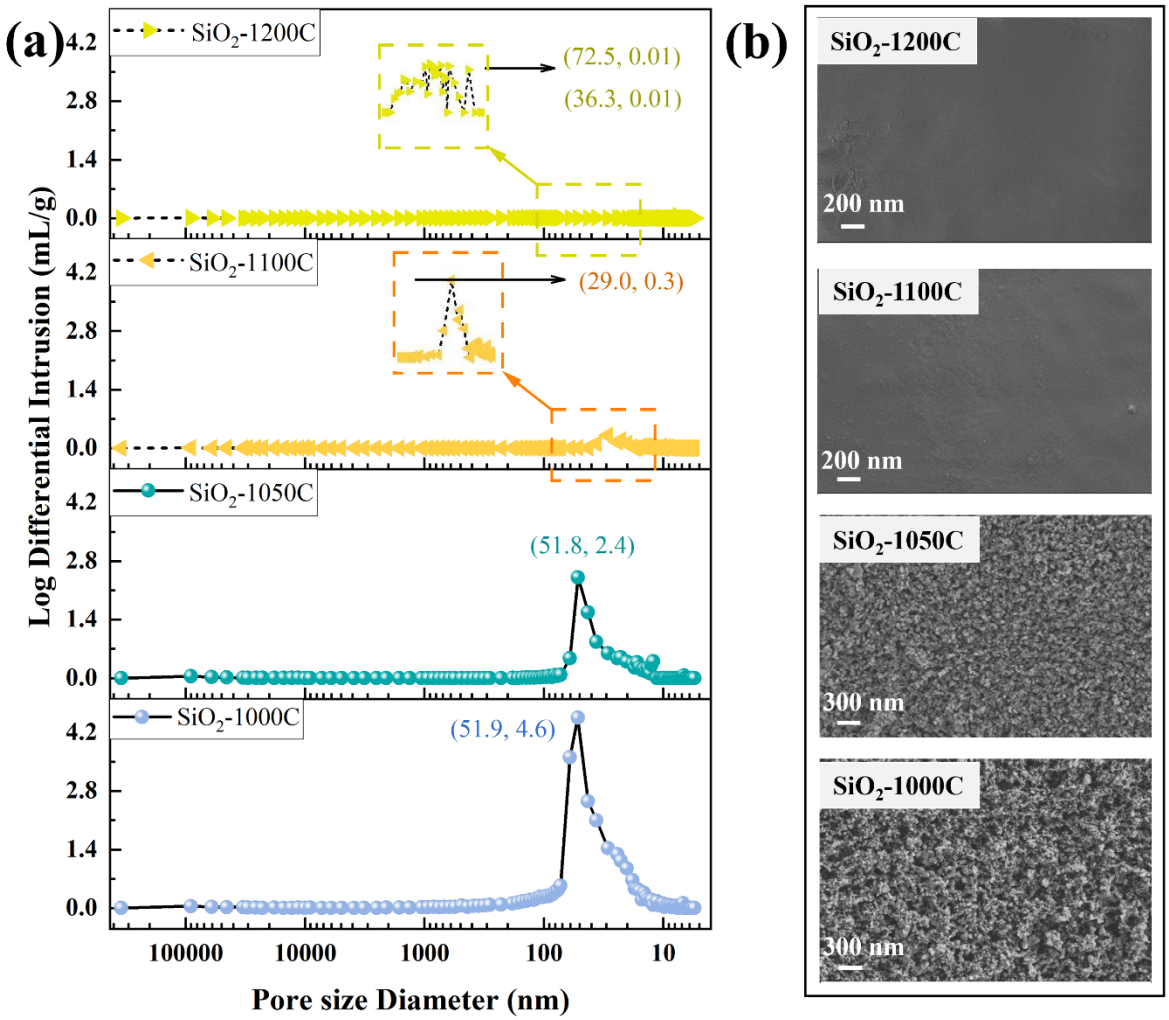

Figure 7-2 (a) MIP results of microchannel-structured silica beads sintered at different temperatures: SiO_2-1000C, SiO_2-1050C, SiO_2-1100C, and SiO_2-1200C, and (b) their SEM images of the surface views.

Table 7-2 MIP results of microchannel-structured silica beads.

Sample	Total pore area (m^2/g)	Median pore diameter (nm)	Porosity (%)	Characteristic length* (nm)
SiO_2-1000C	150.80	51.80	75.88	58.70
SiO_2-1050C	66.29	47.40	57.70	30482.10
SiO_2-1100C	11.12	31.30	15.32	10064.40
SiO_2-1200C	0.63	28.70	3.70	13062.50

*Refers to the pore throat size of the sample when the mercury-intruded pores start to percolate through the sample.

To better visualise the shrinkage of these silica beads and their microstructures, Figure 7-3 presents photographic images, along with cross-sectional morphologies. As expected, SiO_2-1100C (Figure 7-3 (d)) and SiO_2-1200C (Figure 7-3 (e)) had the lowest pellet size (~ 2.0 nm in diameter), and their inner surface (Figure 7-3 (d_3, e_3)) turned out to be sense and smooth. This agrees with the MIP results in Figure 7-2 and Table 7-2. On the contrary, SiO_2-1000C (Figure 7-3 (a-a_6)) exhibited a sparse and coarse texture, which accounted for its relatively larger specific surface area. Moreover, one of the most critical characteristics is its distinctive finger-like microstructures, with exposed facets measuring approximately 10-20 μm in width. Note that the microchannels possessed relatively uniform dimensions, as these structures formed in all directions within the silica beads during the phase-inversion process [164]. However, because silica beads were halved simply by a knife to expose their cross sections prior to the SEM analysis, resulting in varying cross-sectional views each time. As shown, all samples revealed finger-like microstructures with comparable widths, which facilitated the transportation of reactants and products in catalytic reactions.

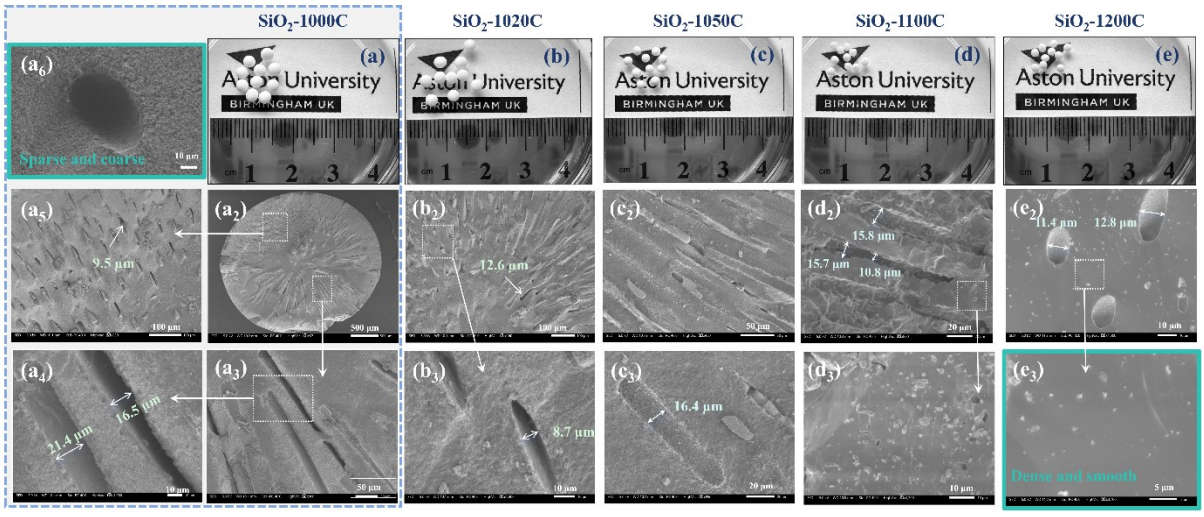

Figure 7-3 Photographic images of (a) SiO_2-1000C, (b) SiO_2-1020C, (c) SiO_2-1050C, (d) SiO_2-1100C, and (e) SiO_2-1200C; SEM images of the cross-sectional views for (a_2-a_6) SiO_2-1000C, (b_2, b_3) SiO_2-1020C, (c_2, c_3) SiO_2-1050C, (d_2, d_3) SiO_2-1100C, and (e_2, e_3) SiO_2-1200C.

The chemical compositions and Co oxidation states of the SiO_2-1000C sample after cobalt incorporation (2Co/SiO_2-1000C) were analysed by XPS spectra. As illustrated in Figure 7-4 (a), the elements Si, O, C, and Co coexisted, though an extremely low peak intensity of Co was observed due to the amorphous structure (Figure 7-1 (b)) and low density (2.2 g/cm^3) of 2Co/SiO_2-1000C. The C 1s spectrum was adventitious carbon originated from the carbon grid during the sampling process. Figure 7-4 (b) displayed the Co 2p spectrum, which was divided into four main weak peaks. Two peaks at 779.8 eV and 794.8 eV corresponded to Co $2p_{3/2}$ and Co $2p_{1/2}$ of Co^{3+}, whereas 781.6 eV and 797.1 eV were associated with Co $2p_{3/2}$ and Co $2p_{1/2}$ of Co^{2+}, respectively [164, 366, 367]. As a matter of fact, a spin energy interval of 15 eV represents the mixed-valence Co_3O_4, which verified the successfully incorporation of Co_3O_4 [294]. This is consistent with the XRD results (Figure 7-1 (b)) and ICP results where the Co content in 2Co/SiO_2-1000C after chemical digestion was measured to be 1.63%. In terms of Si 2p spectra (Figure 7-4 (c)), only one peak cantered at 103.5 eV was detected, which was ascribed to the Si-O bond [368]. In Figure 7-4 (d), the O 1s spectrum could be deconvoluted into two peaks, with 532.8 eV corresponding to Si-O of SiO_2 and 533.4 eV associating with OH groups adsorbed on the surface of SiO_2 [369, 370].

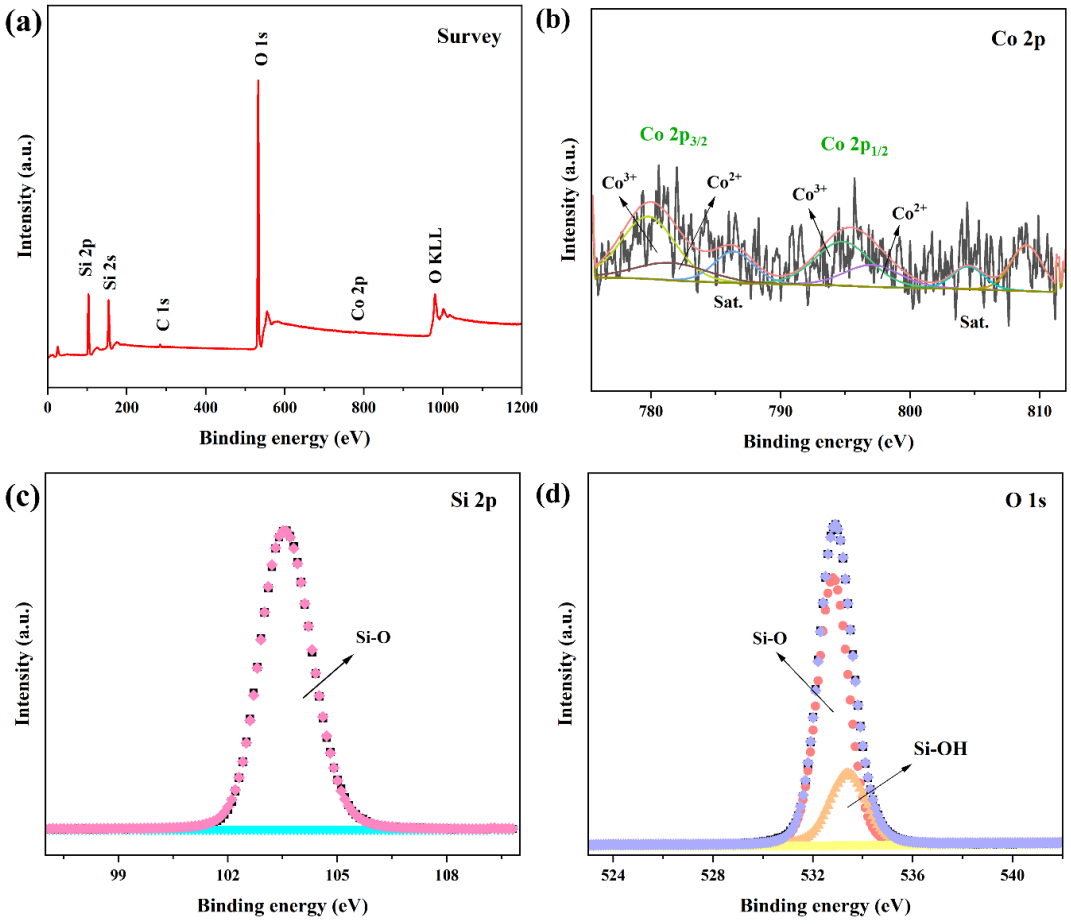

Figure 7-4 (a) XPS survey spectra and high-resolution XPS spectra of (b) Co, (c) Si, and (d) O for the sample 2Co/SiO_2-1000C.

7.3.2 Catalytic degradation of SMX

The catalytic performance of microchannel-structured silica beads was evaluated in a PMS-activated AOPs reaction system for the degradation of SMX aqueous solutions. As shown in Figure 7-5 (a), the self-degradation of SMX was negligible (< 0.1%) and its decontamination by adding PMS only was limited (28.2%). When 2Co/SiO_2-*x*C beads were applied, the SMX removal efficiency significantly enhanced, with 90.7%, 78.4%, 63.5%, 73.9%, and 75.9% for 2Co/SiO_2-1000C, 2Co/SiO_2-1020C, 2Co/SiO_2-1050C, 2Co/SiO_2-1100C, and 2Co/SiO_2-1200C, respectively. As expected, the catalytic performance decreased as the S_{BET} declined for beads sintered at temperatures ranging from 1000˚C to 1050˚C. However, it is important to highlight that 2Co/SiO_2-1100C and 2Co/SiO_2-1200C did not follow this trend, since their densification and low S_{BET} made it challenging to deposit cobalt-based catalysts inside the silica beads. As can be seen from Figure 7-5 (e), only small amounts of cobalt oxides could be loaded onto the 2Co/SiO_2-1100C and 2Co/SiO_2-1200C beads due to their smooth and dense structures, with this issue being even worse for 2Co/SiO_2-1200C. Additionally, the water turbulence caused by the magnetic stirrer during the catalytic reaction easily led to the catalysts peeling off the smooth surface of silica beads due to weak adhesion.

Likewise, when the SMX concentration increased to 40 mg/L (Figure 7-5 (b)), the SMX degradation displayed a similar pattern, with 2Co/SiO_2-1000C (76.3%) > 2Co/SiO_2-1020C (54.1%) > 2Co/SiO_2-1050C (45.3%). The high catalytic efficiency of 2Co/SiO_2-1100C (82.1%) and 2Co/SiO_2-1200C (82.2%) samples was attributed to the involve of relatively more catalyst powder in the reaction system, which was detached during the sample weighing process. As a result, it is inappropriate to compare their SMX removal efficiency with other silica beads. Regardless of these two bizarre samples, the corresponding rate constants at 20 mg/L (Figure 7-5 (c)) and 40 mg/L (Figure 7-5 (d)) also showed a downward trend due to the decrease of S_{BET} (Table 7-1) and porosity (Table 7-2), which is in line with the degradation efficiency. Hence, in this chapter, the specific surface area and porosity of the silica beads played key roles in the catalytic degradation of SMX pollutants.

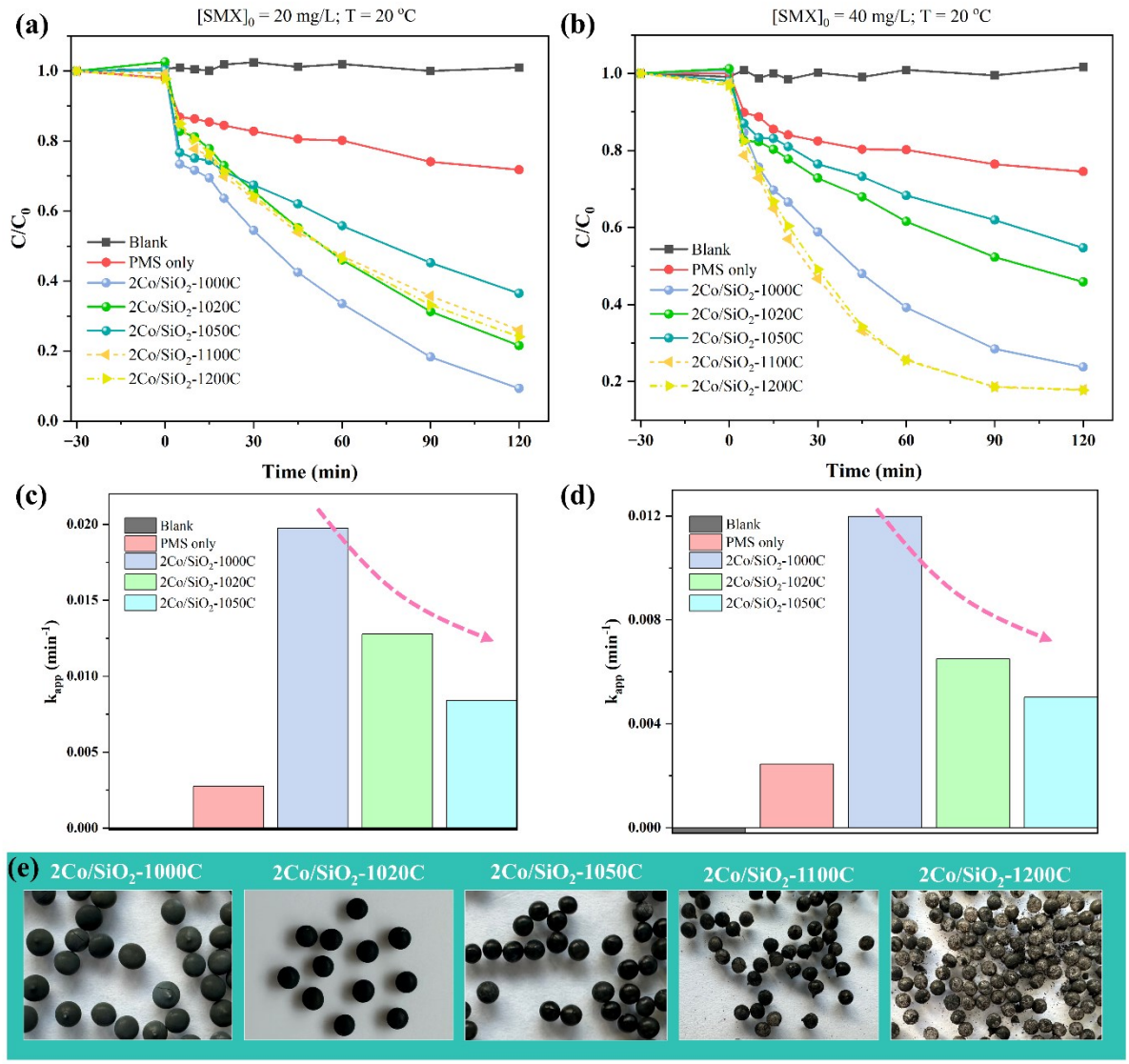

Figure 7-5 (a) Degradation of 20 mg/L SMX using silica beads sintered at different temperatures, (c) the corresponding rate constants; (b) Degradation of 40 mg/L SMX using silica beads sintered at different temperatures, (d) the corresponding rate constants, and (e) photographic images of silica beads sintered at different temperatures. Reaction Conditions: $[PMS]_0$ = 0.1 g/L, $[catalyst]_0$ = 0.2 g/L, r = 150 rpm, T = 20 ˚C.

Furthermore, the influence of initial pH was also carried out by adjusting with either 0.1 M NaOH or 0.1 M HCl, as shown in Figure 7-6 (a). Apparently, 2Co/SiO_2-1000C could degrade organic pollutants in a wide pH range, even in the strong acid (pH = 3) and alkaline (pH = 10) conditions. A slight drop of SMX removal efficiency in acidic solutions (80.4%) was attributed to the consumption of HSO_5^- by H^+, preventing the redox cycles of Co^{2+}/Co^{3+} [341]. In comparison, 86.6% of SMX was removed at pH 10, which is lower than the removal rates at pH 5 (90.7%), pH 7 (96.5%), pH 8 (95.9%), and pH 9 (90.5%). This is because the main reactive species, $SO_4^{\cdot-}$ (E° =2.5-3.1 V, $t_{1/2}$ = 30 μs), could be transformed to ·OH species with lower redox potential (E° =1.8-2.7 V) and a shorter half-life time ($t_{1/2}$ = 20 ns) in strong base solutions [212, 213].

Figure 7-6 (b) depicts the influence of reaction temperature in the range of 20˚C to 50˚C. As expected, the SMX removal efficiency significantly boosted as the reaction temperature went up, with 90.7 % of SMX eliminated at 20˚C and nearly 100% degraded at 30˚C, 40˚C, and 50˚C, respectively, within 120 min. According to the Arrhenius equation (Equation 4-2), the rate constant of the reaction is proportional to the reaction temperature [164]. This implies that as the temperature rises, the probability of overcoming the activation energy barrier also increases. The activation energy was calculated via linear fitting of ln*k* versus 1/T and were determined to be 18.11 kJ/mol for 20 mg/L SMX removal. It was reported that when the E_A values for catalytic reactions were higher than 10-13 kJ/mol, the reactions might be diffusion-controlled [298]. Therefore, the degradation process at the solid-liquid interface in 2Co/SiO_2-1000C might be dominated by the chemical reaction rate. Exposing more and larger pores on the surface of the silica beads might be advantageous to the diffusional resistance, which will be explored in our future work.

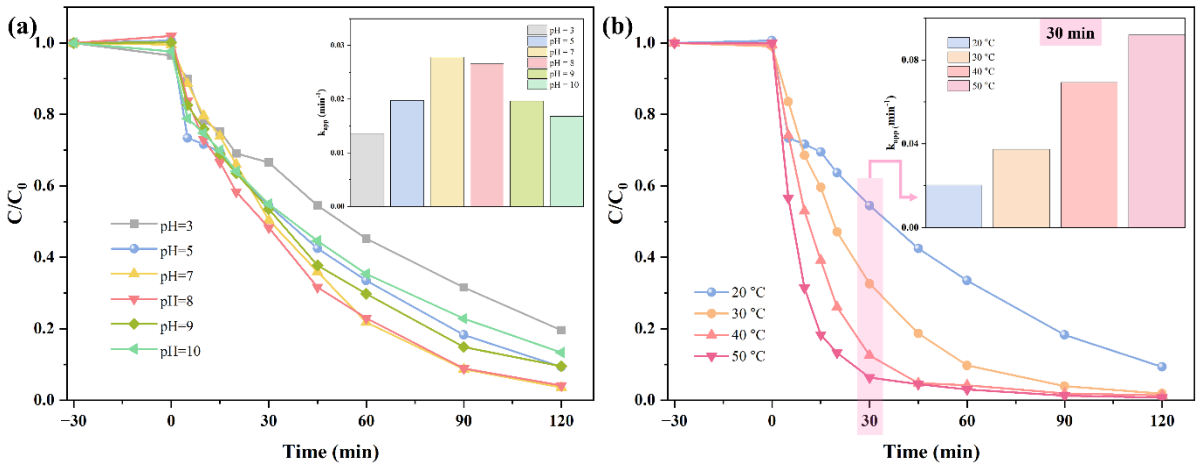

Figure 7-6 (a) Influence of initial pH for the degradation of 20 mg/L SMX, (b) Influence of reaction temperature for the degradation of 20 mg/L SMX (catalyst: 2Co/SiO_2-1000C). Reaction Conditions: $[PMS]_0$ = 0.1 g/L, $[catalyst]_0$ = 0.02 g/L, r = 150 rpm, T = 20 ˚C.

7.3.3 Possible catalytic reaction pathways and mechanism

To distinguish the main reactive species and their contributions to the 2Co/SiO_2-1000C|PMS system, MeOH was used as a quencher of both $SO_4^{\cdot-}$ and ·OH for SMX decontamination, while certain amounts of NaN_3, p-BQ, and tBA were used as scavengers to capture $^1O_2$, $\cdot O_2^-$, ·OH, respectively [300, 301]. As shown in Figure 7-7, when NaN_3 was added, the reaction efficiency was significantly suppressed from 88.6% to 10.2%, suggesting that $^1O_2$ might be the dominant radical. Given that the two main $^1O_2$ quenchers, both NaN_3 and furfuryl, might consume $SO_4^{\cdot-}$ during the quenching experiment [284], additional characterisation techniques such as the electron spin resonance analysis are required to

determine the involvement of $^1O_2$. However, the role of $^1O_2$ in relation to Co_3O_4 catalyst has been extensively investigated [371-373] and is beyond the scope of this research. In contrast, the introduction of p-BQ, tBA, and MeOH caused a suppression of 35.6%, 3.2%, and 54.4% for SMX removal, indicating the pivotal role of both $\cdot O_2^-$ and $SO_4^{\cdot-}$, as well as the negligible contribution of $\cdot OH$, respectively. Besides, Figure 7-7 (b-d)) illuminated that the SMX removal efficiency for p-BQ, MeOH, and tBA levelled off at 5 mM, 400 mM, and 100 mM, respectively, supporting the appropriateness of the scavenger dose in Figure 7-7 (a).

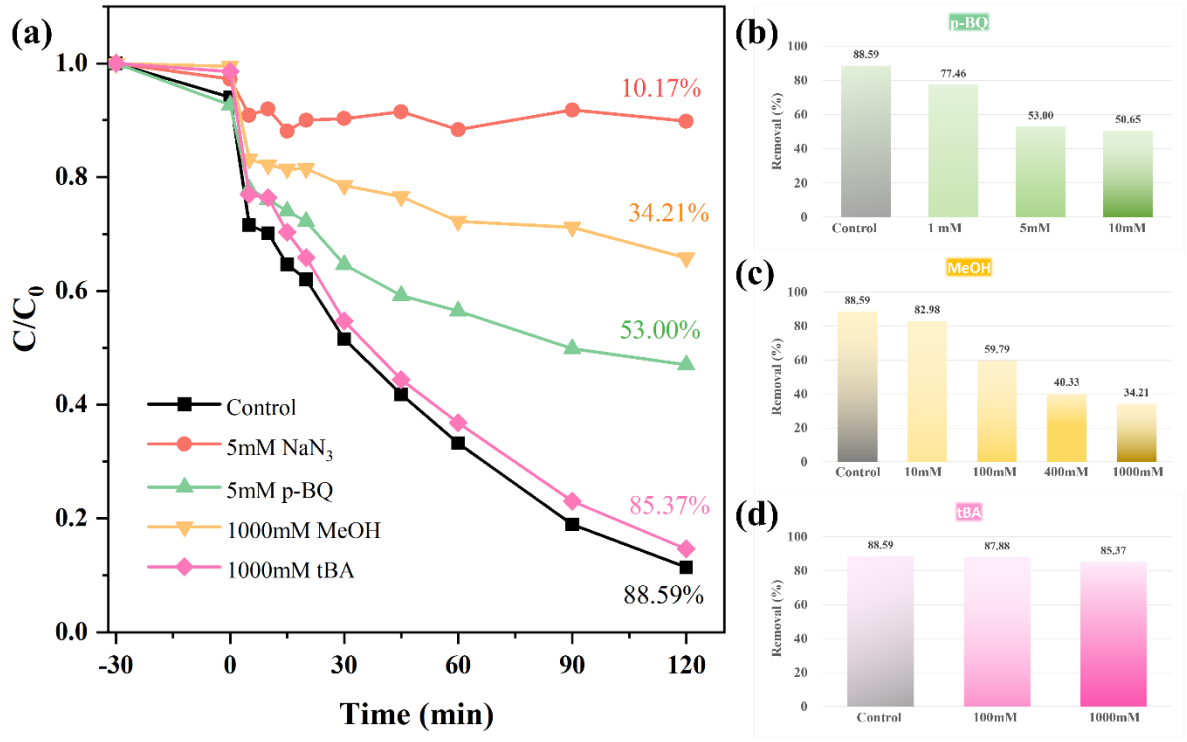

Figure 7-7 (a) Influence of quenching agents on SMX degradation, (b) influence of the p-BQ dosage, (c) influence of MeOH addition, and (d) influence of tBA addition (catalyst: 2Co/SiO₂-1000C). Reaction Conditions: $[PMS]_0$ = 0.1 g/L, $[catalyst]_0$ = 0.02 g/L, r = 150 rpm, T = 20 ˚C.

Based on the quenching experimental results, a possible activation mechanism of SMX decontamination in 2Co/SiO_2-1000C|PMS system was revealed. As shown in Figure 7-8, when the oxidizing agent PMS (HSO_5^-) was introduced, it was activated by the cobalt active phase (Co^{2+}), both on the surface of the silica beads and microchannels. The activation process broke down the PMS molecules into reactive species $SO_4^{\cdot-}$, accompanying with the generation of Co^{3+} (Equation 4-3). At the same time, Co^{3+} accepted electrons from HSO_5^- to yield Co^{2+}, $SO_5^{\cdot-}$, and $^1O_2$ (Equations 4-4, 4-9, 5-1, 5-2), which facilitated the redox cycle of Co^{2+}/Co^{3+} and thus a robust and long-term catalytic mineralisation of organic contaminants. Besides, $\cdot OH$ and $\cdot O_2^-$ radicals were also generated by the side reactions (Equations 4-5, 4-7, 4-8). In short, the degradation of SMX molecules into smaller

intermediates or complete mineralisation (Equation 4-10) was driven by the generated radicals ($SO_4^{\cdot-}$ and $\cdot O_2^-$) and non-radical species ($^1O_2$) in 2Co/SiO_2-1000C|PMS system.

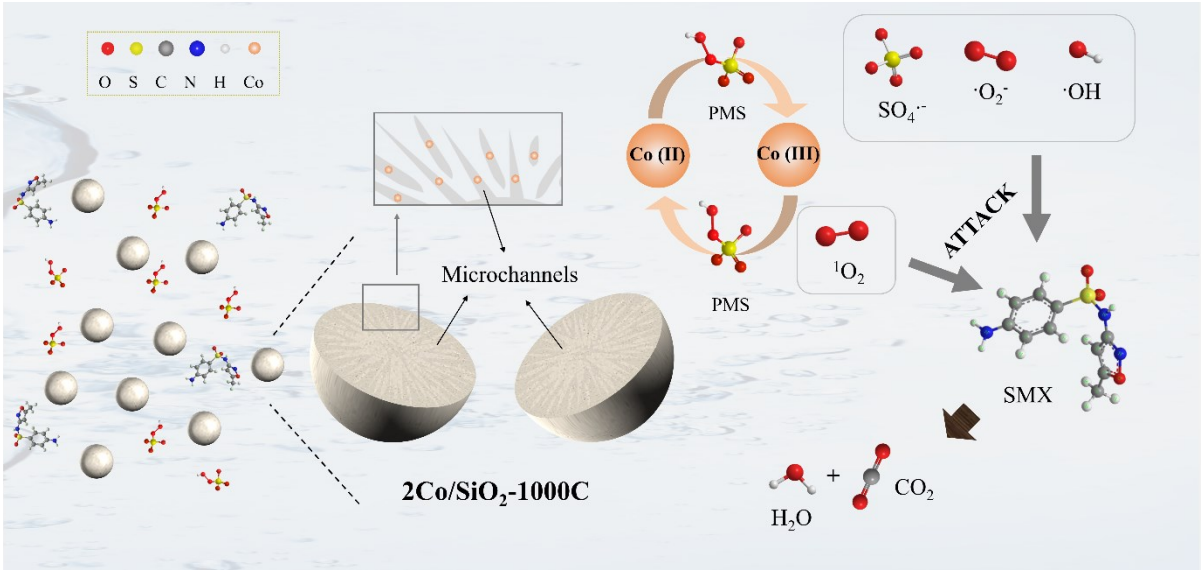

Figure 7-8 A proposed catalytic mechanism for SMX removal by 2Co/SiO_2-1000C|PMS system

7.3.4 Reusability and stability

The cycling reusability and stability of 2Co/SiO_2-1000C was assessed to explore its potential for practical wastewater treatment applications. After each cycle, silica beads were separated by simply pouring out the SMX aqueous solution and rinsing them with deionised water. For comparison, catalyst regeneration was performed by post-sintering at 450 ˚C for 1h prior to the 5th, 9th, and 13th runs. As shown in Figure 7-9, when the silica beads were washed only with deionised water, the SMX degradation efficiency declined from 91.02% to 86.02%, 74.76%, 66.00%, within 120 min in the 2nd, 3rd, and 4th run, respectively. This might be related to the adsorption of reactants and by-products on the surface of the cobalt-based catalysts, which lowered the amounts of exposed active sites, preventing pollutant decontamination efficiency, as evidenced by the SEM images (Figure 7-10 (c_2)).

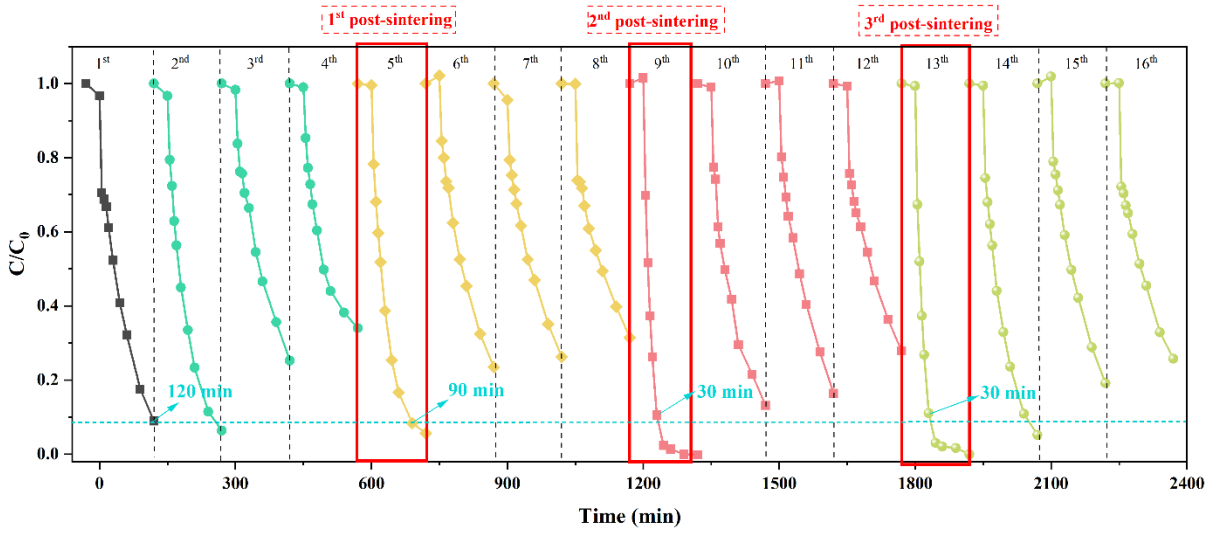

Figure 7-9 Reusability and stability of the sample 2Co/SiO_2-1000C on SMX removal for 16 consecutive cycles with being cleaned by DI water only (1^{st}, 2^{nd}, 3^{rd}, 4^{th}, 6^{th}, 7^{th}, 8^{th}, 10^{th}, 11^{th}, 12^{th}, 14^{th}, 15^{th}, 16^{th}) or being regenerated by post-sintering at 450 ˚C for 1h (5^{th}, 9^{th}, 13^{th}). Reaction Conditions: $[PMS]_0$ = 0.1 g/L, $[catalyst]_0$ = 0.2 g/L, r = 150 rpm, T = 20 ˚C.

Notably, the SMX elimination efficiency was instantly recovered after the post-sintering treatment (5^{th} cycle), achieving a comparable efficiency of 91.57% within 90 minutes, compared to the fresh sample`s 91.02% in 120 min. This tendency was echoed in the second (9^{th} cycle, 89.44% removal in 30 min) and third regenerations (13^{th} cycle, 88.91% removal in 30 min), representing the efficiency of the regeneration method as well as the extraordinary stability and reusability of the silica beads. Likewise, it is rare for the used catalyst to exhibit significantly higher catalytic performance than the fresh one, as the intrinsic properties of catalyst powders typically display a downward trend in the mineralisation of organic pollutants due to the unceasing depletion of exposed active sites. As illustrated in Chapter 4 and Chapter 5, the distinctive catalyst substrates (ceramic beads of 3 mm in diameter) in this research promoted the persistent exposure of accessible cobalt sites and eased the intraparticle diffusion resistance. As shown in Figure 7-10 (d_2-d_3), the sample used for 16 times after regeneration in this chapter also displayed extra larger open channels on the surface (~ 1-2 μm), and thus facilitating the transportation of reactants and products. It is reasonable to infer that the catalytic performance could be further enhanced by removing the thin skin layer on the surface of the silica beads, a hypothesis that will be explored in future work. Finally, the XRD patterns of used silica beads in Figure 7-10 (a) and Figure A27 displayed no obvious changes, indicating the exceptional stability of the beads.

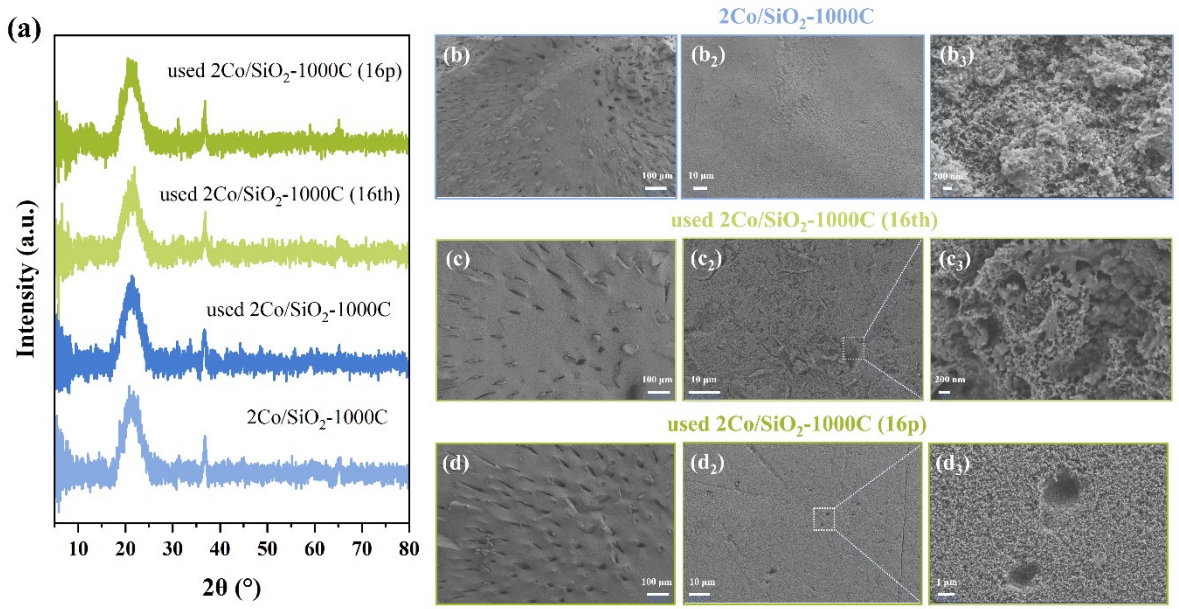

Figure 7-10 (a) XRD patterns of the 2Co/SiO_2-1000C before and after used for once, 16 times, and 16 times after post-sintering; SEM images of the (b) cross-sectional view and (b_2-b_3) surface views of 2Co/SiO_2-1000C; (c) cross-sectional view and (c_2-c_3) surface views of 2Co/SiO_2-1000C used for 16 times (2Co/SiO_2-1000C (16th)); (d) cross-sectional view and (d_2-d_3) surface views of 2Co/SiO_2-1000C used for 16 times after post-sintering (2Co/SiO_2-1000C (16p)).

7.4 Conclusion

In summary, this chapter introduced the preparation of novel microchannel-structured silica beads of 2-3 mm in diameter, depending on the sintering temperature, for the first time by the phase-inversion and sintering-assisted method. The catalytic performance of these beads was examined by the degradation of SMX in a PMS-activated reaction system, with key findings summarised as below:

(1) Before sintering, the diameter of the beads was 3.5 mm, but it reduced to 3.1 mm, 2.8 mm, 2.2 mm, 2.0 mm, and 1.9 mm after being sintered at 1000˚C, 1020˚C, 1050˚C, 1100˚C, and 1200˚C, respectively.

(2) The sintering process also caused a densification and decrease in the specific surface area that significantly affecting the catalytic performance, particularly for beads 2Co/SiO_2-1100C and 2Co/SiO_2-1200C. As expected, 2Co/SiO_2-1000C with the highest specific surface area resulted in the best catalytic activity for the degradation of SMX in the PMS activated AOPs system, which could be ascribed to the sufficient accessible active sites on the substrates, allowing for uniform dispersion of the cobalt-based catalysts.

(3) The influence of reaction temperature and the pH of the initial aqueous SMX solutions demonstrated that this catalytic reaction system (2Co/SiO_2-1000C|PMS) was stable and active across a broad pH range (3.0-10.0), with the reaction being kinetically controlled.

(4) More importantly, 2Co/SiO_2-1000C after being used and regenerated exhibited a significantly higher catalytic performance (13^{th} run, 88.91% in 30 min) than the fresh one (91.02% removal in 120 min), which is similar to the findings observed in Chapter 4 and Chapter 5.

The unique finger-like microstructures, wide pH applicability, and exceptional reusability of these silica beads would be favourable to large-scale diffusion-limited chemical reactions.

Chapter 8 Summary and outlook

Chapter 8 functions as the concluding chapter of this PhD thesis, delivering a thorough summary of the key research findings. Besides, this chapter presents an in-depth exploration of future avenues for the development and application of innovative microchannel-structured ceramic beads, highlighting potential strategies for their synthesis and application.

8.1 Summary

The long-standing challenge of balancing mass transfer resistance with pressure drop in catalytic reactions continues to limit advancements in catalysis and reaction engineering technology. Process intensification holds tremendous promise for cleaner, safer, and more energy efficient process in achieving both satisfying diffusional resistance and pressure drop. However, each process-intensifying technology has its own set of benefits and drawbacks. Innovations for catalyst substrates, particularly spherical beads of millimetres in diameter with unique microstructures, are of highly demanded. This thesis investigated the fabrication and characterisation of innovative microchannel-structured alumina beads and silica beads, featuring finger-like microstructures of tens of microns in width, for the first time. The large bead sizes (2-3 mm in diameter) and distinctive microchannels within the beads are capable of achieving both low pressure drop and reduced mass transfer resistance. These transferable advantages can advance the development of a broad spectrum of heterogeneous catalysis for efficient and durable catalytic reactions, benefiting both academia and industry.

In order to validate the structural advantages of this catalyst substrate design, a PMS-activated AOPs reaction system was applied to degrade organic pollutants under different reaction conditions, e.g. SMX concentrations, reaction temperatures. Chapter 4 examined the catalytic performance of three different configurations of alumina beads, with 2Co/MSCB2 (beads with finger-like microstructures and no outer skin layer) exhibiting the best degradation efficiency towards SMX degradation as compared to 2Co/MSCB0 (beads with a common isotropic pore structure) and 2Co/MSCB1 (beads with radial finger-like microstructures and a denser outer skin-layer), particularly when operating at higher SMX concentrations and higher reaction temperatures. The improved SMX removal efficiency could be attributed to the reduced diffusional resistance and abundant available active sites on the micro-channels within the beads, which experimentally evidenced the structural advantages of this catalyst substrate design.

Considering the inherent small specific surface area of the alpha-phase alumina beads, **Chapter 5** introduced gamma-phase alumina, a commonly used washcoatings with relatively large surface area (202.00 m^2/g), onto the inner surface of the microchannels within the alumina beads using a combined sol-gel and dip-coating method. In this chapter, cobalt-based catalysts were incorporated by two impregnation methods, i.e., two-step sequential impregnation method (2Co/AS*x*) and one-step co-

impregnation method (2Co/AS*x* (co-imp.)). As expected, the degradation efficiency for 2Co/AS*x* and 2Co/AS*x* (co-imp.) greatly improved with the rise in specific surface area (6.31-21.05 m^2/g) under all reaction conditions (10 mg/L SMX, 20 mg/L SMX, 40 mg/L SMX, 20˚C, 40˚C), owing to the increased accessible active sites. However, the specific surface area and sizes of exposed open channels on the bead surface for 2Co/AS*x* and 2Co/AS*x* (co-imp.) varied, which led to discrepancy in the distribution of catalytic active sites and mass transfer resistance. As noted, 2Co/AS*x* (co-imp.) tended to be more easily blocked by γ-Al_2O_3 granules at high γ-Al_2O_3 sol loadings, which boosted the mass transfer resistance. A balanced surface area and open channel size were beneficial to achieve the best catalytic performance.

In **Chapter 5**, the specific surface area of the sample could reach as high as 21.05 m^2/g, and a blockage of the exposed open channels on the bead surface at high γ-Al_2O_3 loadings hindered the growth of more gamma-Al_2O_3 sols, thereby limiting any additional increase in surface area. Therefore, **Chapter 6** introduced an alternative mesoporous material, carbon xerogel, which offered a higher specific surface area (49.33 m^2/g) and additional functionalities compared to γ-Al_2O_3, beneficial to fulfil their potential for diverse applications in the future. It was found that alumina beads with increased SSA by incorporating CX washcoatings (2Co/ACX1) exhibited the highest catalytic activity than the base one (2Co/ACX0) and γ-Al_2O_3 washcoatings (2Co/AS4). Under identical reaction conditions, the reaction rate of 2Co/ACX1 was 10.83 times higher than that of 2Co/ACX0 (labelled as 2Co/MSCB2 in **Chapter 4** and 2Co/AS0 in **Chapter 5**) and 6.39 times higher than that of 2Co/AS4. This was attributed to a synergistic effect resulting from a better dispersion of cobalt catalytic phase (higher SSA), remarkable adsorption capacity of carbon xerogels, the coexistence of two PMS activation species (activated by Co_3O_4 and carbon xerogels), nanoconfined pore effect, and reduced mass transfer resistance, within the AOPs system.

Apart from alumina-based beads detailed in **Chapter 4** to **Chapter 6**, **Chapter 7** highlighted the fabrication and characterisation of silica-based beads of 2-3 mm in diameter. These innovative microchannel-structured silica beads with finger-like microstructures (10-20 μm in width) were prepared using a combined phase-inversion and sintering-assisted method for the first time. Sintering temperature played a key role in the properties of silica beads, such as the specific surface area, the bead sizes, degree of crystallinity, and porosity. This had an enormous impact on the diffusional resistance, and thereby significantly affecting the catalytic performance. In this chapter, 2Co/SiO_2-1000C with the highest specific surface area resulted in the best catalytic activity for the degradation of SMX in the PMS activated AOPs system, which could be ascribed to the sufficient accessible active sites on the substrates, allowing for uniform dispersion of the cobalt-based catalysts.

Most importantly, 2Co/MSCB2 (**Chapter 4**), 2Co/AS4 (**Chapter 5**), and 2Co/SiO_2-1000C (**Chapter 7**) after being used and regenerated all exhibited a significantly higher catalytic performance than the fresh ones. Specifically, 2Co/MSCB2 could degrade 70.83% of SMX in 20 min for the16th run and 70.47% of SMX in 120 min for the fresh sample; 2Co/AS4 could remove 96.32% of SMX in 20 min

for the 9th run and 95.75% of SMX in 120 min for the fresh sample; 2Co/SiO_2-1000C could remove 88.91% of SMX in 20 min for the 13th run and 91.02% of SMX in 120 min for the fresh sample. This could be ascribed to the more and larger exposed open channels on the surface layer of micro-structured ceramic beads, which further reduced the intraparticle diffusion resistance in the AOPs reactions.

Finally, the radical quenching experiment and the catalytic mechanism of all reaction systems – 2Co/MSCB2|PMS (**Chapter 4**), 2Co/AS4|PMS (**Chapter 5**), 2Co/ACX1|PMS (**Chapter 6**), and 2Co/SiO_2-1000C|PMS (**Chapter 7**) towards SMX degradation were explored. We believe that the structural advantages of this catalyst substrate design – distinctive finger-like microstructures within the millimetre-size ceramic beads to balance mass transfer resistance with pressure drop – exceptional stability and reusability of the beads, can advance the development of a broad spectrum of heterogeneous catalysis in large-scale diffusion-limited chemical reactions, including process intensification at the microscale level.

8.2 Outlook

8.2.1 Moving from batch process to continuous flow process

In this PhD research, the feasibility of finger-like microstructures for significantly enhancing mass transfer in millimetre-sized spherical ceramic beads has been experimentally validated. This work focused on the catalytic reactions in a batch process, which was simpler than continuous flow process. For practical applications, it is recommended to conduct reactions in a continuous operation mode, benefiting from its higher efficiency, enhanced scalability flexibility, and improved productivity [374]. The major drawback of moving from batch to continuous manufacturing process for large ceramic beads is the need to operate at low flow rates to minimise diffusional resistance. However, microchannel-structured ceramic beads, any of MSCB2, AS*x*, ACX*x*, or SiO2-*x*C in this thesis, hold great potential for continuous manufacturing process at high flow rates/GHSV. As shown in Figure 8-1, a continuous flow process has been set up, where commercial ceramic beads undergo random stacking, while microchannel-structured ceramic beads are easily packed randomly with higher packing density owing to their uniform spherical shape. Wastewater can be pumped through pipes and gauged using a flow meter before being directed to the catalyst beds, where it reacts with the activate sites. Subsequently, the treated water can be collected in a clean container for further analysis. However, this reaction has not been carried out as planned due to time constraints and will be continued in future projects.

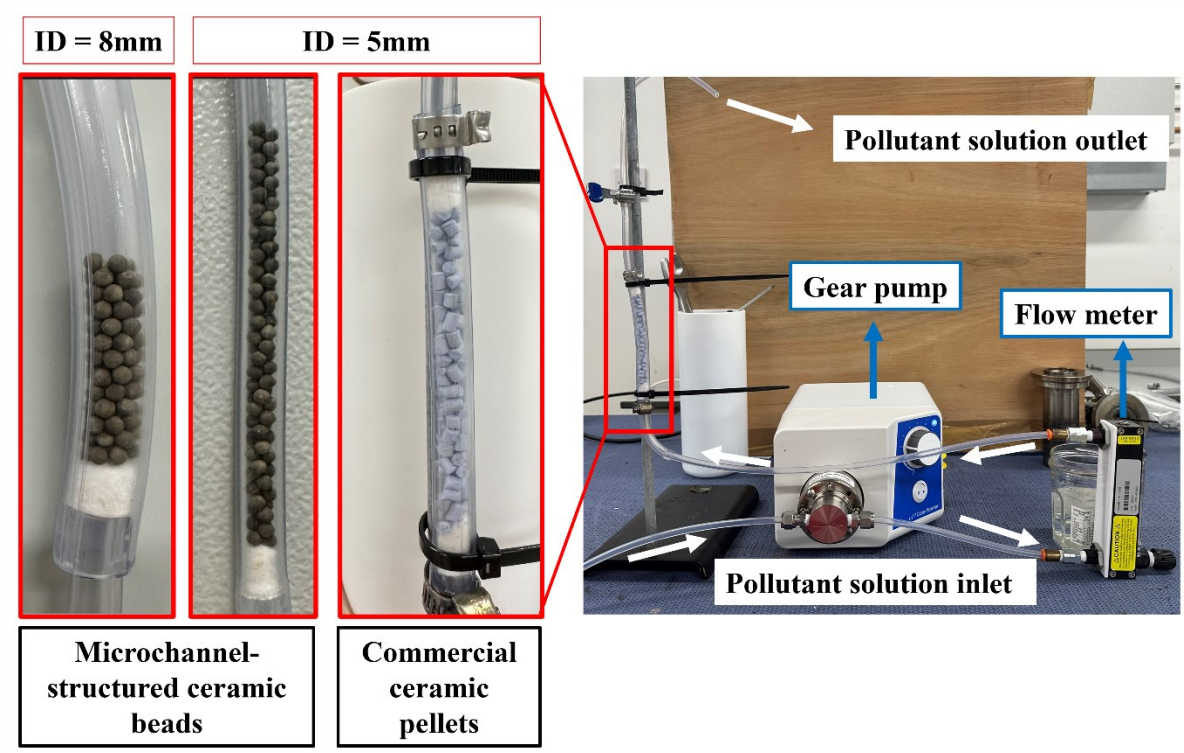

Figure 8-1 Photographic image of the setup for a continuous flow using commercial ceramic beads and microchannel-structured ceramic beads as the catalyst bed.

8.2.2 Transparent microchannel-structured silica beads for photocatalysis

In addition, as noted in **Chapter 7**, higher sintering temperatures resulted in a dense structure of the silica beads. Figure A25 displayed the graphic images of silica beads sintered at temperatures from 1100˚C to 1350˚C for either 3 hours or 6 hours. It can be seen that transparent silica beads can be formed at a limited range of sintering temperatures (1100˚C -1250˚C), with 1100˚C for 6 hours exhibiting a completely transparent morphology for all beads. Figure A25 (i) confirmed that these beads (SiO_2-1100C-6h) are amorphous and non-crystalline, which can serve as catalyst supports for large-scale photocatalysis. Figure 8-2 also shows the graphic images of these transparent microchannel-structured silica beads. Finger-like microstructures were distinctly visible in the cross section, and this is even more obvious in water, as shown in Figure 8-2 (a_1, a_3).

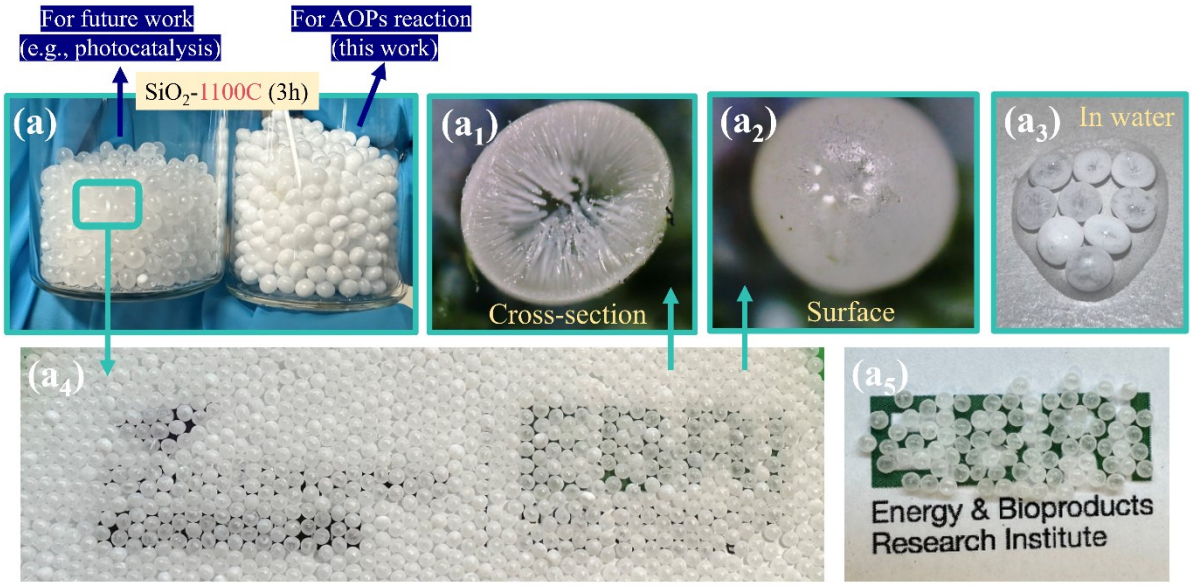

Figure 8-2 Photographic images of (a) transparent and non-transparent silica beads, (a_1) cross-sectional view and (a_2) surface view of transparent silica beads, (a_3) transparent silica beads in two drops of water, (a_4-a_5) transparent silica beads on the printed paper.

8.2.3 Fabrication of other microchannel-structured beads

In this thesis, two inorganic materials, i.e., alpha-phase alumina (high density) and silica (low density) have been applied to prepare innovative microchannel-structured beads. The mass transfer has been validated to be improved owing to the distinctive finger-like microstructures. Heat transfer, however, is another crucial factor that determines the reaction rate and productivity, particularly for temperature-sensitive reactions, such as Fischer-Tropsch synthesis (FTS) [375]. For instance, Akbarzadeh et al. reported that as temperature increased from 200˚C to 280˚C over $95Co_5Mn$/CNT, CO conversion increased from 59.5% to 88.2%, while the C^{5+} selectivity decreased from 83.2% to 61.7% [376]. Moreover, it is known that FTS is a highly exothermic reaction, but the FT product distribution is extremely sensitive to the reaction temperature [377]. Therefore, it is foremost for strategies to maintain a heterogeneous gradient in the catalyst bed to remove the extra heat from the reactor, such as by introducing a heat-conducting additive into/on the catalyst [378], utilising high thermal conductive materials as catalyst support [379], and using micro-structured and monolith-reactors [380]. Otherwise, an inefficient temperature control would shift the product distribution to lighter hydrocarbons, such as undesired methane, because of the formation of localised “hot spots” inside the catalytic bed by exposing parts of the catalysts to too high temperatures [381]. Herein, it is worth noting that high thermal conductive materials, such as copper, are ideal inorganic materials for the preparation of microchannel-structured beads for achieving improved mass and heat transfer.

List of publications

1. J. Zheng, H. Sun, K. Li, Z. Wu*. Catalytic micro-structured ceramic beads and efficacy evaluation through SMX degradation in PMS-activated systems [J]. Separation and purification Technology, 354 (2025): 129060.

2. M. Subramaniam, **J. Zheng**, Z. Wu*, P. Goh, G. Zhang. Visible Light-Driven Organic Pollutant Removal Using Fe-Based Photocatalysts Supported by Wheat Straw Biochar[J]. Catalysts, 14 (2024): 43.

3. F. Chang*, Z. Zhao, W. Bao, J. Wang, **J. Zheng***. Facile construction of novel Z-scheme $Bi_4O_5I_2/CuFe_2O_4$ heterojunctions for NO_2-inhibited and robust photocatalytic removal of NO under visible light, Molecular Catalysis, 547 (2023): 113414.

4. J. Zheng, Z. Wu*. Innovative microchannel-structured beads for microscale process intensification: A case study on water treatment for sulfamethoxazole abatement [J]. Chemical Engineering Journal, 504 (2025): 158527.

5. J. Zheng, F. García-García, Y. Yang, K. Li, T. Bridgwater, H. Yang, Z. Wu*. Carbon xerogel-enhanced microchannel-structured beads for organic pollutants degradation: A novel catalyst for synergistic microscale process intensification [J]. Applied Catalysis B: Environment and Energy, 366 (2025): 125069.

6. J. Zheng, Z. Wu*. Innovative microchannel-structured SiO_2 beads for the degradation of SMX in a PMS-activated advanced oxidation processes, manuscript is ready for submitting to Water Research.

7. S. Wang, Z. Shen, **J. Zheng**, Z. Wu, M. Zhu. Catalytic ammonia cracking using Ni-based catalysts supported on microchannel-structured porous alumina, manuscript is ready for submitting to Journal of Environmental Chemical Engineering.

8. M. Rawlins, **J. Zheng**, Z. Wu*. Cobalt-based catalyst supported on the innovative microchannel-structured alumina beads for selective Fischer-Tropsch (FT) synthesis, manuscript is ready for submitting to Fuel.

9. **J. Zheng**, Z. Wu*, M. Rawlins, T. Bridgwater. Innovative catalyst technology for selective Fischer-Tropsch (FT) Synthesis of bio-fuels and bio-chemicals, Catalysis: Fundamentals and practice, Liverpool, UK, 2022 (**Poster**).

10. **J. Zheng**, M. Rawlins, Z. Wu*. Fischer-Tropsch synthesis via micro-structured catalytic ceramic membranes, 16th International Conference on Catalysis in Membrane Reactors, San Sebastian, Spain, 2023 (**Oral**).

11. J. Zheng, Z. Wu*. Innovative catalyst technology for selective Fischer-Tropsch (FT) synthesis of bio-fuels and bio-chemicals, Huazhong University of Science and Technology, Wuhan, China, 2023

(**Oral**).

12. J. Zheng, Z. Wu*. “Smart pellets”: A new perspective on heterogenous catalysis? Wuhan University of Technology, Wuhan, China, 2024 (**Oral**).

13. J. Zheng, Z. Wu*. “Smart pellets”: A new perspective on heterogenous catalysis? Huazhong University of Science and Technology, Wuhan, China, 2024 (**Oral**).

14. J. Zheng, Z. Wu*. “Smart pellets”: A new perspective on heterogenous catalysis? University of Shanghai for Science and Technology, Shanghai, China, 2024 (**Oral**).

15. J. Zheng, Z. Wu*. “Smart pellets”: A new perspective on heterogenous catalysis? EcoMat Conference 2024, Newcastle Upon Tyne, UK, 2024 (**Oral**).

Reference

1. Chen, L., et al., *Recent advances in water-mediated multiphase catalysis.* Current Opinion in Colloid & Interface Science, 2023. **65**: p.101691.
2. Zou, L., et al., *Product catalysis dual entropy-driven amplification reaction strategy for miRNA-21 detection in glioblastoma.* Microchemical Journal, 2024. **206**: p.111515.
3. Sun, S., et al., *Ni-functionalized Ca@Si yolk-shell nanoreactors for enhanced integrated CO2 capture and dry reforming of methane via confined catalysis.* Applied Catalysis B: Environment and Energy, 2024. **348**: p.123838.
4. Gao, J., et al., *Porous graphene-assisted dynamic Pd catalysis for superior hydrogenation.* Applied Catalysis B: Environment and Energy, 2024. **352**: p.124026.
5. Yan, R., et al., *Hollow PdCuCo medium-entropy alloy on reduced graphene oxide with proton-mediator boosted tandem catalysis for high-performance nitrate reduction.* Applied Catalysis B: Environment and Energy, 2025. **361**: p.124609.
6. Hu, Y., et al., *Research on V2O3 preparation by stepwise catalysis solution-phase hydrogen reduction from shale V-rich solution.* Separation and Purification Technology, 2024. **338**: p.126496.
7. Zou, Y., et al., *Highly sensitive fluorescence detection of chloramphenicol based on product catalysis of tetrahedral DNA framework and fluorescent quenching of MIL-101(Fe).* Food Chem, 2024. **463**(Pt 1): p. 141144.
8. Zhang, J., et al., *Photo-thermal coupling catalysis boosts the degradation of 1,1,1,2-tetrafluoroethane over γ-Al2O3/C3N4 catalyst.* Process Safety and Environmental Protection, 2024. **190**: p. 1105-1113.
9. Zhao, X., et al., *Enhanced Li bonds enable bidirectional sulfur catalysis by a molecular Co-N4 catalyst for lithium-sulfur batteries.* Energy Storage Materials, 2024. **72**: p.103728.
10. Yang, X., et al., *Influence of heterogeneous catalysis on aerothermodynamics at hypersonic speeds based on gas-interface-solid coupling simulation.* International Journal of Heat and Mass Transfer, 2023. **214**: p.124450.
11. Unnikrishnan, P. and D. Srinivas, *Chapter 3 - Heterogeneous Catalysis*, in *Industrial Catalytic Processes for Fine and Specialty Chemicals*, S.S. Joshi and V.V. Ranade, Editors. 2016, Elsevier: Amsterdam. p. 41-111.
12. Lin, L., Z. Zhang, and Y. Min, *Microfluidic plasma: Novel process intensification strategy.* Green Processing and Synthesis, 2022. **11**(1): p. 1064-1071.
13. Grützner, T., D. Ziegenbalg, and R. Güttel, *Process Intensification – An Unbroken Trend in Chemical Engineering.* Chemie Ingenieur Technik, 2018. **90**(11): p. 1823-1831.
14. Chen, Q., J. Deng, and G. Luo, *Process intensification of chemical phosphorus removal in a microreaction system.* Separation and Purification Technology, 2024. **330**: p. 125544.
15. Yue, J., *Green process intensification using microreactor technology for the synthesis of biobased chemicals and fuels.* Chemical Engineering and Processing - Process Intensification, 2022. **177**: p. 109002.
16. Mandić, M., et al., *Effects of Catalyst Activity, Particle Size and Shape, and Process Conditions on Catalyst Effectiveness and Methane Selectivity for Fischer–Tropsch Reaction: A Modeling Study.* Industrial & Engineering Chemistry Research, 2017. **56**(10): p. 2733-2745.
17. Singh, J., A. Montesinos-Castellanos, and K.D.P. Nigam, *Process Intensification for Compact and Micro Heat Exchangers through Innovative Technologies: A Review.* Industrial & Engineering Chemistry Research, 2019. **58**(31): p. 13819-13847.
18. Stankiewicz, A.I., *Process Intensification: Transforming Chemical Engineering.* Chemical Engineering Progress, 2000. **96**: p. 22-34.
19. Zhang, L., et al., *ZSM-5@ceramic foam composite catalyst derived from spent bleaching clay for continuous pyrolysis of waste oil to produce monocyclic aromatic hydrocarbons.* Sci Total Environ, 2024. **926**: p. 171887.

20. Vega, G., et al., *3D honeycomb monoliths with interconnected channels for the sustainable production of dihydroxybenzenes: towards the intensification of selective oxidation processes.* Chemical Engineering and Processing - Process Intensification, 2021. **165**: p.108437.
21. Parsa, M., et al., *Regenerable carbon honeycomb monoliths directly prepared from brown coal: A novel carbon product.* Chemical Engineering Journal, 2023. **471**: p.144699.
22. Mahyon, N.I., et al., *A new hollow fibre catalytic converter design for sustainable automotive emissions control.* Catalysis Communications, 2019. **120**: p. 86-90.
23. Cheng, L., et al., *High efficiency photothermal synergistic degradation of toluene achieved through the utilization of a nickel foam loaded Pt-CeO2 monolithic catalyst.* Separation and Purification Technology, 2024. **333**: p.125742.
24. Patcas, F.C., G.I. Garrido, and B. Kraushaar-Czarnetzki, *CO oxidation over structured carriers: A comparison of ceramic foams, honeycombs and beads.* Chemical Engineering Science, 2007. **62**(15): p. 3984-3990.
25. Munnik, P., P.E. de Jongh, and K.P. de Jong, *Recent developments in the synthesis of supported catalysts.* Chem Rev, 2015. **115**(14): p. 6687-718.
26. Fratalocchi, L., et al., *A novel preparation method for "small" eggshell Co/γ-Al2O3 catalysts: A promising catalytic system for compact Fischer–Tropsch reactors.* Catalysis Today, 2015. **246**: p. 125-132.
27. Usón, L., et al., *VOCs abatement using thick eggshell Pt/SBA-15 pellets with hierarchical porosity.* Catalysis Today, 2014. **227**: p. 179-186.
28. Howeizi, J., et al., *Effect of the distribution and dispersion of palladium nanoparticles on the reducibility and performance of Pd/Al2O3 catalyst in liquid-phase hydrogenation of olefins.* Reaction Kinetics, Mechanisms and Catalysis, 2020. **130**(2): p. 777-795.
29. Othman, N.H., Z. Wu, and K. Li, *Bi1.5Y0.3Sm0.2O3-δ-based ceramic hollow fibre membranes for oxygenseparation and chemicalreactions.* Journal of Membrane Science, 2013. **432**: p. 58-65.
30. Li, T., et al., *X-ray tomography-assisted study of a phase inversion process in ceramic hollow fiber systems – Towards practical structural design.* Journal of Membrane Science, 2017. **528**: p. 24-33.
31. Reay, D., C. Ramshaw, and A. Harvey, *Process Intensification: Engineering for efficiency, sustainability and flexibility*. 2013: Butterworth-Heinemann.
32. Stankiewicz, T.V.G.a.A., *Structure, Energy, Synergy, TimesThe Fundamentals of Process Intensification.* Ind. Eng. Chem. Res., 2009. **48**(5): p. 2465–2474.
33. Stankiewicz, A., Van Gerven, T, Stefanidis, GD, *The Fundamentals of Process Intensification*. 2019, Weinheim, Germany: Wiley. 360.
34. Etim, U.J., Y. Chen, and Z. Zhong, *Cu nanoparticles immobilized in mesopores generated in zeolite for high-performing CO2 hydrogenation to methanol.* Chemical Engineering Journal, 2024. **498**: p.155783.
35. Moulijn, J.A., et al., *Process intensification and process systems engineering: A friendly symbiosis.* Computers & Chemical Engineering, 2008. **32**(1-2): p. 3-11.
36. Freund, H. and K. Sundmacher, *Towards a methodology for the systematic analysis and design of efficient chemical processes.* Chemical Engineering and Processing: Process Intensification, 2008. **47**(12): p. 2051-2060.
37. Sollier, B.M., et al., *Oxidative coupling of methane on Sr/La2O3 catalysts: Improving the catalytic performance using cordierite monoliths and ceramic foams as structured substrates.* Applied Catalysis A: General, 2017. **532**: p. 65-76.
38. Cornejo, I., *A new model for pressure drop correction for series-arranged misaligned monoliths.* Chemical Engineering Science, 2024. **299**: p.120515.
39. Wang, C.-q., et al., *Oil-based drilling cutting pyrolysis residues- phosphogypsum foamed ceramics: Basic properties, microsintering mechanism and heavy metals solidification.* Construction and Building Materials, 2024. **449**: p.138568.

40. Zhang, L., et al., *Preparation of lightweight foam glass-ceramics from copper slag tailings: Secondary aluminum slag as pore-forming agent.* Ceramics International, 2024. **50**(21): p. 43699-43709.
41. Liu, S., et al., *Structure sensitivity reaction of chloroform hydrodechlorination to light olefins using Pd catalysts supported on carbon nanotubes and carbon nanofibers.* J Colloid Interface Sci, 2023. **648**: p. 427-439.
42. Tuo, Y., et al., *Kinetic behavior of Pt catalyst supported on structured carbon nanofiber bed during hydrogen releasing from decalin.* International Journal of Hydrogen Energy, 2016. **41**(25): p. 10755-10765.
43. Liu, X., et al., *Thermoelectric cooler with embedded teardrop-shaped milli-channel heat sink for electronics cooling.* Applied Thermal Engineering, 2024. **244**: p.122763.
44. Abiev, R.S., *Gas-liquid and gas-liquid-solid mass transfer model for Taylor flow in micro (milli) channels: A theoretical approach and experimental proof.* Chemical Engineering Journal Advances, 2020. **4**: p.100065.
45. Khalifa, O., et al., *Ozonation-assisted electro-membrane hybrid reactor for oily wastewater treatment: A methodological approach and synergy effects.* Journal of Cleaner Production, 2021. **289**: p.125764.
46. Tsubaki, S., et al., *Process intensification of the ultra-rapid pyrolysis of bamboo by spatially separated microwave electric and magnetic fields.* Chemical Engineering Journal, 2024: p.156260.
47. Shestakova, A.K., et al., *Orientation of molecules by magnetic field as a new source of information on their structures.* Russian Chemical Bulletin, 2006. **55**(8): p. 1359-1367.
48. Dion, C.M., A. Keller, and O. Atabek, *Orienting molecules using half-cycle pulses.* The European Physical Journal D - Atomic, Molecular, Optical and Plasma Physics, 2001. **14**(2): p. 249-255.
49. Friedrich, B. and D.R. Herschbach, *Spatial orientation of molecules in strong electric fields and evidence for pendular states.* Nature, 1991. **353**(6343): p. 412-414.
50. Sakai, H., et al., *Controlling the Orientation of Polar Molecules with Combined Electrostatic and Pulsed, Nonresonant Laser Fields.* Physical Review Letters, 2003. **90**(8): p. 083001.
51. Bizualem, Y.D. and A.G. Nurie, *A review on recent biodiesel intensification process through cavitation and microwave reactors: Yield, energy, and economic analysis.* Heliyon, 2024. **10**(2): p. e24643.
52. Stankiewicz, A., *Energy Matters: Alternative Sources and Forms of Energy for Intensification of Chemical and Biochemical Processes.* Chemical Engineering Research and Design, 2006. **84**(7): p. 511-521.
53. Chen, T.-L., Y.-H. Chen, and P.-C. Chiang, *Enhanced performance on simultaneous removal of NOx-SO2-CO2 using a high-gravity rotating packed bed and alkaline wastes towards green process intensification.* Chemical Engineering Journal, 2020. **393**: p.124678.
54. Chen, T.-L., et al., *Enhancing NOx removal in a high-gravity rotating packed bed with gaseous ClO2 oxidation-absorption: Kinetic, mass transfer, and cost analysis.* Chemical Engineering Journal, 2023. **469**: p.144072.
55. Liao, M., et al., *Quinary metal oxide NiCoMnCeCaOx nanorod as a multifunctional catalyst towards hydrogen production from ethanol steam reforming: Synergistic effect of polymetallic component.* Chemical Engineering Journal, 2024. **497**: p.154646.
56. Hao, X., et al., *Synchronized sulfur resource recovery and hydrogen production via a self-powered system based on multifunctional Co3S4 catalyst.* International Journal of Hydrogen Energy, 2024. **69**: p. 31-38.
57. Dietrich, W., et al., *Theoretical studies on multifunctional catalysts with integrated adsorption sites.* Chemical Engineering Journal, 2005. **107**(1-3): p. 103-111.
58. Liu, Y., et al., *Fabrication of a family of porous azo polymers with multifunctional adsorption and separation performances.* Journal of Environmental Chemical Engineering, 2024. **12**(5) : p.113653.

59. Lu, Y., et al., *A multi-vortex micromixer based on the synergy of acoustics and inertia for nanoparticle synthesis.* Anal Chim Acta, 2023. **1239**: p. 340742.
60. Zheng, P., et al., *Synergy of micron graphite and fly ash for alkali-activated cementitious material: Electromagnetic absorption characteristics and mechanism.* Cement and Concrete Composites, 2024. **149**: p.105513.
61. Jiang, W., et al., *Metal-free electrified membranes for contaminants oxidation: Synergy effect between membrane rejection and nanoconfinement.* Water Res, 2024. **248**: p. 120862.
62. Behloul, C.R., J.-M. Commenge, and C. Castel, *Influence of the synergy between reaction, heat exchange and membrane separation on the process intensification of the dimethyl ether direct synthesis from carbon dioxide and hydrogen.* Chemical Engineering and Processing - Process Intensification, 2021. **167**: p.108513.
63. Yahiat, F., et al., *Swirl influence on thermo-hydraulic performances within a heat exchanger/reactor with macro deformed walls in laminar flow regime.* Chemical Engineering and Processing - Process Intensification, 2023. **189**: p.109373.
64. Ducrée, J., et al., *Patterning of flow and mixing in rotating radial microchannels.* Microfluidics and Nanofluidics, 2005. **2**(2): p. 97-105.
65. Silveston, P.L. and R.R. Hudgins, *Periodic temperature forcing of catalytic reactions.* Chemical Engineering Science, 2004. **59**(19): p. 4043-4053.
66. Boelhouwer, J.G., H.W. Piepers, and A.A.H. Drinkenburg, *The induction of pulses in trickle-bed reactors by cycling the liquid feed.* Chemical Engineering Science, 2001. **56**(8): p. 2605-2614.
67. Dalanta, F., et al., *Recent implementations of process intensification strategy in membrane-based technology: A review.* Chemical Engineering Research and Design, 2024. **202**: p. 74-91.
68. Jensen, K.F., *Microreaction engineering — is small better?* Chemical Engineering Science, 2001. **56**(2): p. 293-303.
69. Tsachouridis, K., Y. Zhou, and A.D. Anastasiou, *Comparison of three droplet microreactors for the continuous production of nano and micro particles.* Chemical Engineering Science, 2024. **293**: p.119956.
70. Ganapathy, H., et al., *Process intensification characteristics of a microreactor absorber for enhanced CO2 capture.* Applied Energy, 2016. **162**: p. 416-427.
71. Iliuta, I., H. Rasouli, and M.C. Iliuta, *Intensified CO2 capture in wall-coated microreactors with immobilized carbonic anhydrase: Experimental and modeling.* Separation and Purification Technology, 2023. **307**: p.122590.
72. LeViness, S., et al., *Velocys Fischer–Tropsch Synthesis Technology—New Advances on State-of-the-Art.* Topics in Catalysis, 2013. **57**(6-9): p. 518-525.
73. Mohammad, N., et al., *Fischer-Tropsch studies in a 3D-printed stainless steel microchannel microreactor coated with cobalt-based bimetallic-MCM-41 catalysts.* Catalysis Today, 2020. **358**: p. 303-315.
74. Bepari, S., et al., *Co-Ru catalysts with different composite oxide supports for Fischer–Tropsch studies in 3D-printed stainless steel microreactors.* Applied Catalysis A: General, 2020. **608**: p..
75. Truter, L.A., et al., *The application of palladium and zeolite incorporated chip-based microreactors.* Applied Catalysis A: General, 2016. **515**: p. 72-82.
76. John, J.J., et al., *Effect of fluid properties on ultrasound assisted liquid-liquid extraction in a microchannel.* Ultrasonics Sonochemistry, 2018. **42**: p. 68-75.
77. Dong, G., et al., *Advanced oxidation processes in microreactors for water and wastewater treatment: Development, challenges, and opportunities.* Water Res, 2022. **211**: p. 118047.
78. Sattari-Najafabadi, M. and M. Nasr Esfahany, *A liquid-liquid microreactor for the intensification of hexavalent chromium removal from wastewaters.* Journal of Environmental Chemical Engineering, 2021. **9**(6) : p.106543.
79. Suhadolnik, L., et al., *Continuous photocatalytic, electrocatalytic and photo-electrocatalytic degradation of a reactive textile dye for wastewater-treatment processes: Batch, microreactor*

and scaled-up operation. Journal of Industrial and Engineering Chemistry, 2019. **72**: p. 178-188.
80. Tan, Z., et al., *Research progress and application exploration of typical microreactor technologies for health monitoring and disease Diagnosis/Treatment.* Chemical Engineering Journal, 2024. **499**: p.155938.
81. Feng, J., et al., *Microfluidic trends in drug screening and drug delivery.* TrAC Trends in Analytical Chemistry, 2023. **158**: p.116821.
82. Ghaffari, R., et al., *State of Sweat: Emerging Wearable Systems for Real-Time, Noninvasive Sweat Sensing and Analytics.* ACS Sens, 2021. **6**(8): p. 2787-2801.
83. Fukuda, T., et al., *Double-layered catalytic wall-plate microreactor for process intensification of dry reforming of methane: Reaction activity improvement and coking suppression.* Chemical Engineering and Processing - Process Intensification, 2021. **164**: p.108406.
84. Yue, J., *Green process intensification using microreactor technology for the synthesis of biobased chemicals and fuels.* Chemical Engineering and Processing - Process Intensification, 2022. **177**: p.109002.
85. Gorges, R., S. Meyer, and G. Kreisel, *Photocatalysis in microreactors.* Journal of Photochemistry and Photobiology A: Chemistry, 2004. **167**(2-3): p. 95-99.
86. Chen, Y., et al., *Facile fabrication of rGO/PPy/nZVI catalytic microreactor for ultrafast removal of p-nitrophenol from water.* Applied Catalysis B: Environmental, 2023. **324**: p.122270.
87. Puigmartí-Luis, J., *Microfluidic platforms: A mainstream technology for the preparation of crystals.* Chemical Society Reviews, 2014. **43**(7): p. 2253-2271.
88. Zong, J. and J. Yue, *Continuous Solid Particle Flow in Microreactors for Efficient Chemical Conversion.* Industrial & Engineering Chemistry Research, 2022. **61**(19): p. 6269-6291.
89. Wang, X., et al., *Scale-up of microreactor: Effects of hydrodynamic diameter on liquid–liquid flow and mass transfer.* Chemical Engineering Science, 2020. **226**: p.115838.
90. Saber, M., J.M. Commenge, and L. Falk, *Microreactor numbering-up in multi-scale networks for industrial-scale applications: Impact of flow maldistribution on the reactor performances.* Chemical Engineering Science, 2010. **65**(1): p. 372-379.
91. Zhang, J., et al., *Design and Scaling Up of Microchemical Systems: A Review.* Annu Rev Chem Biomol Eng, 2017. **8**: p. 285-305.
92. Yang, Z., M. Liu, and C. Lin, *Photocatalytic activity and scale-up effect in liquid–solid mini-fluidized bed reactor.* Chemical Engineering Journal, 2016. **291**: p. 254-268.
93. Krummradt, H., U. Koop, and J. Stoldt. *Experiences with the use of microreactors in organic synthesis*. in *Microreaction Technology: Industrial Prospects*. 2000. Berlin, Heidelberg: Springer Berlin Heidelberg.
94. Elvira, K.S., et al., *The past, present and potential for microfluidic reactor technology in chemical synthesis.* Nat Chem, 2013. **5**(11): p. 905-15.
95. Khader, E.H., et al., *Current trends for wastewater treatment technologies with typical configurations of photocatalytic membrane reactor hybrid systems: A review.* Chemical Engineering and Processing - Process Intensification, 2023. **192**: p.109503.
96. Mohsen Alardhi, S., J.M. Alrubaye, and T.M. Albayati, *Removal of Methyl Green Dye from simulated waste water using Hollow Fiber Ultrafiltration Membrane.* IOP Conference Series: Materials Science and Engineering, 2020. **928**(5): p. 052020.
97. Khoiruddin, K., et al., *Enhanced hydrogen production in membrane reactors: A novel approach.* International Journal of Hydrogen Energy, 2024. **83**: p. 946-966.
98. Xue, K., et al., *Hydrogen production by glucose reforming using a nickel hollow fiber membrane reactor.* Journal of Membrane Science, 2024. **695**: p.122488.
99. Gallucci, F., L. Paturzo, and A. Basile, *An experimental study of CO2 hydrogenation into methanol involving a zeolite membrane reactor.* Chemical Engineering and Processing: Process Intensification, 2004. **43**(8): p. 1029-1036.

100. Yue, W., et al., *Highly Selective CO2 Conversion to Methanol in a Bifunctional Zeolite Catalytic Membrane Reactor.* Angewandte Chemie International Edition, 2021. **60**(33): p. 18289-18294.
101. Zhang, W., et al., *Hydrogen-driven autotrophic degradation of halogenated organic pollutants in a membrane biofilm reactor: Advances and challenges.* Chemical Engineering Journal, 2024. **479**: p.147754.
102. Boese-Cortés, I., F.A. Díaz-Alvarado, and A.L. Prieto, *Biocatalytic membrane reactor modeling for fermentative hydrogen production from wastewater: A review.* International Journal of Hydrogen Energy, 2023. **48**(35): p. 13024-13043.
103. Chen, L., P. Xu, and H. Wang, *Photocatalytic membrane reactors for produced water treatment and reuse: Fundamentals, affecting factors, rational design, and evaluation metrics.* Journal of Hazardous Materials, 2022. **424**: p.127493.
104. Kim, H., et al., *Novel propane dehydrogenation process design integrated with membrane reactor and solid oxide fuel cell: Economic and environmental aspects.* Journal of Environmental Chemical Engineering, 2023. **11**(5) : p.110830.
105. Lei, S., et al., *Simultaneous generation of electricity, ethylene and decomposition of nitrous oxide via protonic ceramic fuel cell membrane reactor.* Journal of Energy Chemistry, 2023. **77**: p. 359-368.
106. Behroozi, A.H. and R. Xu, *Photocatalytic CO2 reduction: Photocatalysts, membrane reactors, and hybrid processes.* Chem Catalysis, 2023. **3**(3) : p.100550.
107. Jiao, H., et al., *On-demand continuous H2 release by methanol dehydrogenation and reforming via photocatalysis in a membrane reactor.* Green Chemistry, 2022. **24**(21): p. 8345-8354.
108. Biao, W., et al., *An innovative strategy for polyester microplastic fiber elimination from laundry wastewater via coupled separation and degradation using TiO2-based photocatalytic membrane reactor.* Separation and Purification Technology, 2025. **356**: p.129929.
109. Song, W., et al., *Mechanistic analysis of membrane fouling by microplastics in a gravity-driven ceramic membrane reactor for roofing rainwater reuse.* Journal of Membrane Science, 2024. **707**: p.122995.
110. Qin, Q., et al., *A review of flow field characteristics in submerged hollow fiber membrane bioreactor: Micro-interface, module and reactor.* J Environ Manage, 2024. **365**: p. 121525.
111. Gapp, E. and P. Pfeifer, *Membrane reactors for hydrogen production from renewable energy sources.* Current Opinion in Green and Sustainable Chemistry, 2023. **41**: p.100800.
112. Hyeon, M.-H., et al., *Equilibrium shift, poisoning prevention, and selectivity enhancement in catalysis via dehydration of polymeric membranes.* Nature Communications, 2023. **14**(1) : p.1673.
113. Poto, S., F. Gallucci, and M. Fernanda Neira d'Angelo, *Direct conversion of CO2 to dimethyl ether in a fixed bed membrane reactor: Influence of membrane properties and process conditions.* Fuel, 2021. **302**: p.121080.
114. Zhang, Y., et al., *Effect of the main properties of membrane materials on denitrification of hydrogen-based membrane biofilm reactors (H2-MBfRs).* Journal of Water Process Engineering, 2024. **66**: p.105975.
115. Choi, H., et al., *CFD analysis and scale up of a baffled membrane reactor for hydrogen production by steam methane reforming.* Computers & Chemical Engineering, 2022. **165**: p.107912.
116. Chompupun, T., et al., *Experiments, modeling and scaling-up of membrane reactors for hydrogen production via steam methane reforming.* Chemical Engineering and Processing - Process Intensification, 2018. **134**: p. 124-140.
117. Ma, R., et al., *Scalability of multitube membrane modules for hydrogen separation: Technical considerations, issues and solutions.* Journal of Membrane Science, 2018. **564**: p. 887-896.
118. Yoo, J.Y., et al., *A computational-fluid-dynamics study on scaling up a single flat membrane reactor for on-site hydrogen production.* Chemical Engineering Research and Design, 2023. **200**: p. 670-681.

119. Dong, Z., et al., *Scale-up of micro- and milli-reactors: An overview of strategies, design principles and applications.* Chemical Engineering Science: X, 2021. **10**: p.100097.
120. Dong, H., et al., *Iron oxide and alumina nanocomposites applied to Fischer-Tropsch synthesis.* Chem Commun (Camb), 2011. **47**(13): p. 4019-21.
121. Zhang, Q., J. Kang, and Y. Wang, *Development of Novel Catalysts for Fischer-Tropsch Synthesis: Tuning the Product Selectivity.* ChemCatChem, 2010. **2**(9): p. 1030-1058.
122. Khodakov, A.Y., W. Chu, and P. Fongarland, *Advances in the Development of Novel Cobalt Fischer−Tropsch Catalysts for Synthesis of Long-Chain Hydrocarbons and Clean Fuels.* Chemical Reviews, 2007. 107: p.1692-1744.
123. Sun, P., et al., *Nickel foam based monolithic catalyst supporting transition metal oxides for toluene combustion: Experimental and theoretical study of interfacial synergistic oxidation and water resistance.* Chemical Engineering Journal, 2024. **483**: p.149176.
124. Zhang, J., et al., *Highly stable 3D-printed monolithic Al2O3-supported Ni-based structured catalysts for dry reforming of methane.* Additive Manufacturing, 2024. **80**: p.103983.
125. Liu, H., et al., *S-scheme Bi12TiO20/Bi4Ti3O12 heterojunction immobilized on 3D-printed support as a monolithic photocatalyst for NO removal.* Applied Surface Science, 2024. **654**: p. 159477.
126. Shao, Y., et al., *Co/SBA-16 coating supported on a 3D-printed ceramic monolith for peroxymonosulfate-activated degradation of Levofloxacin.* J Colloid Interface Sci, 2023. **643**: p. 137-150.
127. Liu, J., et al., *Preparation of β-SiAlON/SiC composite ceramic foam filters and their oxidation resistance.* Ceramics International, 2024. **50**(20): p. 38200-38208.
128. Wang, C., et al., *A review on recent development of foam Ceramics prepared by particle-stabilized foaming technique.* Adv Colloid Interface Sci, 2024. **330**: p. 103198.
129. Zhao, K., et al., *Constructing high-performance nanofiltration membranes using nanofiber supports: Effects of structural stability and polyvinyl alcohol interlayers.* Separation and Purification Technology, 2024. **345**: p.127445.
130. Zou, Q., et al., *Construction of Ru-doped Co nanoparticles loaded on carbon nanosheets in-situ grown on carbon nanofibers as self-supported catalysts for efficient hydrogen evolution reaction.* International Journal of Hydrogen Energy, 2024. **85**: p. 758-765.
131. Wang, S., et al., *3D self-supporting core-shell silicon-carbon nanofibers-based host enables confined Li+ deposition for lithium metal battery.* Nano Energy, 2024. **131**: p.110255.
132. Kuhlmann, K., et al., *A bio-inspired, monolithic catalyst support structure for optimized conductive heat removal in catalytic reactors.* Chemical Engineering Research and Design, 2024. **201**: p. 534-550.
133. Baharudin, L. and M.J. Watson, *Monolithic substrate support catalyst design considerations for steam methane reforming operation.* Reviews in Chemical Engineering, 2018. **34**(4): p. 481-501.
134. Avila, P., M. Montes, and E.E. Miró, *Monolithic reactors for environmental applications.* Chemical Engineering Journal, 2005. **109**(1-3): p. 11-36.
135. Jacquot, C., et al., *A multi-scale study of 3D printed Co-Al2O3 catalyst monoliths versus spheres.* Chemical Engineering Journal Advances, 2023. **16**: p.100538.
136. Ibrahim, H.A., et al., *Experimental and numerical investigations of flow through catalytic converters.* International Journal of Heat and Mass Transfer, 2018. **127**: p. 546-560.
137. Zuo, Q., et al., *NO catalytic performance analysis of gasoline engine tapered variable cell density carrier catalytic converter.* Environ Sci Pollut Res Int, 2022. **29**(1): p. 1413-1429.
138. Giani, L., G. Groppi, and E. Tronconi, *Mass-Transfer Characterization of Metallic Foams as Supports for Structured Catalysts.* Industrial & Engineering Chemistry Research, 2005. **44**(14): p. 4993-5002.

139. Xia, X.-L., et al., *Prediction of spectral radiative property based on the microscopic ligament morphology and pore-level structure of open-cell alumina foam.* Infrared Physics & Technology, 2022. **126**: p.104331.
140. Liu, Y., et al., *High performance structured platelet milli-reactor filled with supported cobalt open cell SiC foam catalyst for the Fischer–Tropsch synthesis.* Chemical Engineering Journal, 2013. **222**: p. 265-273.
141. Aguirre, A., et al., *Controlling the selectivity in the Fischer-Tropsch synthesis using foam catalysts: An integrated experimental and modeling approach.* Chemical Engineering Journal, 2021. **409**: p.128139.
142. Barokh, H., M. Siavashi, and R. Tousi, *The role of voronoi catalytic porous foam in reactive flow for hydrogen production through steam methane reforming (SMR): A pore-scale investigation.* International Journal of Hydrogen Energy, 2024. In press.
143. Yeetsorn, R., S. Tungkamani, and Y. Maiket, *Fabrication of a Ceramic Foam Catalyst Using Polymer Foam Scrap via the Replica Technique for Dry Reforming.* ACS Omega, 2022. **7**(5): p. 4202-4213.
144. Ochuma, I.J., et al., *Three-phase photocatalysis using suspended titania and titania supported on a reticulated foam monolith for water purification.* Catalysis Today, 2007. **128**(1-2): p. 100-107.
145. Murr, C.G., et al., *Foamed glass functionalized with iron compounds: A strategic material for heterogeneous photocatalysis.* Materials Chemistry and Physics, 2023. **304**: p.127880.
146. Twigg, M.V. and J.T. Richardson, *Fundamentals and Applications of Structured Ceramic Foam Catalysts.* Industrial & Engineering Chemistry Research, 2007. **46**(12): p. 4166-4177.
147. Yanxia, L., et al., *Catalytic Combustion of CH4/Air Mixtures Over Metal Foam Monoliths.* Energy Procedia, 2015. **66**: p. 249-252.
148. Gao, F., et al., *Nickel foam supported CuCe mixed metal oxide as monolith catalyst for NO removal.* Chemical Engineering Journal, 2023. **474**: p.145713.
149. Zhang, Y., et al., *High-strength, 3D interconnected alumina ceramic foams with high porosity comparable to aerogels.* Ceramics International, 2023. **49**(23): p. 39070-39075.
150. Colombo, P., *Conventional and novel processing methods for cellular ceramics.* Philosophical Transactions of the Royal Society A: Mathematical, Physical and Engineering Sciences, 2006. **364**(1838): p. 109-124.
151. Song, J., et al., *Mechanically stable and highly permeable porous alumina foam with immobilized copper hexacyanoferrate (Cu-HCF@AF) for the removal of radioactive cesium (137Cs) from seawater.* Separation and Purification Technology, 2025. **353**: p.128504.
152. Al-Qutub, A., et al., *Evaluation of durability of alumina, silicon carbide and siliconized silicon carbide foams as absorber materials for concentrated solar power applications.* Solar Energy, 2022. **242**: p. 45-55.
153. Al-Alam, J., et al., *Measuring current-use pesticides in air: A comparison of silicon carbide foam to XAD as passive air samplers.* Environmental Technology & Innovation, 2021. **24**: p.101876.
154. Khristoforova, I.A., A.I. Khristoforov, and E.A. Timakov, *Characteristics of heat insulating foam aluminum silicate under change of heat treatment parameters.* IOP Conference Series: Materials Science and Engineering, 2020. **896**(1): p. 012082.
155. Long, Y., et al., *Preparation of foam glass ceramics from hazardous waste vitrification slag with the addition of Na2CO3.* Construction and Building Materials, 2023. **404**: p.133225.
156. Luo, Y., et al., *Preparation of sintered foamed ceramics derived entirely from coal fly ash.* Construction and Building Materials, 2018. **163**: p. 529-538.
157. Xia, F., S. Cui, and X. Pu, *Performance study of foam ceramics prepared by direct foaming method using red mud and K-feldspar washed waste.* Ceramics International, 2022. **48**(4): p. 5197-5203.

158. Zhang, X., et al., *Comprehensive utilization of red mud and blast furnace dust: Synergistic preparation of direct reduced iron and functional ceramsite.* Separation and Purification Technology, 2024. **345**: p.127436.
159. Chen, X., A. Lu, and G. Qu, *Preparation and characterization of foam ceramics from red mud and fly ash using sodium silicate as foaming agent.* Ceramics International, 2013. **39**(2): p. 1923-1929.
160. Thompson, C.R., et al., *Evaluation of the use of ceramic foams as catalyst supports for reverse-flow combustors.* Chemical Engineering Journal, 2013. **221**: p. 44-54.
161. Dimopoulos Eggenschwiler, P., et al., *Ceramic foam substrates for automotive catalyst applications: fluid mechanic analysis.* Experiments in Fluids, 2009. **47**(2): p. 209-222.
162. Liu, X., et al., *Investigation of spherical alumina supported catalyst for carbon nanotubes production from waste polyethylene.* Process Safety and Environmental Protection, 2021. **146**: p. 201-207.
163. Fajardo, H.V. and L.F.D. Probst, *Production of hydrogen by steam reforming of ethanol over Ni/Al2O3 spherical catalysts.* Applied Catalysis A: General, 2006. **306**: p. 134-141.
164. Zheng, J., et al., *Catalytic micro-structured ceramic beads and efficacy evaluation through SMX degradation in PMS-activated systems.* Separation and Purification Technology, 2025. **354**: p.129060.
165. Wärnå, J., et al., *Influence of intraparticle reaction–diffusion in a catalytic reactor.* Chemical Engineering Journal, 2002. **90**(1): p. 209-212.
166. Afandizadeh, S. and E.A. Foumeny, *Design of packed bed reactors: guides to catalyst shape, size, and loading selection.* Applied Thermal Engineering, 2001. **21**(6): p. 669-682.
167. Wu, Z., et al., *A novel inorganic hollow fiber membrane reactor for catalytic dehydrogenation of propane.* AIChE Journal, 2009. **55**(9): p. 2389-2398.
168. Gimeno, M.P., et al., *Combination of a Two-Zone Fluidized Bed Reactor with a Pd hollow fibre membrane for catalytic alkane dehydrogenation.* Chemical Engineering Journal, 2009. **155**(1-2): p. 298-303.
169. Kingsbury, B.F.K., Z. Wu, and K. Li, *A morphological study of ceramic hollow fibre membranes: A perspective on multifunctional catalytic membrane reactors.* Catalysis Today, 2010. **156**(3-4): p. 306-315.
170. Li, T., Z. Wu, and K. Li, *Co-extrusion of electrolyte/anode functional layer/anode triple-layer ceramic hollow fibres for micro-tubular solid oxide fuel cells–electrochemical performance study.* Journal of Power Sources, 2015. **273**: p. 999-1005.
171. Prasetya, N., et al., *Compact hollow fibre reactors for efficient methane conversion.* Journal of the European Ceramic Society, 2017. **37**(16): p. 5281-5287.
172. Kingsbury, B.F.K. and K. Li, *A morphological study of ceramic hollow fibre membranes.* Journal of Membrane Science, 2009. **328**(1-2): p. 134-140.
173. Lee, M., et al., *Formation of micro-channels in ceramic membranes – Spatial structure, simulation, and potential use in water treatment.* Journal of Membrane Science, 2015. **483**: p. 1-14.
174. Naidu Subramaniam, M., et al., *Enhancing nanofiltration in thin film nanocomposite membranes using Bi-Metal modified biochar nanofillers.* Separation and Purification Technology, 2025. **352**: p.128236.
175. Ye, D., et al., *High sphericity and diameter controllable B4C ceramic pellets prepared via simple low-cost PVA assisted planet-type rotation method.* Ceramics International, 2021. **47**(1): p. 836-841.
176. Santos, C.J.E., et al., *A Forming Technique to Produce Spherical Ceramic Beads Using Sodium Alginate as a Precursor Binder Phase.* Journal of the American Ceramic Society, 2013. **96**(11): p. 3379-3388.
177. Santos, C.J.E., et al., *Design and fabrication of ceramic beads by the vibration method.* Journal of the European Ceramic Society, 2015. **35**(13): p. 3587-3594.

178. Yun, H.-s., S.-e. Kim, and Y.-t. Hyun, *Preparation of bioactive glass ceramic beads with hierarchical pore structure using polymer self-assembly technique.* Materials Chemistry and Physics, 2009. **115**(2-3): p. 670-676.
179. Chalkia, V., E. Marathoniti, and V.N. Stathopoulos, *A facile method for the preparation of ceramic beads with hierarchical porosity.* Ceramics International, 2017. **43**(18): p. 17238-17242.
180. Truter, L.A., et al., *Washcoating of H-ZSM-5 zeolite onto steel microreactor plates – Filling the void space between zeolite crystallite agglomerates particles.* Chemical Engineering Journal, 2014. **257**: p. 148-158.
181. Yue, J., *Multiphase flow processing in microreactors combined with heterogeneous catalysis for efficient and sustainable chemical synthesis.* Catalysis Today, 2018. **308**: p. 3-19.
182. Li, L., et al., *Direct synthesis of zeolite coatings on cordierite supports by in situ hydrothermal method.* Applied Catalysis A: General, 2005. **292**: p. 312-321.
183. He, L., et al., *Preparation of Pt/γ-Al2O3 catalyst coating in microreactors for catalytic methane combustion.* Chemical Engineering Journal, 2020. **380**: p.122424.
184. Baloyi, S.J. and J.A. Moma, *Catalytic wet air oxidation of phenol by cordierite honeycomb washcoated with Al/Zr pillared bentonite in a plug flow reactor.* Journal of Environmental Chemical Engineering, 2020. **8**(5) : p.104186.
185. Han, B., et al., *High-entropy perovskite oxide washcoated porous alumina ceramic as a superb catalyst for activating peroxymonosulfate to eliminate refractory organic pollutants.* Chemical Engineering Journal, 2023. **455**: p.140828.
186. Bakker, J.J., et al., *Heterogeneously Catalyzed Continuous-Flow Hydrogenation Using Segmented Flow in Capillary Columns.* ChemCatChem, 2011. **3**(7): p. 1155-1157.
187. Sebastián, V., et al., *Preparation of zeolite films as catalytic coatings on microreactor channels.* Microporous and Mesoporous Materials, 2008. **115**(1-2): p. 147-155.
188. Santos, D.F.M., et al., *Degradation and mineralization of oxalic acid using catalytic wet oxidation over carbon coated ceramic monoliths.* Journal of Environmental Chemical Engineering, 2021. **9**(4) : p.105369.
189. Albornoz, L.L., et al., *Degradation and mineralization of erythromycin by heterogeneous photocatalysis using SnO2-doped TiO(2) structured catalysts: Activity and stability.* Chemosphere, 2021. **268**: p. 128858.
190. Ding, J., et al., *Enhancing the active site accessibility of cobalt-silica catalysts for improved Fenton-like performance.* Chemical Engineering Journal, 2022. **432**: p.134435.
191. Amrousse, R., et al., *Preparation of monolithic catalysts for space propulsion applications*, in *Scientific Bases for the Preparation of Heterogeneous Catalysts - Proceedings of the 10th International Symposium, Louvain-la-Neuve, Belgium, July 11-15, 2010*. 2010. p. 755-758.
192. Protasova, L.N., et al., *A kinetic study of the liquid-phase hydrogenation of citral on Au/TiO2 and Pt–Sn/TiO2 thin films in capillary microreactors.* Applied Catalysis A: General, 2011. **399**(1-2): p. 12-21.
193. Kataoka, S., et al., *Microreactor containing platinum nanoparticles for nitrobenzene hydrogenation.* Applied Catalysis A: General, 2012. **427-428**: p. 119-124.
194. Feng, H., et al., *High-performance gas-liquid-solid microreactor with polydopamine functionalized surface coated by Pd nanocatalyst for nitrobenzene hydrogenation.* Chemical Engineering Journal, 2016. **306**: p. 1017-1025.
195. Paunovic, V., J.C. Schouten, and T.A. Nijhuis, *Direct synthesis of hydrogen peroxide in a wall-coated microchannel reactor over Au–Pd catalyst: A performance study.* Catalysis Today, 2015. **248**: p. 160-168.
196. García, D.C., et al., *A Comprehensive Study of the Washcoating of MCM-41 on Stainless Steel Tubular Microreactors.* Journal of Materials Engineering and Performance, 2021. **30**(8): p. 6345-6354.

197. Wang, Y., et al., *Development of a centrifugal coating method to load catalyst washcoat onto porous substrates with high uniformity and adhesive strength.* Surface and Coatings Technology, 2022. **434**: p.128204.
198. Saud, S., et al., *Plasma-catalytic ethylene removal by a ZSM-5 washcoat honeycomb monolith impregnated with palladium.* J Hazard Mater, 2022. **426**: p. 127843.
199. Liu, W., et al., *Parametric study of methane catalytic combustion in a micro-channel reactor: Effects of porous washcoat properties.* Fuel, 2021. **290**: p.120099.
200. Jarrah, N., J.G. van Ommen, and L. Lefferts, *Development of monolith with a carbon-nanofiber-washcoat as a structured catalyst support in liquid phase.* Catalysis Today, 2003. **79-80**: p. 29-33.
201. Richardson, J.T., Y. Peng, and D. Remue, *Properties of ceramic foam catalyst supports: pressure drop.* Applied Catalysis A: General, 2000. **204**(1): p. 19-32.
202. da Silva, S.W., et al., *TiO2 thick films supported on stainless steel foams and their photoactivity in the nonylphenol ethoxylate mineralization.* Chemical Engineering Journal, 2016. **283**: p. 1264-1272.
203. Singh, R. and D. Kunzru, *Hydrodesulfurization of dibenzothiophene on NiMo/γ-Al2O3 washcoated monoliths.* Fuel, 2016. **163**: p. 180-188.
204. Ballarini, A.D., et al., *n-Butane dehydrogenation on Pt, PtSn and PtGe supported on γ-Al2O3 deposited on spheres of α-Al2O3 by washcoating.* Applied Catalysis A: General, 2010. **381**(1-2): p. 83-91.
205. Soghrati, E., et al., *Development of a structured monolithic support with a CNT washcoat for the naphtha HDS process.* Journal of the Taiwan Institute of Chemical Engineers, 2014. **45**(3): p. 887-895.
206. Restivo, J., et al., *Carbon nanofibers doped with nitrogen for the continuous catalytic ozonation of organic pollutants.* Chemical Engineering Journal, 2016. **293**: p. 102-111.
207. Glaze, W.H., *Drinking-water treatment with ozone.* Environmental Science & Technology, 1987. **21**(3): p. 224-230.
208. Glaze, W.H., J.-W. Kang, and D.H. Chapin, *The Chemistry of Water Treatment Processes Involving Ozone, Hydrogen Peroxide and Ultraviolet Radiation.* Ozone: Science & Engineering, 1987. **9**(4): p. 335-352.
209. Jamil, T., *Role of advance oxidation processes (AOPs) in textile wastewater treatment: A critical review.* Desalination and Water Treatment, 2024. **318**: p.100387.
210. Deng, Y. and R. Zhao, *Advanced Oxidation Processes (AOPs) in Wastewater Treatment.* Current Pollution Reports, 2015. **1**(3): p. 167-176.
211. Jones, C.W., *Activation of hydrogen peroxide using inorganic and organic species*, in *Applications of Hydrogen Peroxide and Derivatives*, C.W. Jones, et al., Editors. 1999, The Royal Society of Chemistry. p. 0.
212. Asif, M.B., H. Kang, and Z. Zhang, *Gravity-driven layered double hydroxide nanosheet membrane activated peroxymonosulfate system for micropollutant degradation.* J Hazard Mater, 2022. **425**: p. 127988.
213. Zhou, J., et al., *Co(3)O(4) anchored on biochar derived from chitosan (Co(3)O(4)@BCC) as a catalyst to efficiently activate peroxymonosulfate (PMS) for degradation of phenacetin.* J Environ Manage, 2023. **327**: p. 116895.
214. Asaithambi, P., et al., *Sono-alternating current-electro-Fenton process for the removal of color, COD and determination of power consumption from distillery industrial wastewater.* Separation and Purification Technology, 2023. **319**: p.124031.
215. Ferreira, M.B., et al., *Improving biotreatability of hazardous effluents combining ZVI, electrolysis and photolysis.* Science of The Total Environment, 2020. **713**: p.136647.
216. Asif, A.H., et al., *Graphitic carbon nitride engineered α-Fe2O3/rGO heterostructure for visible-light-driven photochemical oxidation of sulfamethoxazole.* Chemical Engineering Journal, 2023. **451**: p.138630.

217. Nguyen, M.K., et al., *Fenton/ozone-based oxidation and coagulation processes for removing metals (Cu, Ni)-EDTA from plating wastewater.* Journal of Water Process Engineering, 2021. **39**: p.101836.
218. Bhargava, N., N. Bahadur, and A. Kansal, *Techno-economic assessment of integrated photochemical AOPs for sustainable treatment of textile and dyeing wastewater.* Journal of Water Process Engineering, 2023. **56**: p.104302.
219. Fedorov, K., et al., *Activated sodium percarbonate-ozone (SPC/O3) hybrid hydrodynamic cavitation system for advanced oxidation processes (AOPs) of 1,4-dioxane in water.* Chemical Engineering Journal, 2023. **456**: p.141027.
220. Zhang, H., et al., *A critical review of ozone-based electrochemical advanced oxidation processes for water treatment: Fundamentals, stability evaluation, and application.* Chemosphere, 2024. **365**: p. 143330.
221. Zheng, J., et al., *A visible-light-driven heterojuncted composite WO(3)/Bi(12)O(17)Cl(2): Synthesis, characterization, and improved photocatalytic performance.* J Colloid Interface Sci, 2018. **510**: p. 20-31.
222. Chang, F., et al., *Oxygen-rich bismuth oxychloride Bi(12)O(17)Cl(2) materials: construction, characterization, and sonocatalytic degradation performance.* Ultrason Sonochem, 2019. **50**: p. 105-113.
223. Zeng, S. and E. Kan, *Comparative insights into performance and mechanisms of Fenton and persulfate oxidation on iron-functionalized activated biochar for removal of aqueous tetracycline antibiotics.* Journal of Water Process Engineering, 2024. **65**: p.105824.
224. Kovács, K., et al., *Free radical chemistry of atenolol and propranolol investigated by pulse and gamma radiolysis.* Radiation Physics and Chemistry, 2022. **196**: p.110141.
225. Zhang, F., et al., *Co-Fe synergy in CoxFe1-xWO4: The new type peroxymonosulfate activator for sulfamethoxazole degradation.* Chemical Engineering Journal, 2023. **461**: p.141989.
226. Hirani, R.A.K., et al., *Heterogeneous activation of persulfate by macroscopic nitrogen-doped graphene oxide cubes for the degradation of antibiotic contaminants in water.* Separation and Purification Technology, 2023. **319**: p.124110.
227. Kohantorabi, M., G. Moussavi, and S. Giannakis, *A review of the innovations in metal- and carbon-based catalysts explored for heterogeneous peroxymonosulfate (PMS) activation, with focus on radical vs. non-radical degradation pathways of organic contaminants.* Chemical Engineering Journal, 2021. **411**: p.127957.
228. Zhou, L., et al., *Development of attapulgite based catalytic membrane for activation of peroxymonosulfate: A singlet oxygen-dominated catalytic oxidation process for sulfamethoxazole degradation.* Separation and Purification Technology, 2023. **312**: p.123382.
229. Duan, X., et al., *Insights into perovskite-catalyzed peroxymonosulfate activation: Maneuverable cobalt sites for promoted evolution of sulfate radicals.* Applied Catalysis B: Environmental, 2018. **220**: p. 626-634.
230. Liang, J. and L. Fu, *Activation of peroxymonosulfate (PMS) by Co3O4 quantum dots decorated hierarchical C@Co3O4 for degradation of organic pollutants: Kinetics and radical-nonradical cooperation mechanisms.* Applied Surface Science, 2021. **563**: p.150335.
231. Wang, J. and S. Wang, *Activation of persulfate (PS) and peroxymonosulfate (PMS) and application for the degradation of emerging contaminants.* Chemical Engineering Journal, 2018. **334**: p. 1502-1517.
232. Wu, H., et al., *Manganese oxide integrated catalytic ceramic membrane for degradation of organic pollutants using sulfate radicals.* Water Research, 2019. **167**: p.115110.
233. Sun, H., et al., *Catalytic oxidation of organic pollutants on pristine and surface nitrogen-modified carbon nanotubes with sulfate radicals.* Applied Catalysis B: Environmental, 2014. **154-155**: p. 134-141.

234. Wu, X., et al., *Constructing confinement-protected Co3O4 into nanocarbon shells onto Mn2O3 nanorod allows for efficient PMS activation and contaminant elimination.* Molecular Catalysis, 2025. **574**: p.114888.
235. Zhu, J., et al., *Degradation of aniline via microbial treated post Fe(II) or Co(II)/PMS advanced oxidation processes.* Separation and Purification Technology, 2025. **359**: p.130809.
236. Anipsitakis, G.P. and D.D. Dionysiou, *Radical generation by the interaction of transition metals with common oxidants.* Environmental Science and Technology, 2004. **38**(13): p. 3705-3712.
237. Luo, R., et al., *Convenient synthesis and engineering of ultrafine Co3O4-incorporated carbon composite: towards practical application of environmental remediation.* Journal of Materials Chemistry A, 2018. **6**(8): p. 3454-3461.
238. Zhang, H., et al., *Enhanced removal of lomefloxacin based on peroxymonosulfate activation by Co3O4/δ-FeOOH composite.* Chemical Engineering Journal, 2019. **369**: p. 834-844.
239. Hafeez, M.A., et al., *Co(2+)/PMS based sulfate-radical treatment for effective mineralization of spent ion exchange resin.* Chemosphere, 2022. **287**(Pt 4): p. 132351.
240. Ma, R., et al., *Cobalt leaching inhibition: Transforming coordination polymers into spherical Co3O4@NC catalysts for accelerated tetracycline degradation via enhanced PMS activation.* Applied Surface Science, 2024. **648**: p.158980.
241. Zhang, L., et al., *Reduced graphene oxide wrapped Fe3O4–Co3O4 yolk–shell nanostructures for advanced catalytic oxidation based on sulfate radicals.* Applied Surface Science, 2017. **396**: p. 945-954.
242. Zhou, X., et al., *Tunable S doping from Co3O4 to Co9S8 for peroxymonosulfate activation: Distinguished Radical/Nonradical species and generation pathways.* Applied Catalysis B: Environmental, 2021. **282**: p.119605.
243. Cai, Z., et al., *Single‐Crystalline Ultrathin Co_3O_4 Nanosheets with Massive Vacancy Defects for Enhanced Electrocatalysis.* Advanced Energy Materials, 2017. **8**(3) : p.1701694.
244. Yang, Q., H. Choi, and D.D. Dionysiou, *Nanocrystalline cobalt oxide immobilized on titanium dioxide nanoparticles for the heterogeneous activation of peroxymonosulfate.* Applied Catalysis B: Environmental, 2007. **74**(1-2): p. 170-178.
245. Yang, Q., et al., *Heterogeneous activation of peroxymonosulfate by supported cobalt catalysts for the degradation of 2,4-dichlorophenol in water: The effect of support, cobalt precursor, and UV radiation.* Applied Catalysis B: Environmental, 2008. **77**(3-4): p. 300-307.
246. Li, M.-C., et al., *Enhanced degradation of 5-sulfosalicylic acid using peroxymonosulfate activated by ordered porous silica-confined Co3O4 prepared via a solvent-free confined space strategy.* Separation and Purification Technology, 2020. **249**: p.116972.
247. Cheng, J., et al., *Direct transformation of bulk cobalt foam into cobalt nanoparticles encapsulated in nitrogen-doped carbon nanotubes for peroxymonosulfate activation toward rhodamine B degradation.* Separation and Purification Technology, 2021. **277**: p.119441.
248. Zhu, W., et al., *ZIF-8-derived nitrogen-doped porous carbon supported CuFeO2 for sulfamethoxazole removal: Performances, degradation pathways and mechanisms.* Journal of Environmental Chemical Engineering, 2023. **11**(3) : p.109587.
249. Macías-Quiroga, I.F., et al., *Research Trends on Pillared Interlayered Clays (PILCs) Used as Catalysts in Environmental and Chemical Processes: Bibliometric Analysis.* The Scientific World Journal, 2022. **2022**: p. 5728678.
250. Kim, A.-R., et al., *Hydrogen production from ammonia decomposition over Ru-rich surface on La2O2CO3-Al2O3 catalyst beads.* Catalysis Today, 2023. **411-412**: p. 113867.
251. Zhu, M.-P., et al., *Deciphering the simultaneous removal of carbamazepine and metronidazole by monolithic Co2AlO4@Al2O3 activated peroxymonosulfate.* Chemical Engineering Journal, 2022. **436**: p.135201.
252. Wang, X., et al., *Functionalized α-Al2O3 supported gold catalyst for photocatalytic oxidative esterification of benzyl alcohol with methanol to corresponding esters.* Journal of Photochemistry and Photobiology A: Chemistry, 2024. **446**: p.115144.

253. Moral-Rodríguez, A.I., et al., *Removal of ronidazole and sulfamethoxazole from water solutions by adsorption on granular activated carbon: equilibrium and intraparticle diffusion mechanisms.* Adsorption, 2016. **22**(1): p. 89-103.
254. Gouveia Gil, A., et al., *A catalytic hollow fibre membrane reactor for combined steam methane reforming and water gas shift reaction.* Chemical Engineering Science, 2015. **137**: p. 364-372.
255. Gouveia Gil, A., et al., *A highly permeable hollow fibre substrate for Pd/Al2O3 composite membranes in hydrogen permeation.* International Journal of Hydrogen Energy, 2015. **40**(8): p. 3249-3258.
256. Irfan Hatim, M.D., et al., *Pd/Al2O3 composite hollow fibre membranes: Effect of substrate resistances on H2 permeation properties.* Chemical Engineering Science, 2011. **66**(6): p. 1150-1158.
257. Othman, N.H., Z. Wu, and K. Li, *A micro-structured La0.6Sr0.4Co0.2Fe0.8O3−δ hollow fibre membrane reactor for oxidative coupling of methane.* Journal of Membrane Science, 2014. **468**: p. 31-41.
258. Othman, N.H., Z. Wu, and K. Li, *Micro‐structured Bi1.5Y0.3Sm0.2O3−δ catalysts for oxidative coupling of methane.* AIChE Journal, 2015. **61**(10): p. 3451-3458.
259. Li, T., Z. Wu, and K. Li, *High-efficiency, nickel-ceramic composite anode current collector for micro-tubular solid oxide fuel cells.* Journal of Power Sources, 2015. **280**: p. 446-452.
260. Li, T., Z. Wu, and K. Li, *Single-step fabrication and characterisations of triple-layer ceramic hollow fibres for micro-tubular solid oxide fuel cells (SOFCs).* Journal of Membrane Science, 2014. **449**: p. 1-8.
261. Ruhi, G., et al., *Effect of sintering temperatures on corrosion and wear properties of sol–gel alumina coatings on surface pre-treated mild steel.* Corrosion Science, 2008. **50**(3): p. 639-649.
262. Singh, I.B., O.P. Modi, and G. Ruhi, *Development of sol–gel alumina coating on 9Cr–1Mo ferritic steel and their oxidation behavior at high temperature.* Journal of Sol-Gel Science and Technology, 2015. **74**(3): p. 685-691.
263. Chandradass, J., D.S. Bae, and K.H. Kim, *Synthesis of γ-Al2O3 Hexagonal Nanoplatelet by Combining Sol–Gel and Hydrothermal Process.* Materials and Manufacturing Processes, 2010. **25**(9): p. 919-922.
264. Leishman, C., et al., *Manganese-based catalysts supported on carbon xerogels for the selective catalytic reduction of NOx using a hollow fibre-based reactor.* Catalysis Today, 2023. **423**: p.114019.
265. Larkin, C., et al., *Retrofitting hollow fibre carbon capture systems to decarbonise surface transport.* Journal of CO2 Utilization, 2023. **67**: p.102336.
266. El Asmar, R., et al., *Iron-based metal organic framework MIL-88-A for the degradation of naproxen in water through persulfate activation.* Chemical Engineering Journal, 2021. **405**: p.126701.
267. Mertah, O., et al., *Peroxymonosulfate enhanced photodegradation of sulfamethoxazole with TiO2@CuCo2O4 catalysts under simulated solar light.* Journal of Environmental Chemical Engineering, 2022. **10**(5).
268. Xu, Y., et al., *Thiourea-assisted one-step fabrication of a novel nitrogen and sulfur co-doped biochar from nanocellulose as metal-free catalyst for efficient activation of peroxymonosulfate.* J Hazard Mater, 2021. **416**: p. 125796.
269. Choong, Z.Y., et al., *Multi-heteroatom-doped carbocatalyst as peroxymonosulfate and peroxydisulfate activator for water purification: A critical review.* J Hazard Mater, 2022. **426**: p. 128077.
270. Asif, A.H., et al., *MIL-53(Fe) derived magnetic CuFe2O4/Fe2O3 composite for catalytic oxidation of sulfamethoxazole via peroxymonsulfate activation.* Chemical Engineering Journal, 2023. **469**: p.143915.

271. Tao, J., et al., *Magnetic MnFe2O4/MoS2 nanocomposites synthesis for rapid degradation of sulfamethoxazole by activated peroxymonosulfate.* Journal of the Taiwan Institute of Chemical Engineers, 2023. **146**: p.104777.
272. Ahmaruzzaman, M., et al., *Phenolic compounds in water: From toxicity and source to sustainable solutions – An integrated review of removal methods, advanced technologies, cost analysis, and future prospects.* Journal of Environmental Chemical Engineering, 2024. **12**(3) : p.112964.
273. Li, L., et al., *Heterogeneous activation of peroxymonosulfate by hierarchically porous cobalt/iron bimetallic oxide nanosheets for degradation of phenol solutions.* Chemosphere, 2020. **256**: p. 127160.
274. Mumtaz, F., et al., *Treatment of phenolic-wastewater by hybrid technologies: A review.* Journal of Water Process Engineering, 2024. **57**: p.104695.
275. Regulations, U.S.E.P.A.O.o.W., S. Criteria, and S. Division, *Ambient Water Quality Criteria for Silver*. 1980: US Environmental Protection Agency, Office of Water Regulations and Standards Criteria and Standards Diviion Washington, D.C.
276. Mohod, A.V., et al., *Degradation of Rhodamine dyes by Advanced Oxidation Processes (AOPs) – Focus on cavitation and photocatalysis - A critical review.* Water Resources and Industry, 2023. **30**: p.100220.
277. Fu, J., et al., *Electrochemical activation of peroxymonosulfate (PMS) by carbon cloth anode for sulfamethoxazole degradation.* Chemosphere, 2022. **287**: p. 132094.
278. Wang, Y., et al., *Natural polyphenols enhanced the Cu(II)/peroxymonosulfate (PMS) oxidation: The contribution of Cu(III) and HO•.* Water Research, 2020. **186**: p. 116326.
279. Zheng, J. and Z. Wu, *Innovative microchannel-structured beads for microscale process intensification: A case study on water treatment for sulfamethoxazole abatement.* Chemical Engineering Journal, 2025. **504**: p. 158527.
280. Wu, H., et al., *Metal-free activation of peroxymonosulfate by boron and nitrogen co-doped graphene nanotubes for catalytic oxidation of 4-hydroxybenzoic acid.* Environmental Functional Materials, 2022. **1**(2): p. 139-148.
281. Irankhah, A., et al., *Fischer-Tropsch Reaction Kinetics of Cobalt Catalyst in Supercritical Phase.* Journal of Natural Gas Chemistry, 2007. **16**(2): p. 115-120.
282. Reza Gheitanchi, A.A.K., Majid Taghizadeh and Yadollah Mortazavib *Effects of ceria addition and pre-calcination temperature on performance of cobalt catalysts for Fischer-Tropsch synthesis.* Reaction Kinetics and Catalysis Letters, 2006. **88**: p. 225–232.
283. Koopi, H. and F. Buazar, *A novel one-pot biosynthesis of pure alpha aluminum oxide nanoparticles using the macroalgae Sargassum ilicifolium: A green marine approach.* Ceramics International, 2018. **44**(8): p. 8940-8945.
284. Wang, S. and J. Wang, *Radiation-induced preparation of nanoscale CoO@graphene oxide for activating peroxymonosulfate to degrade emerging organic pollutants.* Sci Total Environ, 2024. **933**: p. 173211.
285. Kim, K.S. and Y.J. Park, *Catalytic properties of Co3O4 nanoparticles for rechargeable Li/air batteries.* Nanoscale Res Lett, 2012. **7**(1): p. 47.
286. Prabaharan, D.D.M., et al., *Precipitation method and characterization of cobalt oxide nanoparticles.* Applied Physics A, 2017. **123**(4) : p.264.
287. Song, T., et al., *Fabrication of super slippery sheet-layered and porous anodic aluminium oxide surfaces and its anticorrosion property.* Applied Surface Science, 2015. **355**: p. 495-501.
288. Tago, T., et al., *XPS study from a clean surface of Al2O3 single crystals.* Procedia Engineering, 2017. **216**: p. 175-181.
289. Zhang, S., et al., *Enhanced permanganate oxidation of phenolic pollutants by alumina and potential industrial application.* Water Res, 2024. **251**: p. 121170.
290. Li, X., et al., *Influence of oxygen pressure and substrate temperature on the properties of aluminum fluoride thin films.* Applied Surface Science, 2013. **282**: p. 226-230.

291. Fang, R.-C., et al., *High-performance bilayer flexible resistive random access memory based on low-temperature thermal atomic layer deposition.* Nanoscale Research Letters, 2013. **8**(1): p. 92.
292. Guo, Q., et al., *Co(3)O(4) modified polymeric carbon nitride for external light-free chlorine activating degradation of organic pollutants.* J Hazard Mater, 2022. **429**: p. 128193.
293. Zou, J.P., et al., *Electrochemical oxidation and advanced oxidation processes using a 3D hexagonal Co(3)O(4) array anode for 4-nitrophenol decomposition coupled with simultaneous CO(2) conversion to liquid fuels via a flower-like CuO cathode.* Water Res, 2019. **150**: p. 330-339.
294. Liu, Y., et al., *A versatile CeO(2)/Co(3)O(4) coated mesh for food wastewater treatment: Simultaneous oil removal and UV catalysis of food additives.* Water Res, 2018. **137**: p. 144-152.
295. Pashchenko, D., *Intra-particle diffusion limitation for steam methane reforming over a Ni-based catalyst.* Fuel, 2023. **353**: p.144-152.
296. Su, C., et al., *Core-shell magnetic CFO@COF composites toward peroxymonosulfate activation for degradation of sulfamethoxazole from aqueous solution: A comparative study and mechanistic consideration.* Chemosphere, 2023. **311**(Pt 2): p. 137159.
297. Zou, X.-l., H. Yan, and X.-h. Chen, *Evolution of second phases and mechanical properties of 7075 Al alloy processed by solution heat treatment.* Transactions of Nonferrous Metals Society of China, 2017. **27**(10): p. 2146-2155.
298. Xue, X., et al., *Adsorption and oxidation of PCP on the surface of magnetite: Kinetic experiments and spectroscopic investigations.* Applied Catalysis B: Environmental, 2009. **89**(3-4): p. 432-440.
299. Asif, A.H., et al., *Heterogeneous activation of peroxymonosulfate by Co-doped Fe(2)O(3) nanospheres for degradation of p-hydroxybenzoic acid.* J Colloid Interface Sci, 2021. **604**: p. 390-401.
300. Hirani, R.A.K., et al., *Heterogeneous activation of persulfate by macroscopic nitrogen-doped graphene oxide cubes for the degradation of antibiotic contaminants in water.* Separation and Purification Technology, 2023. **319**: p. 124110.
301. Wang, R., et al., *Non-radical mediated reduced graphene oxide/polypyrrole catalytic ceramic membrane-PDS system for source control of SMX.* Chemical Engineering Journal, 2024. **479**: p.147769.
302. Wang, J. and S. Wang, *Reactive species in advanced oxidation processes: Formation, identification and reaction mechanism.* Chemical Engineering Journal, 2020. **401**: p.126158.
303. Zhu, W., et al., *MOFs-derived CuO-Fe(3)O(4)@C with abundant oxygen vacancies and strong Cu-Fe interaction for deep mineralization of bisphenol A.* Environ Res, 2023. **228**: p. 115847.
304. Xiong, M., et al., *Efficient peroxymonosulfate activation by magnetic CoFe2O4 nanoparticle immobilized on biochar toward sulfamethoxazole degradation: Performance, mechanism and pathway.* Applied Surface Science, 2023. **615**: p.156398.
305. Lai, S.-H., et al., *Novel g-C3N4 wrapped γ-Al2O3 microspheres heterojunction for efficient photocatalytic application under visible light irradiation.* Journal of Materials Science: Materials in Electronics, 2017. **29**(6): p. 4509-4516.
306. Chen, F., et al., *High-loading washcoat of γ-alumina on FeCrAlloy mesh with acid-free slurry.* Surface and Coatings Technology, 2020. **403**: p.126394.
307. Guo, Q., et al., *Effect of Lanthanum on Zr–Co/γ-Al2O3 Catalysts for Fischer–Tropsch Synthesis.* Catalysis Letters, 2018. **148**(9): p. 2789-2798.
308. Gheitanchi, R., et al., *Effects of ceria addition and pre-calcination temperature on performance of cobalt catalysts for Fischer-Tropsch synthesis.* Reaction Kinetics and Catalysis Letters, 2006. **88**(2): p. 225-232.
309. Zhao, N., et al., *Preparation of high performance Co3O4/Al2O3 catalysts by doping Al into ZIF-67: Effect of Al sources on Fischer-Tropsch synthesis.* Applied Surface Science, 2021. **570**: p.151127.

310. Guo, S., et al., *Effect of Ba on the catalytic performance of Co-Ru/Al2O3 catalyst for Fischer-Tropsch synthesis.* Fuel, 2021. **292**: p.120398.
311. Agrafiotis, C. and A. Tsetsekou, *The effect of processing parameters on the properties of γ-alumina washcoats deposited on ceramic honeycombs.* Journal of Materials Science, 2000. **35**(4): p. 951-960.
312. Zheng, J., et al., *A visible-light-driven heterojuncted composite WO3/Bi12O17Cl2: Synthesis, characterization, and improved photocatalytic performance.* Journal of Colloid and Interface Science, 2018. **510**: p. 20-31.
313. Zhou, X., et al., *Atomic cation-vacancy modulated peroxymonosulfate nonradical oxidation of sulfamethoxazole via high-valent iron-oxo species.* Applied Catalysis B: Environmental, 2023. **330**: p.122640.
314. Wang, R., et al., *Non-radical mediated reduced graphene oxide/polypyrrole catalytic ceramic membrane-PDS system for source control of SMX.* Chemical Engineering Journal, 2024. **479**: p. 147769.
315. Wang, S. and J. Wang, *Radiation-induced preparation of nanoscale CoO@graphene oxide for activating peroxymonosulfate to degrade emerging organic pollutants.* Science of The Total Environment, 2024. **933**: p. 173211.
316. Yu, C., et al., *Marriage of membrane filtration and sulfate radical-advanced oxidation processes (SR-AOPs) for water purification: Current developments, challenges and prospects.* Chemical Engineering Journal, 2022. **433**: p.133802.
317. Xiong, M., et al., *Efficient peroxymonosulfate activation by magnetic CoFe2O4 nanoparticle immobilized on biochar toward sulfamethoxazole degradation: Performance, mechanism and pathway.* Applied Surface Science, 2023. **615**: p. 156398.
318. Mazzone, S., et al., *A compact non-PGM catalytic hollow fibre converter for on-board hydrogen production.* Sustainable Energy & Fuels, 2022. **6**(6): p. 1554-1567.
319. Hao, L., et al., *Applications of Carbon-Based Materials in Activated Peroxymonosulfate for the Degradation of Organic Pollutants: A Review.* Chem Rec, 2023. **23**(12): p. e202300203.
320. Liang, P., et al., *An insight into metal organic framework derived N-doped graphene for the oxidative degradation of persistent contaminants: formation mechanism and generation of singlet oxygen from peroxymonosulfate.* Environmental Science: Nano, 2017. **4**(2): p. 315-324.
321. Chen, J., et al., *Decolorization of azo dye by peroxymonosulfate activated by carbon nanotube: Radical versus non-radical mechanism.* J Hazard Mater, 2016. **320**: p. 571-580.
322. Perez-Poyatos, L.T., et al., *The dynamic ethylene adsorption on carbon xerogels as a three-way game between porosity, surface chemistry and humidity.* J Colloid Interface Sci, 2024. **678**(Pt A): p. 480-493.
323. Mazzone, S., et al., *Ruthenium-based catalysts supported on carbon xerogels for hydrogen production via ammonia decomposition.* Applied Catalysis A: General, 2022. **632**: p.118484.
324. Zhou, G., et al., *Synthesis of carbon xerogels at varying sol–gel pHs, dye adsorption and chemical regeneration.* Chemical Engineering Journal, 2011. **171**(3): p. 1399-1405.
325. Wan, Y., Y. Hu, and W. Zhou, *Catalytic mechanism of nitrogen-doped biochar under different pyrolysis temperatures: The crucial roles of nitrogen incorporation and carbon configuration.* Sci Total Environ, 2022. **816**: p. 151502.
326. Ye, S., et al., *Nitrogen-doped biochar fiber with graphitization from Boehmeria nivea for promoted peroxymonosulfate activation and non-radical degradation pathways with enhancing electron transfer.* Applied Catalysis B: Environmental, 2020. **269**: p.118850.
327. Zhang, H., et al., *Non-doping 3D porous carbon with rich intrinsic defects for efficient nonradical activation of peroxymonosulfate toward the degradation of organic pollutants.* Separation and Purification Technology, 2022. **292**: p.121048.
328. Tian, Y., et al., *An overview of process systems engineering approaches for process intensification: State of the art.* Chemical Engineering and Processing - Process Intensification, 2018. **133**: p. 160-210.

329. Quach, N.K.N., et al., *Investigation of the Characteristic Properties of Glacial Acetic Acid-Catalyzed Carbon Xerogels and Their Electrochemical Performance for Use as Electrode Materials in Electrical Double-Layer Capacitors.* Advances in Materials Science and Engineering, 2017. **2017**: p. 1-9.
330. Qian, J., X. Gao, and B. Pan, *Nanoconfinement-Mediated Water Treatment: From Fundamental to Application.* Environ Sci Technol, 2020. **54**(14): p. 8509-8526.
331. Bailón-García, E., et al., *New carbon xerogel-TiO2 composites with high performance as visible-light photocatalysts for dye mineralization.* Applied Catalysis B: Environmental, 2017. **201**: p. 29-40.
332. KiciŃSki, W., et al., *Porous graphitic materials obtained from carbonization of organic xerogels doped with transition metal salts.* Bulletin of Materials Science, 2014. **37**(1): p. 141-150.
333. Chen, L., et al., *Hierarchical porous graphitized carbon xerogel for high performance supercapacitor.* Diamond and Related Materials, 2022. **121**: p.108781.
334. Moreno, A.H., et al., *Carbonisation of resorcinol–formaldehyde organic xerogels: Effect of temperature, particle size and heating rate on the porosity of carbon xerogels.* Journal of Analytical and Applied Pyrolysis, 2013. **100**: p. 111-116.
335. Peikolainen, A.-L., et al., *Carbon xerogel from 5-methylresorcinol-formaldehyde gel: The controllability of structural properties.* Carbon Trends, 2021. **3**: p.100037.
336. Li, H., et al., *Facile synthesis of recyclable Co3O4/Co(OH)2/RGO ternary heterostructures with synergistic effect for photocatalysis.* Journal of Nanoparticle Research, 2018. **20**(10) : p.279.
337. Gao, N., et al., *Effect of metals and Co3O4 on the thermal decomposition reaction of sodium chlorate in an area of refuge.* Chemical Papers, 2020. **74**(10): p. 3475-3480.
338. Awadallah-F, A., S.A. Al-Muhtaseb, and H.-K. Jeong, *Selective adsorption of carbon dioxide, methane and nitrogen using resorcinol-formaldehyde-xerogel activated carbon.* Adsorption, 2017. **23**(7-8): p. 933-944.
339. Kim, D.-G. and S.-O. Ko, *Effects of thermal modification of a biochar on persulfate activation and mechanisms of catalytic degradation of a pharmaceutical.* Chemical Engineering Journal, 2020. **399**: p.125377.
340. Zheng, J., et al., *Catalytic micro-structured ceramic beads and efficacy evaluation through SMX degradation in PMS-activated systems.* Separation and Purification Technology, 2025. **354**: p. 129060.
341. Hu, Z., et al., *Activation of Na2S2O8 by MIL-101(Fe)/Co3O4 composite for degrading tetracycline with visible light assistance.* Inorganic Chemistry Communications, 2022. **144**: p.109902.
342. Duan, X., et al., *Unveiling the active sites of graphene-catalyzed peroxymonosulfate activation.* Carbon, 2016. **107**: p. 371-378.
343. Ribeiro, R.S., et al., *Magnetic carbon xerogels for the catalytic wet peroxide oxidation of sulfamethoxazole in environmentally relevant water matrices.* Applied Catalysis B: Environmental, 2016. **199**: p. 170-186.
344. Liang, L., et al., *Sucrose-derived N-doped carbon xerogels as efficient peroxydisulfate activators for non-radical degradation of organic pollutants.* J Colloid Interface Sci, 2021. **604**: p. 660-669.
345. Jo, Y., et al., *Activation of peroxymonosulfate on visible light irradiated TiO2 via a charge transfer complex path.* Chemical Engineering Journal, 2018. **346**: p. 249-257.
346. Tian, W., et al., *Enhanced removals of micropollutants in binary organic systems by biomass derived porous carbon/peroxymonosulfate.* J Hazard Mater, 2021. **408**: p. 124459.
347. Duan, W., et al., *A unique Si-doped carbon nanocatalyst for peroxymonosulfate (PMS) activation: insights into the singlet oxygen generation mechanism and the abnormal salt effect.* Environmental Science: Nano, 2020. **7**(10): p. 2982-2994.

348. Asif, M.B., H. Kang, and Z. Zhang, *Assembling CoAl-layered metal oxide into the gravity-driven catalytic membrane for Fenton-like catalytic degradation of pharmaceuticals and personal care products.* Chemical Engineering Journal, 2023. **463**: p.142340.
349. Grommet, A.B., M. Feller, and R. Klajn, *Chemical reactivity under nanoconfinement.* Nat Nanotechnol, 2020. **15**(4): p. 256-271.
350. Meng, C., et al., *Laminar membranes assembled by ultrathin cobalt-copper oxide nanosheets for nanoconfined catalytic degradation of contaminants.* Chemical Engineering Journal, 2022. **449**: p.137811.
351. Mu, R., et al., *Functionally-designed metal salt and ball milling co-modified sludge biochar for adsorptive removal of trace level sulfamethoxazole: Behavior, characterization, mechanism and DFT study.* Journal of Environmental Chemical Engineering, 2024. **12**(5) : p.113479.
352. Lorenc-Grabowska, E., *Effect of micropore size distribution on phenol adsorption on steam activated carbons.* Adsorption, 2015. **22**(4-6): p. 599-607.
353. Wang, Z., et al., *Honeycomb-like holey Co(3)O(4) membrane triggered peroxymonosulfate activation for rapid degradation of organic contaminants.* Sci Total Environ, 2022. **814**: p. 152698.
354. Yang, J.-C.E., et al., *Novel magnetic rod-like Mn-Fe oxycarbide toward peroxymonosulfate activation for efficient oxidation of butyl paraben: Radical oxidation versus singlet oxygenation.* Applied Catalysis B: Environmental, 2020. **268**: p.118549.
355. Yang, J.-C.E., et al., *The mechanistic difference of 1T-2H MoS2 homojunctions in persulfates activation: Structure-dependent oxidation pathways.* Applied Catalysis B: Environmental, 2021. **297**: p.120460.
356. Hu, X. and M. Zhu, *Were Persulfate-Based Advanced Oxidation Processes Really Understood? Basic Concepts, Cognitive Biases, and Experimental Details.* Environ Sci Technol, 2024. **58**(24): p. 10415-10444.
357. Yang, J.-C.E., et al., *Novel magnetic rod-like Mn-Fe oxycarbide toward peroxymonosulfate activation for efficient oxidation of butyl paraben: Radical oxidation versus singlet oxygenation.* Applied Catalysis B: Environmental, 2020. **268**: p. 118549.
358. Ye, J., et al., *Synergy of pore confinement and co-catalytic effects in Peroxymonosulfate activation for persistent and selective removal of contaminants.* Chemical Engineering Journal, 2024. **496**: p.154034.
359. Shi, X., et al., *Co and N co-doped carbon nanotubes catalyst for PMS activation: Role of non-radicals.* Separation and Purification Technology, 2025. **353**: p.128528.
360. Sholl, D.S. and R.P. Lively, *Seven chemical separations to change the world.* Nature, 2016. **532**(7600): p. 435-437.
361. Dossumov, K., et al., *Morphology and Catalytic Properties of Cobalt-Containing Catalysts Synthesized by Different Means.* Russian Journal of Physical Chemistry A, 2020. **94**(4): p. 880-882.
362. Ghani, N.N.A.M.A., M.A. Saeed, and I.H. Hashim, *Thermoluminescence (TL) response of silica nanoparticles subjected to 50 Gy gamma irradiation.* Malaysian Journal of Fundamental and Applied Sciences, 2017. **13**: p.178-180.
363. Yang, X., et al., *Phase transformation of silica particles in coal and biomass combustion processes.* Environ Pollut, 2022. **292**(Pt A): p. 118312.
364. Xue, S.-H., et al., *Induced transformation of amorphous silica to cristobalite on bacterial surfaces.* RSC Advances, 2015. **5**(88): p. 71844-71848.
365. Knaepen, W., et al., *In-situ X-ray Diffraction study of Metal Induced Crystallization of amorphous silicon.* Thin Solid Films, 2008. **516**(15): p. 4946-4952.
366. Yue, X.-M., et al., *Synthesis of Co3O4/reduced graphene oxide by one step-hydrothermal and calcination method for high-performance supercapacitors.* Ionics, 2020. **27**(1): p. 339-349.

367. Shu, T., et al., *Highly stable Co3O4 nanoparticles/carbon nanosheets array derived from flake-like ZIF-67 as an advanced electrode for supercapacacitor.* Chemical Engineering Journal, 2021. **419**: p.129631.
368. Ma, H.P., et al., *Systematic Study of the SiO(x) Film with Different Stoichiometry by Plasma-Enhanced Atomic Layer Deposition and Its Application in SiO(x)/SiO(2) Super-Lattice.* Nanomaterials (Basel), 2019. **9**(1) : p.55.
369. Daza - Gómez, L.C., et al., *Co3O4@SiO2 3D Monolith Catalysts, Additive Manufactured Structures for Propane Oxidation Reaction.* ChemistrySelect, 2024. **9**(30) : p.e202304849.
370. Wu, Q., et al., *Unveiling the dynamic active site of defective carbon-based electrocatalysts for hydrogen peroxide production.* Nat Commun, 2023. **14**(1): p. 6275.
371. Zhao, K. and Y. Zhang, *Effective and continuous degradation of pollutants via carbon felt loaded with Co3O4 as three-dimensional electrode: Collaboration between ROS.* Separation and Purification Technology, 2023. **308**: p.122962.
372. Li, P., et al., *Defect-engineered Co3O4 with porous multishelled hollow architecture enables boosted advanced oxidation processes.* Applied Catalysis B: Environmental, 2021. **298**: p.120596.
373. Li, H., et al., *Constructing Z-scheme NiMoO(4)@Co(3)O(4) core-shell heterogeneous architectures with prominent photoelectrocatalytic performance toward water purification.* Chemosphere, 2023. **312**(Pt 1): p. 137261.
374. Schmitz, F., M. Minceva, and M. Kampmann, *Comparison of batch and continuous multi-column capture of monoclonal antibodies with convective diffusive membrane adsorbers.* J Chromatogr A, 2024. **1732**: p. 465201.
375. Derevich, I.V., et al., *Heat and mass transfer in Fischer–Tropsch catalytic granule with localized cobalt microparticles.* International Journal of Heat and Mass Transfer, 2018. **121**: p. 1335-1349.
376. Akbarzadeh, O., et al., *Effect of Temperature, Syngas Space Velocity and Catalyst Stability of Co-Mn/CNT Bimetallic Catalyst on Fischer Tropsch Synthesis Performance.* Catalysts, 2021. **11**(7) : p.846.
377. Ghogia, A.C., et al., *Cobalt catalysts on carbon-based materials for Fischer-Tropsch synthesis: a review.* Applied Catalysis a-General, 2021. **609**: p.117906.
378. Sineva, L.V., et al., *Zeolites as a tool for intensification of mass transfer on the surface of a cobalt Fischer–Tropsch synthesis catalyst.* Catalysis Today, 2021. **378**: p. 140-148.
379. Wang, D., et al., *High thermal conductive core-shell structured Al 2 O 3 @Al composite supported cobalt catalyst for Fischer-Tropsch synthesis.* Applied Catalysis A: General, 2016. **527**: p. 60-71.
380. Guettel, R., U. Kunz, and T. Turek, *Reactors for Fischer-Tropsch Synthesis.* Chemical Engineering & Technology, 2008. **31**(5): p. 746-754.
381. Fratalocchi, L., et al., *Intensifying heat transfer in Fischer-Tropsch tubular reactors through the adoption of conductive packed foams.* Chemical Engineering Journal, 2018. **349**: p. 829-837.
382. Lewis, J.A., *Colloidal Processing of Ceramics.* Journal of the American Ceramic Society, 2010. **83**(10): p. 2341-2359.
383. Scott A. McKelvey, W.J.K., *Phase separation, vitrification, and the manifestation of macrovoids in polymeric asymmetric membranes.* Journal of Membrane Science, 1996. **112**: p. 29-39.
384. Nunes, S.P. and K.V. Peinemann, *Membrane Preparation*. 2006: Membrane Technology: in the Chemical Industry, Second, Revised and Extended Edition.
385. Hatta, A.H., et al., *A review on recent bimetallic catalyst development for synthetic natural gas production via CO methanation.* International Journal of Hydrogen Energy, 2022. **47**(72): p. 30981-31002.
386. Nava, R., et al., *Influence of the preparation method on the activity of phosphate-containing CoMo/HMS catalysts in deep hydrodesulphurization.* Applied Catalysis A: General, 2007. **321**(1): p. 58-70.

387. Whelan, J., et al., *Cobalt-Molybdenum Single-Layered Nanocatalysts Decorated on Carbon Nanotubes and the Influence of Preparation Conditions on Their Hydrodesulfurization Catalytic Activity.* Energy & Fuels, 2018. **32**(7): p. 7820-7826.
388. Osakoo, N., et al., *Comparison of PdCo/SBA-15 prepared by co-impregnation and sequential impregnation for Fischer–Tropsch synthesis.* Catalysis Communications, 2015. **66**: p. 73-78.
389. Brockner, W., C. Ehrhardt, and M. Gjikaj, *Thermal decomposition of nickel nitrate hexahydrate, Ni(NO3)2·6H2O, in comparison to Co(NO3)2·6H2O and Ca(NO3)2·4H2O.* Thermochimica Acta, 2007. **456**(1): p. 64-68.
390. Ehrhardt, C., M. Gjikaj, and W. Brockner, *Thermal decomposition of cobalt nitrato compounds: Preparation of anhydrous cobalt(II)nitrate and its characterisation by Infrared and Raman spectra.* Thermochimica Acta, 2005. **432**(1): p. 36-40.
391. Li, K., et al., *Electrolytic nitrate reduction using Co3O4 rod-like and sheet-like cathodes with the control of (220) facet exposure and Co2+/Co3+ ratio.* Electrochimica Acta, 2020. **362**: p.137121.
392. Li, K., et al., *Efficient construction of low shrinkage xerogels via coordination-catalyzed in-situ polymerization for activated carbon xerogels with multi-dyes adsorption.* Nano Materials Science, 2024. In press.
393. Niu, J., T. He, and J. Cheng, *In-situ synthesis of carbon-coated Co3O4 nanowire for efficient activation of peroxymonosulfate while reducing ion leaching through protection and secondary enrichment.* Chemical Engineering Journal, 2024. **500**: p.157301.
394. Liu, D., et al., *Cobalt–aluminum oxide clusters-embedded γ-Al2O3 nanosheets for peroxymonosulfate activation: Interfacial pH-buffering property to eliminate cobalt leaching and boost the catalytic activity.* Applied Catalysis B: Environmental, 2023. **330**: p.122555.
395. Shen, Y., et al., *Composition-dependent PMS activation in SrxLa2-xCoO4±δ perovskite-derivatives: From radical to strengthen the electron-transfer pathway.* Applied Catalysis B: Environment and Energy, 2024. **357**: p.124291.

Appendix 1 Supplementary Information for Chapter 4

A1-1 Preparation of spherical microchannel-structured ceramic beads (MSCBs).

The concept of spherical micro-structured ceramic bead formation via the phase-inversion process for the AOPs processes was first developed in our work. This process is heavily reliant on two key factors: the chemical parameters (the composition of the ceramic suspension) and the physical/mechanical parameters of the shaping process (the dimensions of the flat-tipped tube connected to the syringe, the extrusion flow rates, the air gap between the tube and the water surface, and the height of the water bath). Both define the shaping process and affect the final properties of the micro-structured ceramic beads (MSCBs).

A1-1.1 Effect of the suspension compositions

The composition of the suspension plays a key role in shaping the ceramic beads as it determines the solidification of the droplets. Therefore, apart from the alumina powder dispersed in the solvent NMP, PMMA was applied as a binder and a matrix for the ceramic powder to solidify the droplets. Simplify for description, beads with various weight percentage (*m* wt.%) of α-Al_2O_3 powder in the suspension were named *m* wt.% Al_2O_3. Meanwhile, beads of the best Al_2O_3 content (52 wt.% Al_2O_3) with the adjustment of PMMA addition and change of solvent from NMP to DMSO were named 52 wt.% Al_2O_3 + *n* g of PMMA and 52 wt.% Al_2O_3 + 15 g of PMMA-DMSO, respectively. We can see from Figure A1 (c), (f) and (g) that the introduction of additional PMMA resulted in the formation of short tails, attributed to the increased viscosity of the ceramic suspension. Likewise, larger Al_2O_3 concentrations (Figure A1 (d) and Figure A1 (e)) enhanced suspension viscosity as well, ultimately triggering the occurrence of tails. However, when the weight percentage of Al_2O_3 is insufficient, such as 47 wt.% in Figure A1 (a) and 50 wt.% in Figure A1 (b), the spherical beads could not be generated due to the small Van der Waals forces participating in the particle clustering and forming agglomerates [176, 382]. The optimum Al_2O_3 concentration for the development of spherical ceramic beads is 52 wt.%, as shown in Figure A1 (c). Furthermore, it was observed that substituting the solvent NMP with DMSO (as depicted in Figure A1 (h)) gave rise to the formation of ceramic beads with an ellipsoidal shape and short tails, although other ingredients remained the same.

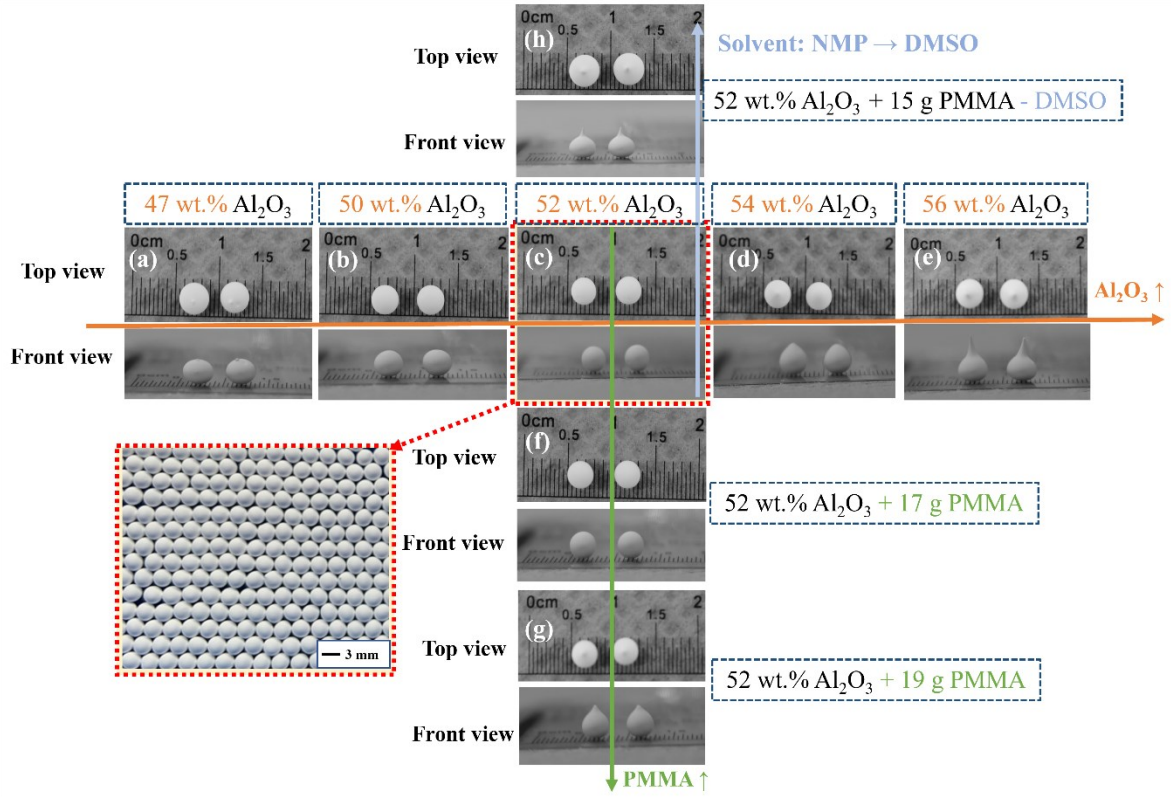

Figure A1 Photographic images of ceramic beads of various alumina contents, PMMA addition, and solvents: (a) 47 wt.% Al_2O_3, (b) 50 wt.% Al_2O_3, (c) 52 wt.% Al_2O_3, (d) 54 wt.% Al_2O_3, (e) 56 wt.% Al_2O_3, (f) 52 wt.% Al_2O_3 + 17g PMMA, (g) 52 wt.% Al_2O_3 + 19g PMMA, and (h) 52 wt.% Al_2O_3 + 15g PMMA-DMSO.

A1-1.2 Effect of the flat-tipped tube

In addition, the dimensions of the flat-tipped tube that connects to the syringe are dependent on the final sizes of the ceramic beads. In this work, two main diameters of the ceramic beads have been synthesised by adjusting the suspension compositions and the inner diameter of the flat-tipped tube/needle, and the photographic images and sizes of these ceramic beads are shown in Figure A2 and Figure A3. When the syringe pump was connected to a 1/8`` tube with an extrusion flow rate of 0.1 mL/min, the diameters of the ceramic beads came out to be approximately 3 mm. In contrast, using a smaller flat-tipped needle with an inner diameter of 0.7 mm resulted in formation of smaller ceramic beads (~2 mm), as expected. Furthermore, as the extrusion flow rate increased, tails emerged owing to inertia during the extrusion process. Further increasing the extrusion flow rates to 1 mL/min or beyond, the ceramic suspension tended to constantly detach from the tube, resulting in the formation of elongated ceramic tubes instead of spherical beads.

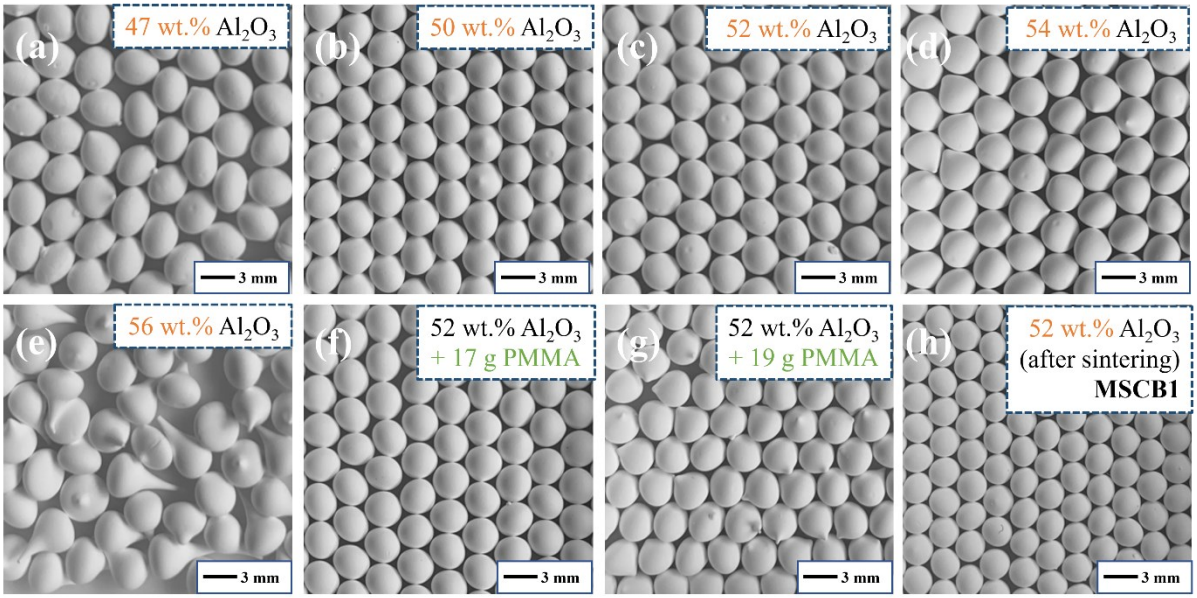

Figure A2 Photographic images of ceramic beads (~3 mm in diameter) of various alumina contents and PMMA addition: (a) 47 wt.% Al_2O_3, (b) 50 wt.% Al_2O_3, (c) 52 wt.% Al_2O_3, (d) 54 wt.% Al_2O_3, (e) 56 wt.% Al_2O_3, (f) 52 wt.% Al_2O_3 + 17g PMMA, (g) 52 wt.% Al_2O_3 + 19g PMMA, and (h) 52 wt.% Al_2O_3 after sintering (i.e., MSCB1).

A1-1.3 Effect of the air gap

During the extrusion process, the droplet adhered to the tube/needle and when gravitational forces exceeded the adhesion force, the droplet was dragged down and released from the tip. After leaving the tube/needle, the droplets can be either floated, squashed, or show peculiar shapes depending on the air gap between the alumina suspension and the water surface. Figure A4 displays the morphological state of ceramic pellets when different air gaps were applied during the extrusion process. Smaller air gaps in Figure A4 (a)-(c) (0 – 1.7 cm) led to floating samples or ceramic particles with short tails, whilst greater air gaps in Figure A4 (e) (> 4 cm) resulted in flat or ellipsoidal beads. The optimum air gap for the formation of spherical ceramic beads from 52 wt.% Al_2O_3 ceramic suspension is 2.0 cm.

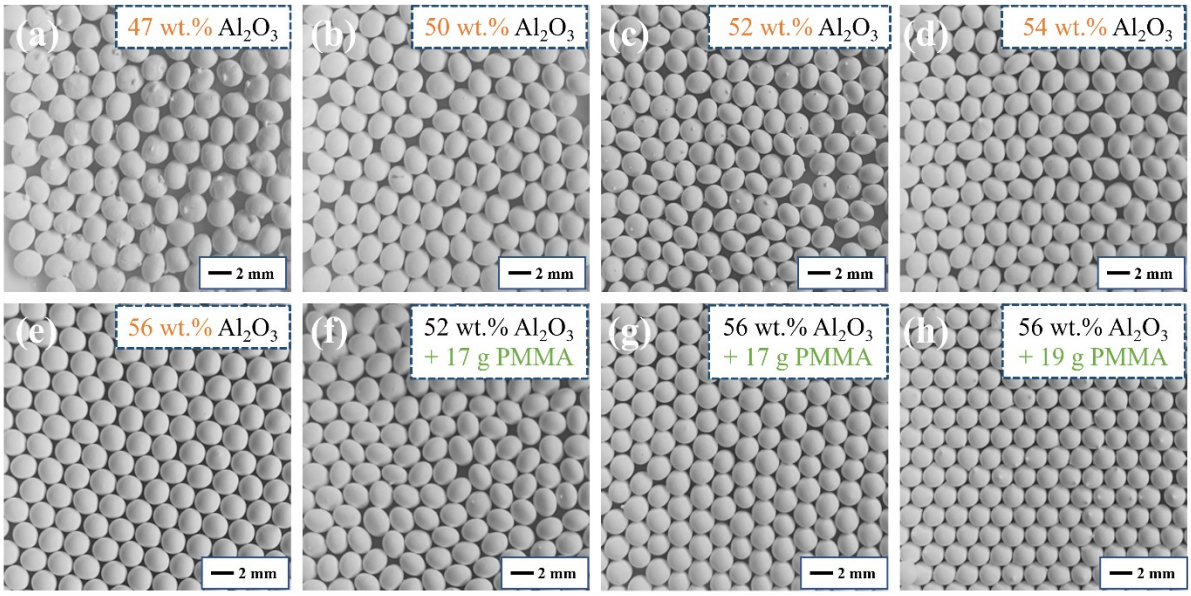

Figure A3 Photographic images of ceramic beads (~2 mm in diameter) of various alumina contents and PMMA addition: (a) 47 wt.% Al_2O_3-2mm, (b) 50 wt.% Al_2O_3-2mm, (c) 52 wt.% Al_2O_3-2mm, (d) 54 wt.% Al_2O_3-2mm, (e) 56 wt.% Al_2O_3-2mm, (f) 52 wt.% Al_2O_3 + 17g PMMA-2mm, (g) 56 wt.% Al_2O_3 + 17g PMMA-2mm, and (h) 56 wt.% Al_2O_3 + 19g PMMA-2mm.

A1-1.4 Effect of the depth of the water bath

It is well-known that the phase-inversion process occurs in seconds at the interface of the nonsolvent-solvent when the first drop of ceramic slurry hits the surface of the nonsolvent [179, 383]. The exchange of solvent (NMP) and nonsolvent (water) introduces phase separation through the suggested non-isotropic nucleus growth, resulting in the formation of finger-like macro-voids inside as well as the micro-meter sized sponge-like structure on the surface of the ceramic beads [384]. While the solidification and phase-inversion are in progress, the spherical ceramic beads should remain in the water rather than settle at the bottom or reach the walls of the water bath. This is because the partial deformation easily induced by the physical extrusion process can have adverse impacts on micro-channel generation. For instance, the region where physical extrusion occurs may develop partial sponge-like structures, as shown in Figure A4 (f) in red dot frames. The micro-structured ceramic beads in this work were prepared when the depth of the water bath was higher than 50 cm.

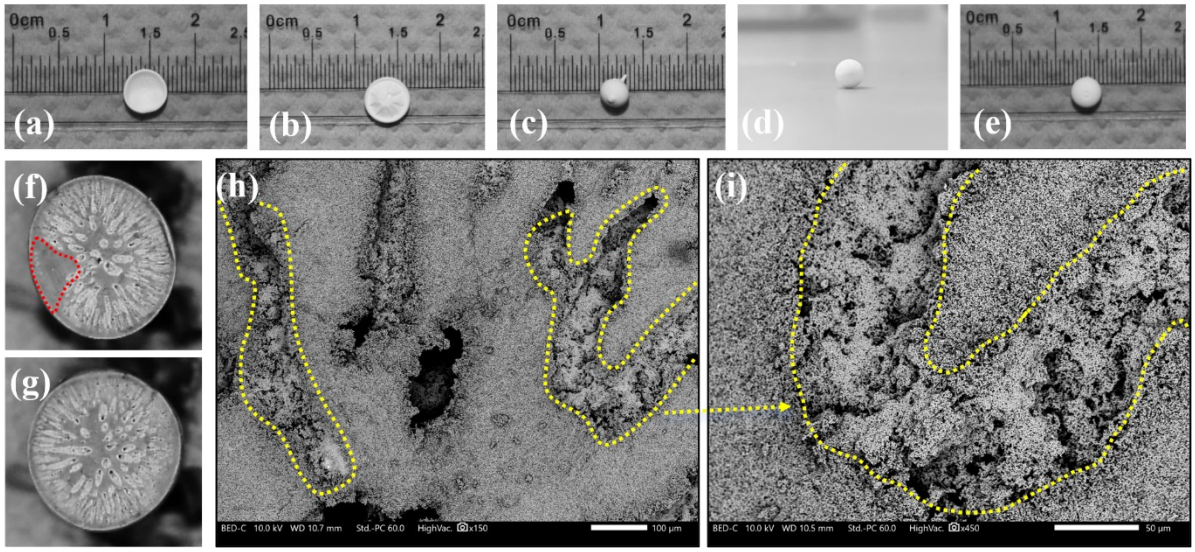

Figure A4 Photographic images of ceramic suspension of 52 wt.% Al_2O_3 + 15 g PMMA-NMP with an air gap of (a) 1 cm, (b) 1.5 cm, (c) 1.7 cm, (d) 2 cm, and (e) 5 cm; Photographic images of ceramic bead 52 wt.% Al_2O_3 with different depths of water bath: (f) < 50 cm; (g) > 50 cm; SEM image of the cross-sectional view of (h) 5Co/MSCB2 and (i) a higher magnification (50 μm).

A1-2 Property of 2Co/MSCB*x* samples

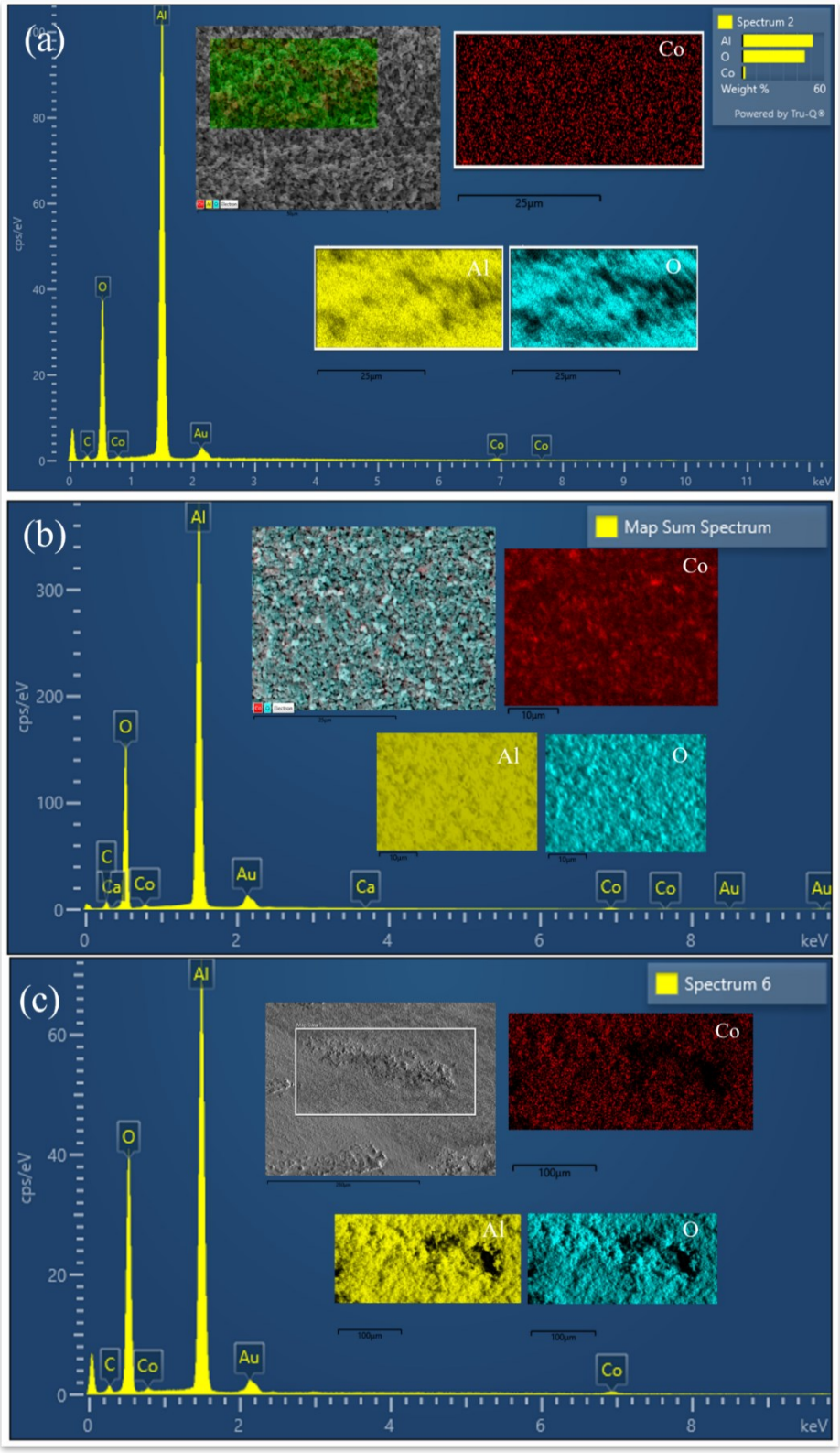

Figure A5 EDS mapping results of Al, O and Co elements for the surface of (a) 2Co/MSCB0; (b) the surface and (c) cross-section of 2Co/MSCB1.

A1-3 MIP results for MSCBs with various alumina concentrations and sizes

Figure A6 provided detailed MIP information for all as-prepared samples, which followed a similar trend to the MSCB1 and MSCB2, with samples without the skin layer exhibiting large pores. Additionally, porosity and pore diameters tend to shift to a smaller value when more alumina was added to the ceramic suspension. This can be attributed to the fact that the more Al_2O_3 contents in the ceramic suspension, the more sponge-like structures can be formed than finger-like structures during the phase-inversion process. In addition, samples with smaller diameters (2 mm) possessed slightly smaller pore diameters on the surface than those of 3 mm samples.

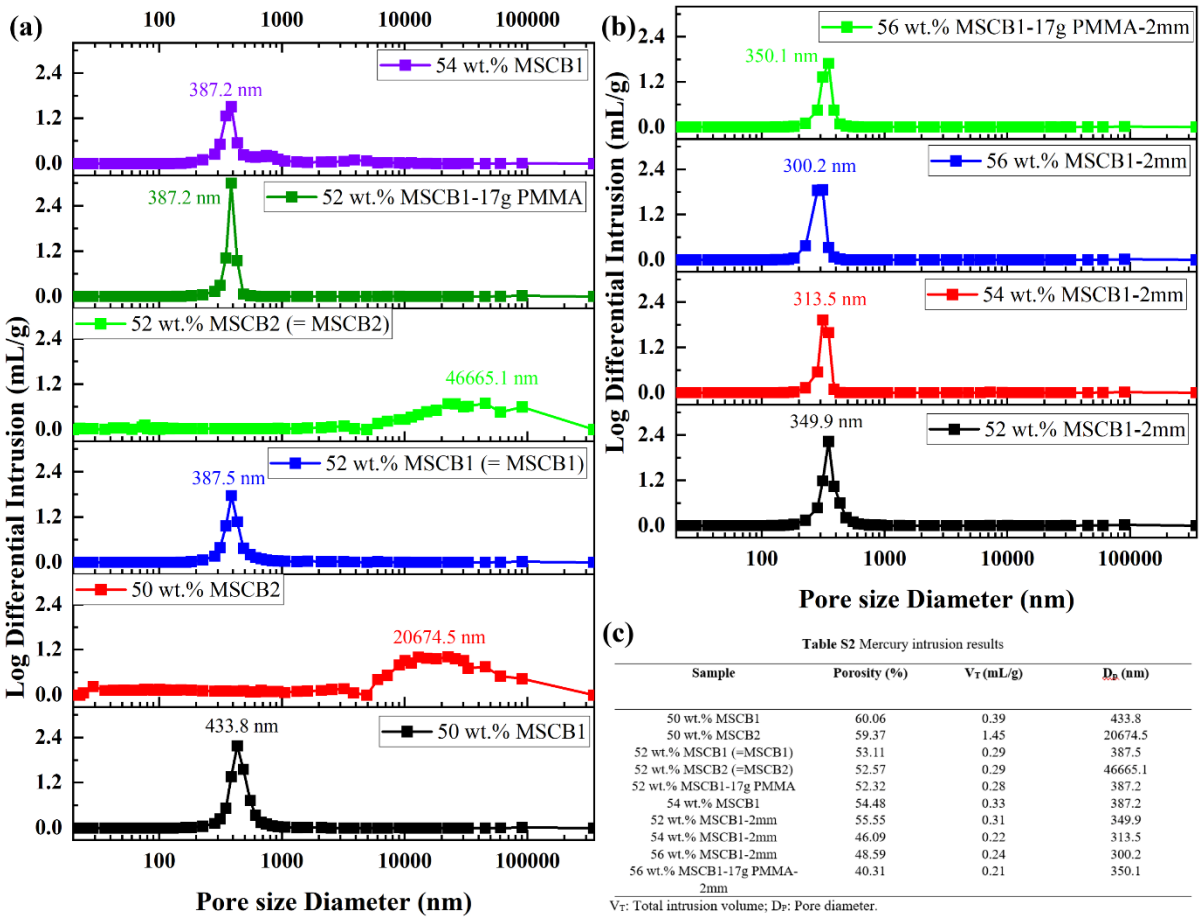

(c)

Table S2 Mercury intrusion results

Sample	Porosity (%)	V_T (mL/g)	D_p (nm)
50 wt.% MSCB1	60.06	0.39	433.8
50 wt.% MSCB2	59.37	1.45	20674.5
52 wt.% MSCB1 (=MSCB1)	53.11	0.29	387.5
52 wt.% MSCB2 (=MSCB2)	52.57	0.29	46665.1
52 wt.% MSCB1-17g PMMA	52.32	0.28	387.2
54 wt.% MSCB1	54.48	0.33	387.2
52 wt.% MSCB1-2mm	55.55	0.31	349.9
54 wt.% MSCB1-2mm	46.09	0.22	313.5
56 wt.% MSCB1-2mm	48.59	0.24	300.2
56 wt.% MSCB1-17g PMMA-2mm	40.31	0.21	350.1

V_T: Total intrusion volume; D_P: Pore diameter.

Figure A6 Pore size distribution of sintered micro-structured ceramic beads of different Al_2O_3 concentrations (a) with dense sponge-like structures (MSCB1) and exposed open channels (MSCB2) on the surface layer and (b) with various slurry compositions or diameters by mercury intrusion porosimetry technique; (c) MIP results of micro-structured ceramic beads.

A1-4 Catalytic performance analysis

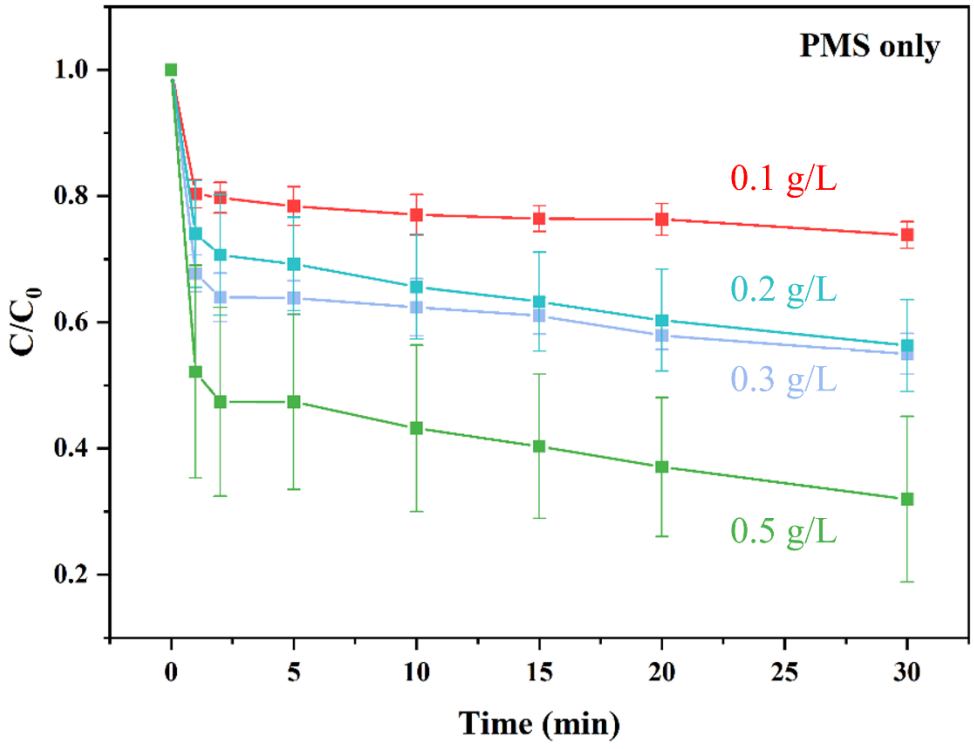

Figure A7 Effect of PMS dosage on the degradation of 20 mg/L SMX at 20 ˚C.

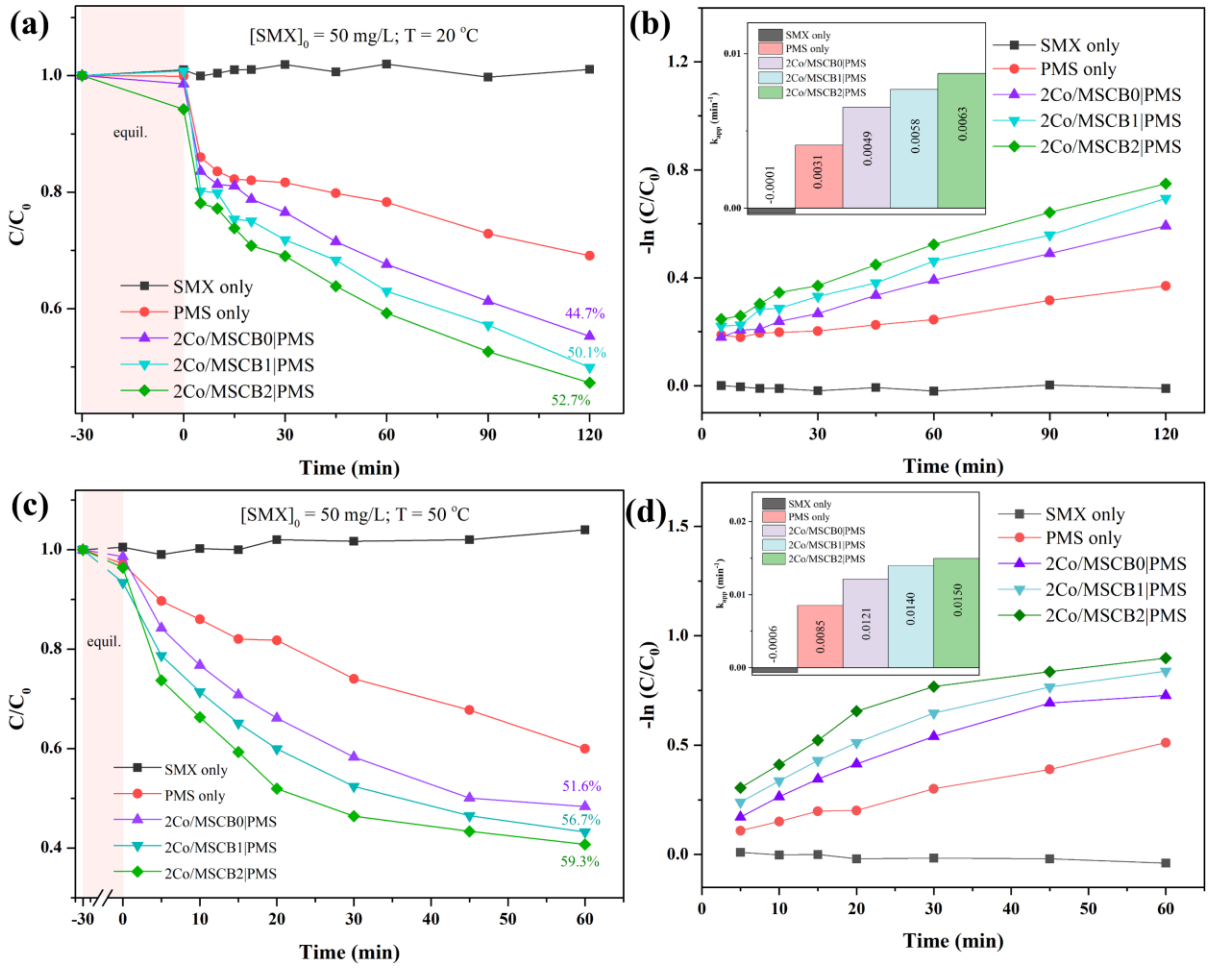

Figure A8 Effect of reaction parameters on the degradation of SMX, their reaction kinetics and the corresponding rate constants (insert): (a, b) $[SMX]_0$ = 50 mg/L, T = 20 °C; (c, d) $[SMX]_0$ = 50 mg/L, T = 50 °C. Reaction Conditions: $[PMS]_0$ = 0.1 g/L, $[catalyst]_0$ = 0.2 g/L, r = 150 rpm.

Table A1 *Textural properties of α-Al_2O_3-based ceramic beads.*

Sample	Surface area (m^2/g)	Total pore volume ($\times10^{-2}$ cc/g)	Average pore diameter (nm)
MSCB0	4.02	1.39	13.78
2Co/MSCB0	2.77	1.16	16.76
MSCB1	4.07	1.37	13.46
2Co/MSCB1	6.85	2.02	11.80
MSCB2	3.65	1.35	14.82
2Co/MSCB2	3.12	1.50	19.23

Appendix 2 Supplementary Information for Chapter 5

A2-1 Effect of sintering temperatures on the Co_3O_4 formation

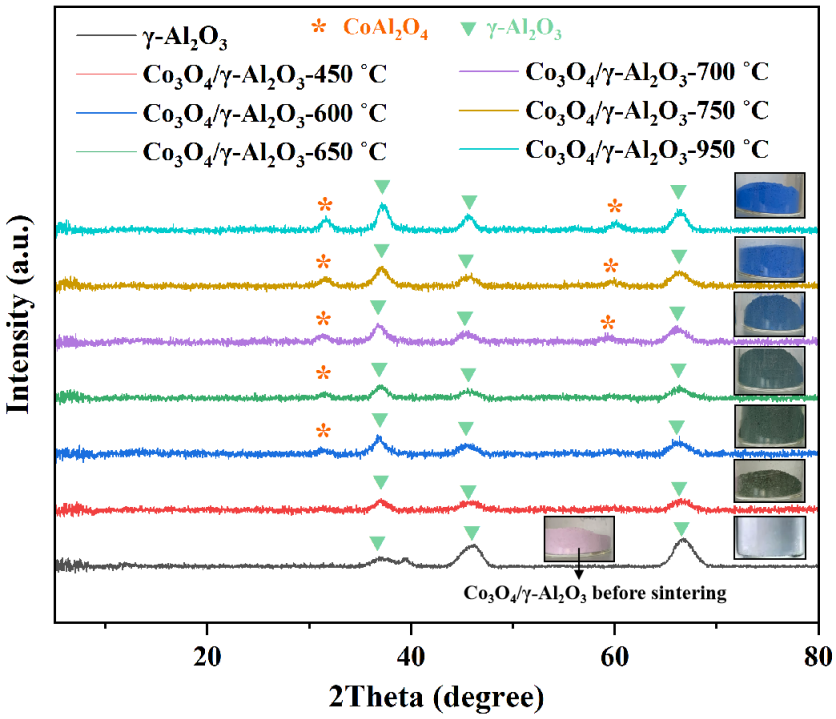

Figure A9 XRD patterns of Co_3O_4/γ-Al_2O_3 sintered at different temperatures.

A2-2 SEM images of AS*x* samples synthesised by two different methods

Test A2-2 SEM images of AS*x* samples after incorporating 2 wt.% Co_3O_4 by two different methods

Figure A10 presented the surface views of 2Co/AS1, 2Co/AS2, 2Co/AS3, 2Co/AS1 (co-imp.), 2Co/AS2 (co-imp.), and 2Co/AS3 (co-imp.) samples. It is observed that the samples prepared using two-step sequential impregnation method generally exhibited relative smaller sizes of exposed open channels on the bead surfaces, with measurements of 7.48 μm, 5.83 μm, and 4.79 μm for 2Co/AS1, 2Co/AS2, and 2Co/AS3, respectively, compared to 8.89 μm, 9.84 μm, and 9.06 μm for 2Co/AS1 (co-imp.), 2Co/AS2 (co-imp.), and 2Co/AS3 (co-imp.). In our recent work, it has been proved that more and larger open channels on the surface could boost the transportation of reactants and products, thereby higher catalytic performance [164]. However, further increasing the γ-Al_2O_3 sol washcoatings (sol 4) resulted in similar pore sizes for samples prepared by these two methods, with 2Co/AS4 and 2Co/AS4 (co-imp.) showing pore sizes of 8.16 μm, and 8.01 μm, respectively, as discussed in the main text. Additionally, Figure A10 (a-c) showed that no obvious γ-Al_2O_3 submicron flakes were visible in the samples prepared by method 1. In contrast, Figure A10 (d-f) demonstrated that all samples prepared by the co-impregnation method exhibited gradually increased amount of γ-Al_2O_3 submicron flakes.

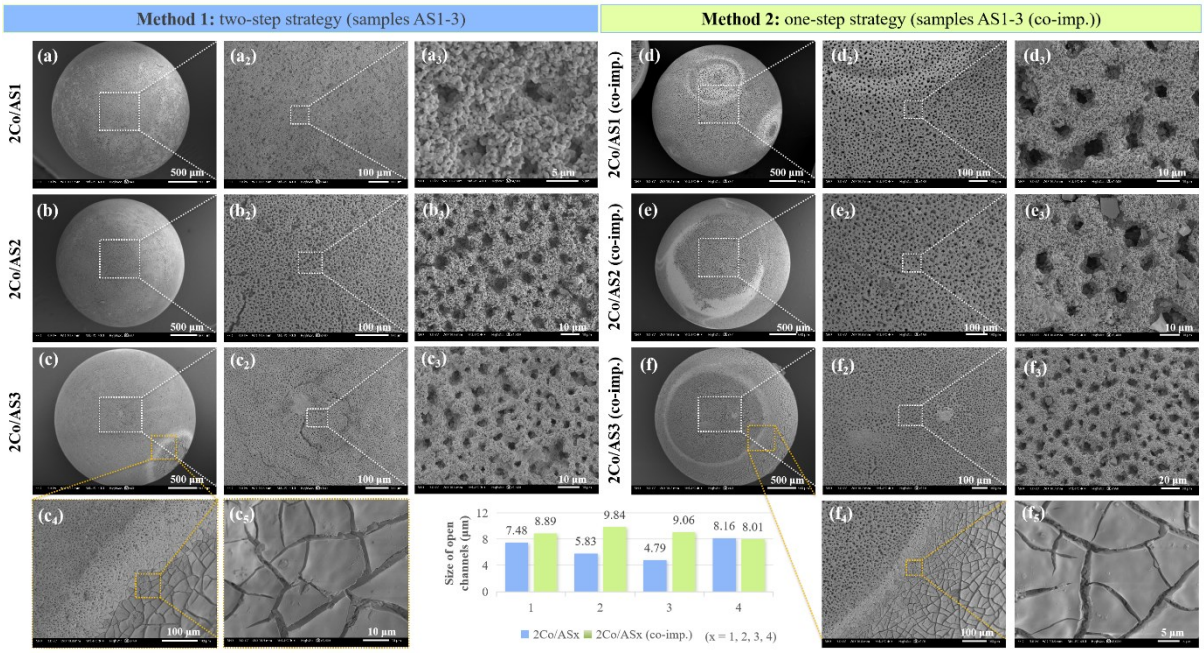

Figure A10 SEM images of surface views of (a-a$_3$) 2Co/AS1, (b-b$_3$) 2Co/AS2, (c-c$_5$) 2Co/AS3, (d-d$_3$) 2Co/AS1 (co-imp.), (e-e$_3$) 2Co/AS2 (co-imp.), and (f-f$_5$) 2Co/AS1-3 (co-imp.); sizes of exposed open channels on the surface of these alumina beads.

Figure A11 (a) shows a high-resolution surface view of 2Co/AS4, revealing densely packed granules. In contrast, the surface view of 2Co/AS4 (co-imp.) in Figure A11 (c, d) revealed a coating of large γ-Al_2O_3 submicron flakes, with a small amount of Co_3O_4 detected in certain area on its surface. The main reason responsible for this might be attributed to the fact that during the one-step co-impregnation process, the mixture of viscous γ-Al_2O_3 sol 4 and cobalt precursor had difficulty in fully infiltrating into the microchannels within the beads due to the low BET surface area of bare AS0 (3.65 m^2/g). As a result, part of the uniform sol and cobalt precursor mixture remained on the bead surface. However, when the AS4 sample was prepared by the sequential impregnation method, the thin layer of washcoated γ-Al_2O_3 sol on the surface of both the finger-like microstructures and the beads initially improved the surface area, allowing for more accessible active sites available for the subsequent deposition of the cobalt precursor. It was reported that although co-impregnation method could generally allow a more uniform dispersion of cobalt [385, 386], sometimes the catalyst support itself plays a more crucial role than the impregnation method and/or the addition order in sequential impregnation process [387]. For example, Rana et al. observed that the dispersion of active phases Mo and Co on various catalyst supports was influenced by the interaction between the precursors of the active phase and the catalyst supports, in addition to the impregnation method used (i.e., Co → (Mo + E), Mo → (Co + E), Co + Mo + E) [386]. Osakoo et al. found that 0.2Pd-10Co-CIP sample, prepared by co-impregnation method, exhibited a larger particle size, whilst 0.2Pd-10Co-SIP sample, prepared by sequential impregnation method, had better dispersion of cobalt [388].

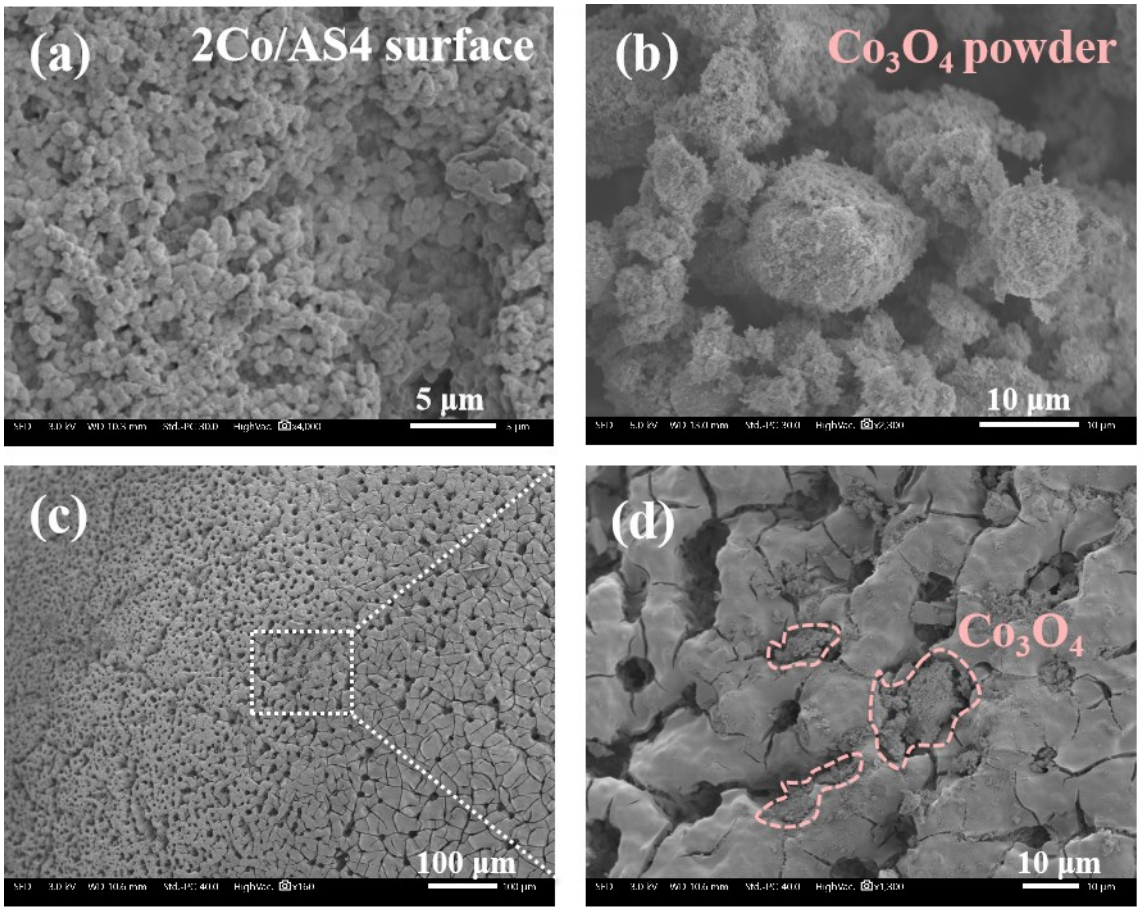

Figure A11 SEM images of (a) surface views of 2Co/AS4, (b) Co_3O_4 powder, and (c-d) surface views of 2Co/AS4 (co-imp.) in certain region with small amount of Co_3O_4.

A2-3 Catalytic performance

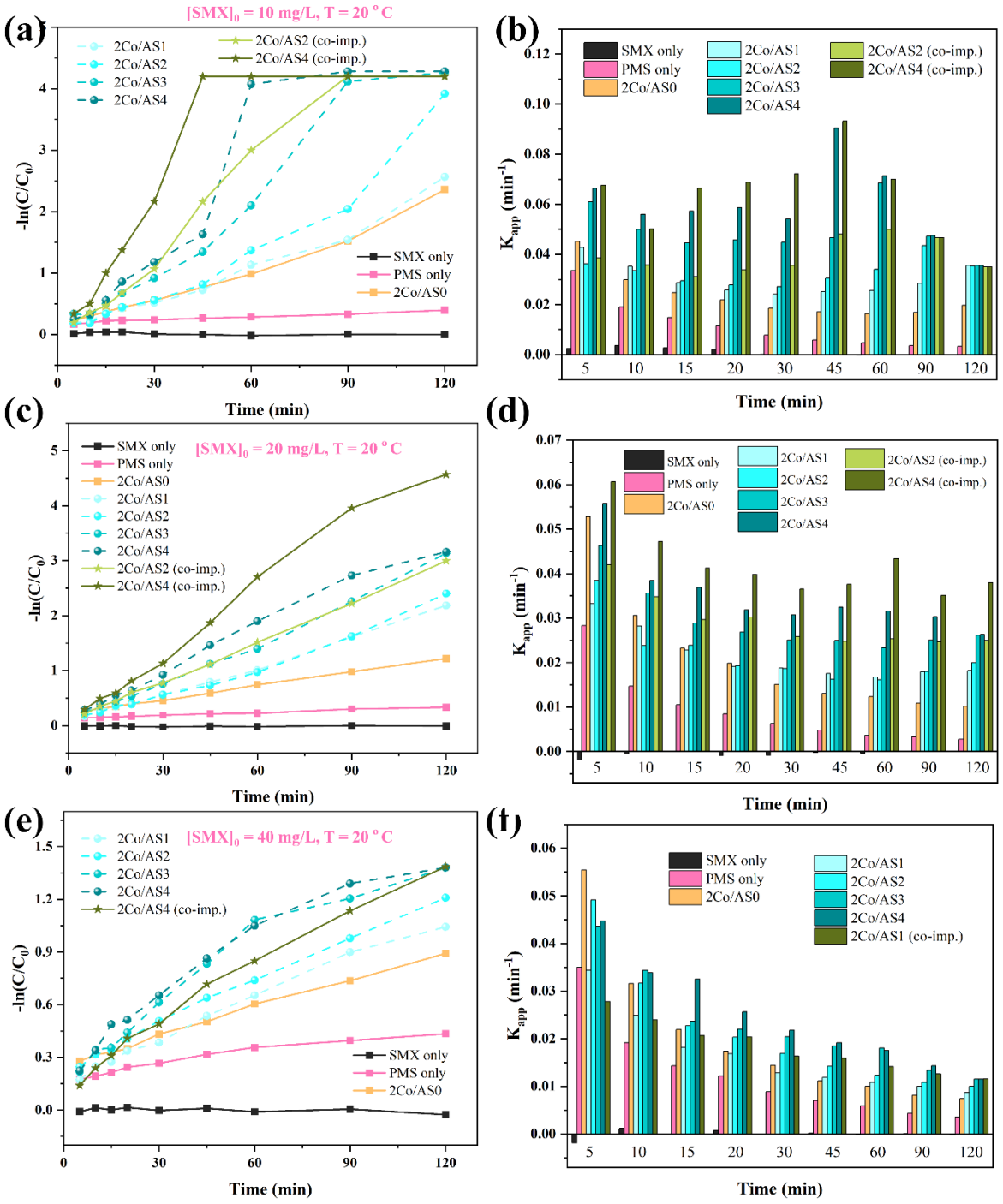

Figure A12 Reaction kinetics and the corresponding rate constants for the degradation of different SMX concentrations at 20 ˚C: (a, b) $[SMX]_0$ = 10 mg/L; (c, d) $[SMX]_0$ = 20 mg/L; (e, f) $[SMX]_0$ = 40 mg/L. Reaction Conditions: $[PMS]_0$ = 0.1 g/L, T = 20 ˚C, $[catalyst]_0$ = 0.2 g/L, r = 150 rpm.

Appendix 3 Supplementary Information for Chapter 6

A3-1 Dip-coating process

Table A2 *Amount of CX in the dip-coated samples and their surface area increment.*

Sample	CX: top up water (vol. ratio)	Mass before CX coating (g)	Mass after CX coating (g)	Coated CX mass (g)	CX mass fraction (%)	S_{BET} increment fraction (%)
ACX1	4:0	10.0091	10.5810	0.5719	5.71	1350.4
ACX2	4:1	10.0077	10.4274	0.4197	4.19	1178.8
ACX3	4:2	10.0080	10.3321	0.3242	3.24	1097.3
ACX4	4:3	10.0082	10.2875	0.2793	2.79	683.2

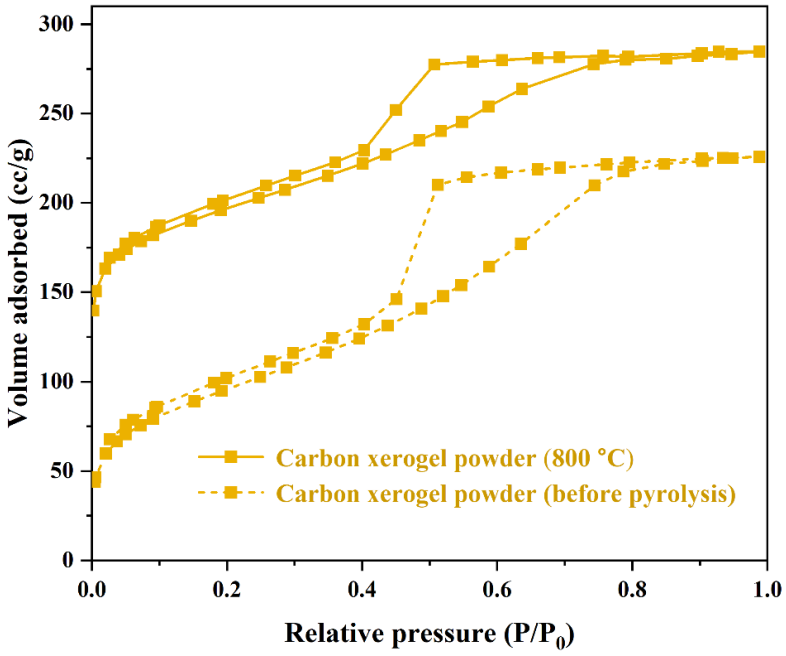

Figure A13 N_2 adsorption-desorption isotherms of carbon xerogel samples before and after pyrolysis.

Text A3-1 Thermal decomposition of Co $(NO_3)_2 \cdot 6H_2O$ in N_2 atmosphere

Figure A14 (a) presents the thermal decomposition of cobalt precursor (Co $(NO_3)_2 \cdot 6H_2O$) in nitrogen atmosphere with a heating rate of 5˚C/min. As illustrated, the thermal decomposition process underwent five stages before completely transformed into cobalt oxide. The weight loss below 240˚C (stage I – stage III) can be attributed to the water loss, with distinct tetra- and dihydrates forming stepwise during these three stages [389]. Afterwards, cobalt nitrate started to decompose into Co_2O_3 (cobalt (III) oxide) at 260˚C and into Co_3O_4 (cobalt (II, III) oxide) at 310˚C [390]. It is noteworthy that the actual mass observed after TGA test (7.10 mg) was consistent with the theoretical result (7.01 mg), suggesting the formation of Co_3O_4 under nitrogen atmosphere. This is further supported by the XRD pattern of the sample after TGA analysis (Fig. S3 (b)), where all diffraction peaks agreed well with the standard cubic spinel phase of Co_3O_4 (PDF#42-1467) [391].

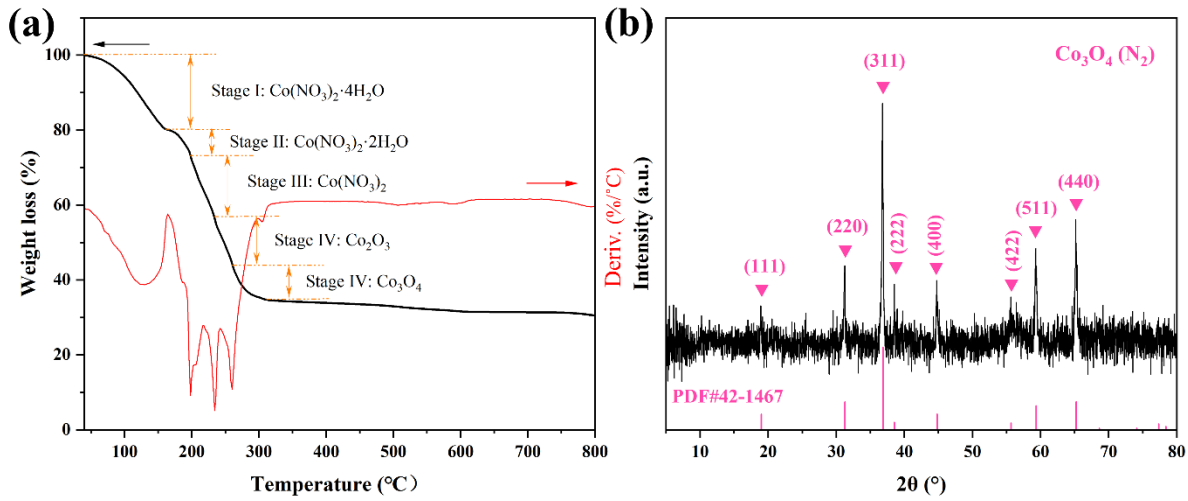

Figure A14 TGA profiles of Co $(NO_3)_2 \cdot 6H_2O$ in nitrogen atmosphere with a heating rate of 5 ˚C/min.

Text A3-2 Evaluation of the catalytic activity

As shown in Figure A15 (a), when the SMX concentration was 10 mg/L, 2Co/ACX1 (99.8%) and 2Co/ACX3 (99.2%) could nearly completely degrade SMX in 60 min. PMS alone could degrade 22.8% of SMX, which is comparable to the literature [185, 296], while catalyst before CX loadings (2Co/ACX0) exhibited higher removal efficiency of 35.7% than that of PMS alone. Likewise, the corresponding reaction kinetics (Figure A15 (b)) and rate constants at 60 min (Figure A15 (c)) followed a similar trend, with 2Co/ACX1 (0.081 min^{-1}) > 2Co/ACX3 (0.079 min^{-1}) > 2Co/ACX0 (0.007 min^{-1}) > PMS only (0.004 min^{-1}). The rate constant for 2Co/ACX1 is 18.7 times higher than PMS alone and 11.0 times higher than 2Co/ACX0, implying that carbon xerogel washcoatings played a key role in the catalytic reactions.

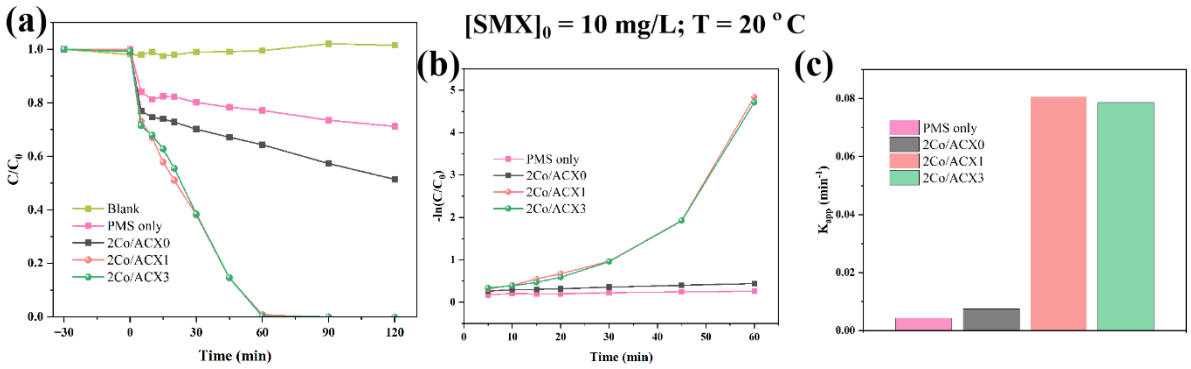

Figure A15 (a) Degradation of 10 mg/L SMX at 20 ˚C, (b) their reaction kinetics, and (c) the corresponding rate constants at 60 min. Reaction Conditions: $[PMS]_0$ = 0.1 g/L, $[catalyst]_0$ = 0.02 g/L, r = 150 rpm.

Figure 6-9 (a) illustrates the degradation of 20 mg/L SMX using 0.02 g/L of catalysts. When the catalyst dosage was increased to 0.2 g/L (Figure A16), 2Co/ACX1 was capable of nearly fully degrading the SMX in just 30 min, far surpassed the other samples. Additionally, the removal efficiency displayed a similar pattern to Figure 6-9 (a), with 17.2%, 36.5%, 60.3%, and 97.2% for PMS alone, 2Co/ACX0, 2Co/AS4, 2Co/ACX1, and 2Co/ACX3 at 30 min, respectively. However, it is worth noting that at this level of catalyst dosage, 8.5% of SMX was eliminated by 2Co/ACX1, which consisted 5.71 % of carbon xerogels, during the adsorption-desorption equilibrium process. This could be attributed to the adsorption capacity of carbonaceous materials, which were extensively used as adsorbents in the practical applications [322, 324, 392]. For reference, Figure A18 shows the adsorption capacity of carbon xerogel powder for SMX removal in comparison with commercial γ-Al_2O_3 beads and powder, as well as γ-Al_2O_3 powder prepared in this work. It is evident that pure carbon xerogel powder was able to completely remove SMX within 2 h without stirring or any additional procedures, whereas all γ-Al_2O_3 samples exhibited limited adsorption capacity even after 10 h (< 10%). This finding further

supports the above-mentioned statement, that is, the adsorption capacity of the carbon xerogel also contributed to the reaction.

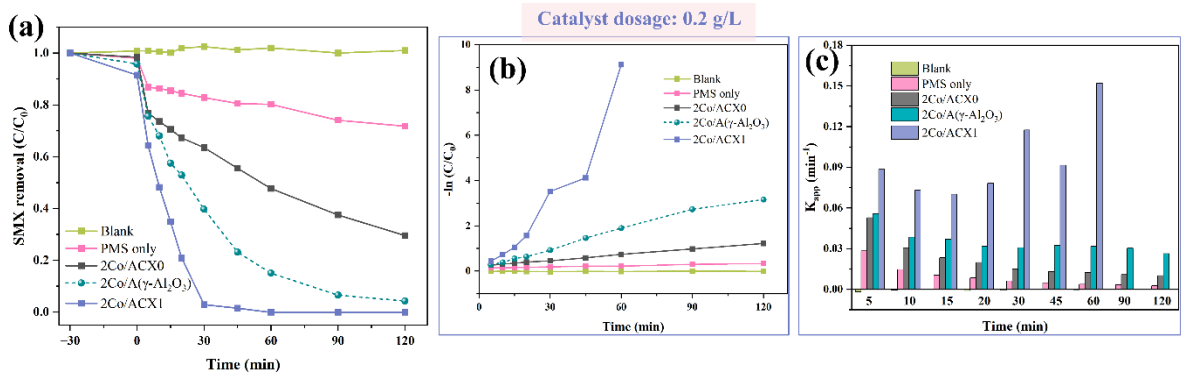

Figure A16 Degradation of 20 mg/L SMX using three types of catalysts at 20 ˚C, (b) their reaction kinetics, and (c) the corresponding rate constants during the whole reaction process. Reaction Conditions: $[PMS]_0$ = 0.1 g/L, $[catalyst]_0$ = 0.2 g/L, r = 150 rpm.

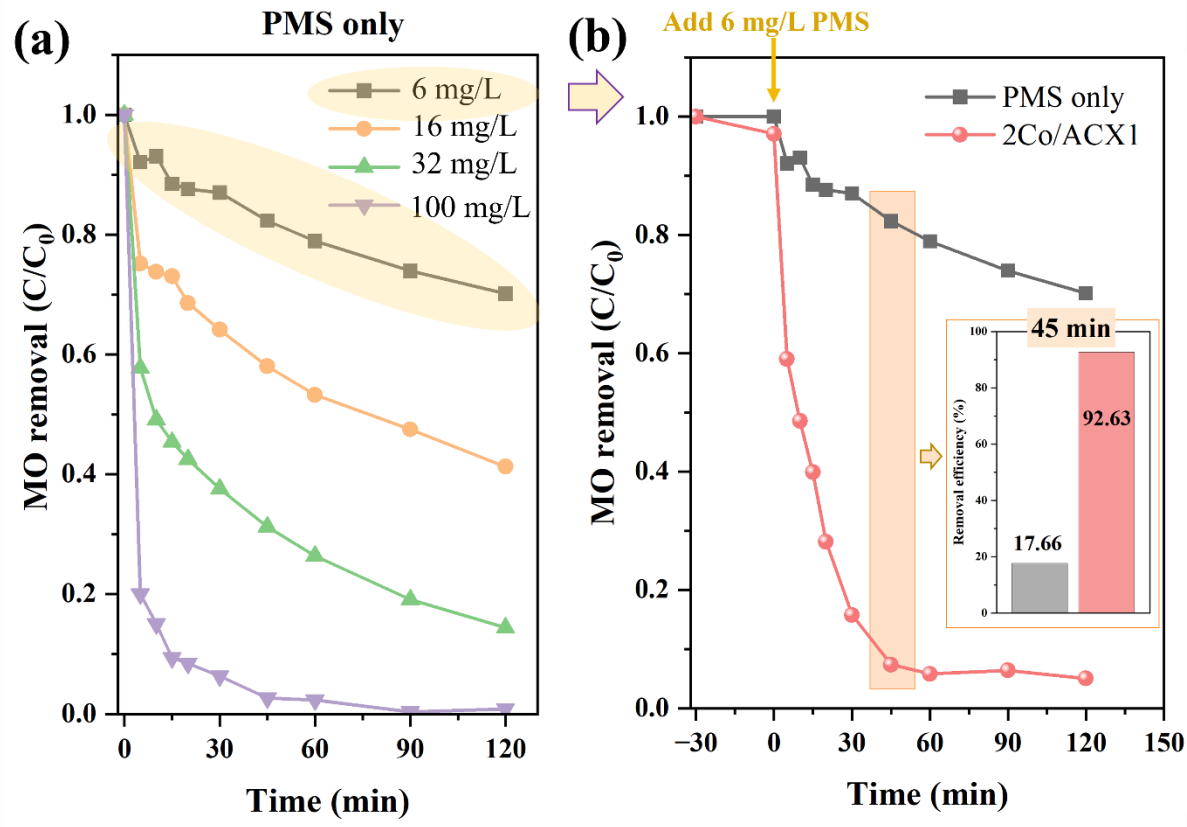

Figure A17 Degradation of 20 mg/L MO with (a) different PMS concentrations and (b) 2Co/ACX1 at 20 ˚C. Reaction Conditions: $[PMS]_0$ = 6 mg/L, $[catalyst]_0$ = 0.1 g/L, r = 150 rpm.

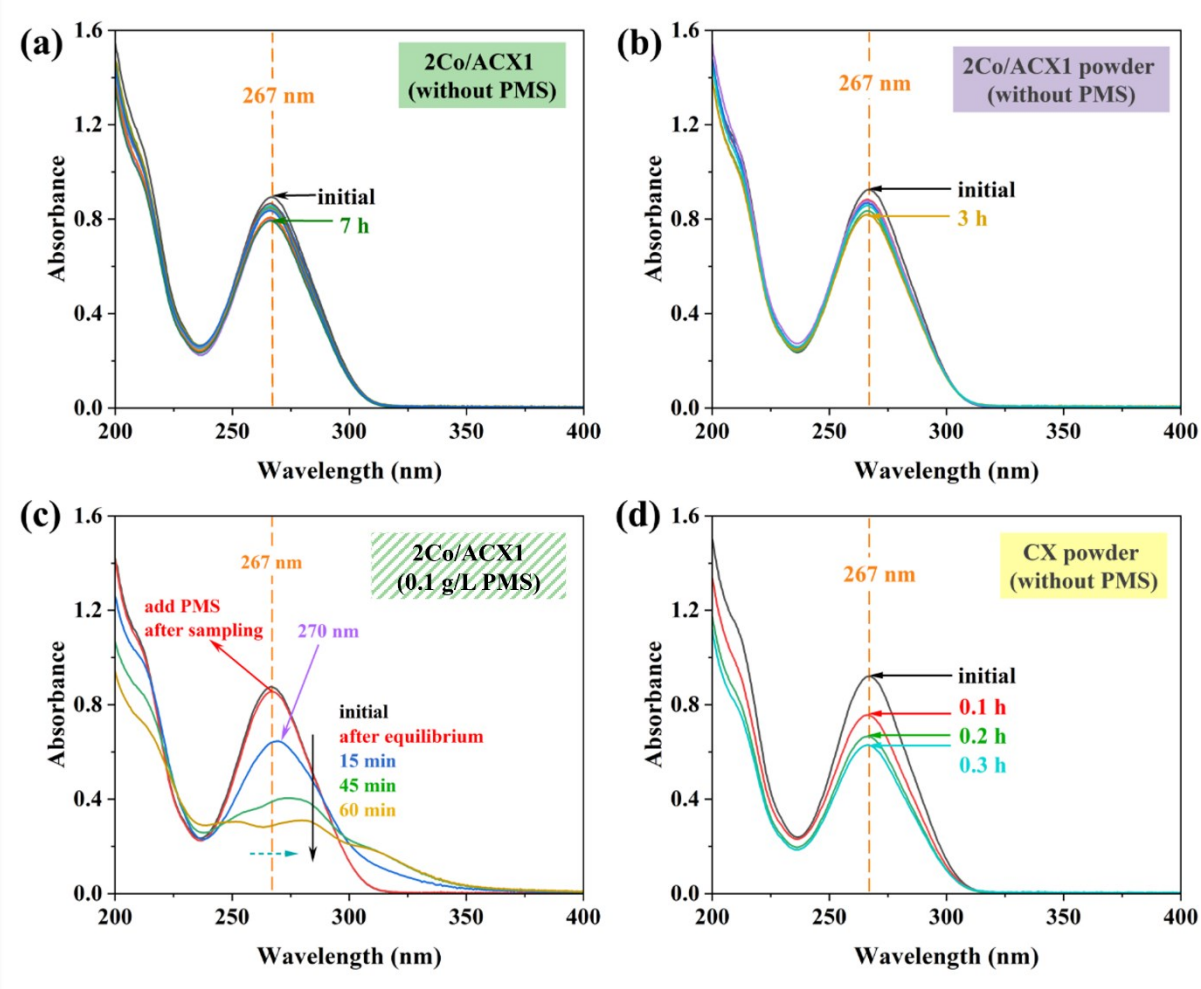

Figure A18 UV-Vis spectra of (a) 2Co/ACX1 without PMS, (b) 2Co/ACX1 powder without, (c) 2Co/ACX1 with 0.1 g/L PMS, and (d) CX powder without PMS for the degradation of SMX. Reaction conditions: [SMX] = 20 mg/L, $[catalyst]_0$ = 0.2 g/L, T = 20 ˚C, r = 150 rpm.

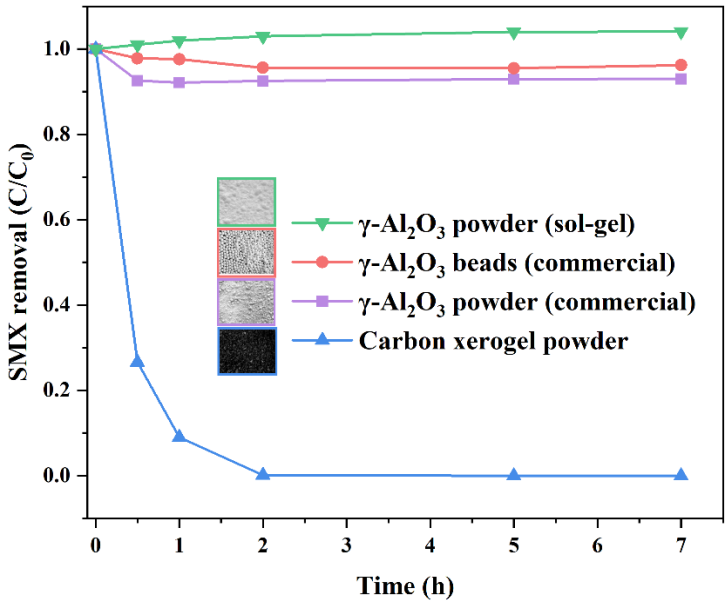

Figure A19 (a) Adsorption capacity analysis using four samples: commercial γ-Al_2O_3 beads and powder, γ-Al_2O_3 powder prepared by a sol-gel method, as well as the carbon xerogel powder. Adsorption conditions: $[SMX]_0$ = 20 mg/L, $[catalyst]_0$ = 0.02 g/L.

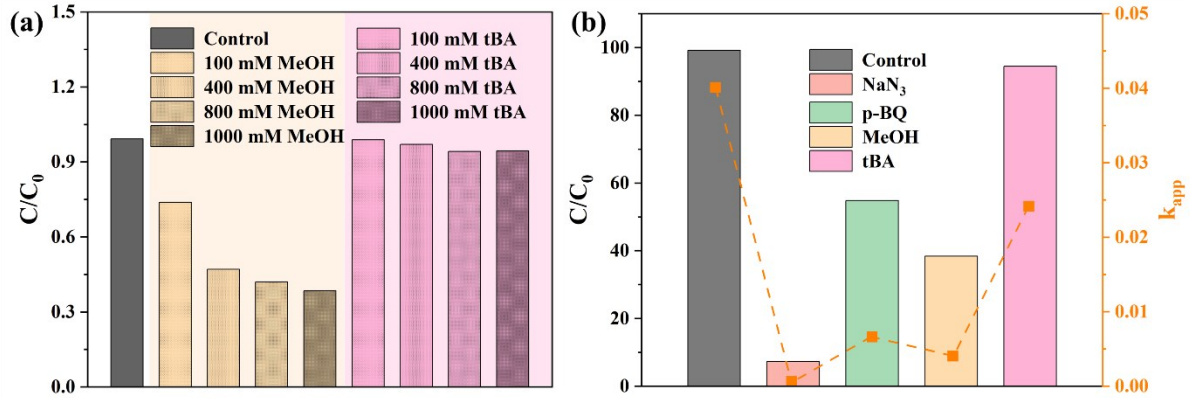

Figure A20 (a) Effect of different concentrations of MeOH and tBA on SMX degradation; (b) Effect of quenching agents on SMX degradation and their reaction rate constants (k). Reaction Conditions: $[SMX]_0$ = 20 mg/L, $[PMS]_0$ = 0.1 g/L, $[catalyst]_0$ = 0.02 g/L, r = 150 rpm (catalyst: 2Co/ACX1).

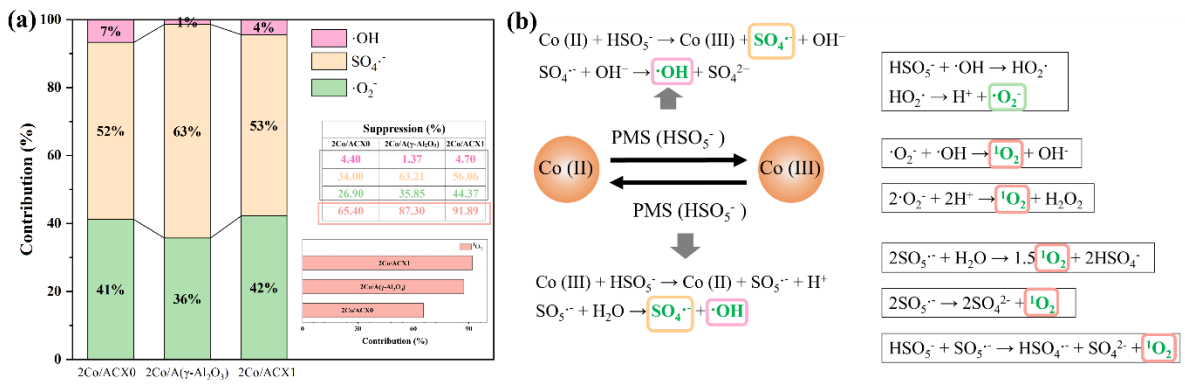

Figure A21 (a) Comparison of reactive radical contributions to SMX degradation under three reaction systems: 2Co/ACX0\PMS, 2Co/AS4\PMS, and 2Co/ACX1\PMS; (b) Main chemical reactions involved in the AOPs process.

Text A3-3 Metal ions test during the reusability tests

Figure A22 (a) illustrated that Co leaching remained low and exhibited a decreasing trend during the cyclic experiment, aligning with findings reported in previously studies [240, 393]. The cobalt leaching values for 2Co/ACX0 were consistently low, decreasing from 0.042 ppm in the 1st run to 0.006 ppm in the 5th run. 2Co/γ-Al_2O_3 exhibited relatively higher values, ranging from 0.082 ppm in the 1st run to 0.042 ppm in the 5th run. In contrast, 2Co/ACX1 started with a higher leaching value of 1.500 ppm in the 1st run, which significantly decreased to 1.002, 0.432, 0.429, and 0.298 ppm in subsequent runs, demonstrating an overall downward trend. Additionally, studies have shown that cobalt leaching is more pronounced under acidic conditions, and this can be mitigated by either minimising pH fluctuations during reactions [394] or increasing the initial pH [395]. Regarding the Al leaching (Figure A22 (b)), all samples exhibited low values, complying with the UK Environment Agency`s standard limit of 1 ppm.

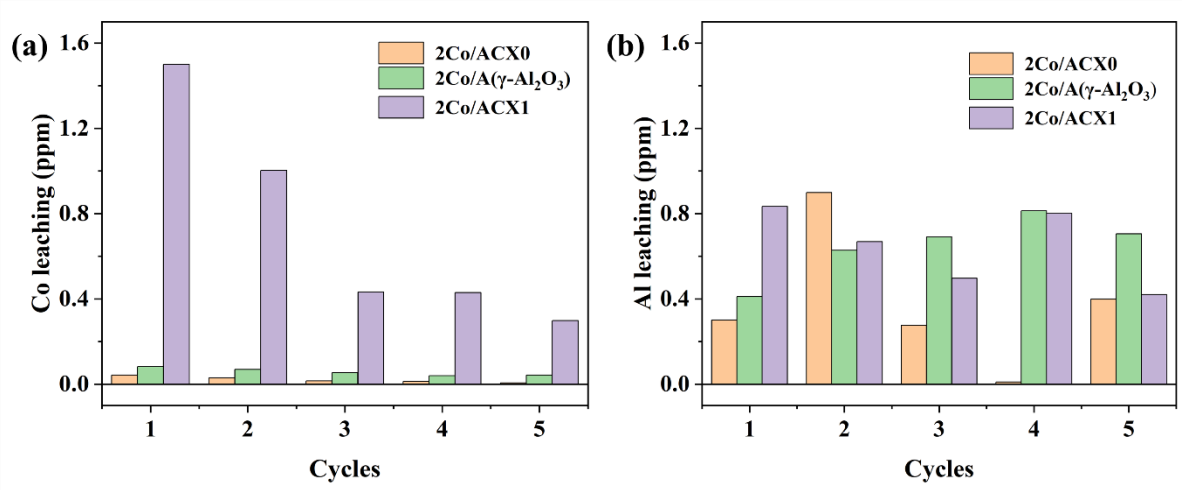

Figure A22 (a) Cobalt ions leaching and (b) aluminium ions leaching results for 2Co/ACX0, 2Co/γ-Al_2O_3, and 2Co/ACX1 samples during the reusability tests. Reaction Conditions: [SMX] = 20 mg/L, $[PMS]_0$ = 0.1 g/L, $[catalyst]_0$ = 0.02 g/L, T = 20 ˚C, initial pH = 5, r = 150 rpm.

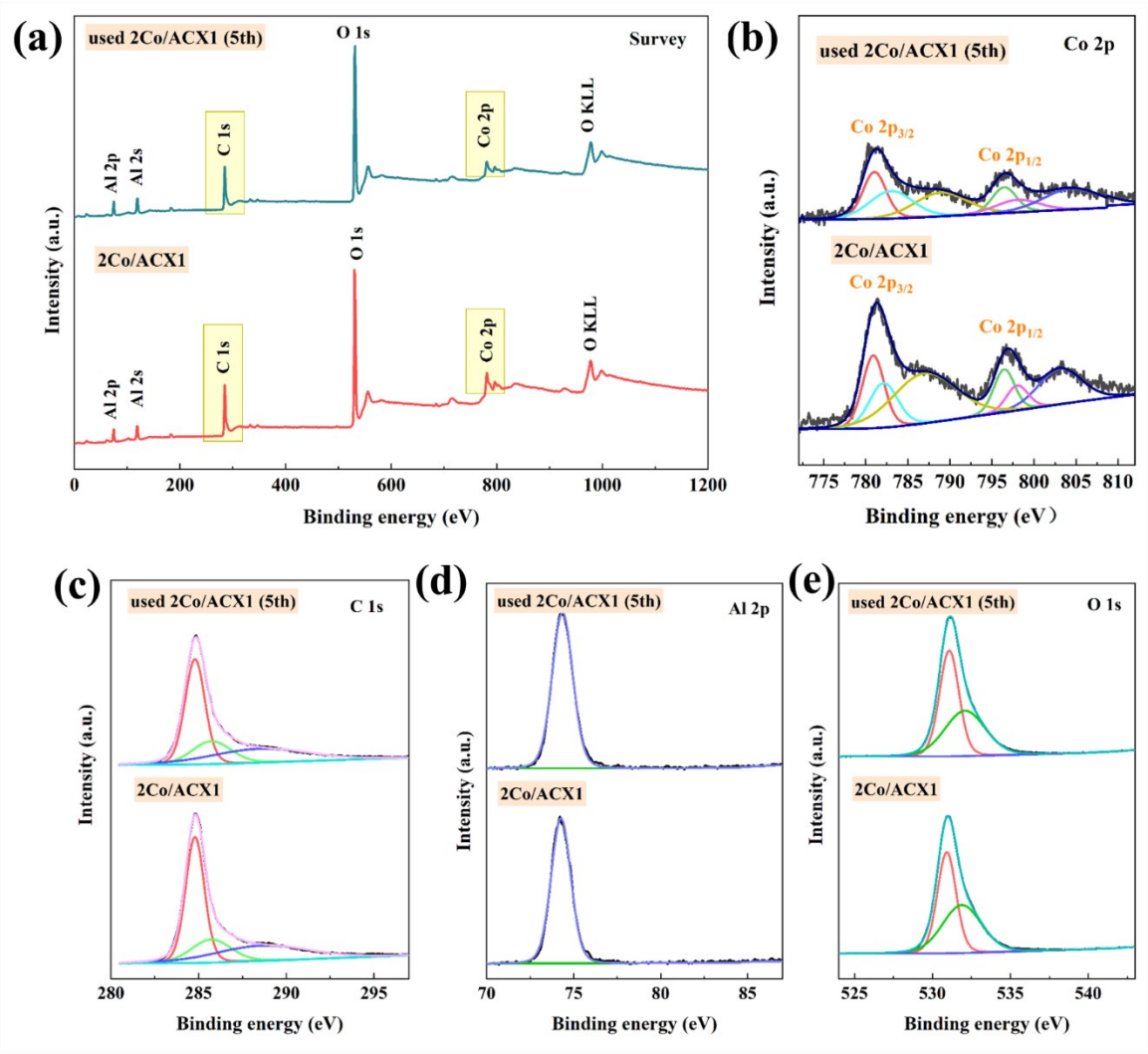

Figure A23 (a) XPS survey spectra, and high-resolution XPS spectra of (b) Co 2p, (c) C 1s, (d) Al 2p, and (e) O 1s of 2Co/ACX1 before and after 5th run.

Appendix 4 Supplementary Information for Chapter 7

Table A3 *Textural properties of silica beads sintered at temperatures ranging from 1000 ˚C to 1200 ˚C.*

Sample	S_{BET} (m^2/g)	V_T (cc/g)	D_p (nm)	Diameter (mm)	Shrinkage percentage (%)
SiO_2 (before sintering)	81.14	0.62	30.52	3.52	/
SiO_2-1000C	112.10	0.84	29.97	3.06	13.07
SiO_2-1020C	94.18	0.66	27.99	2.77	21.31
SiO_2-1040C	42.99	0.45	41.71	2.54	27.84
SiO_2-1050C	26.66	0.16	23.37	2.21	37.22
SiO_2-1060C	21.00	0.07	14.02	2.45	30.40
SiO_2-1080C	10.70	0.05	12.86	2.19	37.78
SiO_2-1100C	8.06	0.02	12.20	2.00	43.18
SiO_2-1120C	0.63	0.01	/	1.89	46.31
SiO_2-1180C	0.62	0.01	/	1.89	46.31
SiO_2-1200C	0.26	0.01	/	1.90	46.02

S_{BET}: Specific surface area; V_T: Total pore volume; D_P: Average pore diameter.

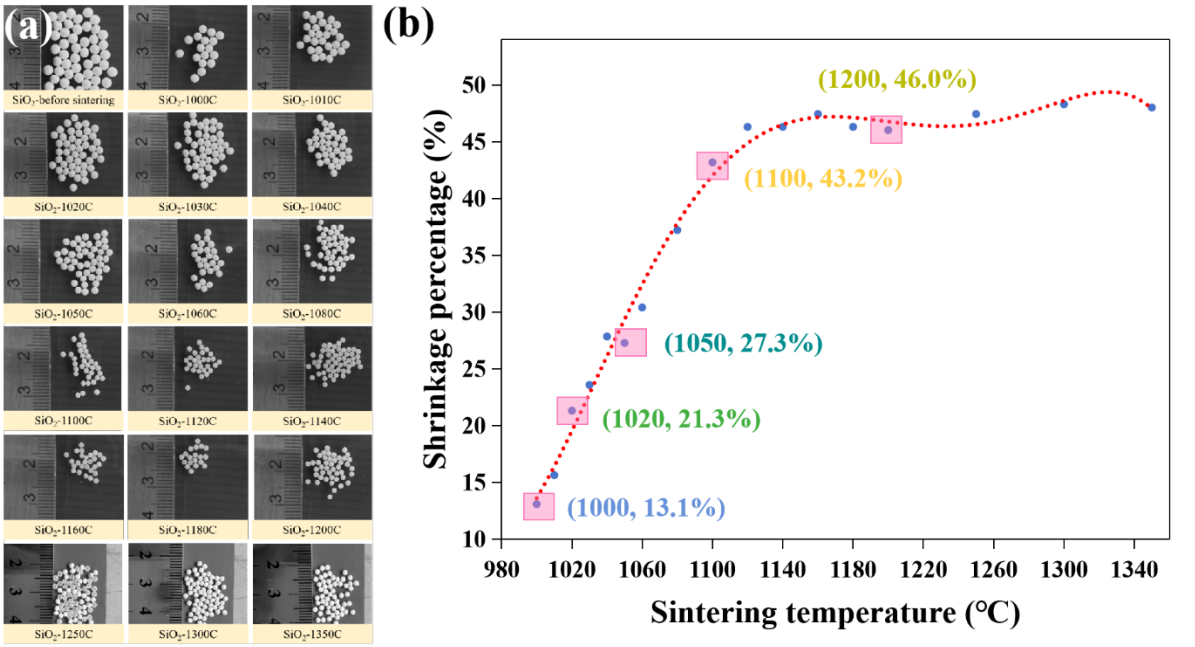

Figure A24 (a) photographic images and (b) shrinkage percentage of microchannel-structured silica beads before and after sintering.

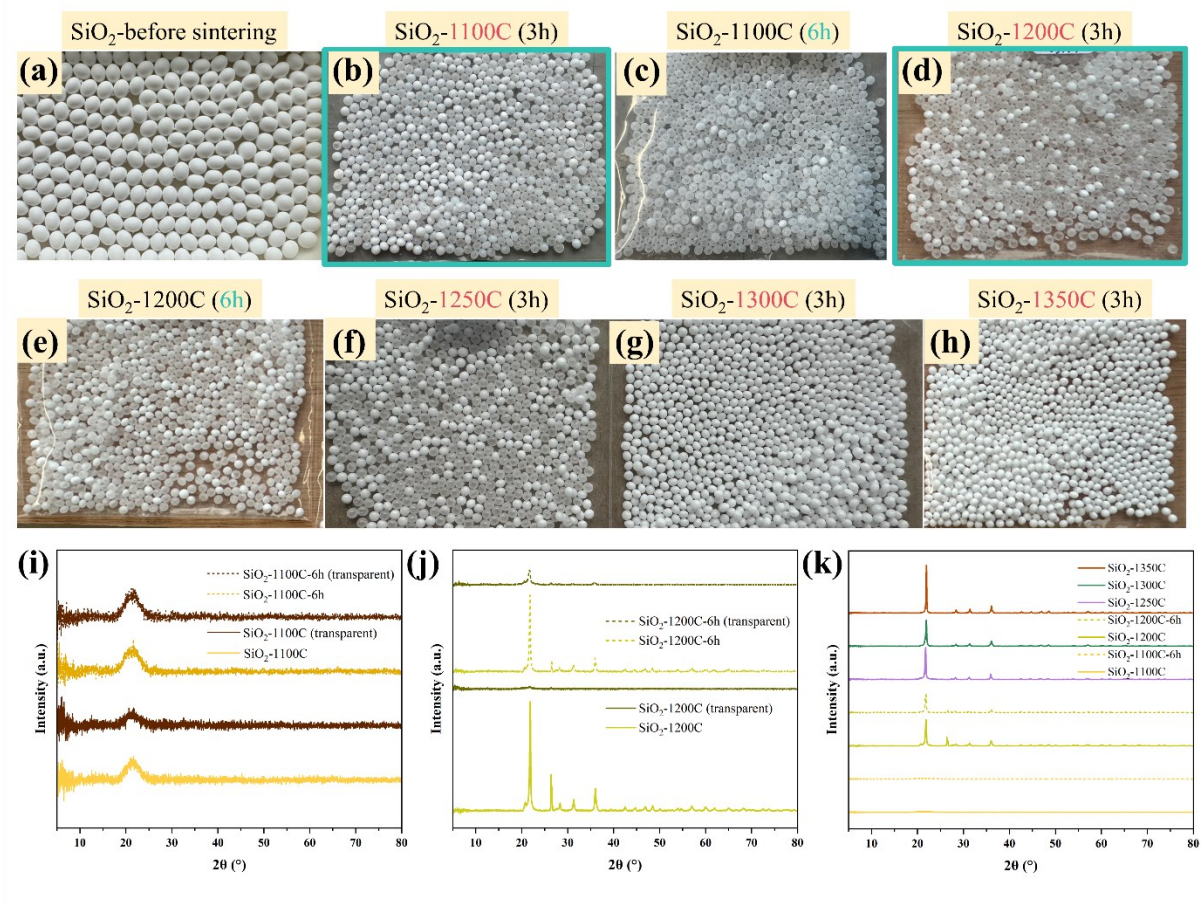

Figure A25 photographic images of microchannel-structured SiO_2 beads (a) before and after sintering at (b) 1100 ˚C for 3 h, (c) 1100 ˚C for 6 h, (d) 1200 ˚C for 3 h, (e) 1200 ˚C for 6 h, (f) 1250 ˚C for 3 h, (g) 1300 ˚C for 3 h, and (h) 1350 ˚C for 3 h; XRD patterns of microchannel-structured SiO_2 beads after sintering at (i) 1100 ˚C, (j) 1200 ˚C, and (k) 1100-1350 ˚C.

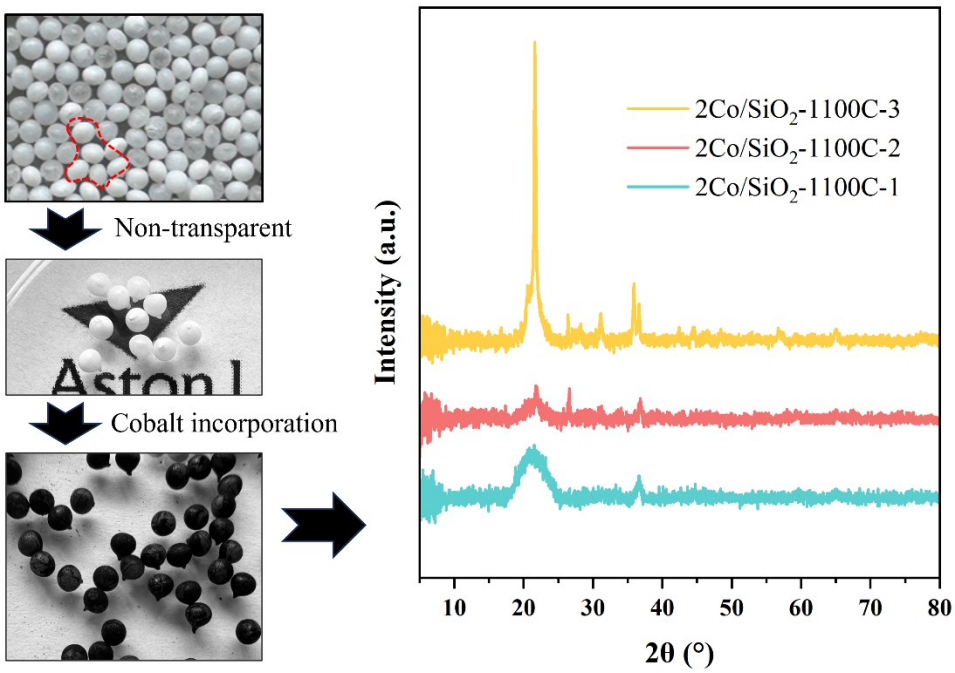

Figure A26 Photographic images of SiO_2-1100C and 2Co/SiO_2-1100C, as well as the XRD patterns of different 2Co/SiO_2-1100C.

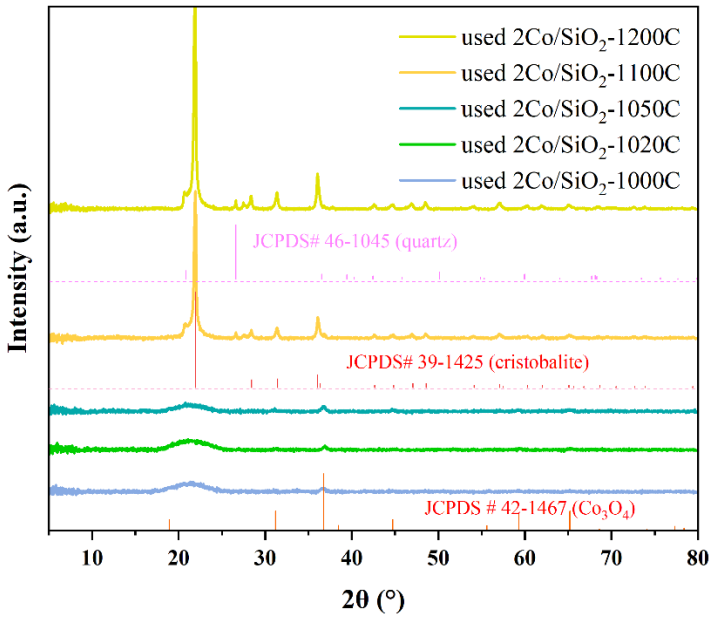

Figure A27 XRD patterns of used microchannel-structured silica beads.